Master's thesis

NTNU
Norwegian University of Science and Technology
Faculty of Engineering
Department of Structural Engineering

Erik Bjørnstad Vådahl and Joachim Slotten

Chloride Ingress Determination in Offshore Concrete Structures Using μ-XRF

Master's thesis in Civil and Environmental Engineering
Supervisor: Klaartje De Weerdt
June 2019

NTNU
Kunnskap for en bedre verden

Erik Bjørnstad Vådahl and Joachim Slotten

Chloride Ingress Determination in Offshore Concrete Structures Using μ-XRF

Master's thesis in Civil and Environmental Engineering
Supervisor: Klaartje De Weerdt
June 2019

Norwegian University of Science and Technology
Faculty of Engineering
Department of Structural Engineering

NTNU
Kunnskap for en bedre verden

Department of Structural Engineering
Faculty of Engineering
NTNU- Norwegian University of Science and Technology

ACCESSIBILITY
Open

MASTER THESIS 2019

SUBJECT AREA:	DATE:	NO. OF PAGES:
Concrete Technology	07.06.2019	155

TITLE:

Chloride Ingress Determination in Offshore Concrete Structures Using µ-XRF

Måling av kloridinntrengning i offshore betongkonstruksjoner ved bruk av µ-XRF

BY:

Erik Bjørnstad Vådahl & Joachim Slotten

SUMMARY:

The purpose of this Master Thesis was to look deeper into chloride ingress determination for offshore concrete structures using µ-XRF. An evaluation of the use of µ-XRF for this purpose was performed through a comparison with two other methods of analysis: potentiometric titration and ICP-MS. µ-XRF was then used to evaluate the chloride ingress in two offshore concrete structures.

A total of 15 concrete cores were received from our industrial partner, Equinor. The cores were collected from two different offshore concrete structures, Structure A and Structure C, both with over 30 years of operation. The oil rigs rest on top of concrete shafts which continue all the way down to the seabed. In Structure A, three cores were collected from the outside of the unsubmerged part of the seawater shaft, and four cores from the inside of the utility shaft. For Structure C all eight cores were collected from the inside of the utility shaft, at elevations ranging between 13 m above to 201 m below sea level. All seven cores from Structure A were analysed using all three methods for the following comparison, while the eight cores obtained from Structure C were analysed solely using µ-XRF.

The comparison was performed by determining chloride content in the seven concrete cores from Structure A. The cores were sawn in two, where one half was used in the µ-XRF and the other was profile ground and used for both potentiometric titration and ICP-MS. The chloride content obtained from all three methods was used to generate chloride profiles which were used for comparison. Accuracy, in addition to other aspects such as complexity, efficiency, and versatility of the different methods, were considered.

The µ-XRF was found to be significantly less accurate for chloride concentration determination than the other methods of analysis. However, the µ-XRF was able to determine the depth at which the chloride concentration had reached below Cl_{crit} = 0.07% Cl/concrete [g/g], with an uncertainty of less than ±2 mm for all concrete cores. Based on this, the accuracy regarding chloride ingress depth measurements with µ-XRF was considered adequate. In addition, µ-XRF surpassed the other methods on several of the other comparison aspects.

Finally, the chloride ingress depth in all of the concrete cores was determined using µ-XRF. Using a critical chloride content of Cl_{crit} = 0.07% Cl/concrete [g/g], we found the chloride ingress in Structure A to range from 3 mm to 29 mm. While for Structure C the range was 0 mm to 34 mm. For Structure A the deepest ingress is found in a core collected from the splash zone on the seawater shaft. While for Structure C the deepest ingress was found in a core collected from the inside of the utility shaft, in an area regularly exposed to seawater. As the cover depth of both structures is 60±10 mm, there is no reason to suspect chloride-induced reinforcement corrosion in the investigated areas.

The 270 mm long concrete core collected from the inside of Structure C, at a depth of 201 m below sea level, showed no detectable signs of mass transport coming from the outside of the 1.2 m thick wall. This led to a conclusion that the hydraulic pressure is not a dominating transport mechanism for such a dense concrete, even at this depth.

RESPONSIBLE TEACHER: Klaartje De Weerdt

SUPERVISORS: Klaartje De Weerdt, Ann-Kristin Kjøs, Kjell Tore Fosså, Mette Rica Geiker

CARRIED OUT AT: NTNU, Trondheim

Institutt for konstruksjonsteknikk
Fakultet for ingeniørvitenskap
NTNU- Norges teknisk- naturvitenskapelige universitet

TILGJENGELIGHET
Åpen

MASTEROPPGAVE 2019

FAGOMRÅDE:	DATO:	ANTALL SIDER:
Betongteknologi	07.06.2019	155

TITTEL:

Måling av kloridinntrengning i offshore betongkonstruksjoner ved bruk av µ-XRF

Chloride Ingress Determination in Offshore Concrete Structures using µ-XRF

UTFØRT AV:

Erik Bjørnstad Vådahl & Joachim Slotten

SAMMENDRAG:

Formålet med denne masteroppgaven var å se nærmere på µ-XRF som målemetode for kloridinntrenging i offshore betongkonstruksjoner. For å evaluere bruk av µ-XRF til dette formålet, ble den sammenlignet med to andre analysemetoder: ICP-MS og potensiometrisk titrering. µ-XRF ble så benyttet for å evaluere kloridinntrengingen i to offshore betongkonstuksjoner.

15 betongkjerner ble sendt fra vår industripartner, Equinor. Disse ble hentet fra to ulike offshore betongkonstruksjoner, «Structure A» og «Structure C», begge med over 30 års operasjonstid. Selve oljeriggen hviler på betongskaft som går ned til havbunnen. Fra «Structure A» ble tre kjerner tatt fra utsiden av sjøvannsskaftet over havnivå, samt fire kjerner fra innsiden av utstyrsskaftet. For «Structure C» ble alle de åtte kjernene hentet fra innsiden av utstyrsskaftet. Alle de syv kjernene fra «Structure A» ble analysert ved bruk av alle tre metodene, mens kjernene fra «Structure C» kun ble analysert ved bruk av µ-XRF.

Målemetodene ble sammenlignet ved at kloridinnholdet i de syv betongkjernene fra «Structure A» ble bestemt. Kjernene ble saget i to, hvor den ene halvdelen ble brukt til µ-XRF mens den andre ble brukt til ICP-MS og titrering. Kloridinnholdet ble så bestemt ved bruk av de respektive analysemetodene og det ble laget kloridprofiler som var grunnlaget for sammenligningen. Nøyaktigheten, sammen med andre aspekter som kompleksitet, effektivitet og allsidighet, ble så vurdert.

Resultatene indikerte at µ-XRF hadde betraktelig lavere nøyaktighet enn de andre metodene for bestemmelse av kloridinnhold. Kloridinntrengningsdybden målt med µ-XRF derimot, vurdert mot et kritisk kloridnivå, Cl_{crit} = 0.07% Cl/betong [g/g], viste seg å kunne bestemmes med en usikkerhet på under ±2 mm for samtlige betongkjerner. Det ble på bakgrunn av dette, konkludert med at nøyaktigheten av kloridinntrengningsdybden var tilstrekkelig ved bruk av µ-XRF. I tillegg, viste den seg å være svært konkurransedyktig på flere av de andre vurderte aspektene.

Til slutt ble kloridinntrengningsdybden i samtlige betongkjerner bestemt med bruk av µ-XRF. Vurdert mot et kritisk kloridnivå, Cl_{crit} = 0.07% Cl/betong [g/g], varierte dybden mellom 3mm og 29 mm i «Structure A» og mellom 0 mm og 34 mm i «Structure C». I «Structure A» finner vi den største inntrengningsdybden i skvalpesonen på utsiden av utstyrsskaftet, mens i «Structure C» finner vi den største inntrengningsdybden på innsiden av utstyrsskaftet, i et område regelmessig eksponert for sjøvann. Siden den tilsiktede betongoverdekningen er 60±10 mm i begge konstruksjonene, er det ingen mistanke om kloridindusert armeringskorrosjon i de undersøkte områdene.

Den 270 mm lange betongkjernen som ble hentet fra innsiden av «Structure C» på 201 meters dyp, viste ingen synlige tegn på massetransport fra utsiden av den 1.2 m tykke veggen. Det ble derfor konkludert med at det hydrauliske trykket ikke er en dominerende transportmekanisme i en så tett betong, selv ved et slikt dyp.

FAGLÆRER: Klaartje De Weerdt

VEILEDERE: Klaartje De Weerdt, Ann-Kristin Kjøs, Kjell Tore Fosså, Mette Rica Geiker

UTFØRT VED: NTNU, Trondheim

Preface

This Master Thesis is the concluding part of our Master of Science in Civil and Environmental Engineering with degree specialisation in Concrete Technology at the Norwegian University of Science and Technology (NTNU), spring 2019. The Master Thesis is a continuation of our specialisation project in Concrete Technology, *Durability Challenges in Offshore Concrete Structures,* fall 2018.

We would like to thank our supervisor Professor Klaartje de Weerdt for exceptional guidance throughout the work. Ph.D. student Petter Hemstad for valued guidance, especially regarding calculations and sample preparation for ICP-MS. Further, we would like to thank co-supervisors Ann-Kristin Kjøs (Equinor), Adjunct Professor Kjell Tore Fosså (Kværner) and Professor Mette Geiker (NTNU) for being available for questions and for valuable discussions and feedback throughout the work. Tobias Danner (SINTEF) for teaching us how to operate the µ-XRF. Ola Skjølsvold (SINTEF) for managing preparation and titration for our cores. Roger Leistad (SINTEF) for performing profile grinding. Siri Trapnes (SINTEF) for performing the potentiometric titration analysis. Syverin Lierhagen (NTNU) for performing the ICP-MS analysis. Steinar Seehuus (NTNU) for sawing of concrete cores. Julian Tolchard (SINTEF) for valuable information regarding radiation physics relevant for µ-XRF analysis.

Abstract

The purpose of this Master Thesis was to look deeper into chloride ingress determination for offshore concrete structures using µ-XRF. An evaluation of the use of µ-XRF for this purpose was performed through a comparison with two other methods of analysis: potentiometric titration and ICP-MS. µ-XRF was then used to evaluate the chloride ingress in two offshore concrete structures.

A total of 15 concrete cores were received from our industrial partner, Equinor. The cores were collected from two different offshore concrete structures, Structure A and Structure C, both with over 30 years of operation. The oil rigs rest on top of concrete shafts which continue all the way down to the seabed. In Structure A, three cores were collected from the outside of the unsubmerged part of the seawater shaft, and four cores from the inside of the utility shaft. For Structure C all eight cores were collected from the inside of the utility shaft, at elevations ranging between 13 m above to 201 m below sea level. All seven cores from Structure A were analysed using all three methods for the following comparison, while the eight cores obtained from Structure C were analysed solely using µ-XRF.

The comparison was performed by determining chloride content in the seven concrete cores from Structure A. The cores were sawn in two, where one half was used in the µ-XRF and the other was profile ground and used for both potentiometric titration and ICP-MS. The chloride content obtained from all three methods was used to generate chloride profiles which were used for comparison. Accuracy, in addition to other aspects such as complexity, efficiency, and versatility of the different methods, were considered.

The µ-XRF was found to be significantly less accurate for chloride concentration determination than the other methods of analysis. However, the µ-XRF was able to determine the depth at which the chloride concentration had reached below Cl_{crit} = 0.07% Cl/concrete [g/g], with an uncertainty of less than ±2 mm for all concrete cores. Based on this, the accuracy regarding chloride ingress depth measurements with µ-XRF was considered adequate. In addition, µ-XRF surpassed the other methods on several of the other comparison aspects.

Finally, the chloride ingress depth in all of the concrete cores was determined using µ-XRF. Using a critical chloride content of Cl_{crit} = 0.07% Cl/concrete [g/g], we found the chloride ingress in Structure A to range from 3 mm to 29 mm. While for Structure C the range was 0 mm to 34 mm. For Structure A the deepest ingress is found in a core collected from the splash zone on the seawater shaft. While for Structure C the deepest ingress was found in a core collected from the inside of the utility shaft, in an area regularly exposed to seawater. As the cover depth of both structures is 60±10 mm, there is no reason to suspect chloride-induced reinforcement corrosion in the investigated areas.

The 270 mm long concrete core collected from the inside of Structure C, at a depth of 201 m below sea level, showed no detectable signs of mass transport coming from the outside of the 1.2 m thick wall. This led to a conclusion that the hydraulic pressure is not a dominating transport mechanism for such a dense concrete, even at this depth.

Sammendrag

Formålet med denne masteroppgaven var å se nærmere på μ-XRF som målemetode for kloridinntrenging i offshore betongkonstruksjoner. For å evaluere bruk av μ-XRF til dette formålet, ble den sammenlignet med to andre analysemetoder: ICP-MS og potensiometrisk titrering. μ-XRF ble så benyttet for å evaluere kloridinntrengingen i to offshore betongkonstuksjoner.

15 betongkjerner ble sendt fra vår industripartner, Equinor. Disse ble hentet fra to ulike offshore betongkonstruksjoner, «Structure A» og «Structure C», begge med over 30 års operasjonstid. Selve oljeriggen hviler på betongskaft som går ned til havbunnen. Fra «Structure A» ble tre kjerner tatt fra utsiden av sjøvannsskaftet over havnivå, samt fire kjerner fra innsiden av utstyrsskaftet. For «Structure C» ble alle de åtte kjernene hentet fra innsiden av utstyrsskaftet. Alle de syv kjernene fra «Structure A» ble analysert ved bruk av alle tre metodene, mens kjernene fra «Structure C» kun ble analysert ved bruk av μ-XRF.

Målemetodene ble sammenlignet ved at kloridinnholdet i de syv betongkjernene fra «Structure A» ble bestemt. Kjernene ble saget i to, hvor den ene halvdelen ble brukt til μ-XRF mens den andre ble brukt til ICP-MS og titrering. Kloridinnholdet ble så bestemt ved bruk av de respektive analysemetodene og det ble laget kloridprofiler som var grunnlaget for sammenligningen. Nøyaktigheten, sammen med andre aspekter som kompleksitet, effektivitet og allsidighet, ble så vurdert.

Resultatene indikerte at μ-XRF hadde betraktelig lavere nøyaktighet enn de andre metodene for bestemmelse av kloridinnhold. Kloridinntrengningsdybden målt med μ-XRF derimot, vurdert mot et kritisk kloridnivå, Cl_{crit} = 0.07% Cl/betong [g/g], viste seg å kunne bestemmes med en usikkerhet på under ±2 mm for samtlige betongkjerner. Det ble på bakgrunn av dette, konkludert med at nøyaktigheten av kloridinntrengningsdybden var tilstrekkelig ved bruk av μ-XRF. I tillegg, viste den seg å være svært konkurransedyktig på flere av de andre vurderte aspektene.

Til slutt ble kloridinntrengningsdybden i samtlige betongkjerner bestemt med bruk av μ-XRF. Vurdert mot et kritisk kloridnivå, Cl_{crit} = 0.07% Cl/betong [g/g], varierte dybden mellom 3 mm og 29 mm i «Structure A» og mellom 0 mm og 34 mm i «Structure C». I «Structure A» finner vi den største inntrengningsdybden i skvalpesonen på utsiden av utstyrsskaftet, mens i «Structure C» finner vi den største inntrengningsdybden på innsiden av utstyrsskaftet, i et område regelmessig eksponert for sjøvann. Siden den tilsiktede betongoverdekningen er 60±10 mm i begge konstruksjonene, er det ingen mistanke om kloridindusert armeringskorrosjon i de undersøkte områdene.

Den 270 mm lange betongkjernen som ble hentet fra innsiden av «Structure C» på 201 meters dyp, viste ingen synlige tegn på massetransport fra utsiden av den 1.2 m tykke veggen. Det ble derfor konkludert med at det hydrauliske trykket ikke er en dominerende transportmekanisme i en så tett betong, selv ved et slikt dyp.

Table of Contents

Dictionary

Abbreviations

% Cl/binder	Mass percent of chlorides per binder
% Cl/Ca	Mass percent of chlorides per calcium
% Cl/concrete	Mass percent of chlorides per dry concrete
% Cl/paste	Mass percent of chlorides per cement paste
$A\%_{agg.\mu XRF}$	Area percentage of aggregates from µ-XRF
$A\%_{paste.\mu XRF}$	Area percentage of paste from µ-XRF
Cl_{crit}	Critical chloride content
CPS	Counts per second
C-S-H	Calcium-Silicate-Hydrate
eV	Electron Volt
ICP-MS	Inductively Coupled Plasma Mass Spectrometry
ITZ	Interfacial Transition Zones
M	Molar mass
m	Mass
M-S-H	Magnesium-Silicate-Hydrate
w/b-ratio	The mass ratio of water content to binder content
µ-XRF	Micro X-ray Fluorescence
σ	Standard deviation
ρ	Density

Elements & Oxides

Al_2O_3	Aluminium oxide
C_3A	Aluminate
C_4AF	Ferrite
$Ca(OH)_2$	Portlandite
CaO	Calcium oxide
Fe_2O_3	Iron (III) oxide
FeO	Iron (II) oxide
K_2O	Potassium oxide
$Mg(OH)_2$	Brucite
MgO	Magnesium oxide
MnO	Manganese oxide
Na_2O	Sodium oxide
Na_2O	Sodium oxide
P_2O_5	Phosphorus pentoxide
SiO_2	Silicon dioxide
SO_3	Sulphur trioxide
TiO_2	Titanium dioxide

1 Introduction

During the 20th-century chloride-initiated reinforcement corrosion got acknowledged as one of the most severe deterioration processes for concrete structures. In Norway, the effect was known to man through deterioration of bridges built along the western coast in the marine environment. In the late 80s, this seemingly suspicious spalling of the concrete bridges initiated several research programs on the topic by the Norwegian Public Road Administration [1].

At the same period-of-time, the construction of concrete oil platforms already was a familiar sight along the southwestern coast of Norway. Due to harsh weather conditions and more upscaled production rate in the North Sea, drilling technology companies had to experiment with structures made of concrete instead of the more common rigs of steel. This to make sure the oil platforms could handle deep waters and massive equipment.

One big actor in this industry is Equinor which is our industrial partner for the following work. They are operating in total 11/12 concrete platforms in the North Sea and have several years of experience regarding inspection and maintenance of these. For further analysis in this thesis, Equinor will provide us with concrete samples that have been exposed to the offshore climate for more than 30 years. In total, we will have access to 15 concrete cores drilled from two different platforms, hereby referred to as Structure A and Structure C.

The challenge with reinforced concrete placed in an offshore environment is the presence of aggressive ions, mainly chlorides, from the seawater. Due to the porosity of concrete, ions may penetrate through the surface and change the inner chemical climate. One of the effects is a breakdown of the passive layers covering the reinforcement, which may lead to reinforcement corrosion. This causes capacity reduction for members of a structure which is supposed to handle the tensile stresses. In addition, the corrosion products are more voluminous and through expansion, it can cause spalling and cracking of the concrete.

There are several methods for measuring the chloride ingress in concrete, both in-situ and in the lab. Rapid Chloride Test (RCT) is the most used in-situ method, while the most used laboratory method for the purpose is a wet chemical analysis by potentiometric titration. Both are frequently used by Equinor. Our motivation is to evaluate a possible additional laboratory method which is utilising micro X-ray fluorescence (μ-XRF). In order to evaluate this method, it is to be compared to two other laboratory methods. One is potentiometric titration, as mentioned, and second ICP-MS (Inductively Coupled Plasma Mass Spectrometry).

Finally, an evaluation of the chloride ingress of the fifteen concrete cores will be performed.

1.1 Research Questions and Limitations

The contributions of this master thesis are:

- An evaluation of the use of μ-XRF for determining chloride ingress in reinforced concrete, based on a comparison with potentiometric titration and ICP-MS.

- An evaluation of the chloride ingress of two offshore concrete structures based on 15 concrete cores.
    - Structure A: Three cores from the outside of the unsubmerged part of the seawater shaft, and four from the inside of the utility shaft.
    - Structure C: Eight cores from the inside of the utility shaft at elevations ranging from 13 m above to 201 m below sea level.

We will not investigate reinforcement corrosion, but rather evaluate the possibility of it by comparing chloride ingress to cover depth and the critical chloride concentration limit. seven cores from Structure A will be analysed using all three methods, while eight cores from Structure C will be analysed solely using μ-XRF. Even though RCT is the most used in-situ method of analysis for Equinor, we will not perform analysis with this method in this thesis.

1.2 Structure of the Thesis

The thesis has the following structure: Chapter 2 is a background chapter where history and technology for the structures of interest for this thesis are presented. In addition, information regarding their exposure is presented. Chapter 3 contains the theory necessary to understand the ingress mechanisms, what makes the seawater harmful to reinforced concrete and the methods of analysis. Chapter 4 gives an overview of the concrete cores and the reference samples used in the analysis together with how the different methods used for analysis are performed. Also, information on how these methods are made comparable is presented. Chapter 5 contains results obtained from the three laboratory methods on cores from Structure A. Further a discussion follows based on these results. The chapter is concluded with an evaluation of the use of μ-XRF as a tool for assessment of chloride ingress. Chapter 6 contains results from both structures regarding chloride ingress, determined by μ-XRF. A discussion regarding the 15 cores will be presented and followed by a conclusion. Concluding remarks is presented in chapter 7, where conclusions from chapter 5 are merged with the ones from chapter 6. Finally, thoughts on future research are presented in chapter 8.

2 Industry Insight

This chapter presents the concrete structures used for production in the oil industry where the concrete cores, used for analysis in this thesis, is collected from. The motivation is to give the reader a brief understanding of the complex and massive structures used to generate oil from the North Sea. This includes some history in section 2.1, an overview of the structures' dimensions in section 2.2, a description of the climate present at their locations and necessary service information in section 2.3.

2.1 History

Extraction of oil from offshore rigs have been done for a long period of time prior to the discovery of oil on the Norwegian continental shelf. The Kerr-McGee Corporation found oil in the Gulf of Mexico as early as in 1947. The technology for this was therefore already existing when oil was first found on Norwegian soil in 1969. The methods used in the Gulf of Mexico, however, proved to be insufficient for use in the North Sea. A much larger production rate demanded bigger construction equipment on the decks of the platform. A larger distance to shore made logistics a much more demanding task, making bigger storage room on the platforms of greater importance. Both of this combined resulted in a need for a platform with a foundation suitable for much larger compression forces than those in use in the Gulf of Mexico. In the mid-'70s, a concept solving this problem was developed by Norwegian Contractors. The solution was called a concrete deep-water platform, or "Condeep" for short. This concept was used for the construction of 14 platforms [2] during a time span of 20 years and most of them are still used in production. Further and more detailed information on this topic can be found in the master thesis by Steffen Larsen [3].

2.2 Condeep Platform Technology

A Condeep platform is a gravity base structure (GBS), which means that it rests on the seabed, held in place by gravity. The top deck of the structure is made from steel, whilst everything beneath is made from reinforced concrete. The shafts are shaped as hollow, thin-walled, cylindrical concrete shells, gradually increasing in diameter and thickness towards the bottom of the sea, to account for the increasing weight and hydraulic pressure. The base of the structure is a set of tanks meant for storage of oil and seawater. These tanks can be filled and emptied with water to generate the buoyancy needed to make transportation and founding of the structure as easy as possible. The shafts carrying the upper deck are merged into these in different ways, dependent on the type of structure.

Most of these structures are built partly on land and partly in the sea. The buoyancy and storage tanks in the bottom are first constructed on land in a drydock. As soon as these

are big enough, water is let into the dock and the structure is towed into the ocean where the rest of the shafts are made. The different platforms still used in production are placed in various depths from 86 meters to 303 meters below sea level. An illustration of the magnitude of these depths is presented in Figure 2-1.

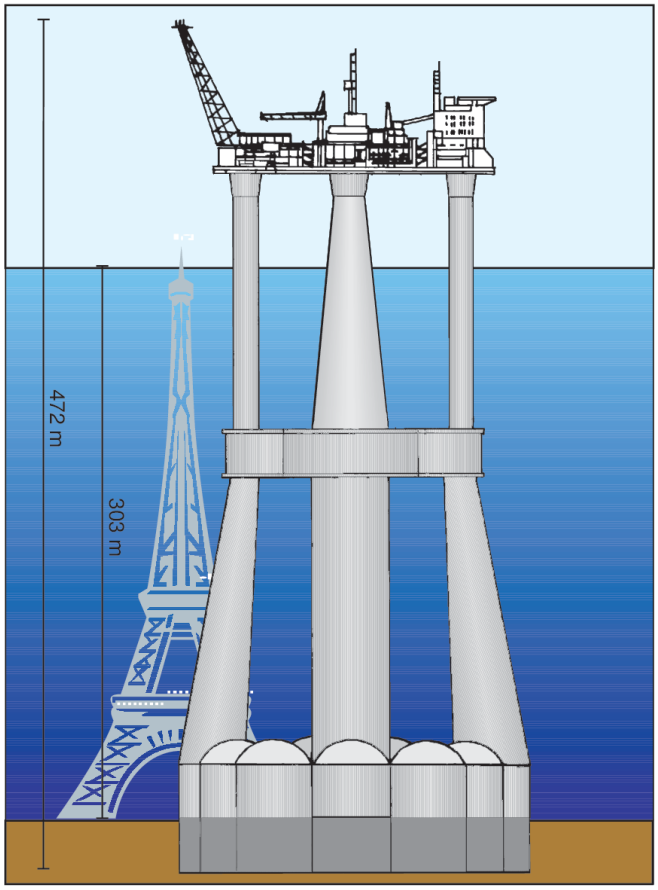

Figure 2-1: The concrete offshore platform "Troll A" compared to the height of the Eiffel tower. Picture extracted from [4].

The use of concrete for this purpose raised questions regarding the material's performance in the offshore climate. At the time, concrete was known to be used in the construction of both ships and ports. Taylor Woodrow Laboratories presented a report on the long-term performance of concrete in the marine environment in 1974. This concluded that the concrete had great duration if the concrete was made and placed properly [3]. A proper concrete for this purpose would be a dense concrete, which will be addressed later in this thesis.

The way of constructing the concrete tanks and shafts was mainly using vertical slip forming. This is a construction method where concrete is poured into a continuously upwards moving form. The planned cover depth for both Structure A and C were 60±10 mm. This cover depth is, however, very variable mainly due to the high difficulty of slip forming of these proportions. As can be seen from Figure 2-1 the diameter of some of the shafts vary with the depth, this is the case for Structure A and C as well. This change in geometry makes it hard to maintain a constant cover depth throughout the process. A report made by SINTEF in 2017 investigating some parts of the inside of the utility shaft of Structure C, found cover depths ranging from 50-90 mm.

2.3 Exposure

The weather conditions in the North Sea are known to be severe. Annually the structures are subjected to wave heights up to 20 meters and wind speeds reaching 32 m/s [6]. This demands a lot of capacity of the structures regarding the structural performance, but also regarding concrete technology. The variation of the sea level together with the waves causes a continuous wetting and drying cycle for the part of the concrete shafts above and a few meters below the mean sea level. Most of the shafts are, however, submerged in the sea. Due to this the outer part of the structures can be partitioned into different exposure zones with different expectations regarding chloride ingress, which we will address later in this thesis.

To be able to fight eventual fires inside the shafts, a deluge fire sprinkler system is installed at selected levels, using seawater for extinguishing. An illustration of the floors where this system is installed is presented in Figure 2-2. Every fourth year there is arranged fire drills in the shafts of the different platforms. These fire sprinkler systems are then activated. To be able to remove this extinguishing water and other excess water in the shafts, each level is equipped with a drainage system. These will allow all excess water to flow down, one level at the time, eventually arriving at the bottom of the shaft. Here, a drainage pump is installed, pumping all the water up and out of the shaft.

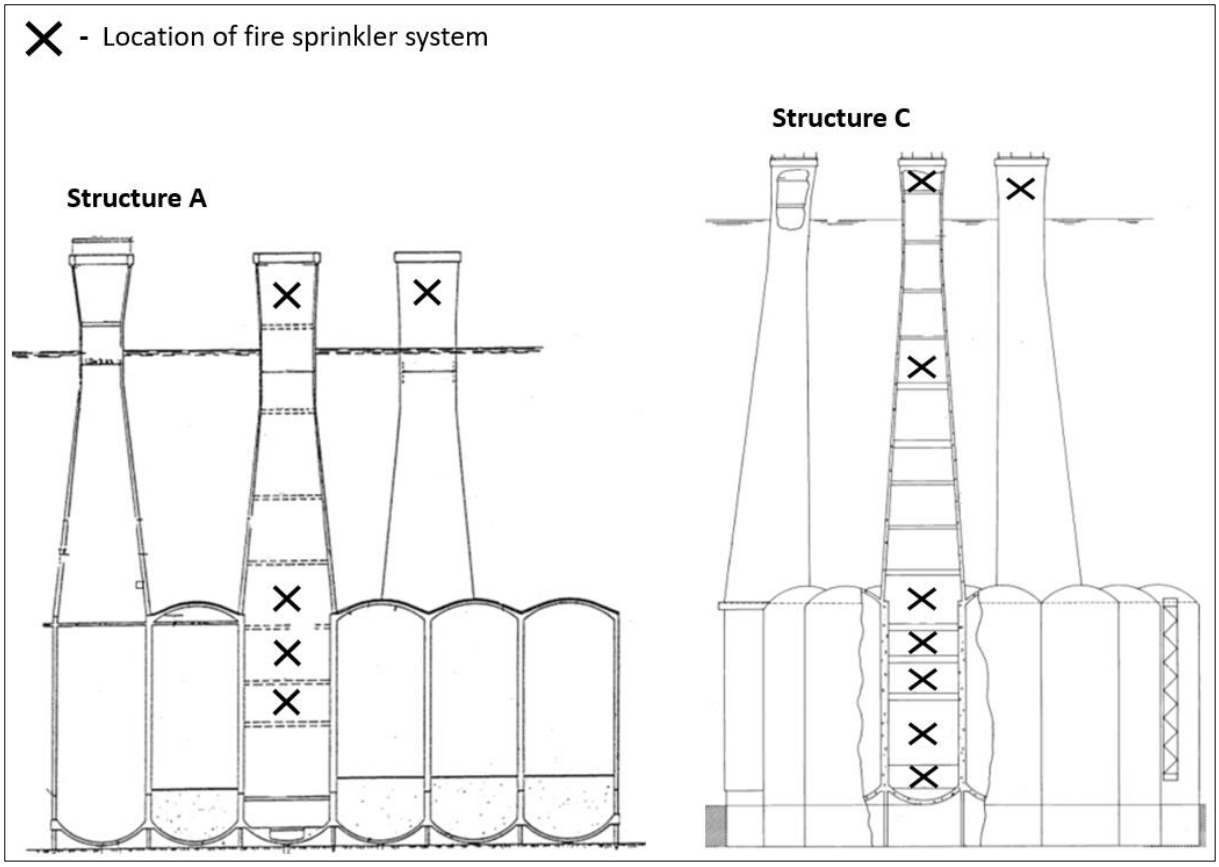

Figure 2-2: Location of the fire sprinkler systems installed in both structures. The illustration is not to scale. Picture reproduced from [7] and [8].

3 Theoretical Background

In this chapter, a literature review governing challenges for reinforced concrete in offshore climate is presented. As the structures are exposed to seawater and hence exposed to chlorides, the focus will be directed to chlorides and the transportation of these in concrete. As the presence of chlorides is known to initiate reinforcement corrosion, a presentation of necessary theory for this is also included. In addition, an introduction to the theory behind the methods of analysis will follow.

Section 3.1 will describe the ingress mechanisms and outline transportation of ions in the concrete. The different exposure zones for the structures will also be outlined. Section 3.2 will present aggressive ions and outline critical chloride content. Section 3.3 will cover the basic theory behind the methods of analysis used in this thesis.

3.1 Ingress Mechanisms

There are several different ways ions, and specifically, chlorides can be transported within the concrete. As ions usually are dissolved in fluids, there are three main mechanisms of interest; permeation, diffusion, and migration. Which one is dominating is very much dependent on the local environment for the relevant area. For further discussion, we will limit the mechanisms most relevant for our study to permeation and diffusion.

3.1.1 Permeation

Permeation is all mass transportation due to a pressure gradient [9]. For an offshore structure, this difference is caused by the hydraulic pressure subjected to the shafts carrying the upper deck. In addition, such a gradient can be created by capillary action in the pore structure of the concrete. This effect is dependent on several factors like the pore size and viscosity of the liquid. Capillary suction is caused by an underpressure and will initiate an absorption of all liquids getting in contact with the concrete surface.

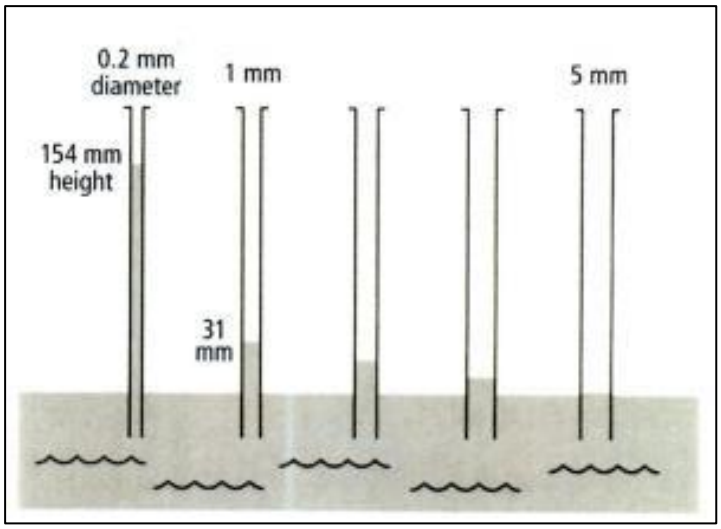

Figure 3-1: Illustration of capillary suction. Picture extracted from [10].

The coefficient of permeability due to a pressure gradient for steady-state and laminar flow can be estimated using Darcy's law [9]:

$$\frac{Dq}{dt} = K\,\frac{\Delta p * A}{L * \mu} \tag{1}$$

with

$$\frac{Dq}{dt} - rate\ of\ fluid\ flow\ \left[\frac{m^3}{\mathrm{s}}\right]$$

$$\mu - viscosity\ of\ the\ fluid\ [Pa * s]$$

$$\Delta p - pressure\ gradient\ [Pa]$$

$$A - surface\ area\ [m^2]$$

$$L - thickness\ of\ the\ solid\ [m]$$

$$K - coefficient\ of\ permeability\ [m^2]$$

Another mechanism, also driven by capillary action, is wick-action. This is what happens when you have one surface of the concrete subjected to a solution, and the opposite surface subjected to air with relative humidity below 100%. The side subjected to the non-saturated air will experience evaporation of the water into the air. This evaporation will then serve as the driving force for continuous capillary action, pulling the solution and dissolved ions towards the drying side of the concrete [11].

3.1.2 Diffusion

Diffusion is transport due to a concentration gradient. Ions will move from pore water with a high concentration towards pore water with lower concentration. In general, this is a very slow process [12]. If we assume an eternal and unchanged supply of ions to the surface of the structure, the concentration of ions at a certain time, t, and depth, x, can be estimated using the error function solution to Fick's second law [9]:

$$c(x,t) = c_s - (c_s - c_0)\mathrm{erf}\left(\frac{x}{2\sqrt{D(x,t) * t}}\right) \quad (2)$$

with

$$c_s - surface\ concentration\ \left[\frac{mol}{m^3}\right]$$

$$c_0 - initial\ concentration\ \left[\frac{mol}{m^3}\right]$$

$$D(x,t) - effective\ diffusion\ coefficient\ [m^2/s]$$

3.1.3 Permeability

The permeability is a measure of how easily substances are transported within a pore structure. The rate of transportation is therefore directly related to the permeability of the concrete and is, by that, also of vital importance for the concretes durability. The permeability is dependent on several factors. Capillary action is, for instance, dependent on the surface tension, the angle of contact between the liquid and the pore walls, the viscosity and density of the liquid and on the radius of the pores. A smaller radius gives a higher magnitude of capillary action, but it will, however, decrease the rate of transport because of an increase in friction. In general, a high porosity will lead to higher permeability, and thus a high rate of transport. Both in the form of diffusion and capillary suction. But to get transport by diffusion, one is dependent on a certain degree of saturation, and certain connectivity of the pores. The ions will need a continuous passage of water they can travel through. If, however, the concrete is fully saturated everywhere, there will be no driving force for capillary suction to occur.

Within the concrete, the cement paste is by far the most permeable part compared to the aggregates. One would then be tempted to assume that more aggregates would lead to a less permeable material. This is not the case. A concrete made from cement paste and aggregates is far more permeable than the cement paste alone. This is due to the interfacial transition zones (ITZ). These are approximately 10 μm thick zones surrounding all aggregates, taking up around 50% of the cement pastes volume, depending on the d_{max} of the aggregates used. Bigger d_{max} results in bigger ITZs. These zones occur due to what is called "the wall effect". A big solid object with a random placement in a concrete mix would cut through the grains. As this is impossible, a

redistribution of the grains, where the smaller ones are packed around the disruptive object, will occur. This effect is illustrated in Figure 3-2.

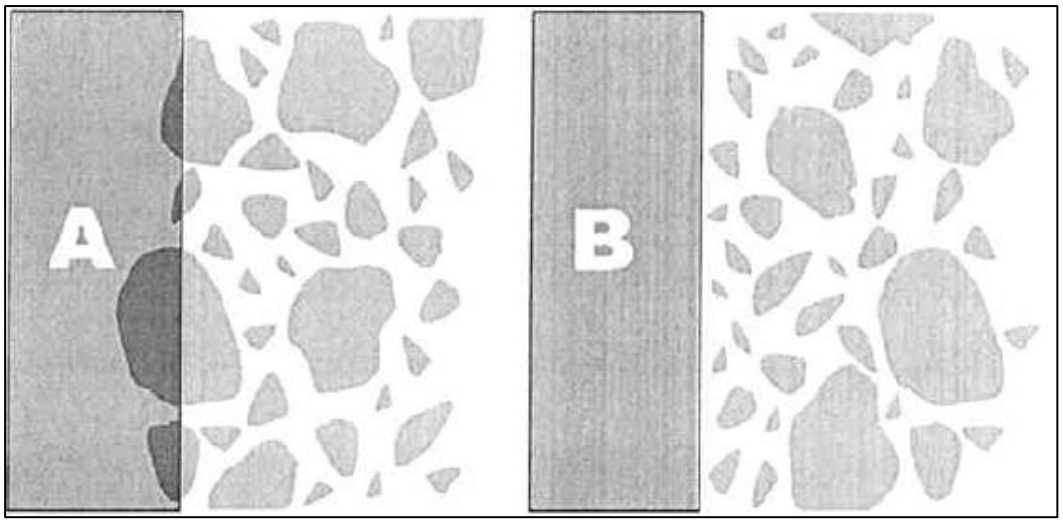

Figure 3-2: Illustration of the wall effect. Picture extracted from [14].

These zones of disruptive packing, the ITZs, have in general much higher porosity than the rest of the paste and they may also, in many cases, contain microcracks. This will lead to a much higher permeability in these areas than in the rest of the concrete, ultimately leading to a more permeable concrete [9].

A similar effect can be seen on the surface of the concrete. Smaller grains and cement particles will be packed closer to the formwork than the aggregates, due to the wall effect. This will lead to a zone of lower aggregate content in the first millimetres from the surface of the concrete.

3.1.4 Exposure Zones

An offshore structure is subjected to different types of exposure conditions on the different parts of the structure. To simplify this, we can divide the structure into three different exposure zones: The atmospheric zone, the submerged zone, and the splash zone. This simplification is also used in the Euro Code, where they are classified as, XS1, XS2, and XS3, respectively [15]. The partitioning of these exposure zones is illustrated in Figure 3-3.

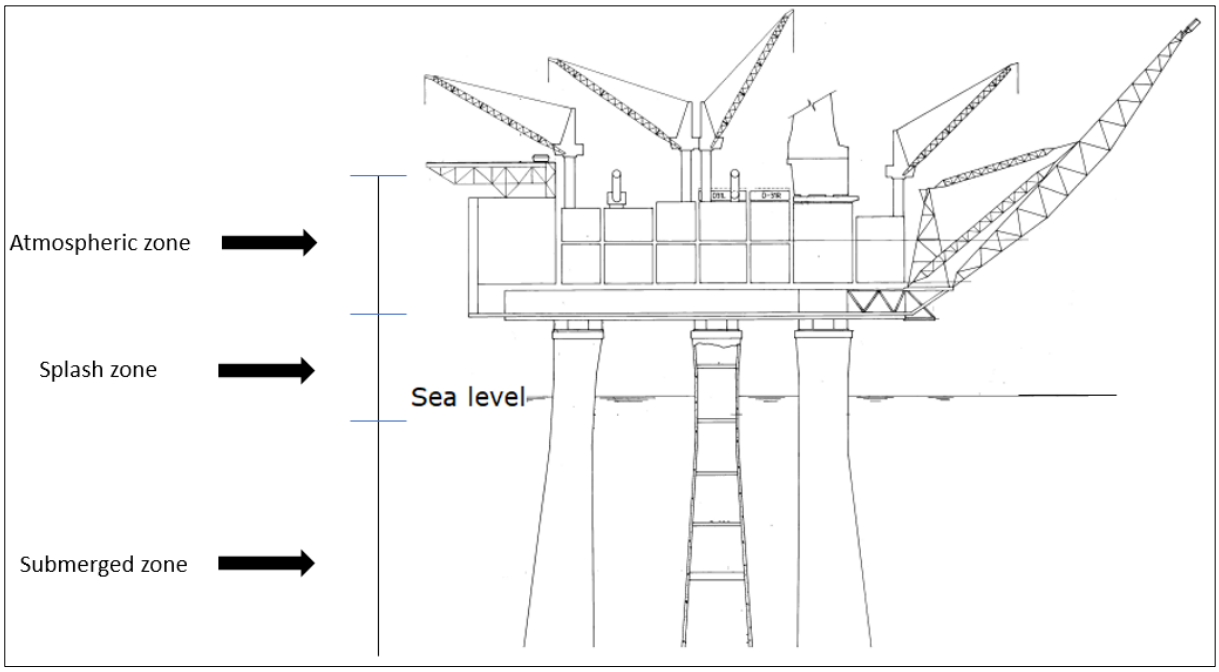

Figure 3-3: Location of the different exposure zones. Illustration reproduced from [8].

The submerged zone is the part of the structure that is constantly fully submerged in the sea. In this part of the structure, one could always expect a 100% saturation in the pores located in the outermost 10-20 mm of the concrete, dependent on the concrete quality. This provides an easy pathway for ions to transport into the concrete through the water-filled pores, mostly through diffusion. At a certain depth, when the hydraulic pressure gets large enough, permeation will also contribute to ionic transport. A fully saturated concrete will have a low electrical resistance, making a redox reaction such as corrosion of steel go fast. The reaction rate of corrosion is, however, greatly reduced by the lack of oxygen in this area.

The splash zone is the zone most vulnerable to chloride-induced corrosion [13]. This is the area surrounding the mean sea level, which is subjected to cycles of wetting and drying caused by wave action and changes in tides. The capillary saturation in this area tends to be around 75-90% [16]. This is enough for diffusion to occur, but as it is not fully saturated, permeation due to capillary suction will occur as well. When the concrete is drying, water gets evaporated, but ions are left in the concrete. This causes an accumulation of ions in the part of the concrete that is experiencing drying and wetting cycles. This part of the concrete is called the convection zone. This accumulation of ions within the convection zone together with a combined transport of ions from permeation and diffusion causes a lot of ions to penetrate the concrete in a short period of time. The

corrosion rate in this zone will also be relatively fast, as the moisture content is just large enough to provide low electrical resistance, and still provide access to oxygen.

The atmospheric zone is the part of the structure never directly subjected to the seawater. The aggressive ions found in this area have mostly been airborne or have come as part of atmospheric precipitation. The capillary saturation in this zone tends to be low, meaning most of the transportation of ions in this area are from diffusion in the gas state, or from capillary suction. The corrosion rate in this area is reduced by a higher electrical resistance in the dry concrete but increased by high access to oxygen.

3.2 Aggressive Ions

The seawater in the North Sea has a salinity of about 3.5 % [17]. This is mostly sodium chloride, but it also contains a lot of other ions as can be seen in Table 3-1. For reinforced concrete, chloride is the most harmful regarding reinforcement corrosion. In addition, magnesium and sulphur are known to be able to affect the concrete itself.

Table 3-1: Elemental composition of seawater. Values extracted from [18].

Element	Mass percent
Oxygen	85.84
Hydrogen	10.82
Chlorine	1.94
Sodium	1.08
Magnesium	0.1252
Sulphur	0.091
Calcium	0.04
Potassium	0,04
Bromine	0.0067
Carbon	0.0028
Vandanium	1.5*10^-11

3.2.1 Chlorides

The ion which is most problematic regarding the durability of reinforced concrete is chloride. They are not harmful to the concrete binder itself, but they can initiate pitting corrosion of the reinforcement when a certain chloride concentration is reached. Chlorides are transported into the concrete through the pore water in the concrete. The literature differs between free and bound chlorides, some of the chlorides will stay in solution, whilst some will be bound to the cement paste. It is only the free chlorides that are directly harmful to the structures because they must serve as an electrolyte for corrosion to be initiated. The paste has a capacity to bind chlorides, and thus remove some of the intruding dissolved chlorides and possibly delay chloride ingress. It is however uncertain how these mechanisms work in practice. Friedel's salt is in some literature suggested to be the only part of the cement that is able to bind the chloride ions [19], whilst others designate the C-S-H phases to have significant binding capacities [20].

When embedded in concrete, steel forms a passive layer of $\gamma - Fe_2O_3$, $FeOH_2$ and $FeOH_3$, due to the high pH in the pore solution, it serves as a protection of the reinforcement steel against corrosion. An illustration of which pH and potential causes passivation of the steel is shown in Figure 3-4.

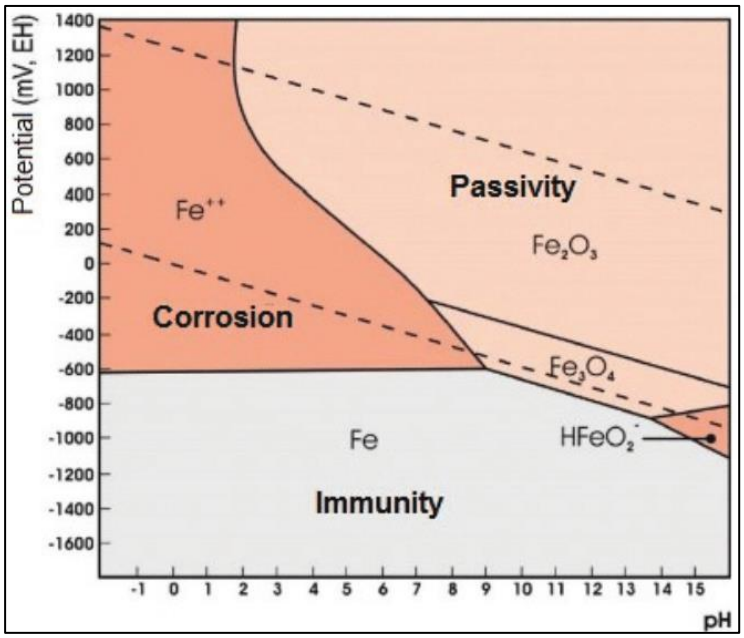

Figure 3-4: Pourbaix diagram for steel, indicating at which pH levels corrosion will occur. Picture extracted from [21].

However, if the reinforcement is subjected to a sufficient concentration of chlorides, the passive layer starts decomposing. The iron in the passive film combines with chloride ions and create Fe(OH)Cl. This is much more soluble than the initial chemical compositions of the passive film and could therefore further be parted into hydroxyl radicals and chloride ions, as shown in Figure 3-5.

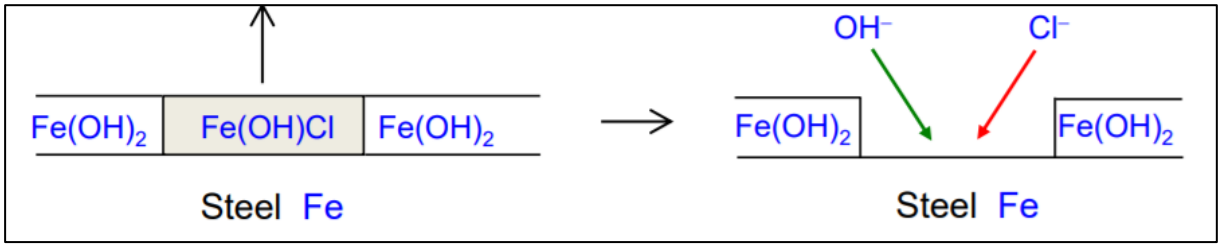

Figure 3-5: Depassivation of steel. Illustration extracted from [22].

With a high $\left[\frac{Cl^-}{OH^-}\right]$ ratio, this process will go on. However, when this ratio is decreasing, the process will reverse, and the film will start repairing itself.

With a high enough concentration of chlorides, the passive film will be penetrated. If also water and oxygen are present, corrosion could be initiated, as illustrated in Figure 3-6.

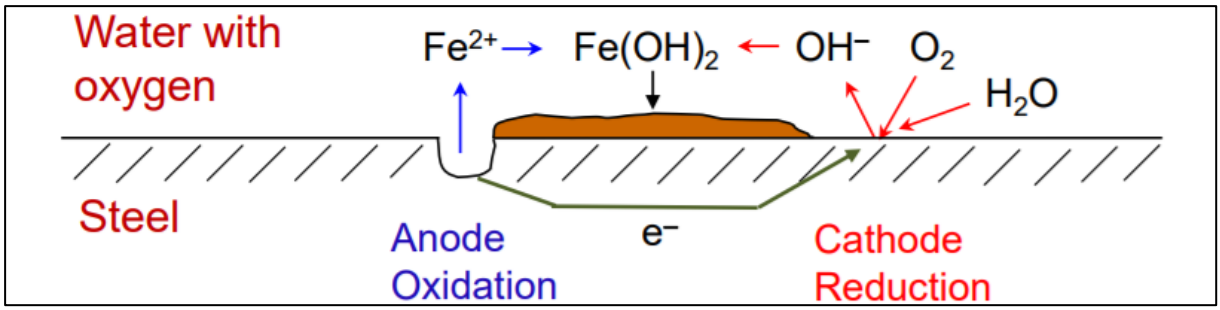

Figure 3-6: Corrosion cycle. Illustration extracted from [22].

3.2.2 Critical Chloride Content

Regarding reinforcement corrosion, the magnitude of the critical chloride content, Cl_{crit}, is of great importance. The threshold value where corrosion occurs, however, has been widely discussed over the years. In Table 3-2 ranges in these values is summed up, extracted from a state-of-the-art report from 2019 [23].

Table 3-2: Scatter in critical chloride threshold values.

By	Chloride concentration
Weight of concrete	0.025-0.18%
Weight of binder	0.09-3.4%

As originally presented by Tuutti in 1982 [24], the service life with respect to reinforcement corrosion is divided into a period of initiation and a period of propagation as illustrated in Figure 3-7.

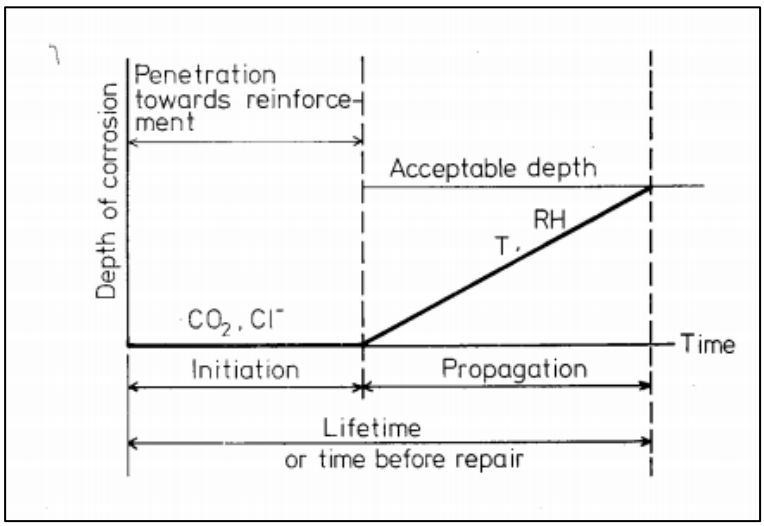

Figure 3-7: Sketch of reinforcement corrosion in concrete. Picture extracted from [24].

Initiation being the time of depassivation of the protective layer of oxide film covering the reinforcement, and propagation is the time when a considerable rate of corrosion has been reached. Whether the critical boundary of chloride content should be set to the amount that leads to depassivation, or the amount needed to generate a considerable corrosion rate is not determined. If depassivation is used to determine the critical content, it may lead to an overly conservative design of concrete structures, while "a considerable corrosion rate" is a very vague and indefinite boundary to choose, which is also tremendously dependent on other parameters, such as environmental conditions and concrete properties. This, in addition to an inconsistency regarding the procedure of retrieving Cl_{crit}, is causing this wide scatter of threshold values, presented in Table 3-2.

The threshold value should be calculated for each specific structure, taking both environmental conditions and concrete properties into account. We have not been able to find such a procedure. For engineering purposes, one is dependent on a threshold value in order to evaluate the risk of reinforcement corrosion. Because of this, a threshold value, used by both the Norwegian Public Roads Administration [1] and Equinor [26], at 0.07% Cl/concrete [g/g] is used for further discussion in this thesis.

3.2.3 Sulphur

As can be seen from Table 3-1, seawater contains approximately 0.091% sulphur. Sulphur can penetrate the concrete along with the seawater. If the concentration of sulphur in the concrete becomes large enough, it will start reacting with Aluminate (C_3A) or eventually also Ferrite (C_4AF) or portlandite ($Ca(OH)_2$) to form ettringite, gypsym or monosulphate [27]. In these cases, the products are much more voluminous than the reactants, causing tensile stresses in the concrete. If these exceeds the tensile capacity of the concrete, the concrete will start to crack. In addition to a capacity reduction of the concrete, these cracks will provide easy access for deeper penetration of ions, causing an acceleration of the ingress rate.

3.2.4 Magnesium

About 0.13% of the total weight of seawater is magnesium. In addition to the previous mentioned sulphate reactions, magnesium produces brucite ($Mg(OH)_2$) at the expense of portlandite ($Ca(OH)_2$). This brucite forms a layer with very little solubility, meaning the formation of brucite will keep on going until almost all portlandite are gone. This consumption of portlandite will cause a decrease in pH, forcing a liberation of more portlandite from the C-S-H gel. This will again start reacting with magnesium, and a continuous loop is initiated. This will ultimately cause a breakdown of the vital C-S-H gel [28]. Eventually, this will result in the formation of M-S-H, which is a non-cementitious material. This could cause disintegration of the concrete.

3.3 Methods of Analysis

For this project, three different laboratory methods for determination of chloride content are to be presented. This section is dedicated to the theory necessary to understand the basic principles of the methods. Analysis with μ-XRF is to be done by the authors, while analysis with ICP-MS and potentiometric titration is to be performed by others.

3.3.1 Micro X-ray Fluorescence (μ-XRF)

Micro X-ray fluorescence is an elemental analysis technique, based on the same principles as X-ray fluorescence (XRF). The difference between regular XRF and μ-XRF is the μ-XRFs ability to create small focal spots of just a few micrometres for the X-ray, using advanced polycapillary focusing optics [29]. This allows for a high resolution regarding the elemental composition of a sample.

The setup, in general, contains an X-ray generating source, a detector which is counting the emitted X-ray fluorescence from the sample of interest and a spectrometer (software) for computing. The sample, X-ray source, and the detector are placed in a vacuum chamber. This is to be able to detect lighter elements as air will absorb low energy radiation. Even in a vacuum chamber, no lighter elements than sodium can be detected with XRF [30]. An illustration of the specific setup used in this master thesis is presented in Figure 3-8.

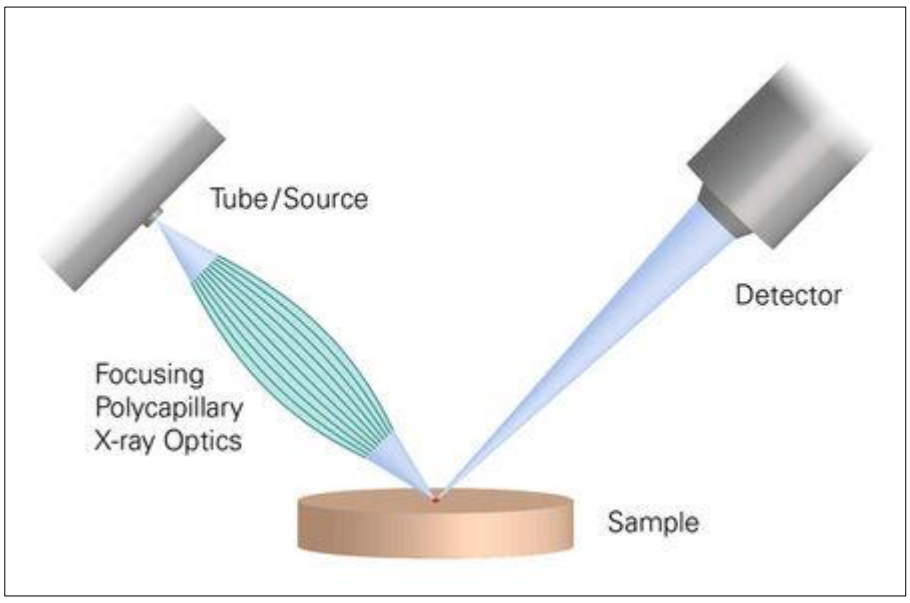

Figure 3-8: Bruker M4 Hardware. Picture extracted from [31].

Spectrometer systems that utilize such a tube source are divided into two groups: energy dispersive systems (EDXRF) and wavelength dispersive systems (WDXRF). In our case, we utilize EDXRF, which means that the detector can measure the different radiation energies coming from the sample [30]. This energy comes from the emitted X-ray fluorescence and is characteristic for each element.

This emitted fluorescence is obtained by irradiating the sample with X-rays from a source. This is illustrated in Figure 3-9.

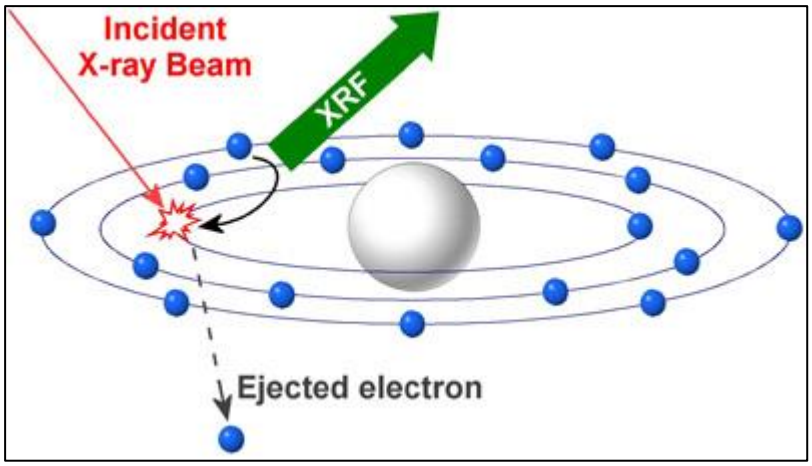

Figure 3-9: Illustration of the basic principle of X-ray fluorescence. Picture extracted from [32].

If an element is exposed to this radiation, one or more electrons will be ejected from the atoms. With a strong enough radiation energy, electrons from the inner orbital shells could be expelled, making the electronic structure of the atoms unstable. Electrons from higher orbital shells will then jump to the lower orbital shells to fill this void in the atom. This jump will cause exciting of X-ray fluorescence equal to the energy difference of the two orbital shells involved. This is a unique number for every atom and can, if detected, be used to determine the atomic composition of the material analysed. This energy is independent of the chemistry of the material which means that the energy level of calcium obtained from $CaCO_3$, CaO and $CaCl_2$ will all be equal.

This method of analysis can be used both for qualitative and quantitative measurements. For qualitative measurements, a spectrum with the different elements' intensities is typically made through deconvolution and background fitting together with the mathematical least squares method [30]. A way of presenting qualitative results is to generate a heat-map of the sample where warmer colours represent higher intensities for the element of interest.

For quantitative measurements one is dependent on a calibration of the spectrometer, relating intensities to concentrations. This can be done by either a standard- or standard-less method. The standard method only allows us to analyse an unknown sample with a similar composition to the reference sample, while the standard-less method makes the calibration independent of the unknown sample's composition [30]. This is done by applying an internal database of intensities to concentration ratios for different elements and use this to quantify the different elements in the composite.

For μ-XRF analysis, only the surface layer is analysed, and hence, the sample needs to be representative and homogenous. Concrete is not homogenous and is also vulnerable to matrix-, absorption and enhancement effects [30].

3.3.2 Inductively Coupled Plasma Mass Spectrometry (ICP-MS)

Inductively coupled plasma mass spectrometry (ICP-MS) is a type of mass spectrometry, which can detect metals and several non-metals at concentrations as low as one part per quadrillion (10^{-15}). Mass spectrometry is an analytical technique where chemical species are ionized and sorted out based on their mass-to-charge ratio, while an inductively coupled plasma is a plasma that is ionized by inductively heating a gas using an electromagnetic coil [33]. These two principles are combined in the ICP-MS. Figure 3-10 shows a generic scheme of how ICP-MS work.

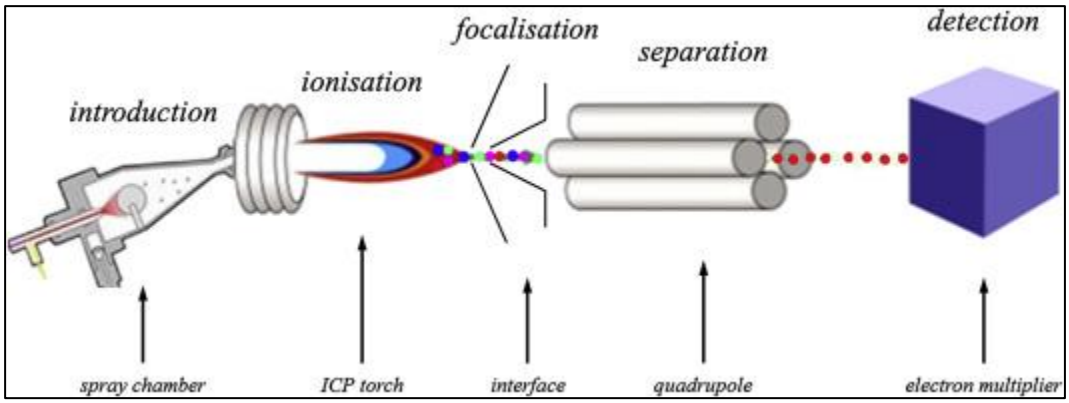

Figure 3-10: Illustration of the principle of ICP-MS. Picture extracted from [34].

First, the ICP is sustained in a torch made of three concentric quartz tubes. The end of this torch is placed inside an induction coil supplied with an electric current. A flow of argon gas is added between the two outermost tubes of the torch. An electric spark is then applied for a short time, to introduce free electrons into the gas stream. It is important that the plasma contains enough concentration of ions and electrons so that it is electrically conductive. These free electrons are then subjected to the electromagnetic field of the induction coil, causing them to accelerate in the direction of the frequently changing electromagnetic field. The accelerated electrons collide with the argon atoms and cause these argon atoms to part with one of its electrons, which then gets affected by the electromagnetic field and starts oscillating along with the other electrons. This process continues until the rate of electrons parted from argon atoms is evened out by the rate of electrons recombining with argon ions. This creates a fireball of mostly argon atoms and a small fraction of free electrons, sometimes reaching temperatures of as much as 10 000K.

Further, the second flow of argon gas is introduced between the central tube and the middle tube to keep the plasma away from the end of the central tube, and shortly after, the third flow of argon gas is introduced to the central tube. This gas flow passes through the centre of the plasma and forms a channel that is cooler than the surrounding plasma. The sample we want to analyse is then introduced into this central channel, where it is evaporated, its molecules start to break apart, and its atoms ionize, much due to the extreme temperatures. The ions are then transferred through a series of cones and into a mass spectrometer. The ions are then sorted after their mass-to-charge ratio. A detector will then receive an ion signal proportionate to the concentration, and one is then, with some calibration, able to determine the concentration of the different particles the sample consists of.

3.3.3 Potentiometric Titration

Potentiometric titration is a laboratory test done to determine a concentration from a given analyte.

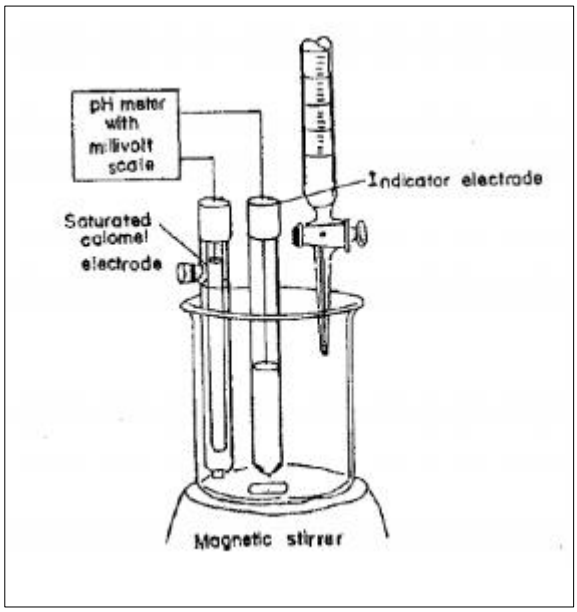

Figure 3-11: Principle of potentiometric titration. Picture extracted from [36].

Figure 3-11 is illustrating the principle of the method. Often, a silver chloride electrode is used instead of the saturated calomel electrode depicted in the figure above. The titrant is added incrementally to the solution, and the potential of this reference electrode with respect to an indicator electrode is measured for each step. This is then plotted against the known and increasing volume of the titrant. When the potential reaches the end point, as illustrated in Figure 3-12, the titrant and the analyte have reached an equilibrium, and the concentration of the analyte can be determined.

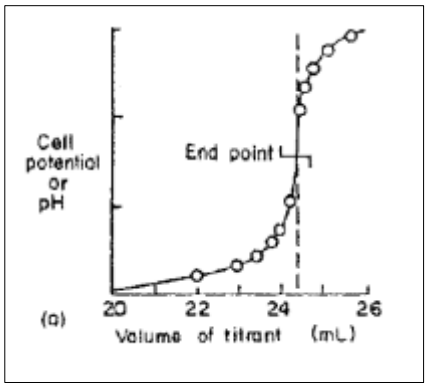

Figure 3-12: Cell potential to titrant volume plot with end point. Picture extracted from [36].

4 Materials & Methods

This chapter outlines the materials and methods used for analysis in this thesis. Section 4.1 presents the concrete used during construction of the two structures of interest for this thesis. The cores received by us is presented in section 4.2 while the reference samples used for calibration is presented in section 4.3. Two of the laboratory methods, potentiometric titration, and ICP-MS, is not performed by us, but the methods are described in section 4.4 and 4.5 respectively. The methods of µ-XRF are explained in detail in section 4.6. How these methods were compared is outlined in section 4.7.

Even though RCT is the standard method of analysing chloride ingress for Equinor, we did not include this method in our thesis. RCT analyses require samplings from a much bigger area than what is obtainable from our concrete samples.

4.1 Concrete Overview

As stated in section 2.2 the density of concrete to be placed in the offshore environment needs to be high. Hence, the w/b-ratio, for both structures, is 0.38 [5]. In addition, a great cover depth is favourable regarding chloride ingress, and the depth aimed for in these two structures is 60 ± 10 mm as stated in [37] and [38].

The cement used in the shafts of the structures is P30 and P30-4A. P30 was used in Structure A, while P30-4 was used in Structure C. P30-4A is a combination of P30 and HS65 made by mixing one part HS65 and three parts P30. Both P30 and P30-4A have a density of 3160 kg/m^3 [39]. An oxide overview of the two cements is presented in Table 4-1.

Table 4-1: Oxide overview of the two cement types in % [g/g]. See Appendix 128A.10 for details.

Oxide	P30	P30-4A
Na2O	0.3	0.3
MgO	2.3	2.1
Fe2O3	3.4	3.4
K2O	1.1	0.9
Al2O3	4.7	4.6
SiO2	20.4	20.8
SO3	2.8	2.9
CaO	63.2	63.5
Free CaO	1.0	1.0

The aggregates used for both of the structures is granitic gneiss from Tøtlandsvik, often referred to as "Årdal-aggregates", with a density of 2680 kg/m^3 [40]. The elemental composition of an arbitrary granitic gneiss is presented in Table 4-2.

Table 4-2: Oxide composition of an arbitrary granitic gneiss. Numbers extracted from [41].

Oxide	Mass %
SiO2	71.77
Al2O3	13.66
Fe2O3	0.81
FeO	1.52
MgO	0.66
CaO	0.59
Na2O	3.99
K2O	5.94
TiO2	0.70
P2O5	0.08
MnO	0.06

Table 4-3 is showing the mix proportions for the concrete in the two different structures.

Table 4-3: Typical mix proportions of the two concretes in [kg/m^3]. Values extracted from [7].

	Structure A	**Structure C**
P30 Cement	440	300
HS65 Cement	0	100
Silica fume	0	8
Aggregates 0/8	863	940
Aggregates 8/16	863	945
Water	167	155

The density of the paste has been calculated by the steps presented in Appendix A.15 and is found to be 1980±34 [kg/m^3].

4.2 Concrete Cores Overview

A total of 15 concrete cores were received from Equinor. We checked them for defects, and if there were any traces of rebar. For the grinding of concrete, which is to be addressed later in Chapter 4, it is important that the concrete does not include any traces of rebar. Further, the cores were remarked, packed in plastic and put to storage at 5°C.

Some of the cores were collected from the outside of a shaft, while most of them were collected from the inside. See Table 4-4 and Table 4-5 for information about the concrete cores collected from the two structures. Core name including "O" is collected from the outside, while "I" means collected from the inside. For an illustration of where the concrete cores were collected from, see Figure 4-1 and Figure 4-2.

Table 4-4: Overview of concrete cores from Structure A.

Core Name	Length [mm]	Approx. distance from sea level [m]	Diameter [mm]	D_{max} [mm]
A.1.O	256	+22	65	32
A.2.O	290	+8	65	32
A.3.O	240	+6	55	32
A.4.I	280	-15	65	32
A.5.I	205	-69	65	32
A.6.I	160	-118	65	32
A.7.I	190	-118	65	32

Table 4-5: Overview of concrete cores from Structure C.

Core Name	Length [mm]	Approx. distance from sea level [m]	Diameter [mm]	D_{max} [mm]
C.1.I	270	+13	55	32
C.2.I	130	+13	55	32
C.3.I	115	-58	55	32
C.4.I	265	-58	55	32
C.5.I	245	-151	55	32
C.6.I	275	-151	55	32
C.7.I	255	-201	55	32
C.8.I	270	-201	55	32

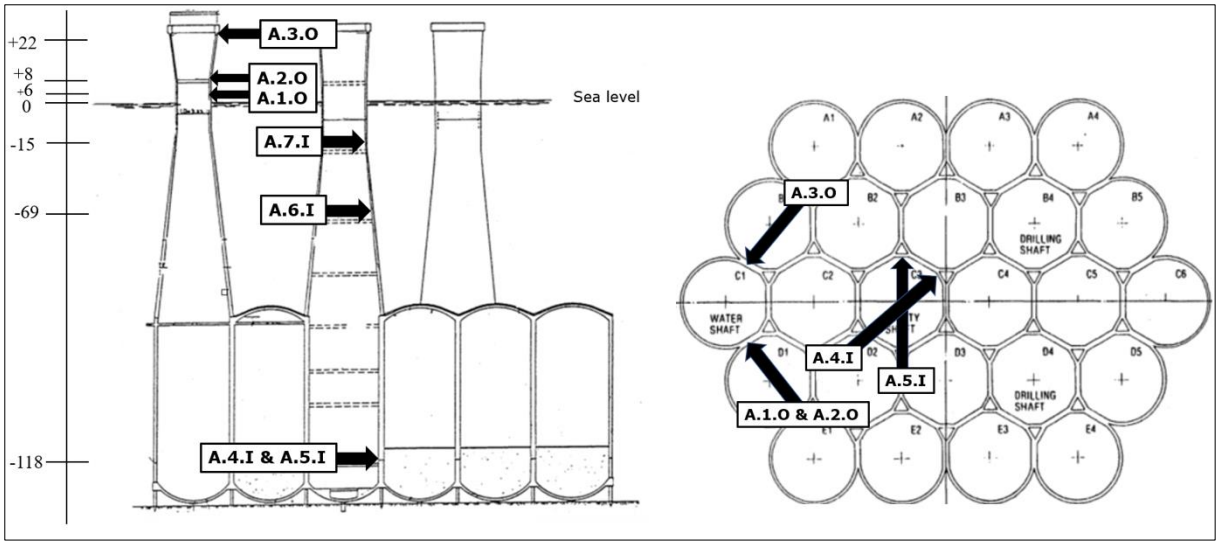

Figure 4-1: Overview of locations of concrete cores collected form structure A, 3 from the outside and 4 from the inside. The orientation of A.6.I and A.7.I is unknown. Picture reproduced from [7].

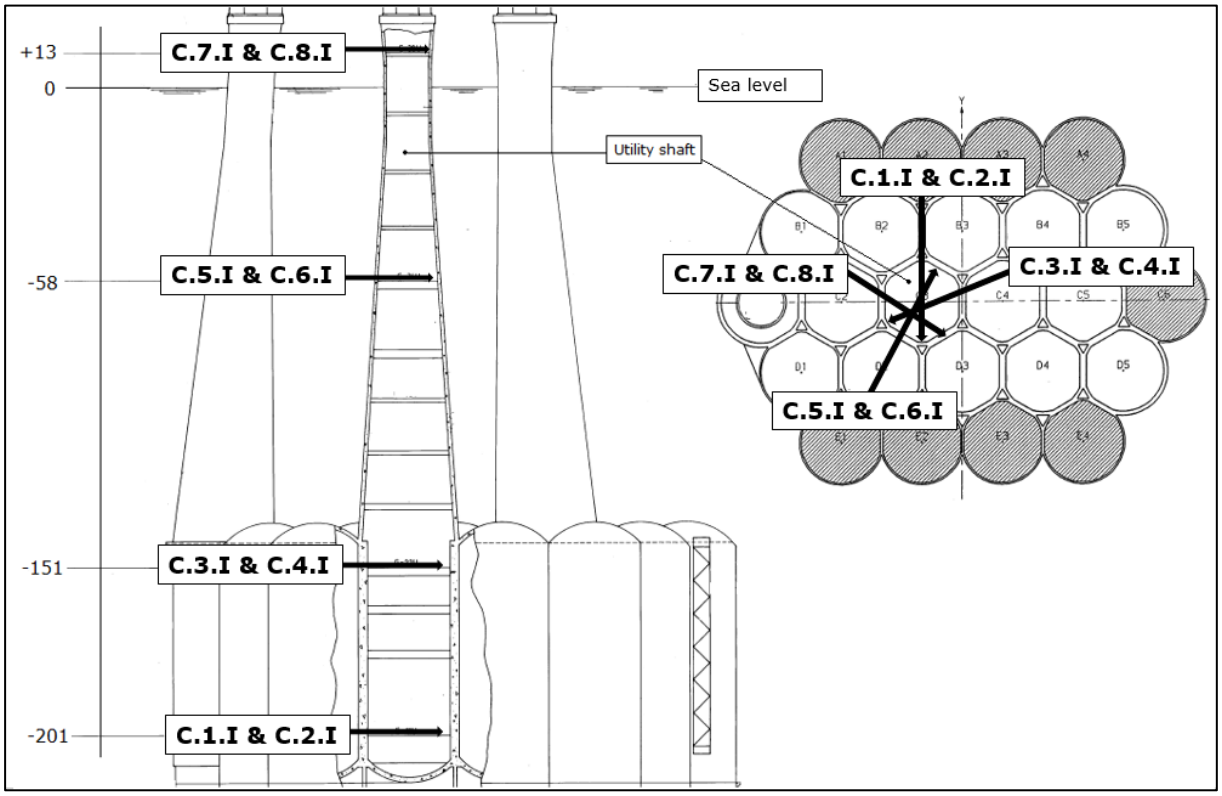

Figure 4-2: Overview of locations of concrete cores collected from structure C, all of them from the inside of the utility shaft. Picture reproduced from [8].

Figure 4-3 shows the operator during the collection process of the concrete cores obtained from the outside of the seawater shaft in Structure A.

Figure 4-3: Collection of concrete cores from the outside of the seawater shaft. [Equinor, 2018]

4.2.1 Concrete Sample Preparation

We had all the concrete cores sawn in two. The sawing was performed partly at the SINTEF laboratory (cores Structure A), and partly by Steinar Seehuus at the NTNU laboratory(cores Structure C). This was done using a circular saw, with a blade thickness of 3mm. It was important to use as little cooling fluid as possible during this process, to prevent a washout of ions. After sawing, one half of the samples from Structure A was profile ground by Roger Leistad at the SINTEF laboratory, while the other half was repacked in plastic and stored at 5°C at the NTNU laboratory together with all halves from Structure C.

The utilisation of cores from Structure A is illustrated in Figure 4-4. For Structure C, only one half of the cores were analysed, and the μ-XRF was the only method of analysis used for these.

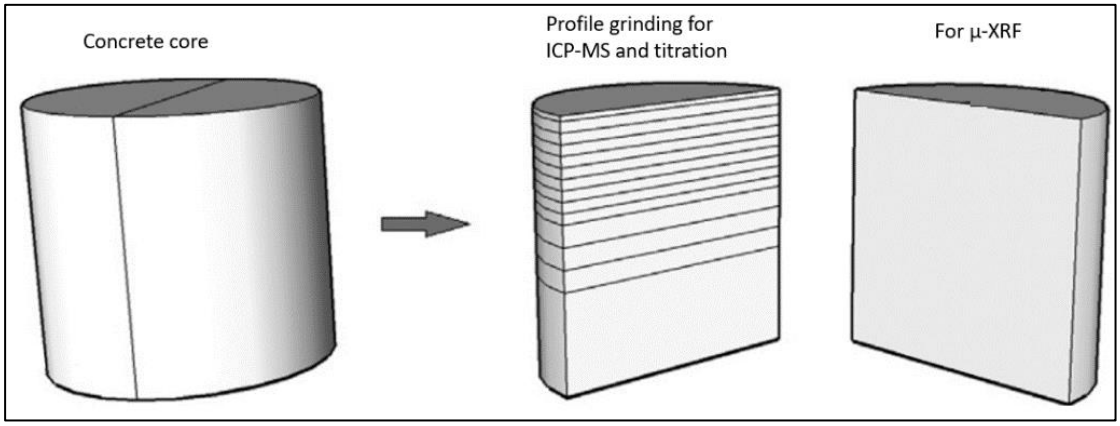

Figure 4-4: Illustration of how the concrete cores were prepared for analysis. Illustration reproduced from [28].

The powder from the profile grinding was used to create samples to be analysed by both titration and ICP-MS. See Table 4-6 and Table 4-7 for details regarding partitioning of the concrete cores.

Table 4-6: Depth and thickness of sections analysed by both potentiometric titration and ICP-MS.

Average depth [mm]	Partition interval [mm]	Thickness [mm]
X.1	0-2	2
X.3	2-4	2
X.5	4-6	2
X.7	6-9	3
X.11	9-13	4
X.15	13-17	4
X.20	17-23	5
X.26	23-29	6
X.32	29-35	6
X.39	35-43	8
X.47	43-51	8
X.55	51-59	8
X.63	59-67	8
X.71	67-75	8
X.80	75-85	10

Table 4-7: Depth and thickness of sections analysed by μ-XRF.

Average depth [mm]	Partition interval [mm]	Thickness [mm]
2.5	0-5	5
7.5	5-10	5
12.5	10-15	5
17.5	15-20	5
22.5	20-25	5
27.5	25-30	5
32.5	30-35	5
37.5	35-40	5
42.5	40-45	5
47.5	45-50	5

4.3 Reference Samples Overview

In order to perform quantitative chloride measurements using μ-XRF, one is dependent on a calibration technique or adequate software. A calibration technique presented by Rannei Ida Kaasa, which is to be addressed later in this work, was presented in her master thesis in the spring of 2018 [43]. This is a standard method where reference samples with known chloride content are required to create calibration points.

The reference samples used in our thesis were made by R. Kaasa. The Portland cement used for these samples was CEM I 52,5N, see Appendix A.11 for further details. In order to add chlorides to the samples, two different mixes of NaCl and distilled water were used. The concentrations were 5 and 25 weight percent. The samples were made by mixing the cement with the NaCl solution and water to obtain a w/b ratio of 0.4. The cement paste was then poured into tubes creating cylindric cores with 20 mm diameter and a height of 25 mm.

Further, the paste cylinders were sealed and stored for 28 days at $20\,^{\circ}\mathrm{C}$. After the curing, 2 mm of the bottom of the cylinder were removed before 5 mm thick discs were sawn from each cylinder and put to storage. A second tube for each batch was then used to created powder to be analysed by potentiometric titration. The samples were used by R. Kaasa in her master thesis and put to storage in plastic bags and then placed in a desiccator over silicone gel and soda lime. The samples had been stored for approximately half a year at the time we started using them. Between measurements performed by us, the samples were also stored in plastic bags and in the same desiccator. An illustration of these reference samples is shown in Figure 4-5.

Figure 4-5: Illustration of the reference samples placed on a rack of LEGO. [Slotten, 2019]

Potentiometric titration was, in the master thesis of R. Kaasa, performed on the reference samples in order to verify their chloride content. The results are shown in Table 4-8.

Table 4-8: Overview of reference samples and their chloride content. Values extracted from [43].

Sample [-]	Intended chloride content [wt-% of dry cement paste]	Measured chloride content [wt-% of dry cement paste]	w/b [-]
F	0	Invalid	0.4
A	0.2	0.250	0.4
B	0.4	0.395	0.4
C	1.5	1.160	0.4
D	3.0	1.827	0.4
E	4.0	2.947	0.4

As can be seen from Table 4-8 the reference F got an invalid result. As the potentiometric titration has a lower detection limit at a mass concentration of 0.005 % Cl per concrete, the actual concentration could not be determined. We have however assumed it to be zero in our calibration curve presented later in this work. The fact that the measured chloride content deviates from the intended is discussed in the master thesis of R. Kaasa [43].

4.4 Potentiometric Titration

Since the procedure of potentiometric titration must be done by trained personnel, Siri Trapnes from SINTEF was hired to complete the task for us.

Initially, the dry weight of the concrete for each of the cores was measured. This was done by weighing out 5g of concrete powder from the section with the greatest amount of powder, into a beaker. This was then heated up to 105 °C in an oven and cooled for 10 minutes in a desiccator. The weight before and after heating was measured, and the dry weight of the concrete could be determined. This was repeated for each core.

Further, 65% HNO_3 solution with a ratio of 1:10 were heated up to 80 °C. 5 grams of powder from each section from each core was added to beakers. 50 ml of the heated HNO_3 solution were then added to each of the beakers. It was then mixed well and set aside for an hour.

10-15mL from each beaker was then extracted using a syringe with microfilters. 1 mL of this filtrated solution for the outermost layer was then extracted and analysed for each core, this to check the highest concentration in the core. Further, 1, 5 or 10 ml, dependent on the chloride concentration, of the filtrated solution were measured out. The lower the concentration, the bigger volume was needed. Into this volume, 2,5 mL of polyvinyl alcohol (PVA) was added. The final mix of filtrated concrete solution and PVA was finally inserted into a *905 Titrando* titrator, and potentiometric titration was performed. 0.01mol/l silver nitrate was used as the titrant. This process is illustrated in Figure 4-6.

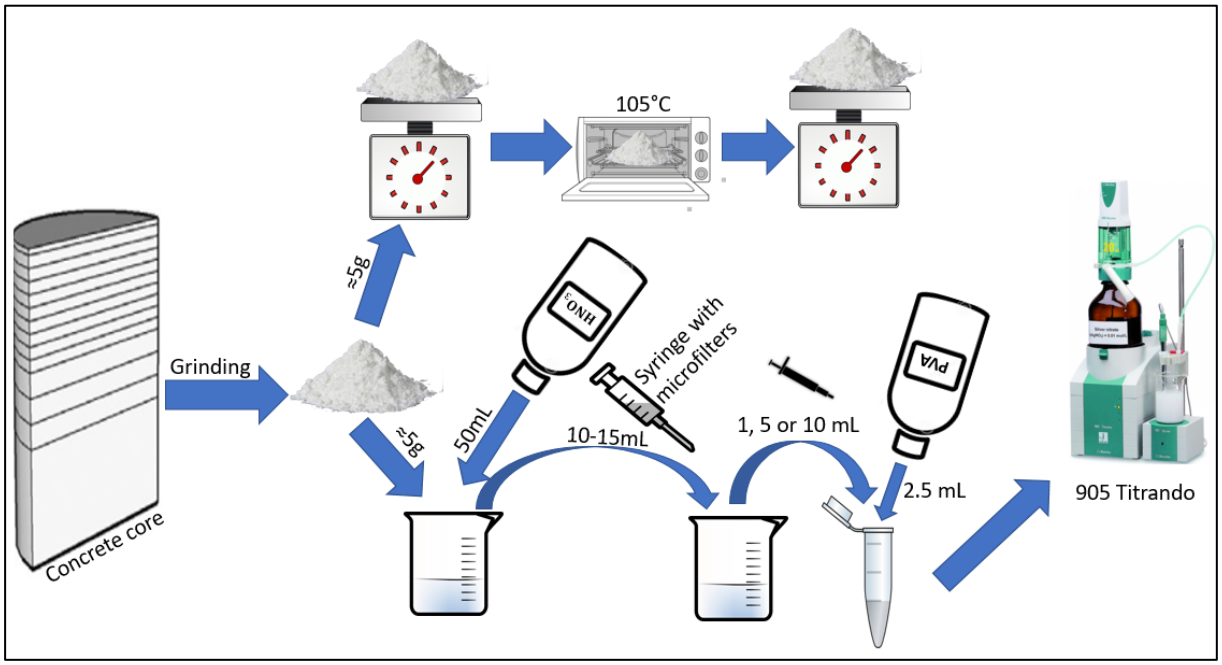

Figure 4-6: Illustration of the titration process. Picture made extracting illustrations from [44].

Results from the potentiometric titration were presented in the form of a table with a mass concentration in percentage Cl/Concrete. See Appendix A.1 for the raw data obtained.

4.5 ICP-MS

Syverin Lierhagen at NTNU performed analysis using ICP-MS of our samples. A good correlation between chloride content found by titration and ICP-MS have been found in previous experiments [1]. ICP-MS is, in addition, a good method for determining the content of other elements of interest within the concrete, such as magnesium, sulphur, and calcium.

For the analysis, the same solutions created for the potentiometric titration could be used: 5 grams of powder in a 50 mL solution of 1:10 0,65% HNO_3. Since spectrometry demands low concentrations they had to be diluted. This process was performed by Petter Hemstad at NTNU. 1 mL of the above solution was measured out and put into a 100 mL beaker and diluted 1:100 with de-ionized water. Further 10 ml of this diluted solution was measured out and put into a sample container. This was done in two portions, using a 5ml pipette. To this, 14 mL of 65% HNO_3 diluted to 1:2 were added to keep the sample stable. This dilution process is illustrated in Figure 4-7.

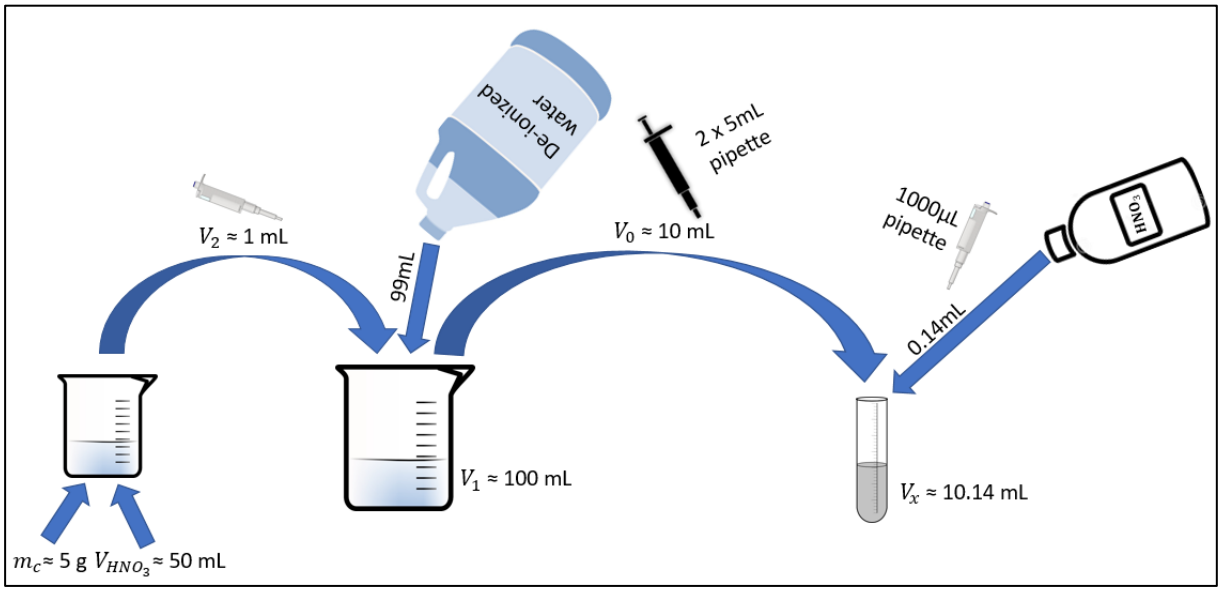

Figure 4-7: Dilution process for ICP-MS. Picture made by extracting illustrations from [44].

The ICP-MS analysis was then performed on this solution.

The concentration measurements had to be converted from µg/L to g/g. To be able to express this as $\frac{\%\ mass\ of\ element}{mass\ of\ concrete}$, we had to do a few calculations.

The concentration of an element in the 10.14 ml solution on which the ICP-MS analysis had been performed is labelled C_x. The volume of this solution is labelled V_x

The concentration of the 10 ml solution before the 0.14ml 0,65% HNO_3 was added is labelled C_0. The volume of this solution is labelled V_0

The concentration of the 100 ml solution the 10 ml solution mentioned above were taken from is labelled C_1. The volume of this solution is labelled V_1

The concentration of the 1 ml solution which was diluted to the 100 ml solution mentioned above is labelled C_2. The volume of this solution is labelled V_2

The 50 ml solution containing the original concrete sample of measured mass, m=m_c, which the 1 ml solution mentioned above were taken from is labelled C_3. The volume of this solution is labelled V_3

Conservation of mass gave the following equations:

$$C_0 = C_x * \frac{V_x}{V_0} \tag{3}$$

$$C_1 = C_0 = C_x * \frac{V_x}{V_0} \tag{4}$$

$$C_2 = C_1 * \frac{V_1}{V_2} = C_x * \frac{V_x}{V_0} * \frac{V_1}{V_2} \tag{5}$$

$$C_3 = C_2 \tag{6}$$

$$C_3 = C_x * \frac{V_x * V_1}{V_0 * V_2} = C_x * \frac{10.14 * 100}{10 * 1} = C_x * 101.4 \tag{7}$$

The mass of this element was then calculated using this formula:

$$m_x = C_3 * V_3 \tag{8}$$

The mass of the element over dry concrete weight could then be obtained:

$$\%element_{concrete} = \frac{m_x}{m_c} \tag{9}$$

4.6 µ-XRF

As stated in section 3.3.1, quantitative measurements with µ-XRF are dependent on a way of calibration. This has been, as mentioned, developed through a master thesis by R. Kaasa [43]. She used reference samples with known chloride content to establish a calibration technique, the calibration method. This is a standard analysis; hence, the reference samples are made using a w/b-ratio close to the one used in the concrete cores.

We started using this method in the µ-XRF, but at first, we got results that did not correlate well with the ones obtained from ICP-MS and potentiometric titration. Since a correlation was presented by R. Kaasa, we had to review the method and look for possible critical sources of error. We eventually suspected that the difference was due to deteriorated reference samples. By comparing the results for the reference samples R. Kaasa obtained in her thesis to our, we saw a lower CPS/eV for Cl in each reference sample. This meant that we had to either create new reference samples or freshen up those we had, by for instance polishing with sandpaper.

This issue also led us into a way of getting quantitative results, without the use of reference samples. By using the built-in functions in the Bruker M4 software, we could get a list of elements registered in the sample in relative mass percentage, i.e. a standard-less analysis. This could then be used to obtain the $\frac{m_{Cl}}{m_{Ca}}$ ratio directly, which could be transformed to $\frac{m_{Cl}}{m_{concrete}}$. This did not give correlating results either, forcing us to polish the reference samples.

Polishing of the reference samples was performed to remove the most deteriorated layer, and then establish a new calibration curve. This new curve was then to be used in the calibration method, and the results corresponded better to the ones from titration and ICP-MS. Details will be presented in the following sections.

4.6.1 Pre-processing

Figure 4-8: Illustration of the µ-XRF machine used. [Vådahl, 2019]

We analysed the concrete cores with two different techniques using the µ-XRF. The pre-processing, however, is equal for both analysing techniques. We had access to the M4 Tornado from Bruker which is used for this type of analysis. See Figure 4-8 for an illustration of the machine.

In the pre-processing, the first thing we had to do was to turn on the X-ray tube. This was important to do roughly 45 minutes prior to analysis, for it to reach a given temperature in order to work properly. If the X-ray had not been warmed up, results could deviate from the expected outcome. More about this in section 5.3.

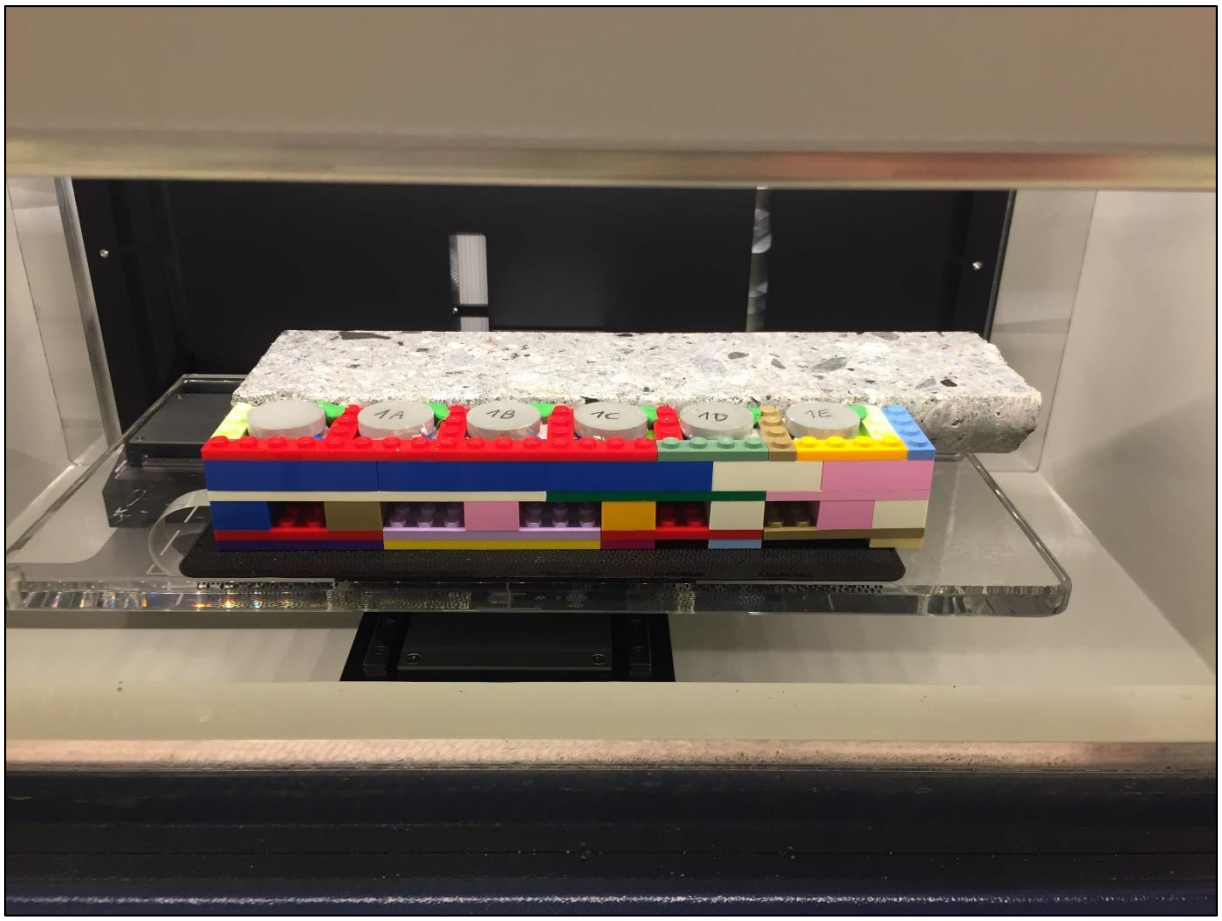

Figure 4-9: Placement of core and reference samples. [Vådahl, 2019]

The M4 has a glass stage with the ability to move in both X, Y, and Z-direction during analysis. This movement is restricted to 270x240x120 mm, and the maximum load it could hold was 5kg. We analysed one sawn core at a time. The cores were placed on the glass stage and levelled using a leveller. Next to the core we placed a rack made of Lego, which carried the six reference samples, previously mentioned. See Figure 4-9 for an illustration of the placement. The reference samples were levelled to the same height as the core surface. Further, the glass stage was loaded and centred into the machine. The chamber door on the machine was then closed before the vacuum was switched on. As this technique is dependent on a calibration curve based on values from several different scans, it was important to have as identical measuring conditions for all scans as possible. This is also why the temperature of the X-ray is of such importance. See Table 4-9 for details regarding the measuring parameters we used.

Table 4-9: Measuring parameters for µ-XRF analysis.

Parameter	Condition
Chamber pressure	Vacuum, 20 mbar
Number of detectors	1
Tube current	600 µA
Accelerating voltage	50 kV
Time pr. step	3 ms for sections/2 ms for overviews
Step width	25 µm for sections/40 µm for overviews
Filter	No filter

For each core, we obtained data from the µ-XRF by running a script, see Appendix A.7 for details. The µ-XRF was scripted to perform the following scans:

- An overview scan, showing both the core and the reference samples.
- Ten consecutive 5 mm thin sections of the core.
- 1 cm^2 quadratic areas from each of the six reference samples.

The overviews were used to generate qualitative heat maps of the entire cores with respect to different elements. This was done by isolating the $\frac{CPS}{eV}$-value from the energy level typical for the respective element. See the Appendix A.12 for the collages from all the received cores. The 5 mm thin sections went through a more thorough scanning, with a greater collection time and smaller step width. This gave us qualitative information about elements within each section for each core, which was later used to obtain chloride profiles. The scans from the reference samples were later used to generate a calibration curve, as these had a known chloride content.

In total, these scans could take up to 24 hours to complete for each core.

4.6.2 Chloride Content Determination Using the Calibration Method (CM)

This is a way of determining chloride concentration from the $\frac{CPS}{eV}$-values obtained from the µ-XRF, using reference samples with known chloride content. Also called a standard method. The reference samples were used to create a calibration curve by plotting the $\frac{cps}{eV}$-values to the known chloride content of the sample. This graph could then be used to convert $\frac{cps}{eV}$ of from the concrete cores to the corresponding chloride concentration in $\frac{m_{Cl}}{m_{paste}}$. A flow chart of the calibration method is presented in Figure 4-10.

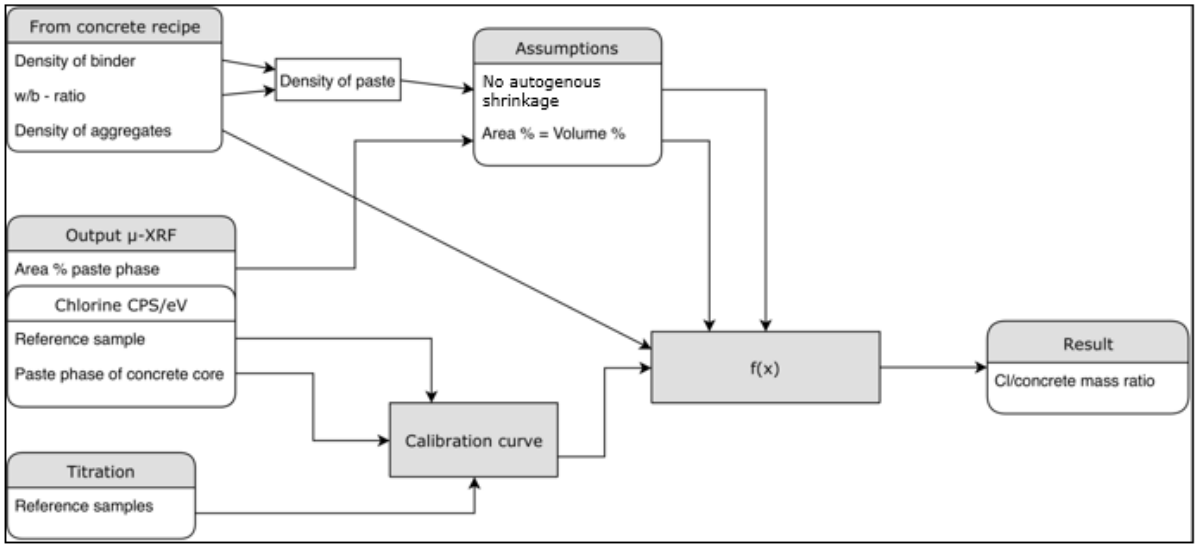

Figure 4-10: Illustration of Calibration Method using a flow chart.

Since the reference samples are not concrete but solely paste mixed with sodium chloride, we needed to isolate the paste part of the concrete cores from the aggregate part. By doing this we could compare the paste phase from the concrete with the reference samples. In the post-processing of the results, we were able to separate the thin sections of the concrete into the cement paste phase, and the aggregate phase by which element was dominant in which area. This was done using the auto-phase tool in the Bruker software.

The auto-phase tool was told which elements to look for and separated the areas in which the respective elements were dominating into different phases. In the case of concrete, there are several elements that could be used for this purpose, but we chose to use calcium, sulphur, and silicone. Calcium and sulphur to reveal the cement, and silicone for the aggregates. See Table 4-1 and Table 4-2 for an oxide overview of the cement and aggregates in the concrete. Cement also contain silicone, but not as much as the aggregates, making the silicone dominant areas become the aggregate phase when auto-phasing. This can be seen from the overview scans in Appendix A.12

An illustration of the auto-phasing process can be seen in Figure 4-11. We tried to make two phases, the cement paste phase, and aggregates phase. This was done in three different ways. First by only looking for calcium, then calcium and silicone and finally calcium, silicone, and sulphur. The calcium and sulphur dominated area became the cement paste phase, and the silicon dominated area the aggregate phase. This way, we were able to separate cement paste from aggregate, so that we could study chloride concentration in the paste alone. The area percentage of each phase and the CPS/eV-values of chloride in the cement paste phase for each thin section is then collected.

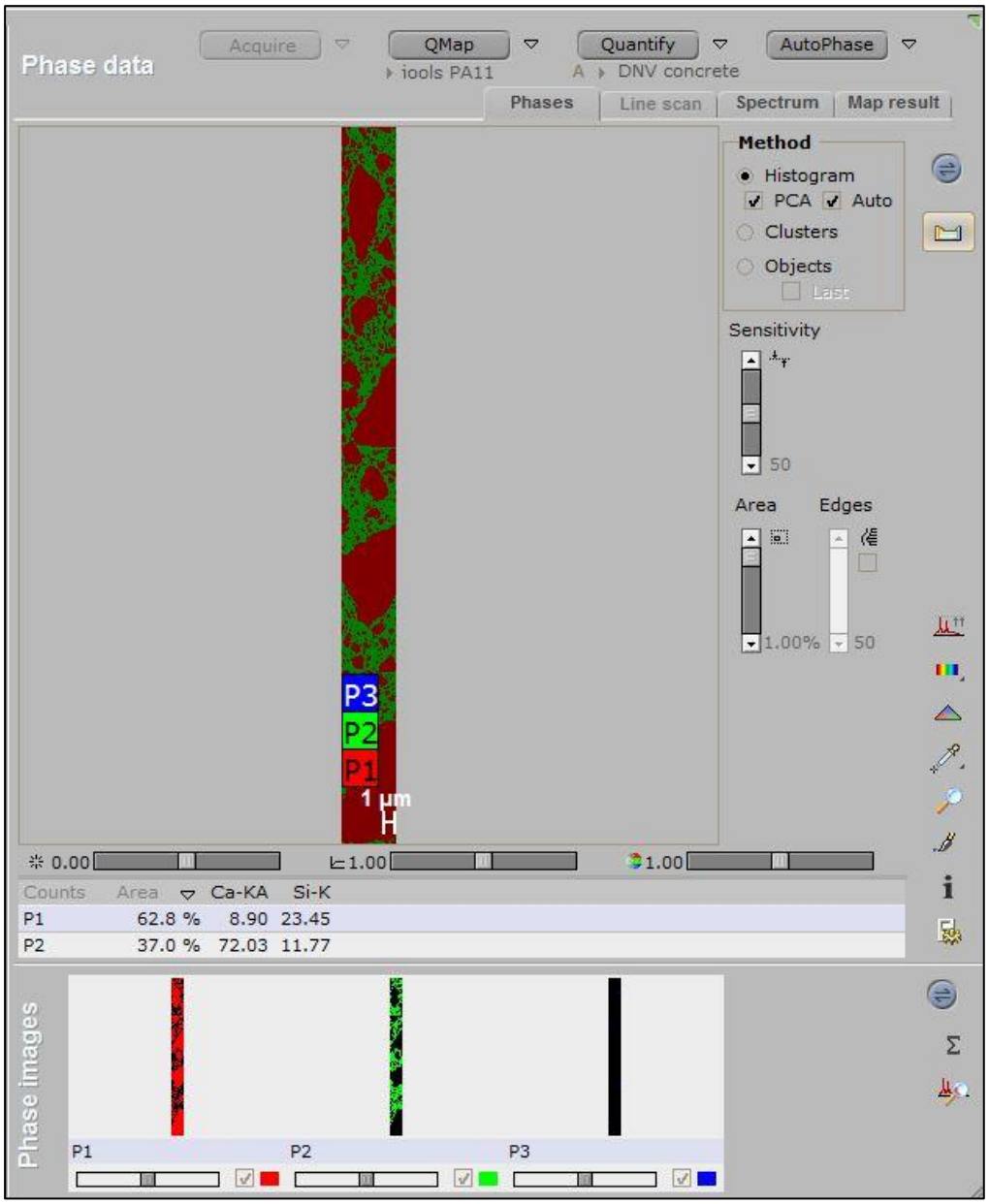

Figure 4-11: An example of auto-phasing.

In the auto-phasing tool, we had the option to adjust the "Sensitivity". This means we could adjust this to make the tool distinguish between fewer or more phases in the section. If we used a high sensitivity, we got many different phases, which we had to merge into either the aggregate or cement paste phase. See Figure 4-12 for illustration of the effect of the sensitivity adjustment. In general, we used medium sensitivity throughout every section.

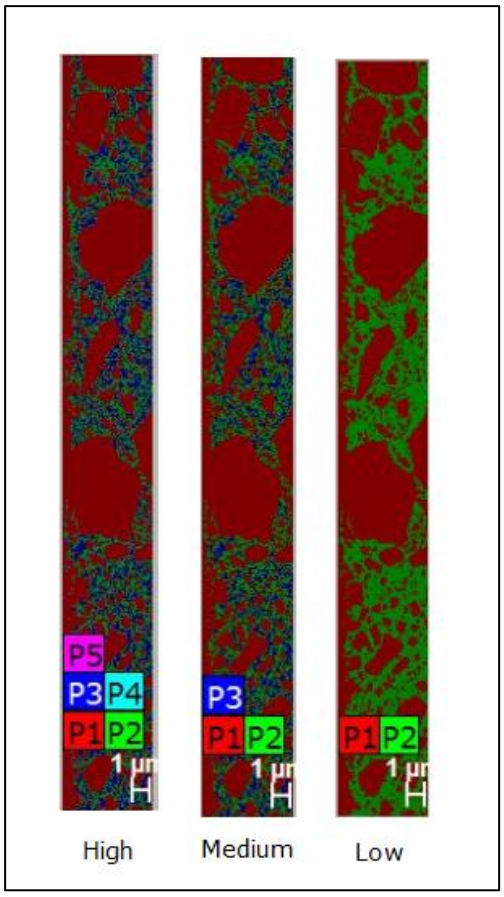

Figure 4-12: An illustration of the effect of the sensitivity adjustment, from high to low.

In addition, we had the option to adjust "Area" and "Edges". The "Area" could restrict the minimum sizes of the phases, preventing very small phases from occurring. We put this to 1 area % of the total section. The "Edges" feature was switched off but would if switched on, automatically merge smaller phases along grain boundaries to the phase of the grains.

From each of these auto-phasings, we collected the area percentage of the aggregate phase, which later was to be used to obtain chloride profiles. In addition, the $\frac{CPS}{eV}$ for chloride was collected from the cement paste phase. This was done by creating a spectrum with the $\frac{CPS}{eV}$ for all the elements found in the cement paste phase. In the spectrum, the $\frac{CPS}{eV}$-value for chloride was found, and the peak value was collected, as illustrated in Figure 4-13.

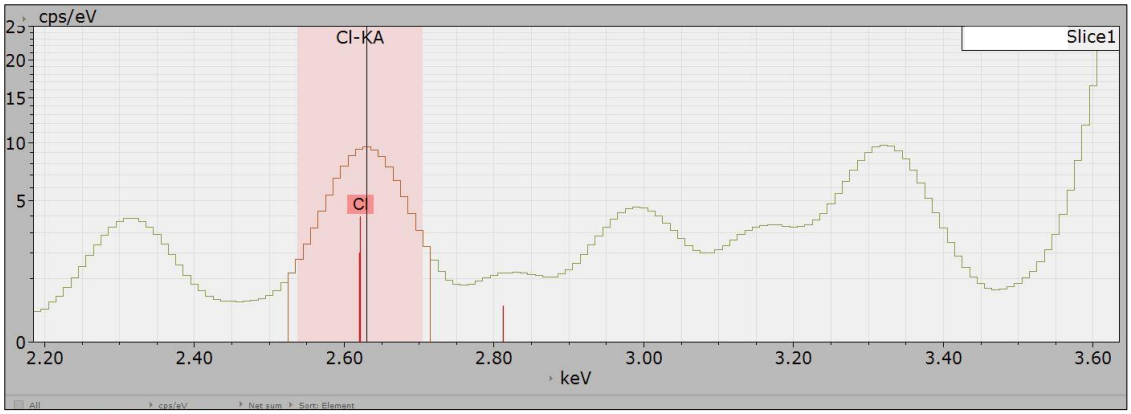

Figure 4-13: Peak value of $\frac{CPS}{eV}$ for chloride.

In total, we collected three values for the area percentage of the aggregates and three values of the $\frac{CPS}{eV}$ for chloride in the cement phase for each 5 mm section. These numbers were based on the Ca, Ca-Si and Ca-Si-S auto-phasings. An average of these was used in further calculations. All data obtained from the different auto-phasing methods can be found in Appendix A.3 and A.5.

For the reference samples, we did not need to perform any auto-phasing since they only contained cement. The $\frac{CPS}{eV} - value$ of the chloride peak was collected from each of these samples. An average from all analyses of the $\frac{CPS}{eV}$ for chloride from the reference samples, were then plotted against the known chloride content of these reference samples, $\frac{m_{Cl}}{m_{paste}}$, to establish the calibration curve.

We assumed the relation between $\frac{CPS}{eV}$ for chloride to be linear to the $\frac{m_{Cl}}{m_{paste}}$, and got the following equation:

$$\frac{CPS}{eV} = a * \frac{m_{Cl}}{m_{paste}} + b \tag{10}$$

a and b were then found using linear regression, and we could then transform from $\frac{CPS}{eV}$ to $\frac{m_{Cl}}{m_{paste}}$.

As we wanted the results in the form of $\frac{m_{Cl}}{m_{concrete}}$, and not $\frac{m_{Cl}}{m_{paste}}$, we needed to transform the output to the preferred form. This is done by

$$\frac{m_{Cl}}{m_{Concrete}} = \frac{m_{Cl}}{m_{paste} + m_{agg}} = \frac{m_{Cl}}{m_{paste} * (1 + \frac{a}{p})} \tag{11}$$

Where

$$\frac{m_{Cl}}{m_{Concrete}} - Chloride\ in\ concrete\ mass\ ratio\ [g/g]$$

$$\frac{m_{Cl}}{m_{paste}} - Chloride\ in\ paste\ mass\ ratio\ obtained\ from\ calibration\ curve\ [g/g]$$

$$\frac{a}{p} = Mass\ ratio\ of\ aggregate\ to\ paste\ [-]$$

Aggregate-paste mass ratio is found by:

$$\frac{a}{p} = \frac{m_{agg}}{m_{paste}} = \frac{\rho_{agg} * A\%_{agg.\mu XRF}}{\rho_{paste} * (1 - A\%_{agg.\mu XRF})} \quad (12)$$

With

$$\rho_{agg} - Density\ of\ the\ aggregates = 2700\ \left[\frac{kg}{m^3}\right]$$

$$A\%_{agg.\mu XRF} - Area\ percentage\ of\ aggregate\ phase\ from\ \mu - XRF\ [-]$$

$$\rho_{paste} - Density\ of\ the\ paste = 1980\ \left[\frac{kg}{m^3}\right]$$

$$m_{agg} - Mass\ of\ aggregates$$

$$m_{paste} - Mass\ of\ paste$$

And the paste density is calculated by:

$$\rho_{paste} = \frac{\rho_{binder} * \rho_{water} * \left(\frac{w}{b} + 1\right)}{\rho_{binder} * \frac{w}{b} + \rho_{water}} \quad (13)$$

Where,

$$\rho_{binder} - Density\ of\ binder = 3150\ [kg/m^3]$$
$$\rho_{water} - Density\ of\ water = 1000\ [kg/m^3]$$

and the water to binder mass ratio

$$\frac{w}{b} = \frac{m_{water}}{m_{binder}} = 0.38 \quad (14)$$

With

$$m_{water} - Mass\ of\ water$$

$$m_{binder} - Mass\ of\ binder$$

Since the µ-XRF is analysing an area and not a volume, we had to assume that the analysed area was representative for the entire volume. This led us to the assumption that Area percentage = Volume percentage. This assumption was used in (12). When calculating the density of the cement paste, we assumed no autogenous shrinkage to simplify the equation. The densities of the cement and the aggregate, in addition to the w/b-ratio, were all known.

When all the results had been transformed to % Cl/concrete, we could make chloride profiles by graphing chloride content against the average depth for the respective 5 mm section.

4.6.3 Chloride Content Determination Using the Direct Method (DM)

The Bruker M4 software includes a feature that will give mass concentration for the elements found in the object analysed. This is also recognized as a standard-less analysis for μ-XRF. We wanted to investigate the opportunity of utilizing this for a porous and in-homogenous material such as concrete.

As illustrated in Figure 4-14, the quantifying tool gives output as a list of elements and its mass concentration.

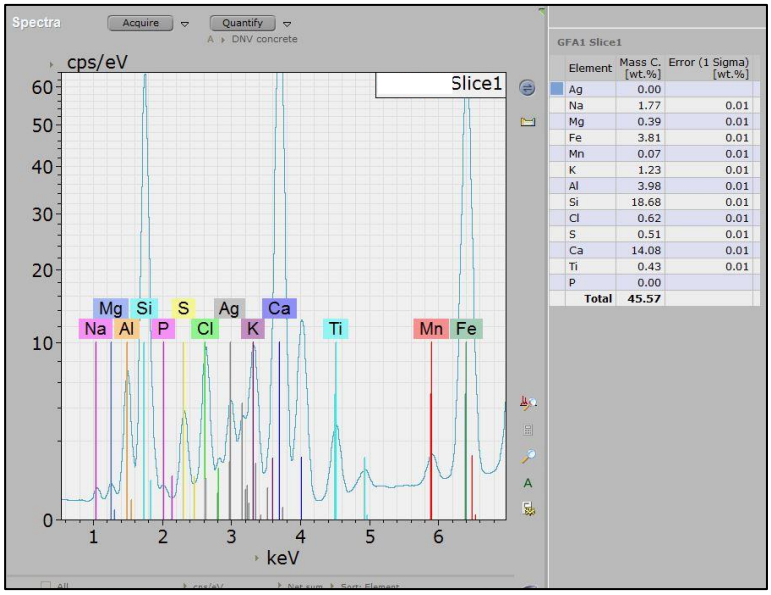

Figure 4-14: Illustration of the quantifying tool in the μ-XRF.

We retrieved the mass percentage of both chloride and calcium from each section of the samples, treating the entire section as one phase. In order to make this ratio comparable to the two other methods of analysis, we had to transform the mass ratio of Cl/Ca to Cl/Concrete.

Since we in the following transformation were dependent on the ratio between aggregates and cement, an auto-phasing was necessary using this method as well. In addition, the CaO-content of the cement was needed, which we found in the chemical composition of the cement used, provided by Norcem. See Appendix A.10 for details.

Cl/concrete was found by:

$$\frac{m_{Cl}}{m_{concrete}} = \frac{m_{Cl}}{m_{Ca}} * \frac{m_{Ca}}{m_{CaO}} * \frac{m_{CaO}}{m_{binder}} * \frac{1}{1+\frac{w}{b}} * \frac{1}{1+\frac{a}{p}} \quad (15)$$

With

$$\frac{m_{Cl}}{m_{Ca}} = Mass\ ratio\ of\ Cl\ to\ Ca\ \ from\ XRF[-]$$

$$\frac{m_{Ca}}{m_{CaO}} = Mass\ ratio\ of\ Ca\ to\ CaO\ [-]$$

$$\frac{m_{CaO}}{m_{binder}} = Mass\ ratio\ of\ CaO\ to\ binder\ from\ Norcem[-]$$

Water-binder- and aggregate-paste mass ratio is found by (14) and (12) respectively. Further information regarding this transformation can be found in Appendix A.14.

The output was then used together with the average depth for each section to generate chloride profiles.

A flow chart for the method is presented in Figure 4-15.

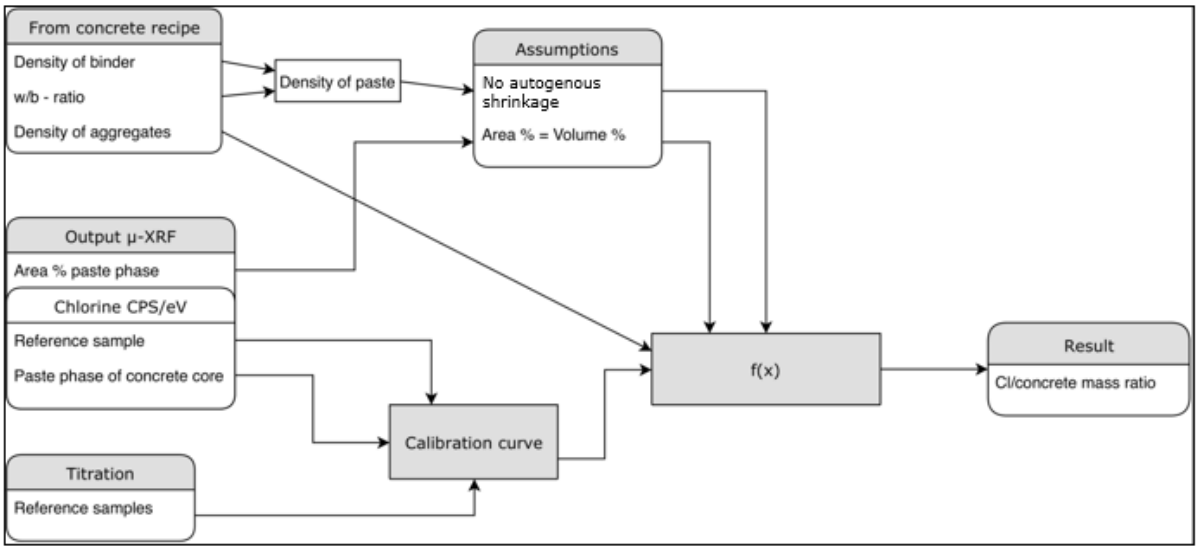

Figure 4-15: Illustration of Direct Method using a flow chart.

4.6.4 Polishing of Reference Samples

After 12 scans we decided to try to polish the reference samples in order to remove any deteriorated surfaces. We performed a wet polish of the reference samples, a method which is to be discussed in section 5.3. This was done by using sandpaper with a grading of 600. The sandpaper was placed on an even glass plate and sprayed with water. We polished the samples by moving them in an unpredictable pattern for about one minute. An illustration of the process is shown in Figure 4-16. As soon as we reached one minute of polishing, the sample was dried using paper. The sandpaper was cleaned between the polishing of each sample using water, dried and rewetted.

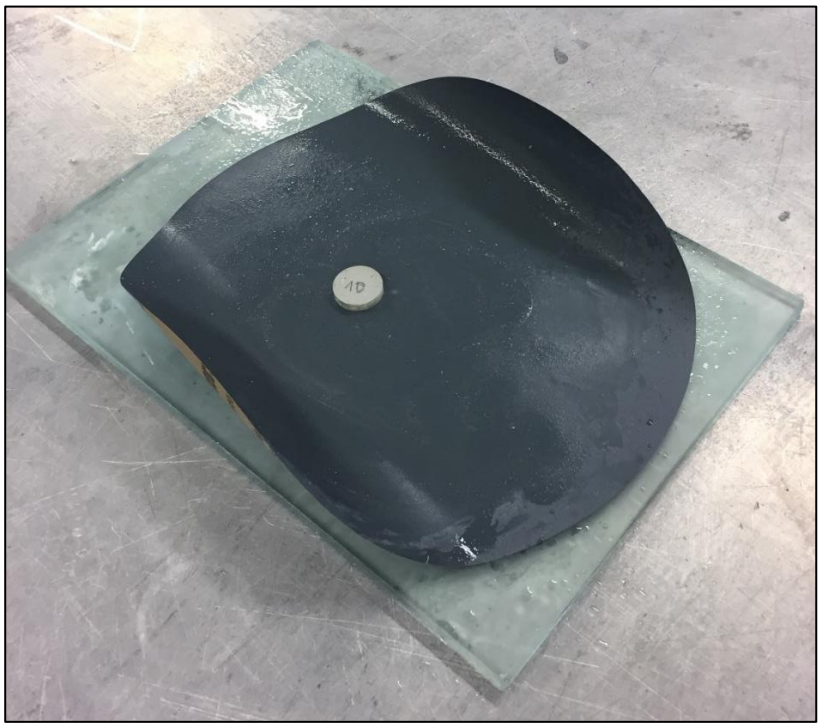

Figure 4-16: Polishing of reference sample.

These samples were then scanned in the μ-XRF with the newly polished side facing the X-ray, and a new calibration curve was established.

4.7 Comparison Tools

In this section, three tools used to compare the results from the different methods is presented. As much of the focus was directed towards accuracy, the uncertainty of the three methods was an important factor to quantify. Further, to be able to evaluate the µ-XRF's ability to isolate the paste share in the concrete, formulas necessary to compare the paste share from ICP-MS to µ-XRF was generated. This could help us understand how the auto-phasing works. In addition, formulas needed to obtain one of the most important results, the ingress depth and its uncertainty, is presented.

4.7.1 Propagation of Uncertainty

This chapter will provide the main formulas used for the propagation of uncertainty for the µ-XRF(CM), ICP-MS and potentiometric titration. Equations (16), (19) and (20) shown in the next sections, were used for determining the total uncertainty of % Cl/concrete from the calibration method with µ-XRF, ICP-MS and titration, respectively. The tables below the equations illustrate the function and corresponding uncertainty of the propagated uncertainty (in bold letters), in addition to the function and respective uncertainty of the components included in the uncertainty propagation equation.

More details regarding the calculations can be found in Appendix A.13.

4.7.1.1 µ-XRF

$$\sigma_{\mu-XRF} = \frac{m_{Cl}}{m_{concrete}} * \sqrt{\left(\frac{\sigma_{m.p}}{m_{paste}}\right)^2 + \left(\frac{\sigma_{calibration}}{\frac{m_{Cl}}{m_{paste}}}\right)^2 + \left(\frac{{\sigma_{m.a}}^2 + {\sigma_{m.p}}^2}{(m_{aggregates} + m_{paste})^2}\right.} \qquad (16)$$

Table 4-10: The functions and corresponding uncertainties within the µ-XRF uncertainty propagation equation

f	STD
$\frac{\boldsymbol{m_{Cl}}}{\boldsymbol{m_{concrete}}} = \frac{\boldsymbol{m_{Cl}}}{\boldsymbol{m_{paste}}} * \frac{\boldsymbol{m_{paste}}}{\boldsymbol{m_{agg}+m_{paste}}}$	$\boldsymbol{\sigma_{\mu.XRF}}$
$m_{paste} = \rho_{paste} * V_{paste}$	$\sigma_{m.paste}$
$m_{agg} = \rho_{agg} * V_{agg}$	$\sigma_{m.a}$
$\frac{m_{Cl}}{m_{paste}}$ – from calibration curve	σ_{cali}

The following equations were used to determine the uncertainty of the calibration curve:

$$\sigma_{Y.cali} = \sqrt{\frac{\sum(Y_i - Y'(x_i))^2}{N}} \quad (17)$$

$$\sigma_{X.cali} = \frac{\sigma_{Y.cali} - b}{a} \quad (18)$$

With

$$Y_i = y - value\ at\ point\ [CPS/eV]$$
$$N = Number\ of\ points$$
$$Y'(x_i) = Calibration\ curve = ax + b\ [CPS/eV]$$
$$x_i = The\ x - coordinate\ corrosponding\ to\ Y_i\ [g/g]$$

Equation (17) is obtained from [45].

4.7.1.2 ICP-MS

$$\sigma_{ICP-MS} = \frac{f_1}{m_{initial}} \sqrt{\frac{\sigma_{f_1}{}^2}{f_1} + \frac{\sigma_{m_{initial}}{}^2}{m_{initial}}} \quad (19)$$

Table 4-11: The functions and corresponding uncertainties within the ICP-MS uncertainty propagation equation

f	STD
$\boldsymbol{\frac{\mu g}{g} = \frac{\mu g}{L} * 101.4 * \frac{V_{initial} * 0.001 \frac{L}{mL}}{m_{initial}}}$	$\boldsymbol{\sigma_{ICP-MS}}$
$V_{initial}$	$\sigma_{V_{initial}}$
$m_{initial}$	$\sigma_{m_{initial}}$
$f_z = \mu \frac{g}{L} * 101.4$	σ_{f_z}
$f_1 = f_z * V_{initial}$	σ_{f_1}

4.7.1.3 Potentiometric Titration

$$\sigma_{titration} = \frac{f_a}{m_c * M_{Cl}} \sqrt{\left(\frac{\sigma_{f_a}}{f_a}\right)^2 + \left(\frac{\sigma_{m_c}}{m_c}\right)^2} \quad (20)$$

Table 4-12: The functions and corresponding uncertainties within the potentiometric titration uncertainty propagation equation

f	STD
$\boldsymbol{\frac{Cl}{Concrete}\left[\frac{g}{g}\right] = \frac{f_a}{m_c * M_{Cl}}}$	$\boldsymbol{\sigma_{titration}}$
$f_a = C_{Cl} * V_{HNO3}$	σ_{f_a}
m_c	σ_{m_c}

4.7.2 Variation of Paste from ICP-MS and μ-XRF

To compare paste variation in ICP-MS and μ-XRF, we had to be able to represent both outputs as $\frac{m_{paste}}{m_{concrete}}$.

The output from ICP-MS was in the form of $\frac{m_{Ca}}{m_{Concrete}}$. This was transformed to $\frac{m_{paste}}{m_{concrete}}$ using the following formula:

$$\frac{m_{paste}}{m_{concrete}} = \frac{m_{ca}}{m_{concrete}} * \frac{m_{CaO}}{m_{Ca}} * \frac{m_{binder}}{m_{CaO}} * \left(1 + \frac{w}{b}\right) \tag{21}$$

With

$$\frac{m_{ca}}{m_{concrete}} - Mass\ percentage\ of\ calcium\ in\ the\ concrete\ from\ ICP - MS\ analysis\ [-]$$

$$\frac{m_{CaO}}{m_{Ca}} - Mass\ ratio\ of\ calcium\ oxide\ to\ calcium\ [-]$$

$$\frac{m_{binder}}{m_{CaO}} - Mass\ ratio\ of\ binder\ to\ calcium\ oxide\ obtained\ from\ Norcem\ [-]$$

$$\frac{w}{b} - Mass\ ratio\ of\ water\ to\ binder\ in\ the\ cement\ paste\ [-]$$

From the μ-XRF, we got the area percentages of the different phases obtained using the auto-phasing tool previously mentioned. We assumed that the area percentage of paste from the μ-XRF can represent the volume percentage of the paste in the entire section. The next step was then to convert from volume percentage to a weight percent of $\frac{m_{paste}}{m_{concrete}}$.

$$\begin{aligned} \frac{m_{paste}}{m_{concrete}} &= \frac{V_{paste}}{(V_{paste} + V_{agg})} * \frac{(V_{paste} + V_{agg}) * \rho_{paste}}{V_{paste} * \rho_{paste} + V_{agg} * \rho_{agg}} \\ &= A\%_{paste.\mu XRF} * \frac{\rho_{paste}}{A\%_{paste.\mu XRF} * \rho_{paste} + A\%_{agg.\mu XRF} * \rho_{agg}} \end{aligned} \tag{22}$$

With

$$A\%_{paste.\mu XRF} - Area\ percentage\ of\ paste\ phase\ obtained\ from\ \mu - XRF$$

$$A\%_{agg.\mu XRF} = 1 - A\%_{paste.\mu XRF} - \ Area\ percentage\ of\ aggregate\ phase\ obtained\ from\ \mu - XRF$$

$$\rho_{agg} - Density\ of\ the\ aggregates = 3150\ [kg/m^3]$$

$$\rho_{paste} - Density\ of\ the\ paste = \ 1980\ [kg/m^3]$$

4.7.3 Location of Depth Where Cl_{crit} Has Been Reached

To be able to compare the depths where critical chloride content had been reached, we had to find this point on all graphs for all methods. This point was found by first locating the two values surrounding the critical chloride value,(y_1, y_2), and the corresponding depths of these values, (x_1, x_2), and then interpolate between these points. A linear relation between these points were assumed, and the following equation was used to interpolate:

$$x_{crit} = (Cl_{crit} - y_1) * \frac{x_2 - x_1}{y_2 - y_1} + x_1, \qquad Cl_{crit} \epsilon [y_1, y_2] \tag{23}$$

with

$$Cl_{crit} - critical\ chloride\ content = 0.07\ \%\ of\ concrete\ weight.$$
$$x_{crit} - Depth\ where\ critical\ chloride\ content\ is\ reached$$

To find the uncertainties for these depths, the same formula was used with the maximum chloride content values for all measurements, based on each of the corresponding propagated uncertainties. An illustration of this is presented in Figure 4-17.

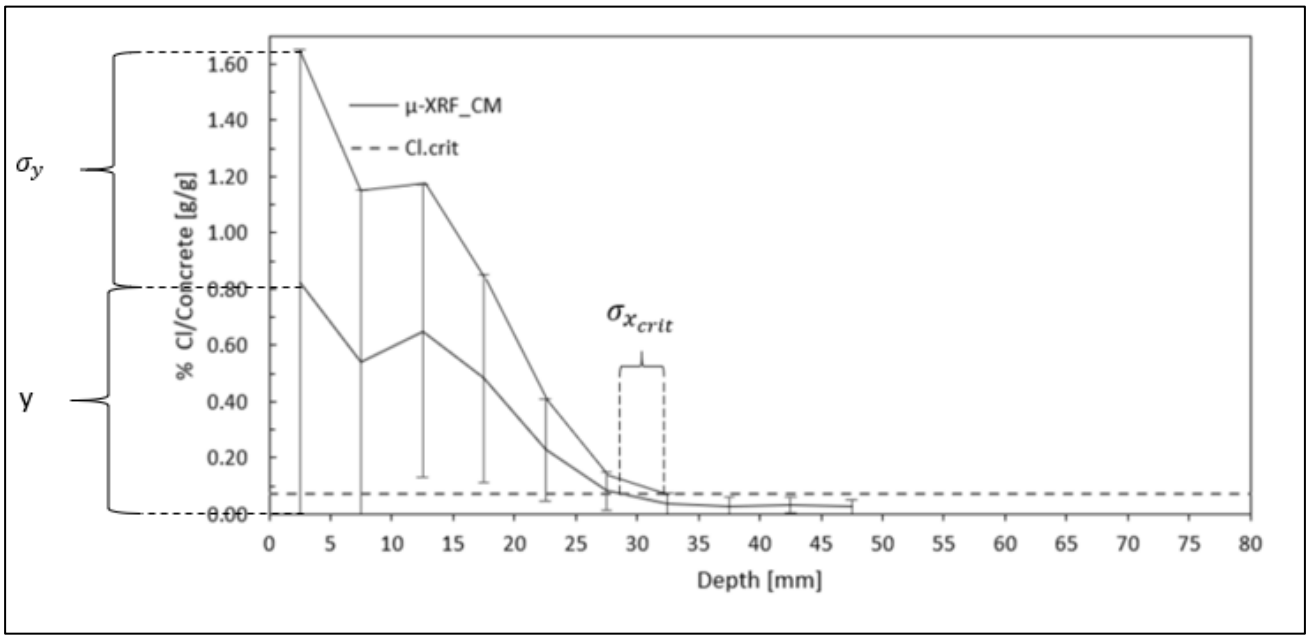

Figure 4-17: Illustration of how $\sigma_{x_{crit}}$ is found, with superficially large uncertainty for each concentration, for illustration purposes.

The calculations are then the following:

$$x_{crit} + \sigma_{x_{crit}} = (Cl_{crit} - y_1 + \sigma_{y_1}) * \frac{x_2 - x_1}{y_2 + \sigma_{y_2} - y_1 + \sigma_{y_1}} + x_1\,, \qquad Cl_{crit} \epsilon [y_1 + \sigma_{y_1}, y_2 + \sigma_{y_1}] \tag{24}$$

To simplify the procedure, instead of also finding where the minimum chloride content would intersect the critical chloride content line, we say that:

$$\rightarrow x_{crit} = x_{crit} \pm \sigma_{x_{crit}}$$

with

$$\sigma_{x_{crit}} - standard\ deviation\ for\ x_{crit}$$
$$\sigma_{y_1} - standard\ deviation\ for\ y_1$$
$$\sigma_{y_2} - standard\ deviation\ of\ y_2$$

5 Evaluation of μ-XRF for Chloride Ingress Determination

In this chapter, the μ-XRF's ability to determine the chloride ingress in concrete structures will be discussed. A comparison of potentiometric titration, ICP-MS and μ-XRF will be presented regarding the quantitative analysis of chloride in the concrete cores.

Section 5.1 will present the results for Structure A obtained by the three methods of analysis. In section 5.2 the variation of the paste share in the concrete will be compared from ICP-MS and μ-XRF. Section 5.3 will present the effect of polishing of the reference samples. A discussion on qualitative measurements in section 5.4. The full comparison of the methods will be outlined in section 5.5. Factors that will be evaluated are their accuracy, complexity, efficiency, and versatility. A conclusion will be given in section 5.6.

5.1 Results

Results from potentiometric titration, ICP-MS and µ-XRF are presented as chloride profiles below. For the µ-XRF, both direct method (DM) and calibration method (CM), are included. The exposed side of the concrete cores is to the left in all graphs.

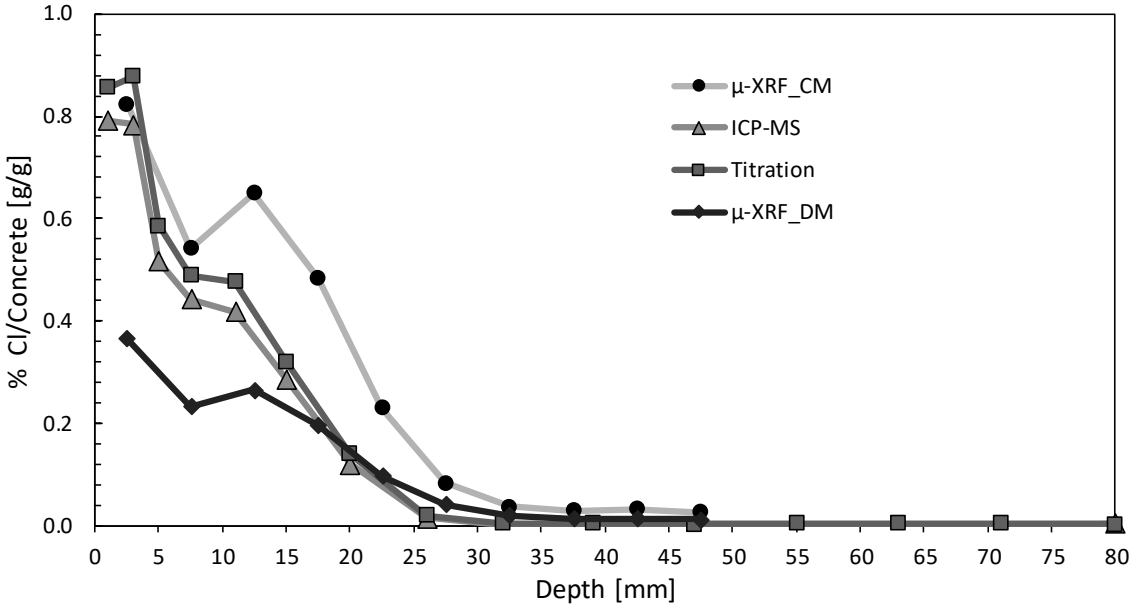

Figure 5-1: Chloride content in mass % Cl/Concrete [g/g] in core A.1.O. The exposed side is to the left.

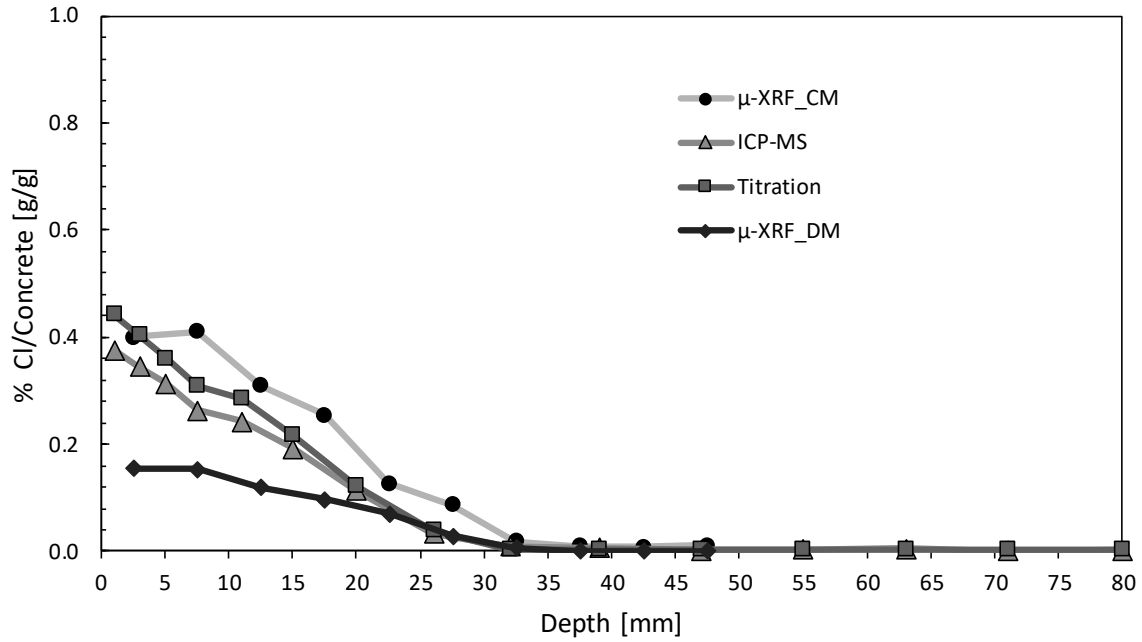

Figure 5-2: Chloride content in mass % Cl/Concrete [g/g] in core A.2.O. The exposed side is to the left.

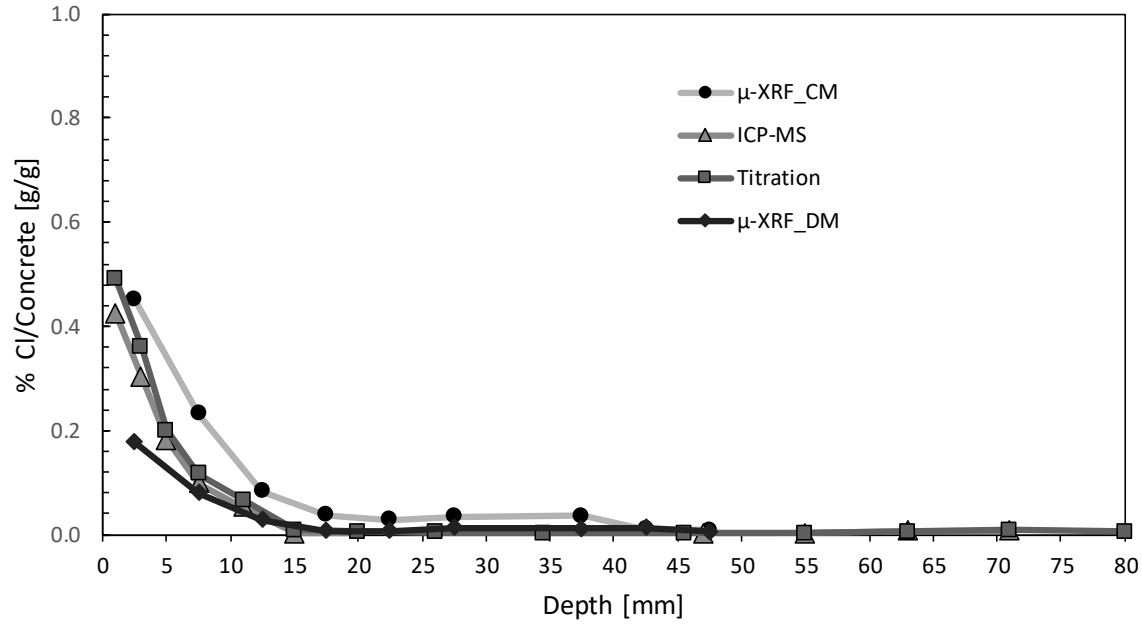

Figure 5-3: Chloride content in % Cl/Concrete [g/g] in core A.3.O. The exposed side is to the left.

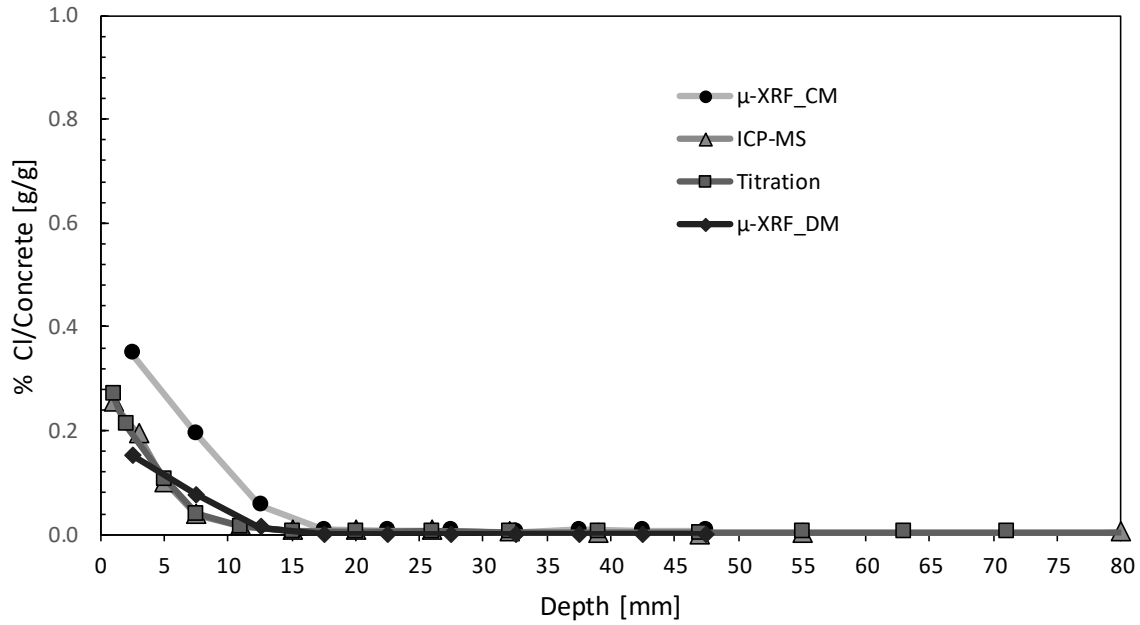

Figure 5-4: Chloride content in % Cl/Concrete [g/g] in core A.4.I. The exposed side is to the left.

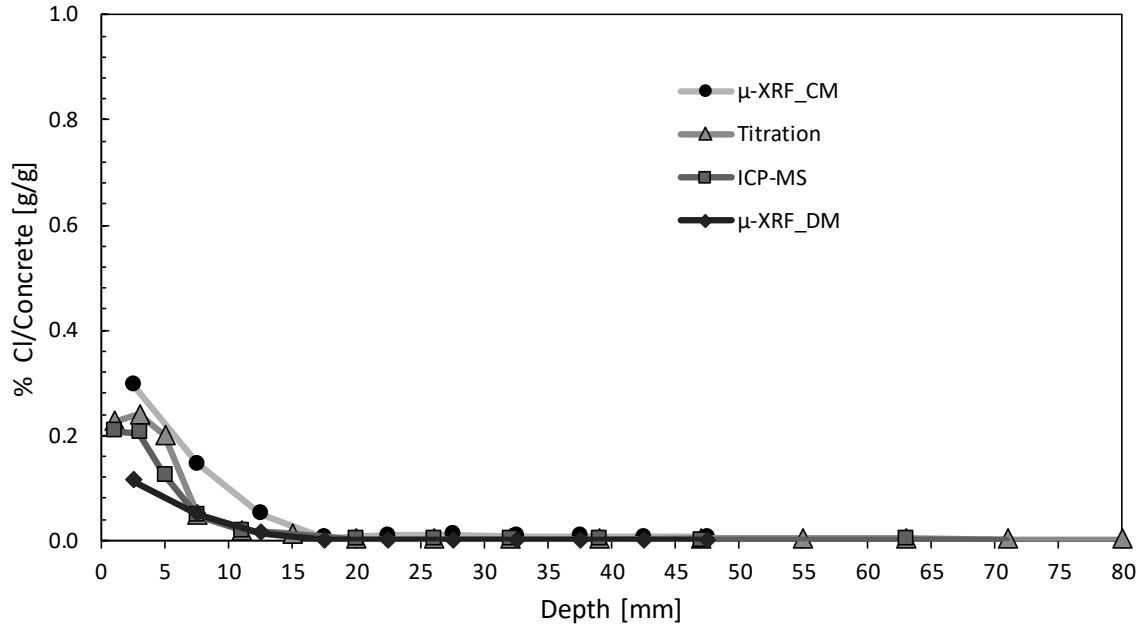

Figure 5-5: Chloride content in % Cl/Concrete [g/g] in core A.5.I. The exposed side is to the left.

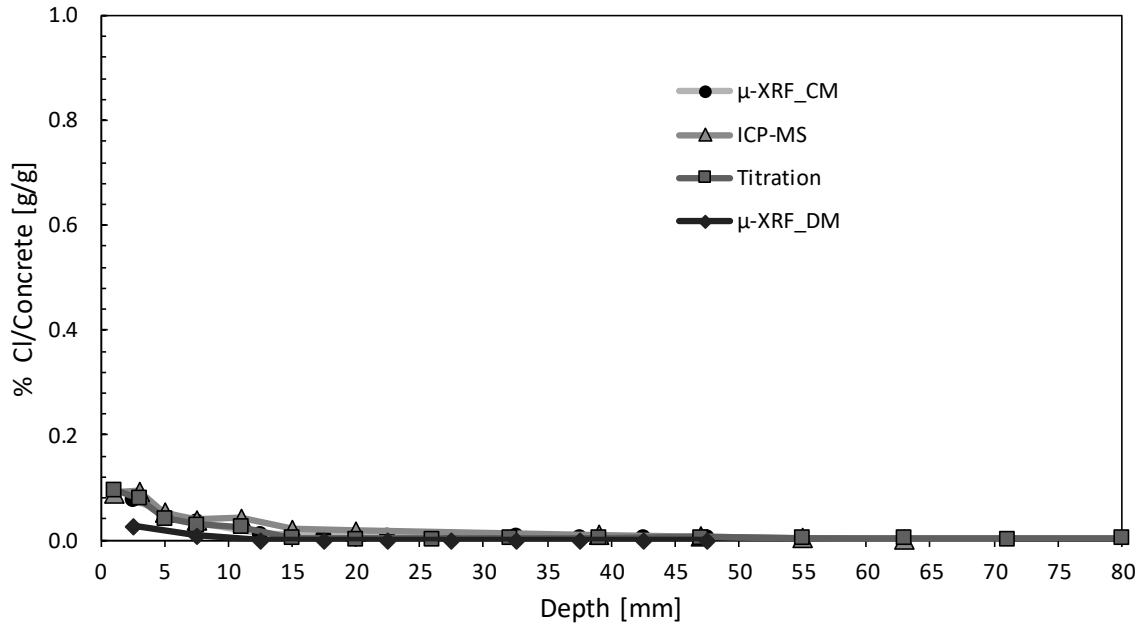

Figure 5-6: Chloride content in % Cl/Concrete [g/g] in core A.6.I. The exposed side is to the left.

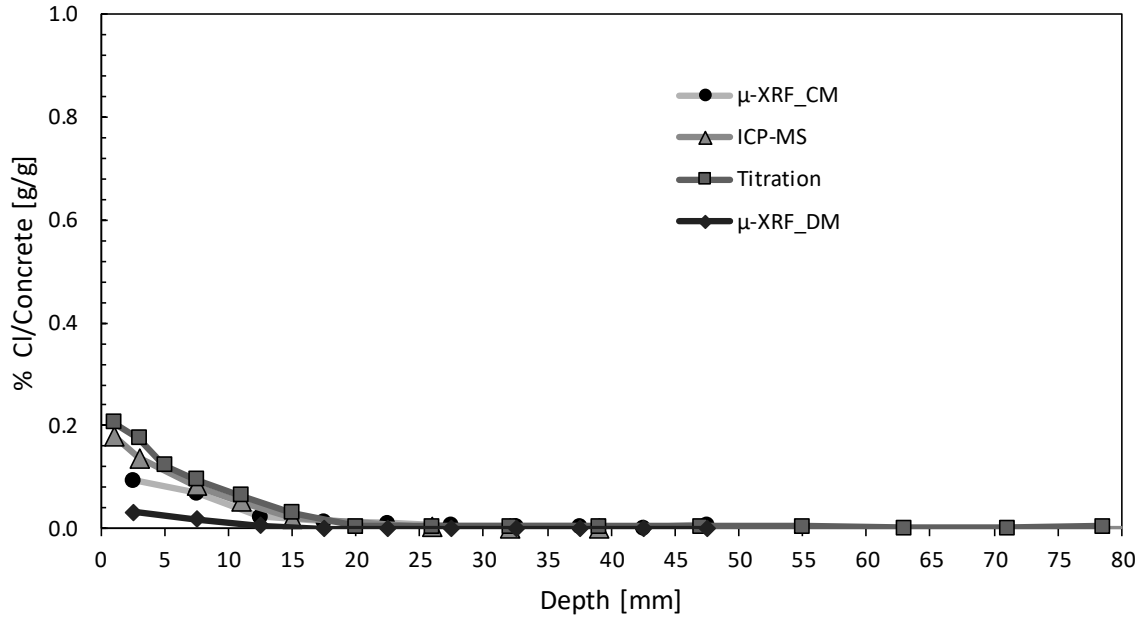

Figure 5-7: Chloride content in % Cl/Concrete [g/g] in core A.7.I. The exposed side is to the left.

5.2 Difference in Amount of Paste

In order to present results from μ-XRF as % Cl/concrete, we are dependent on knowledge regarding the paste share of the different sections. The methods used to determine the paste share in the cores are described in section 4.7.2. The mass ratio of paste to concrete obtained from ICP-MS and μ-XRF, are presented graphically below.

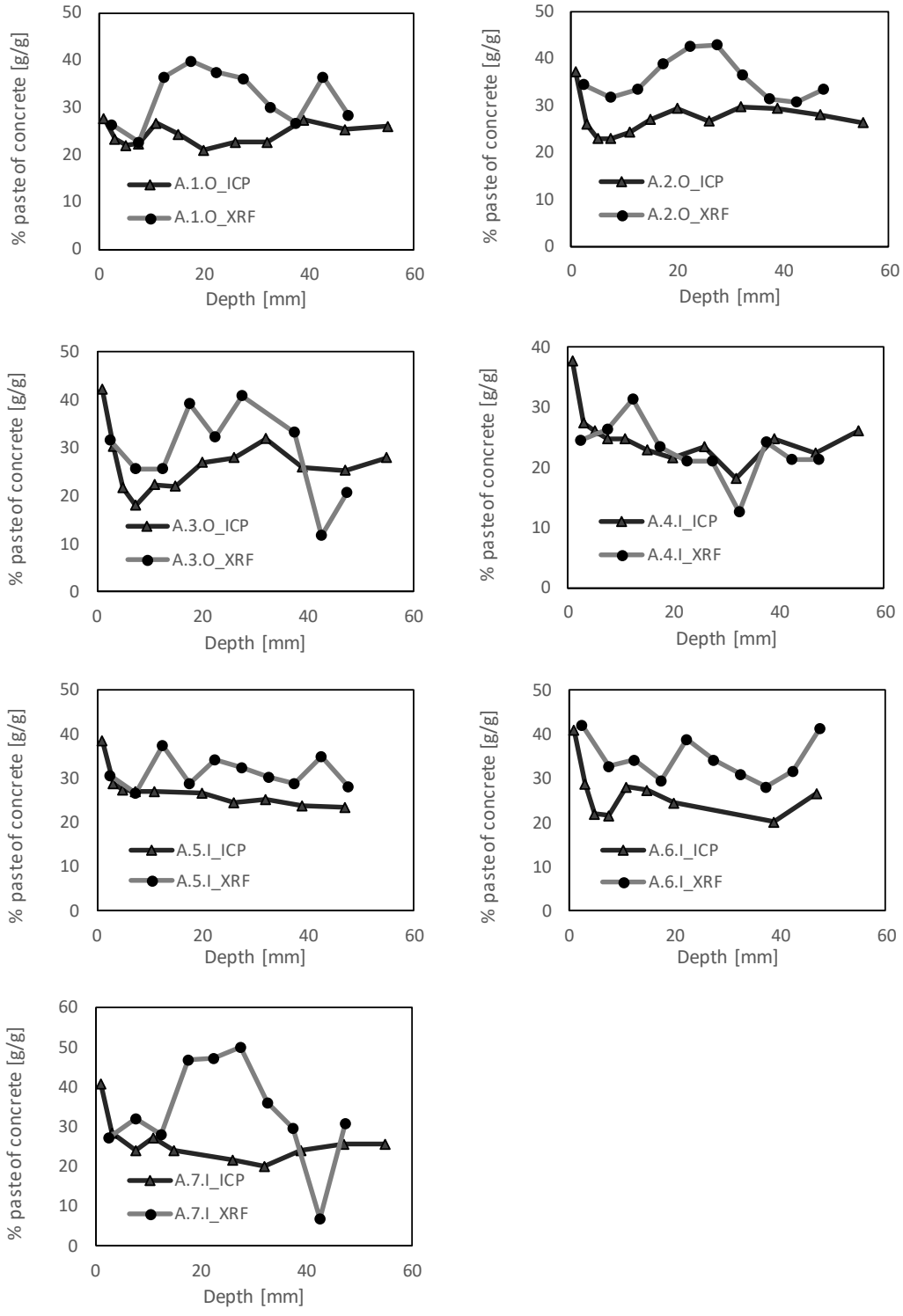

Figure 5-8: Variation of paste content with depth, measured with both ICP-MS and μ-XRF.

5.3 Effect of Polishing Reference Samples

The polishing was done with sandpaper and water, i.e. a wet polish. Subsequently, this should have been done without water and with separate sandpapers for each sample, to prevent contamination. The consequences of the wet polish are not certain, but in order to eliminate that possible source of error, a dry polish should have been performed instead.

Polishing the reference samples influenced the CPS/eV for Cl. A calibration curve utilising the new numbers generated final results in a better agreement with the results obtained from titration and ICP-MS. The variation of CPS/eV for chloride in the reference samples before and after polishing, is presented in Figure 5-9. The change of the calibration curve caused by this action is shown in Figure 5-10.

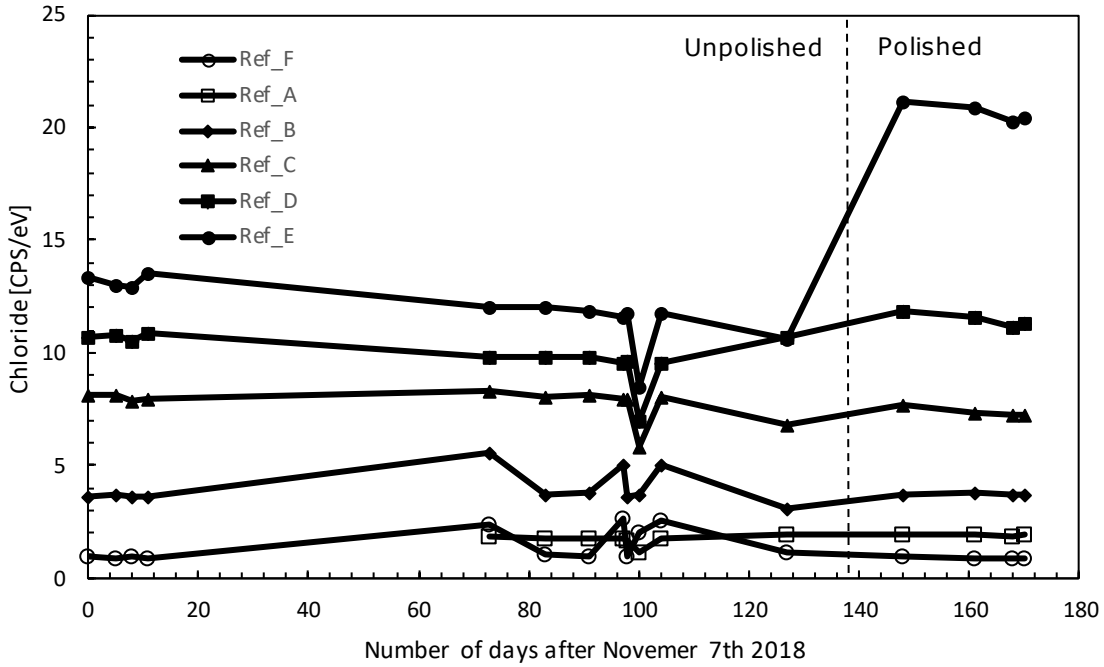

Figure 5-9: The effect of polishing reference samples with sandpaper.

Around day 100, we can clearly see a drop in CPS/eV for every sample. When that analysis was run, we forgot to switch on the X-ray in sufficient time prior to the analysis, preventing the X-ray from getting warmed up properly. We suspect this to be the explanation to this general deviation.

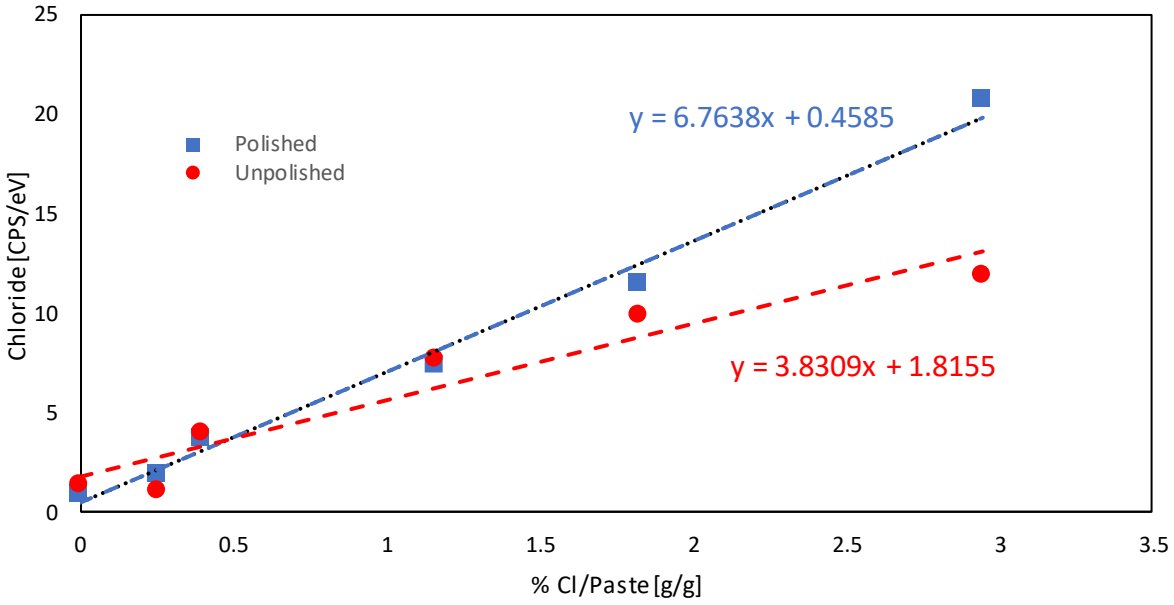

Figure 5-10: Change of calibration curve after polishing of reference samples.

5.4 Qualitative Measurements with μ-XRF

In order to see if the μ-XRF provide proper qualitative information, elemental heat maps obtained by μ-XRF is to be compared to elemental profiles from ICP-MS. Based on the composition of seawater, an increased concentration of chloride, magnesium and sulphur is expected at the exposed side of the cores. Profiles made from ICP-MS data for magnesium and sulphur is presented in Figure 5-11. Calculation of data obtained from ICP-MS is described in section 4.5. Profiles for chloride is presented in section 5.1.

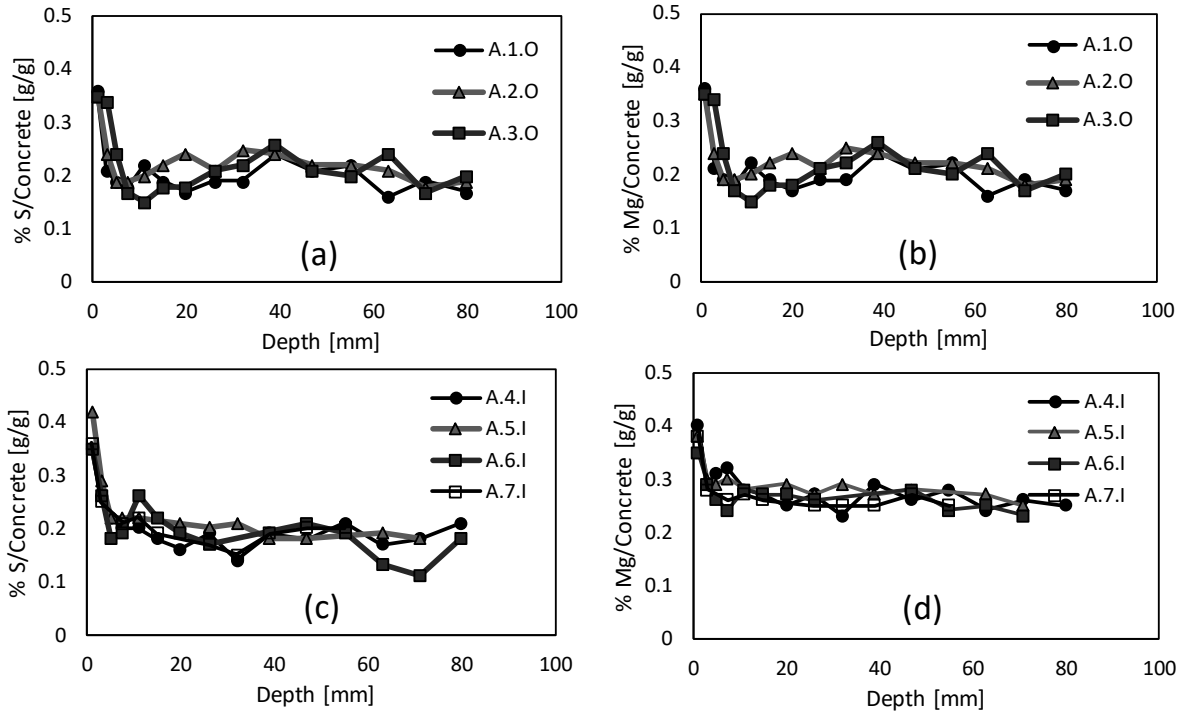

Figure 5-11: Variation of sulphur and magnesium concentration by ICP-MS in Structure A for outside cores in (a) and (b), for inside cores in (c) and (d). The exposed surface is to the left. Values obtained from Appendix A.2.

From the ICP-MS results, every core shows an increased concentration of both sulphur and magnesium at the exposed side of the concrete cores. This seems to be the case solely for the first 4 mm of the core.

From the μ-XRF, all the qualitative overviews are presented in Appendix A.12. For further discussion, core A.1.O is used as an example. Elemental overviews of magnesium, sulphur and chloride are presented in Figure 5-12, Figure 5-13 and Figure 5-14 respectively.

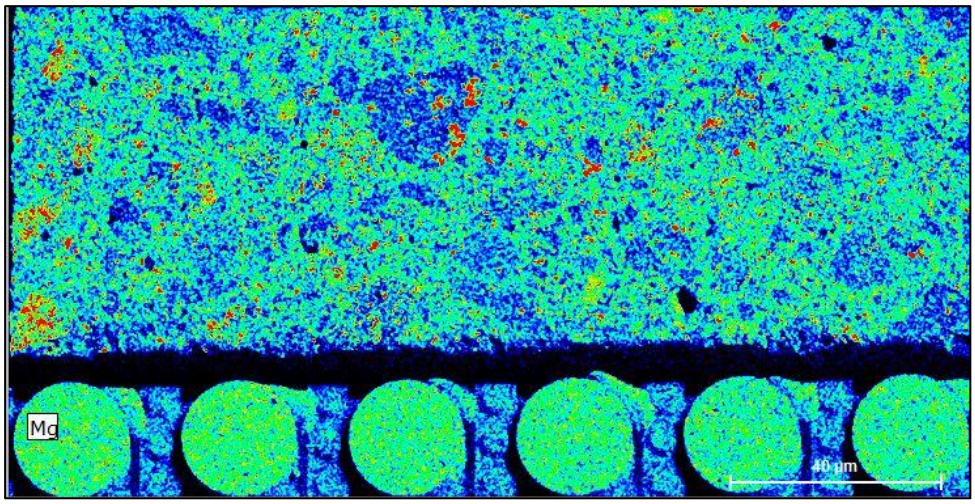

Figure 5-12: Overview of A.1.O with respect to magnesium. The exposed side is to the left.

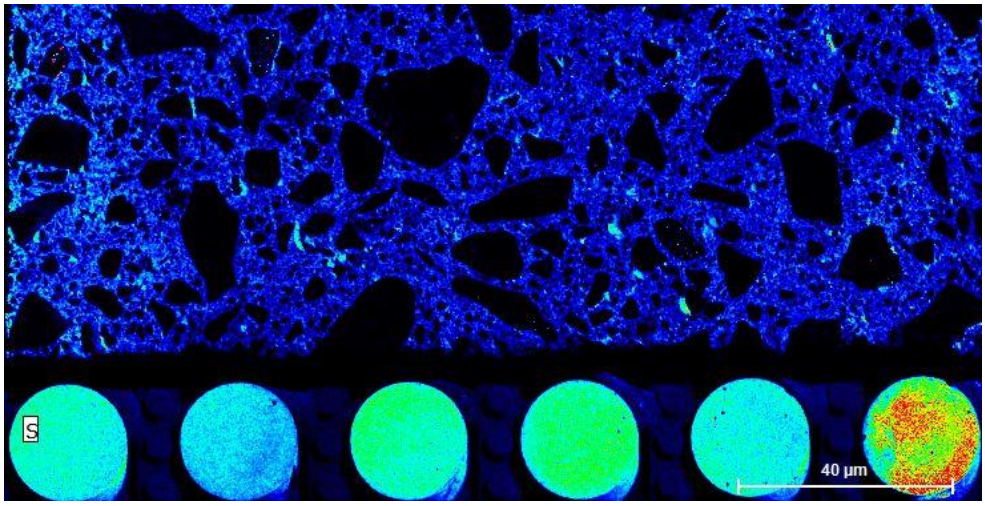

Figure 5-13: Overview of A.1.O with respect to sulphur. The exposed side is to the left.

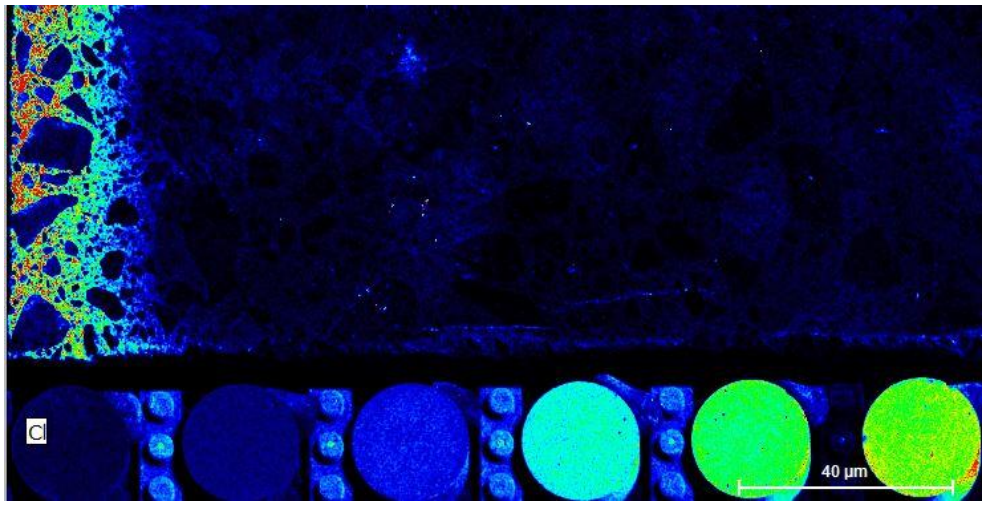

Figure 5-14: Overview of A.1.O with respect to chloride. The exposed side is to the left.

A gradient of chloride is clearly visible at the outermost part of the exposed side of the concrete core in Figure 5-14. This corresponds very well the profile made from ICP-MS in section 5.1 for chloride. For sulphur in Figure 5-13, a small gradient is barely observable in the first few millimetres of the core. This does also, to some degree, correspond with the results obtained from ICP-MS in Figure 5-11

A gradient of magnesium is even vaguer as seen in Figure 5-12. As seen from the oxide overview of granitic gneiss in Table 4-2, the aggregates contain 0.66 % MgO [g/g] i.e. 0.4 % Mg [g/g]. The ICP-MS results show a maximum concentration of roughly 0.4 % Mg [g/g] in the first few millimetres of the concrete. As the concentration of Mg is approximately the same for the concrete and for the aggregates alone, a clear gradient might be difficult to observe from the elemental heat map.

A comparison with the elemental overviews from all cores in Appendix A.12 to the ICP-MS variation in Figure 5-11, indicates that the above-mentioned observations are representative.

5.5 Comparison of Methods

In this section, we are going to discuss the main differences between the methods of analysis used in this thesis. The focus will primarily be directed towards accuracy, before aspects such as versatility, complexity, and efficiency also will be considered.

5.5.1 Direct Method (DM) vs. Calibration Method (CM) in μ-XRF

When using DM, we did not expect the weight percentages of each element to be completely accurate, but we thought that the $\frac{m_{Cl}}{m_{Ca}}$ ratio could be correct. We wanted to use this ratio to obtain the correct chloride concentration in the concrete.

As can be seen from the results in section 5.1, compared to the other methods of analysis, DM, in general, gives a lower concentration for every core. To investigate the reason for this further, we compared the mass ratio of Ca to concrete and Cl to concrete found from DM to the ones obtained from ICP-MS. In Figure 5-15 the average amount of Ca per concrete weight in the concrete cores from Structure A is presented for both DM and ICP-MS.

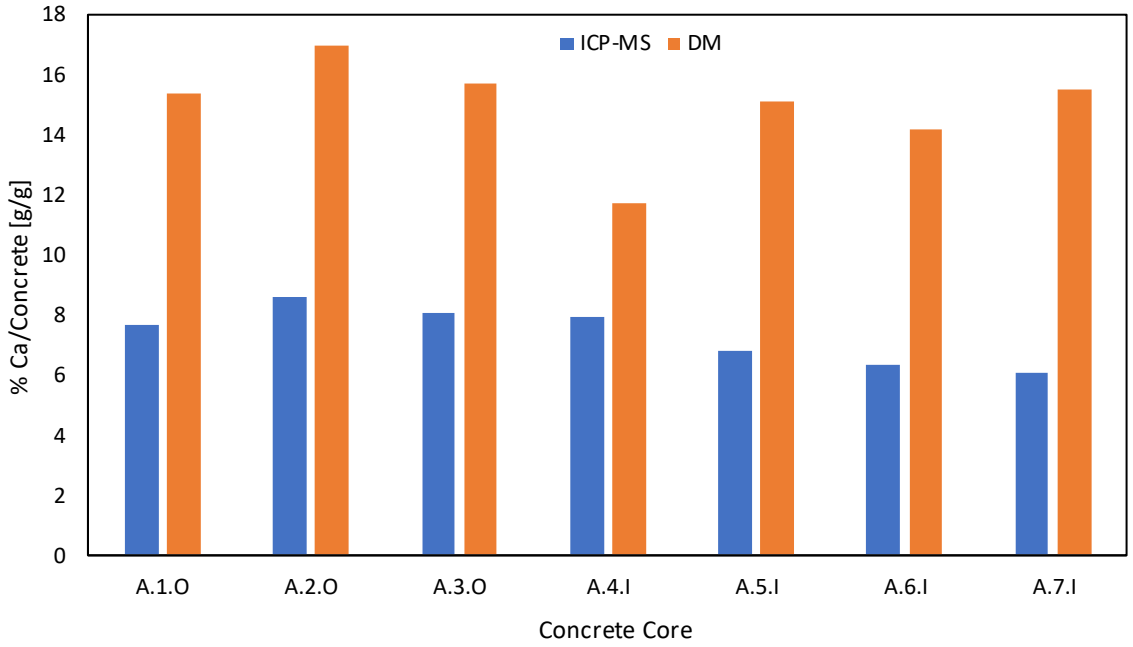

Figure 5-15: Illustration of the difference in the amount of Ca found in cores from Structure A by ICP-MS and DM.

This indicates that the DM, in general, overestimates the amount of Ca in the concrete.

In Figure 5-16 the same comparison is done with an average of the chloride content in the seven cores.

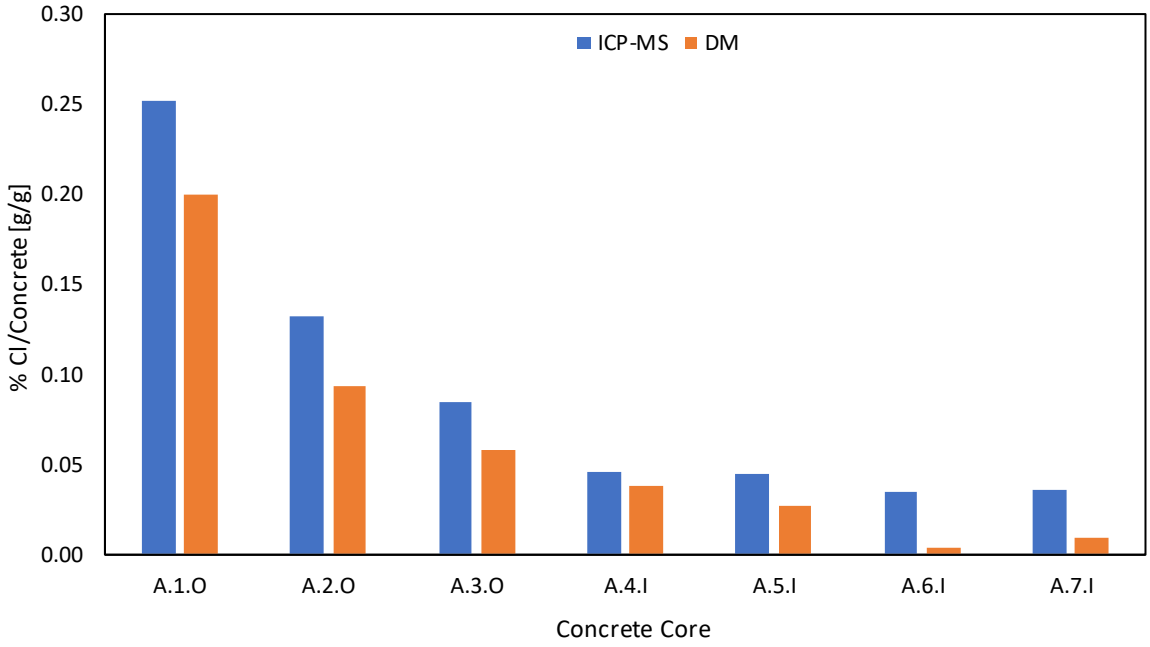

Figure 5-16: Illustration of difference in the amount of Cl found in cores from Structure A by ICP-MS and DM.

This indicates that the chloride, in general, is underestimated. An overestimation of calcium together with an underestimation of chlorides, ultimately lead to a substantial underestimation of the Cl/Ca ratio.

The same comparison is done with the six reference samples. In Appendix A.11 the chemical composition of the cement used in these reference samples is given. Together with their w/b-ratio and chloride content given in Table 4-8, the calcium- and chloride concentration in the paste were found. These values are in Figure 5-17 and Figure 5-18 compared to the values obtained by DM.

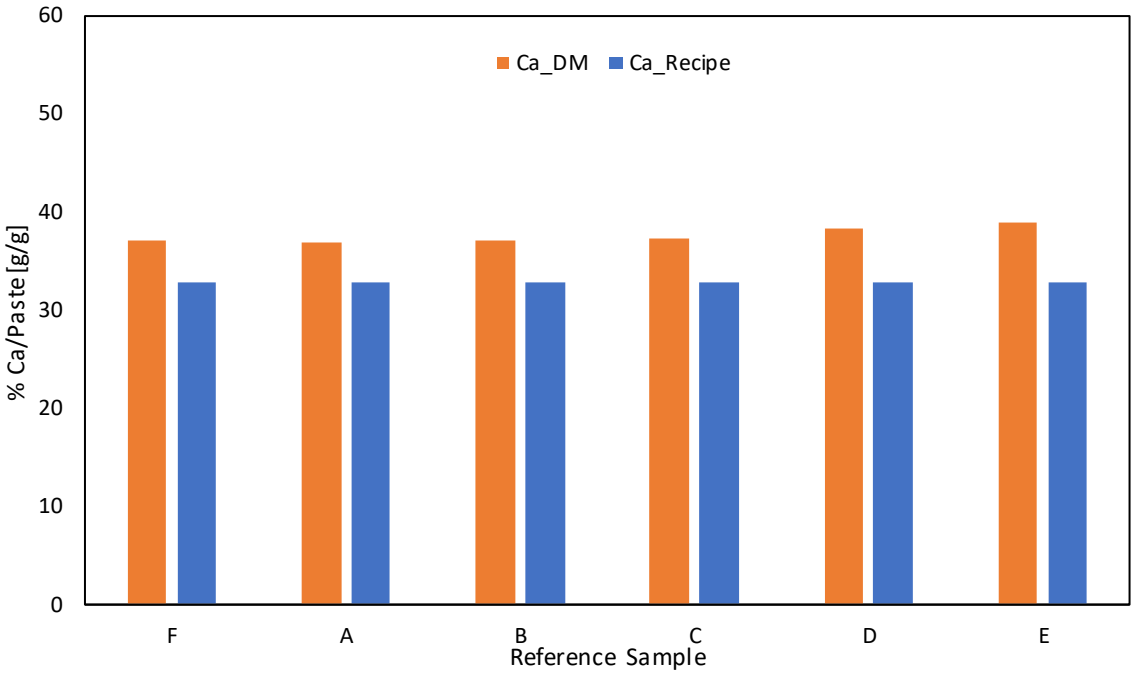

Figure 5-17: Illustration of difference in the amount of calcium found in the six reference samples by DM compared to the recipe given in Appendix A.11.

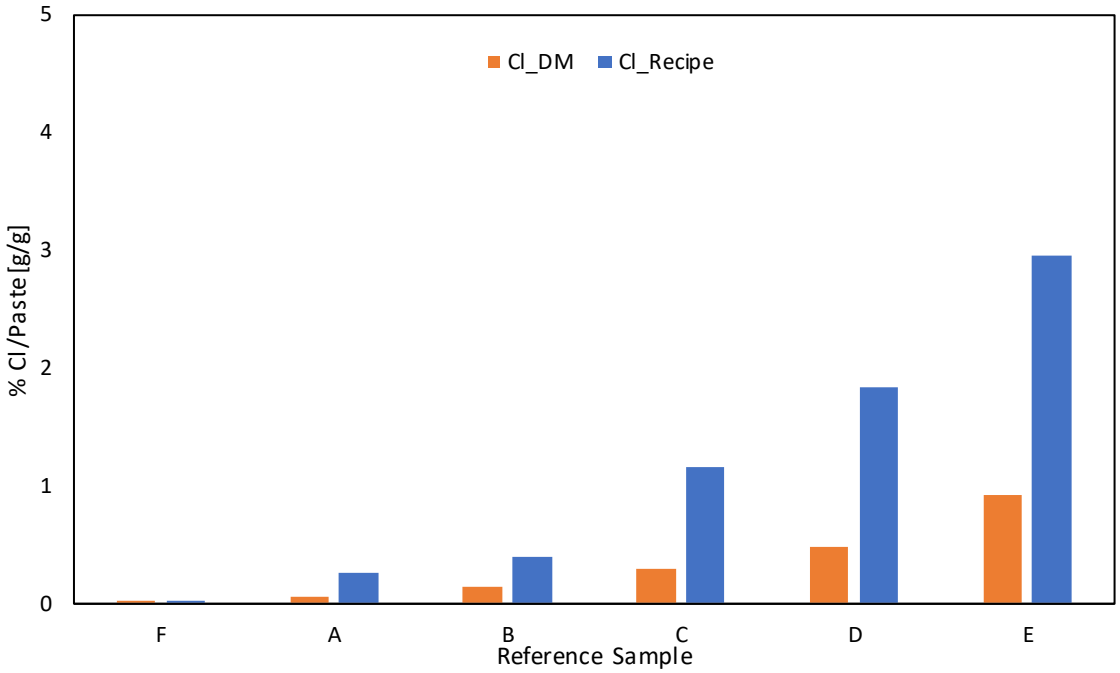

Figure 5-18: Illustration of difference in the amount of chloride found in the six reference samples by DM compared to the amounts given in Table 4-8.

This only substantiates the idea of an overestimation of calcium and an underestimation of chloride in the DM.

The DM results above are all based on raw mass concentration data from the µ-XRF. To evaluate the credibility of this, the raw µ-XRF data from reference sample F was normalised based on the known oxide composition of the cement. In Table 5-1 selected elements from reference sample F is presented, both obtained from the DM and from the chemical composition given in Appendix A.11. See Appendix A.8 for details regarding this comparison.

Table 5-1: Selected raw- and normalised data from µ-XRF DM of reference sample F, compared to the chemical composition of the cement. Values extracted from Appendix A.8.

	Raw data		**Normalized data**	
Element	**µ-XRF DM**	**Oxide**	**µ-XRF DM**	**Chemical composition**
Ca	39.14	CaO	63.90	63.78
Si	6.66	SiO2	17.22	21.31

As can be seen, more accurate results are obtained by performing this normalisation. This indicates that if the software is told which oxides to expect in the cement, it might present more accurate results.

This also indicates that the reason for the big deviation of DM results compared to the other methods is due to calculations based on faulty assumptions within the software of the µ-XRF. How the µ-XRF software processes the information it gets from the scanning and turns it into weight percentages is unclear to us. Allegedly there are assumptions made within the software regarding the properties of the sample that is analysed [46]. As mentioned in section 3.3.1, an internal database is utilised when the software is performing such a standard-less analysis. This database might be scarce for concrete. This is an area where our expertise is limited. We will therefore not try to explain this in further detail. Nor will we try to calculate any uncertainties for this method, as it is quite unclear what exactly causes the errors.

The Calibration Method, however, is a method where sources of error are much clearer. This method also gave results that correlated better with ICP-MS and titration. The calibration method will, because of this, be the only µ-XRF based method we will investigate further in this thesis.

5.5.2 Uncertainties μ-XRF (CM)

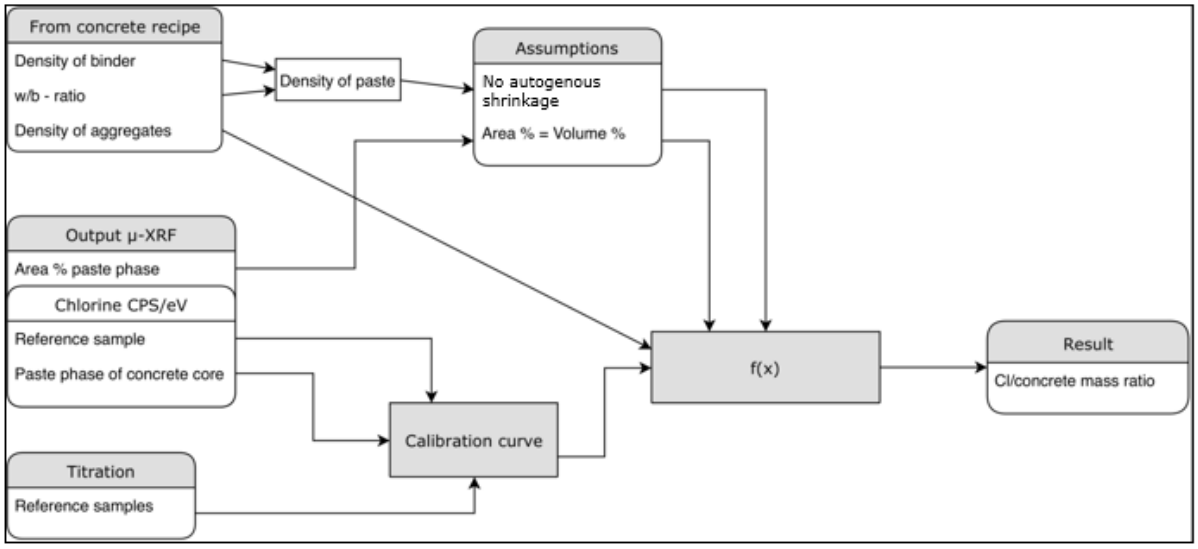

Figure 5-19: Illustration of the Calibration Method using a flow chart.

There are a lot of uncertainties to consider within the calibration method. Figure 5-19 shows a flow chart of the method where it is clear that the calibration curve is a big part of the process, built on many different measurements with various degrees of uncertainty.

Our calibration curve is based on the four different scans we had performed on the six reference samples after they had been polished. There were two different ways of determining the calibration curve from this data. The first option was to plot all points of CPS/eV values to the known chloride content in one graph and establish a calibration curve from a trend line of all these 24 points. This is illustrated in Figure 5-20.

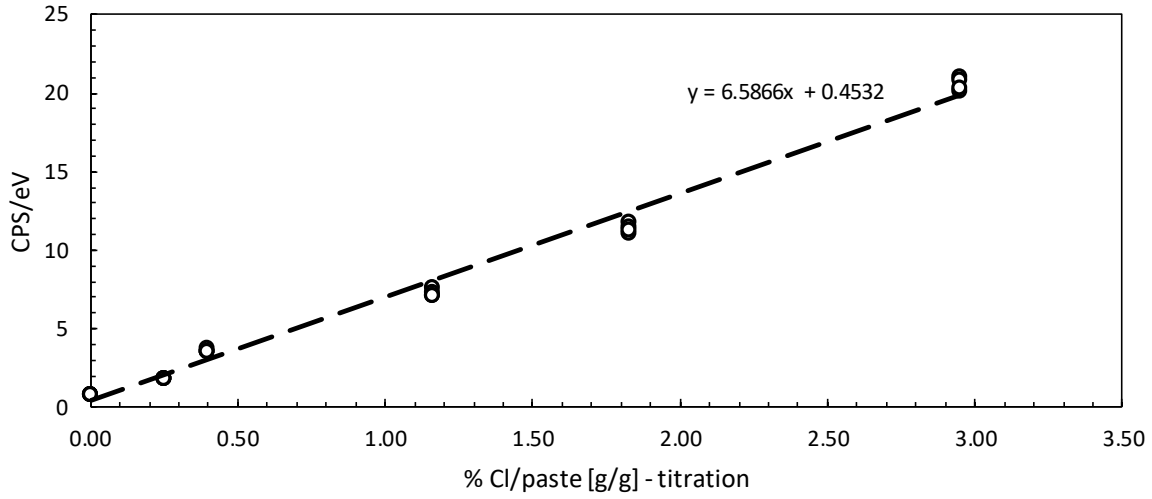

Figure 5-20: A calibration graph obtained from all points in the same graph.

The second option was to first calculate the average CPS/eV-value for each of the reference samples and plot the average value of CPS/eV for each of the six reference samples against the known chloride content. A calibration curve was then established from a trend line of these six points, as shown in Figure 5-21.

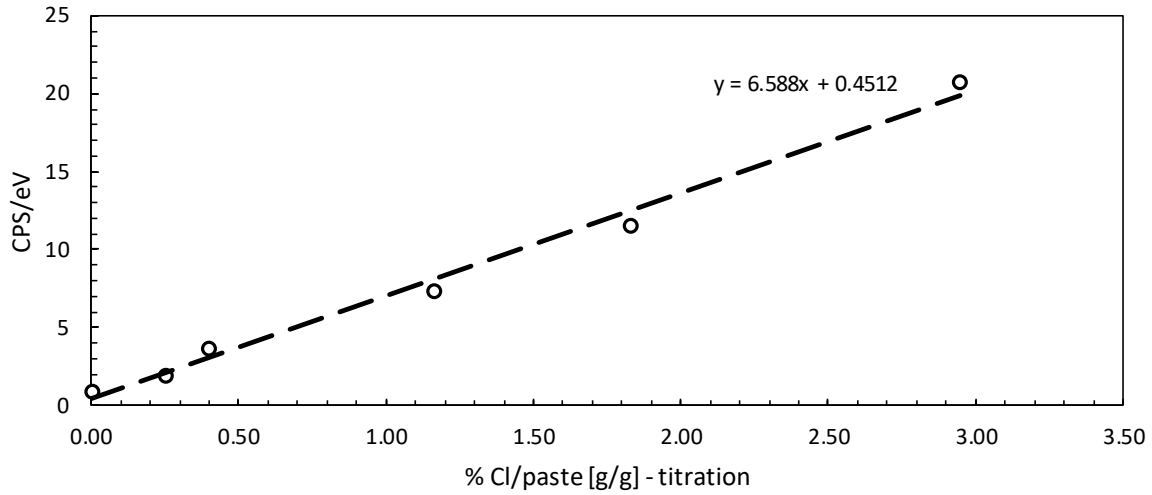

Figure 5-21: A calibration curve obtained from the average values of each reference sample.

The uncertainty of the calibration curve in the Y-direction was then calculated using (17) The uncertainty in X-direction is the one we wanted to figure out since this is the uncertainty in Cl/paste obtained from the graph. We, therefore, had to figure out the impact the uncertainty in Y-direction had on the uncertainty in X-direction. This was done by simply looking at what a change in Y, equal to the uncertainty, would do to the change in X. This is illustrated in Figure 5-22. This was the background for equation (18).

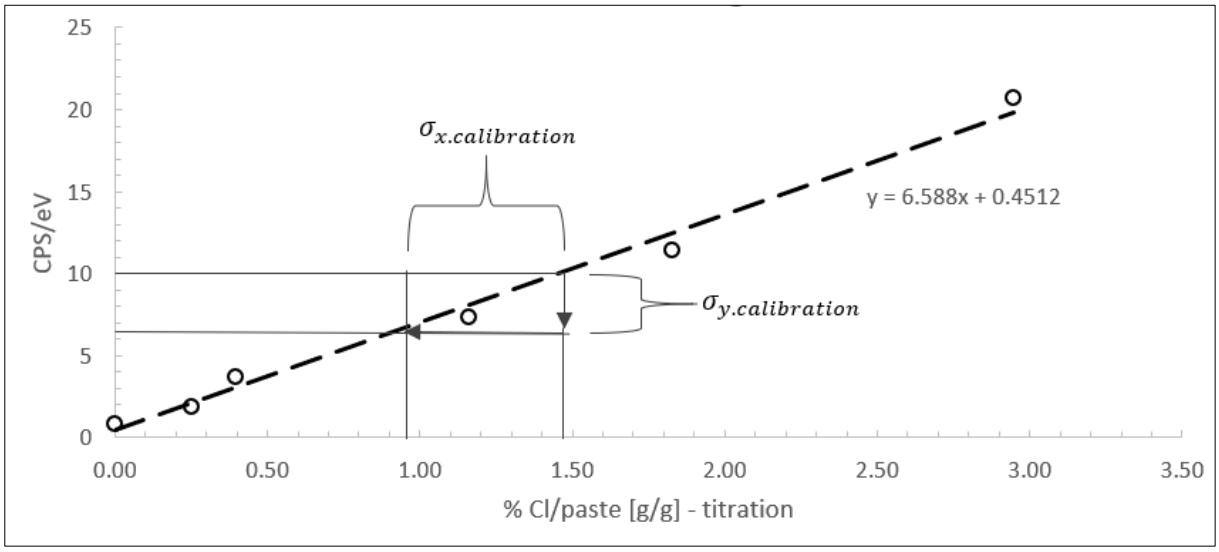

Figure 5-22: Illustration of the effect an error in CPS/eV has on the error in % Cl/Paste.

A marginally lower uncertainty was found from the last alternative, as seen in Table 5-2. We, therefore, decided to use the calibration curve from average values and its corresponding uncertainty, for the rest of the thesis.

Table 5-2: Uncertainties of the two different calibration curves.

Average calibration		**All points calibration**	
$\sigma_{y.calibration}$	$\sigma_{x.calibration}$	$\sigma_{y.calibration}$	$\sigma_{x.calibration}$
0.74 [CPS/eV]	0.04 [g/g]	0.77 [CPS/eV]	0.05 [g/g]

A potentially big source of error in the calibration method is the assumption that the area percentage of aggregates we get from the µ-XRF can be assumed to represent the actual volume percentage of aggregates in the entire volume of the thin section. To look deeper into the error caused by these assumptions, we made a comparison of the $\frac{m_{paste}}{m_{concrete}}$ from the µ-XRF and ICP-MS as can be seen in section 5.2. $\frac{m_{paste}}{m_{concrete}}$ for µ-XRF were a function of both the area percentage and density of the paste, while the one obtained from ICP-MS were a function of the calcium and chloride per concrete obtained from the ICP-MS, together with information from the oxide overview of the cement. These are generally deviating for all cores, where the µ-XRF is consequently giving a higher $\frac{m_{paste}}{m_{concrete}}$ than the ICP-MS

When the auto-phasing is performed within the µ-XRF software, we noticed that with high sensitivity, the concrete often gets separated into more than two different phases. Often one phase that quite clearly are the aggregates, one or two that is representing most of the paste, and a few phases containing a lot of small dots within the paste or on the edges of the aggregate grains. Figure 5-23 shows a phase separation that has resulted in five different phases. As you can see, it is not always easy to determine whether the smaller phases are part of the paste or the aggregates.

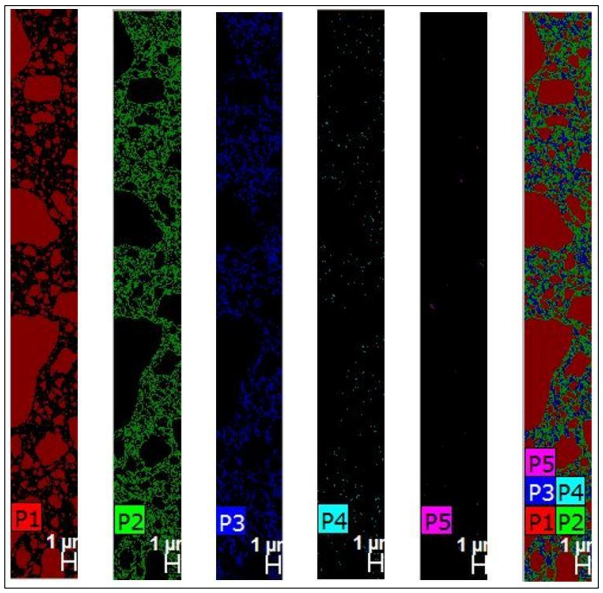

Figure 5-23: Auto-phasing resulting in five different phases.

These smaller dots must be merged with either the cement paste phase or the aggregate phase since a separation into these two phases are what we want to accomplish. It is difficult to know whether these phases are a part of the paste or smaller grained aggregates. The choice we made was only made based on what visually looked correct. We used a medium sensitivity for our scans, meaning we did not have to make these choices very often. This, however, indicates that the phase separation tool has trouble identifying some parts of the section.

To investigate this further, we extracted the weight percent of all the elements within the cement paste of all thin sections of A.1.O, obtained the average values of them within the core, and normalised them based on the chemical composition of the cement (As shown in Appendix A.8). The result, illustrated in Table 5-3, shows that the paste phase, in general, included more silicone and less calcium than expected based on the chemical composition of the cement used in Structure A, obtained from Norcem.

Table 5-3: Mass percent of elements obtained from the cement paste phase of A.1.O from µ-XRF vs Norcem cement composition.

Raw data			**Normalised data**	
Element	**µ-XRF**	**Oxide**	**µ-XRF**	**Norcem Chemical Composition**
Ca	29.92	CaO	59.76	64.2
Si	12.15	SiO2	24.27	20.4

This led us to believe that parts of the aggregates often are included in the cement paste phase when auto-phasing, bumping up the area percentage of the paste phase. This is believed to be the reason for the general error that the µ-XRF is giving a higher $\frac{m_{paste}}{m_{concrete}}$ than the ICP-MS. According to the mix proportions of the concrete used, an average of 26% of $\frac{m_{paste}}{m_{concrete}}$ is to be expected. This is closer to the values obtained from ICP-MS than those from the µ-XRF, indicating that the µ-XRF is overestimating the paste fraction value, rather than the ICP-MS underestimating it. In the outermost parts of the concrete core, however, the situation is the opposite for most of the cores. The µ-XRF was generally underestimating the paste fraction of these parts. The ICP-MS, however, gave a higher paste percentage in the outer part than in the rest of the core, as expected due to the wall effect. This is illustrated in Figure 5-24.

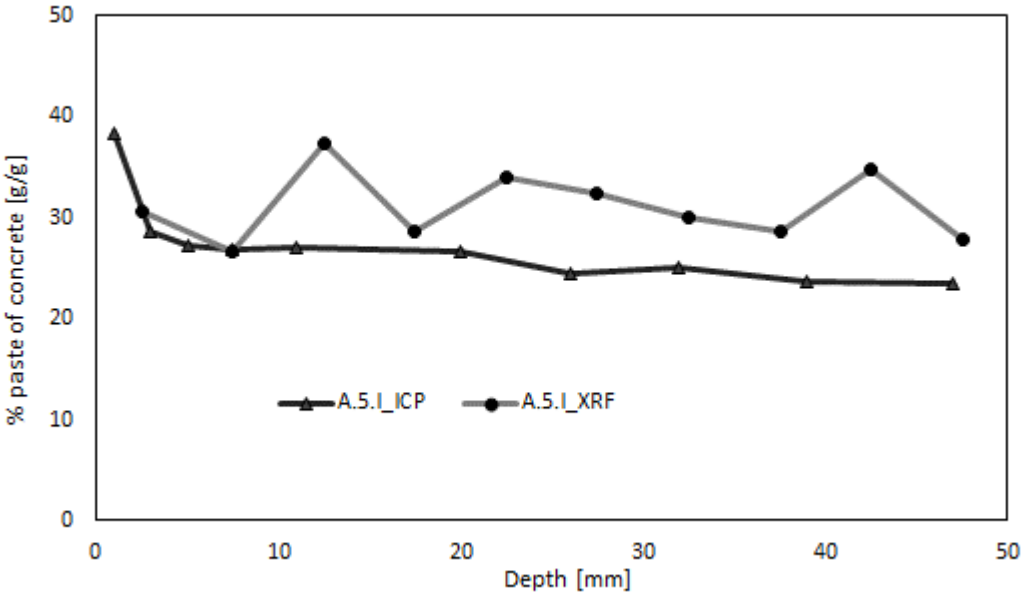

Figure 5-24: Variation of paste fraction with depth for ICP-MS and µ-XRF.

When we perform scans of a concrete core with the µ-XRF, we are scripting the coordinates of the area we want to analyse. This script is based on coordinates with mm as the unit and can only create completely squared areas. Decimals within the coordinates were not used during the analysis, hence our sections have a 1 mm accuracy in all directions. As we cannot adapt the scan area to fit the rough edges of the concrete core completely, we must choose between leaving out some of the concrete on the edges or include some areas in the scan where there is no concrete at all. As the outer parts of the concrete are where most of the chlorides are, we prioritized to include these in the scan. In the auto-phasing tool, these non-concrete parts of the sections were always included automatically as part of the aggregate phase, as illustrated in Figure 5-25.

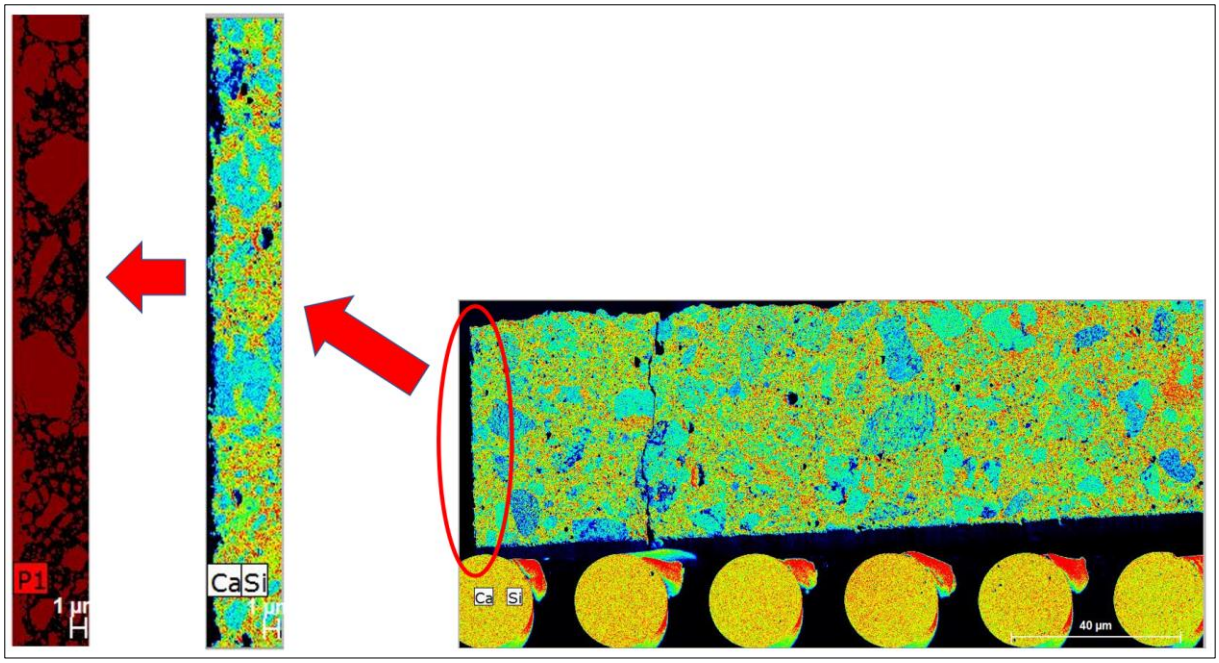

Figure 5-25: An auto-phasing of the outermost thin section of the concrete core.

P1 is the aggregate phase, and it is clear from the image that the non-concrete part of the section gets auto-phased into this phase. This led to an overestimation of the aggregate fraction, which means an underestimation of the paste fractions in these sections. This could be an explanation to why the $\frac{m_{paste}}{m_{concrete}}$-graph from the µ-XRF are showing generally lower paste amount in the first 5 mm.

The biggest deviation of $\frac{m_{paste}}{m_{concrete}}$ between ICP-MS and µ-XRF is a difference of as much as 30%, as illustrated in Figure 5-26.

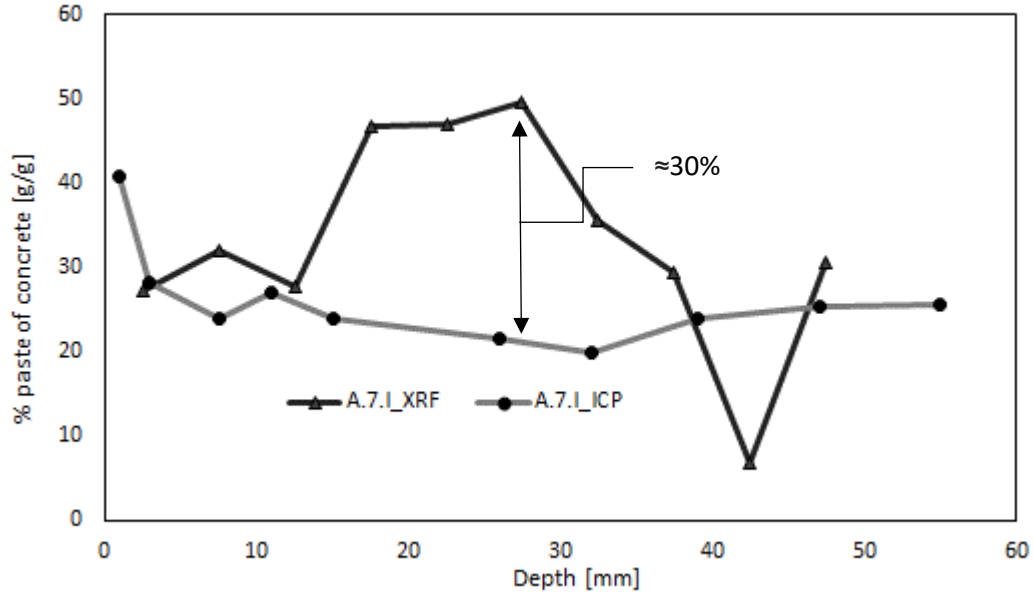

Figure 5-26: Biggest deviation in paste variation between µ-XRF and ICP-MS.

A 30% deviation is the maximum deviation, but the average deviation of the other cores seems to be around 10 %, as seen from Figure 5-8. As core A.7.I is the only core where we observe such a deviation, choosing 0.3 as the standard deviation for the paste and aggregate fraction seem overly conservative.

The variation of the graph from μ-XRF is due to the varying volume percentage of paste from the different thin sections. We see that the graph is not varying correspondingly with the one from ICP-MS. We see a much bigger variation from the μ-XRF than from the ICP-MS, which is expected, as the μ-XRF analyses a much smaller part of the core compared to ICP-MS. The μ-XRF is scanning the surface area of the concrete cores, rather than an entire volume of each section, as seen from Figure 5-27.

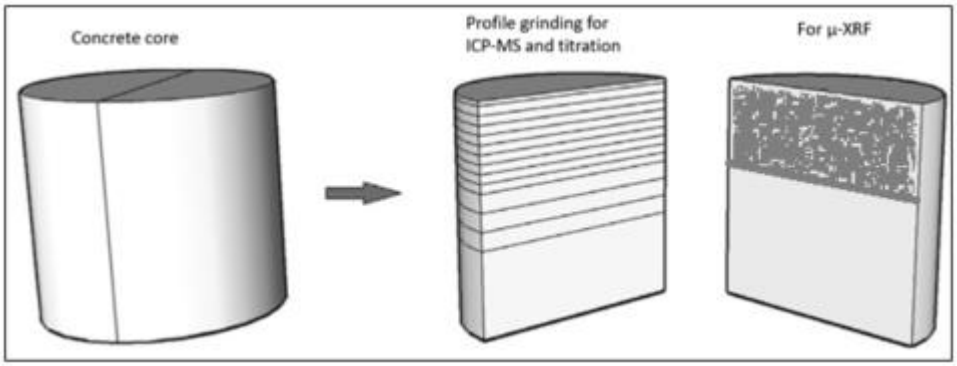

Figure 5-27: Illustration of which part of the core is used for which analysis.

The ICP-MS data are obtained from the other half of the same concrete core the μ-XRF data are from. However, since the blade used to saw the core in half is only 3 mm thick, one would think that the area of the surface of both cores should be quite similar regarding paste and aggregate distribution. This indicates that the assumption that the area percentages from the top surface of the core, obtained from the μ-XRF can represent the entire volume of the thin slice, is rather inaccurate. The $\frac{m_{paste}}{m_{concrete}}$-value is obtained using uncertain assumptions for densities of both aggregates and paste, but only the volume percentages obtained from the μ-XRF are variable. Even though the worst case gave a deviation of 30%, a 10% deviation seem to be the average value. A standard deviation of 0.1 will therefore be assumed for the volume fraction of paste ($\boldsymbol{\sigma_{V.paste}}$) and aggregates ($\boldsymbol{\sigma_{V.agg}}$) in the propagation of uncertainty calculations for the calibration method.

$\boldsymbol{\sigma_{\rho.paste}}$ is calculated based on the uncertainties of the densities of water and the cement used. The calculation does not include the assumption of no autogenous shrinkage. See Appendix A.13 for more details regarding the uncertainty propagation calculations.

A list of the uncertainties for the μ-XRF CM is presented in Table 5-4.

Table 5-4: List of the uncertainties in μ-XRF CM.

$\boldsymbol{\sigma_{x.cali}}$	$\boldsymbol{\sigma_{V.agg}}$	$\boldsymbol{\sigma_{V.paste}}$	$\boldsymbol{\sigma_{\rho.agg}}$	$\boldsymbol{\sigma_{\rho.binder}}$	$\boldsymbol{\sigma_{\rho.paste}}$
0.04 [g/g]	0.1 [-]	0.1 [-]	10 $[kg/m^3]$	10 $[kg/m^3]$	34 $[kg/m^3]$

The uncertainties have been propagated into a single uncertainty per data point. See Figure 5-28 for an illustration of the uncertainty.

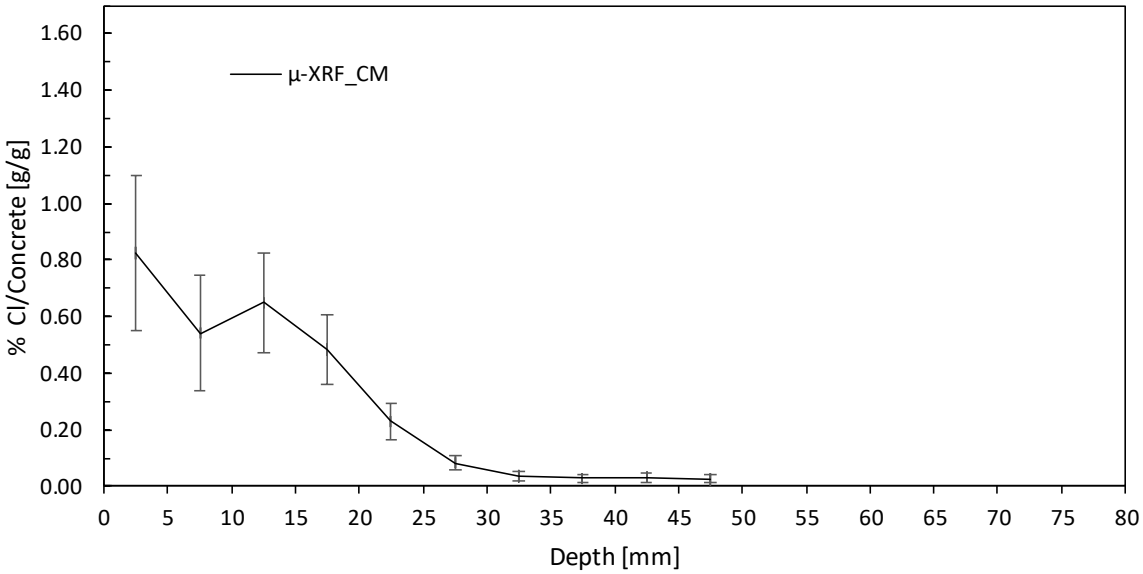

Figure 5-28: Chloride concentration in A.1.O determined by CM including uncertainties from Table 5-4.

The total uncertainty is, based on the assumed uncertainties in Table 5-4, ranging from 55-25% relative deviation. These numbers indicate that results obtained by CM with the assumed uncertainties used are unfit for quantifying chloride concentration. At least for the outer 20-30 mm of the core. In order to investigate which uncertainty parameter influenced the total uncertainty the most, a sensitivity analysis is performed. The effect of a 50% reduction in uncertainty of the different factors influencing the total uncertainty had on the total uncertainty, is shown in Figure 5-29.

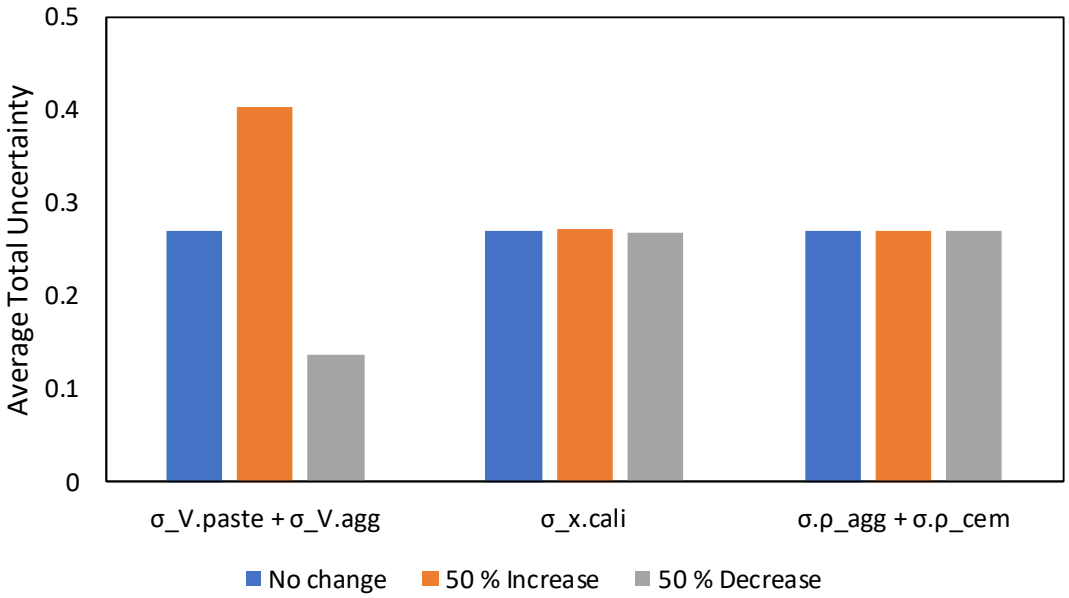

Figure 5-29: Average total uncertainty in chloride content for A.1.O when uncertainties for volume percentages, calibration curve, and densities are increased and decreased 50%, compared to the original value.

This analysis indicates that a variation of the assumed uncertainty of the volume distribution of aggregates and paste is the most influential factor for the final uncertainty. This was also found to be the most influential factor in a different kind of sensitivity analysis done by R. Kaasa in 2018 [43]. The uncertainties for each core are calculated assuming a 10% uncertainty for the volume share of paste and aggregates. If this uncertainty is increased to 20% or 30%, an increase in the total uncertainties of A.1.O would be as shown in Figure 5-30, on the next page.

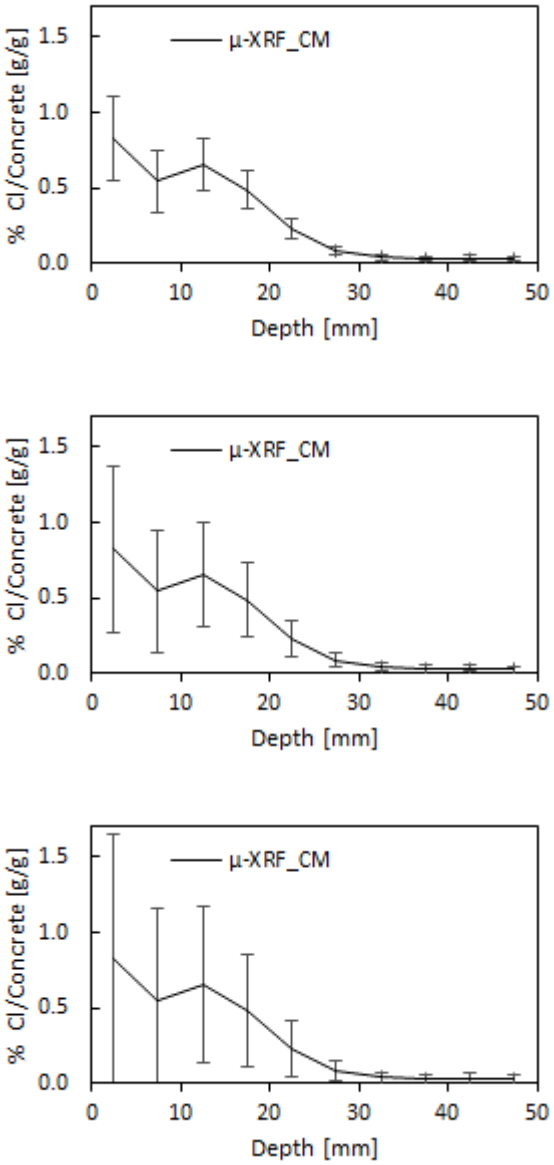

Figure 5-30: Chloride concentration in A.1.O determined by CM, with assumed uncertainties for the paste share at 0.1, 0.2 and 0.3, respectively.

All propagated uncertainties for µ-XRF are listed in Appendix A.4 and A.6.

5.5.3 Uncertainties Potentiometric Titration

Potentiometric titration does not have as many sources of error as CM. An illustration of the factors contributing to the total uncertainty is shown in Figure 5-31.

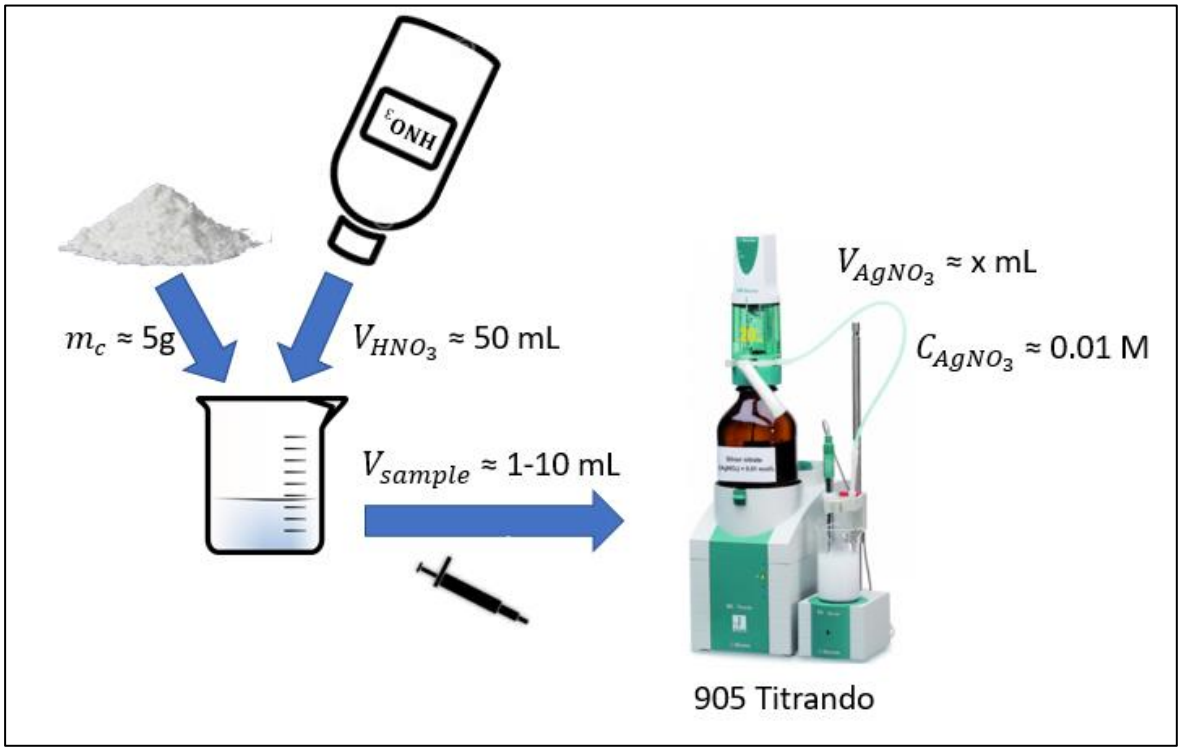

Figure 5-31: Illustration showing factors contributing to the total uncertainty for potentiometric titration.

The first sources of errors occur when the concrete powder is weighed and mixed with 50 mL 1:10 0.65% HNO_3. Followed by an error when 1, 5 or 10 mL is measured out to be put in the 905 Titrando. The 905 Titrando uses 5 mL $AgNO_3$ as the titrant, which can be added in 10 000 steps, giving the low uncertainty in this step.

Table 5-5: An overview of the uncertainties for potentiometric titration.

σ_{m_c}	$\sigma_{V_{HNO_3}}$	$\sigma_{V_{sample}}$	$\sigma_{V_{AgNO_3}}$	$\sigma_{C_{AgNO_3}}$
0.001	0.1	0.005/0.05	0.0005	0.00001

The uncertainties have been propagated into a single uncertainty per data point, see Appendix A.13.1 for details regarding the calculation. See Figure 5-32 for the illustration of the uncertainty.

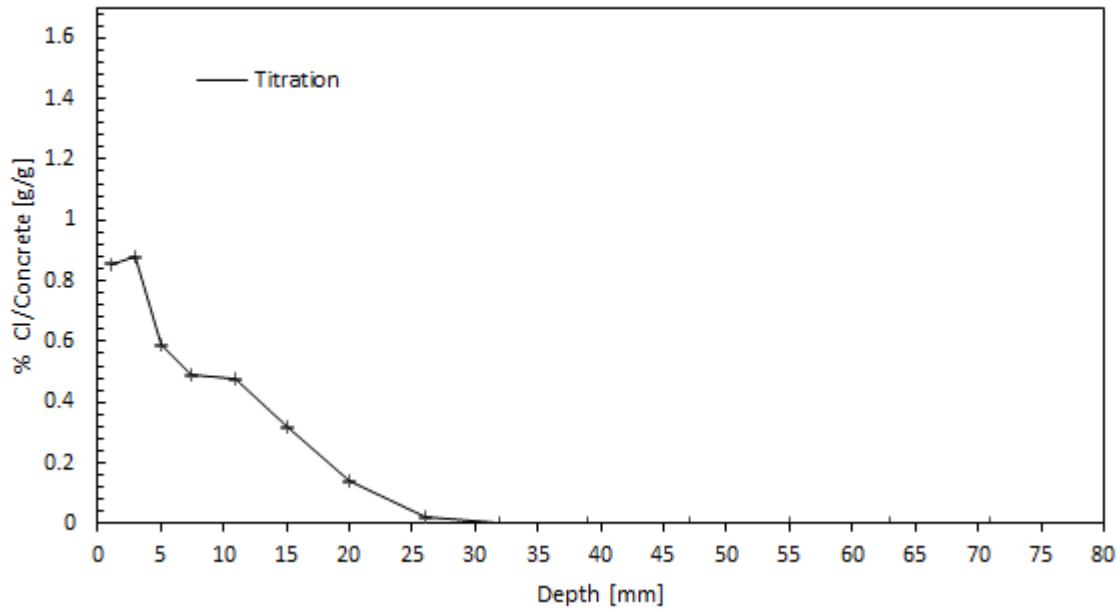

Figure 5-32: Chloride content in A.1.O using potentiometric titration, including uncertainty bars.

The total uncertainty for the method is so low that it can barely be seen in the example above. This indicating that potentiometric titration is a method of very high accuracy. As only 5g of concrete for each thin section is analysed, whether the measurements are representative or not is uncertain.

5.5.4 Uncertainties ICP-MS

ICP-MS is performed on the same sample volume as the potentiometric titration: the ground powder from the different thin sections. ICP-MS, however, demands an extremely low concentration of each element. Because of this, a dilution process must be executed prior to the analysis. An illustration of this is shown in Figure 5-33.

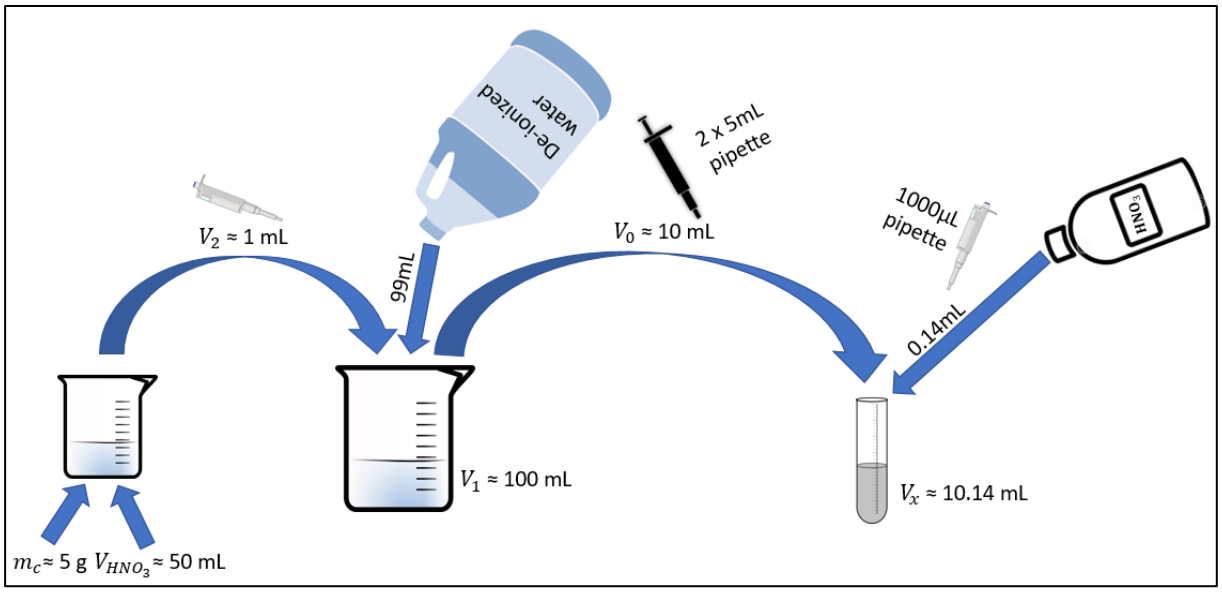

Figure 5-33: An illustration of the sample preparation for ICP-MS.

In general, this is a process with only minor uncertainties coming from the pipettes and the volume in the beakers. The uncertainties from the original sample volume, 5 grams of concrete in 50 mL 1:10 0.65% HNO_3, is the same as for titration.

The final step in this method is the analysis itself. Elements are found and listed as µg/L in our raw data from ICP-MS, and the relative standard deviation of these numbers are ranging between 0.4-11.4 %.

Table 5-6: An overview of the uncertainties in the sample preparation for ICP-MS.

σ_{V_x}	σ_{V_0}	σ_{V_1}	σ_{V_2}	σ_{m_c}	$\sigma_{V_{HNO_3}}$
0.07	0.07	0.5	10	0.001	0.1

The uncertainties have been propagated into a single uncertainty per data point, see Appendix A.13.2 for details regarding the calculation. See Figure 5-34 for the illustration of the uncertainty for ICP-MS.

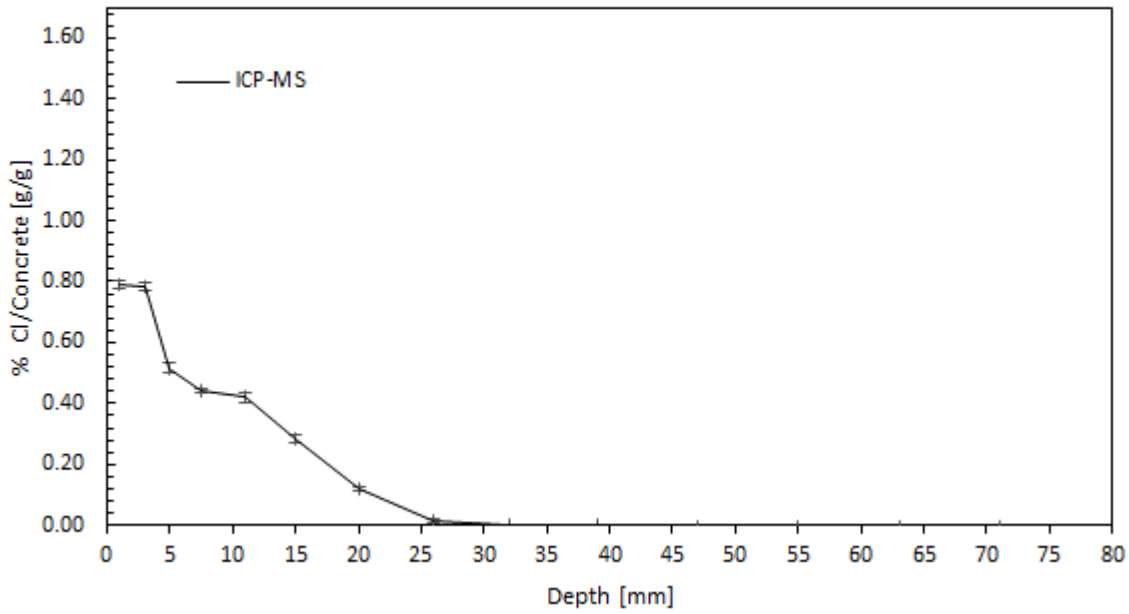

Figure 5-34: Chloride concentration in A.1.O including uncertainty bars.

As can be seen from the figure, the uncertainty is low. This indicates that this method of analysis is very accurate, i.e. we can be sure of that the elements detected in the sample, is correct. If the sample is representative, however, is uncertain as only a small fraction of the concrete is included in the analysis.

5.5.5 Accuracy

Analyses done by potentiometric titration and ICP-MS are based on the same volume fraction of concrete, the only difference is the dilution process. Because of this, we expected them to give equal results. To investigate this, we made correlation graphs between these two methods. The graphs are presented in Figure 5-35 and Figure 5-36. Cores taken from the outside and inside of Structure A is separated into two different curves due to the big difference in chloride concentration between these two areas.

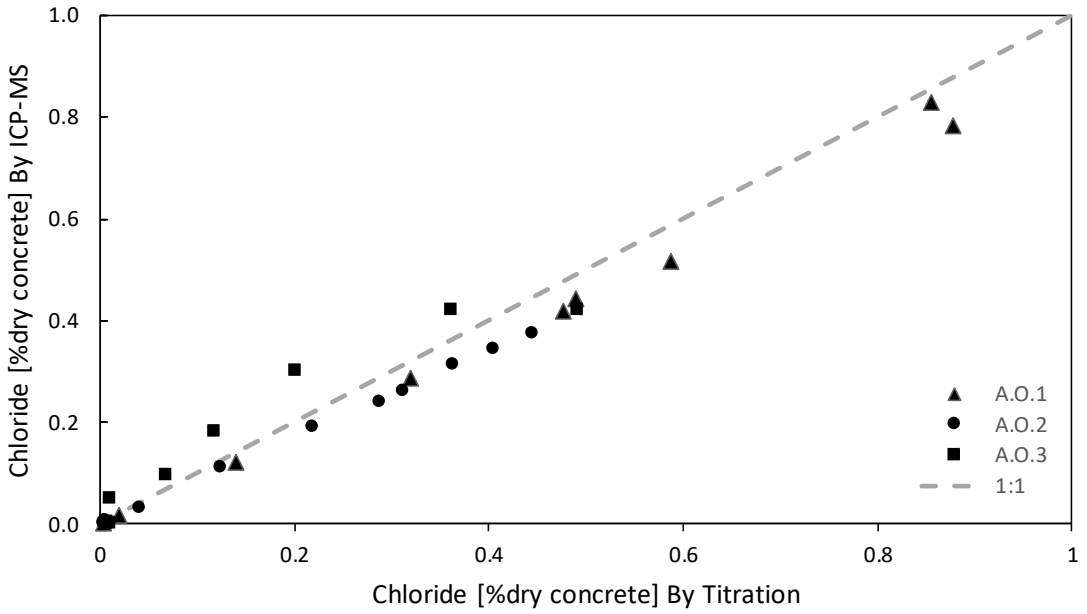

Figure 5-35: Correlation of ICP-MS and titration, cores from outside of Structure A.

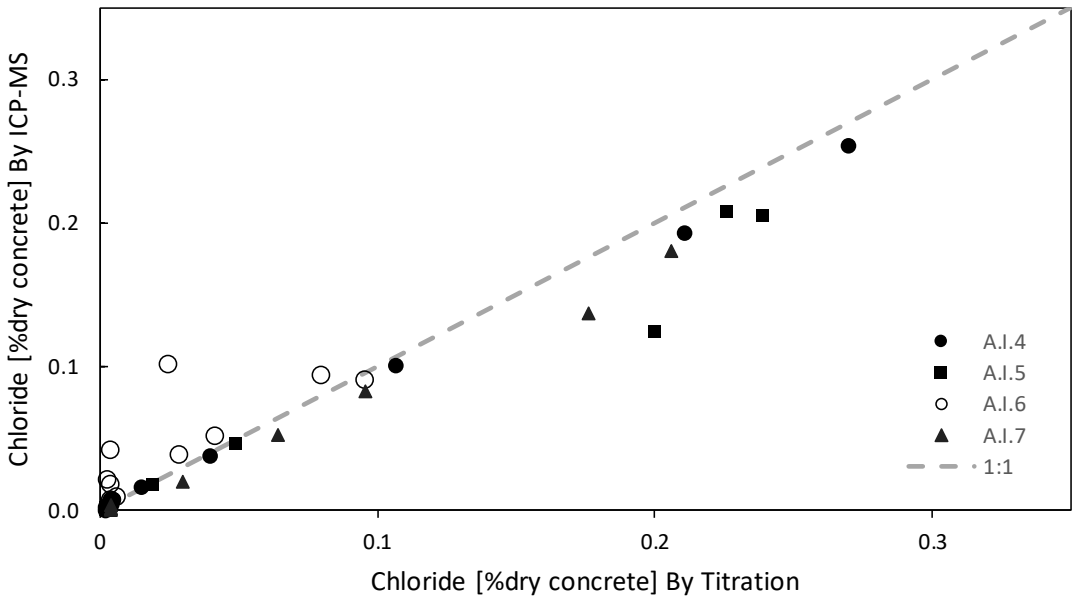

Figure 5-36: Correlation of ICP-MS and titration, cores from inside of Structure A.

Both graphs indicate that the two methods visually correlate very well. This was confirmed by the correlation coefficients obtained by Excel, which is presented in Table 5-7.

Table 5-7: Correlation coefficient for ICP-MS and Titration for all cores in structure A.

A.1.O	A.2.O	A.3.O	A.4.I	A.5.I	A.6.I	A.7.I
1.00	1.00	1.00	1.00	0.98	0.80	1.00

A high correlation between these methods was, as previously mentioned, expected because the exact same concrete containing solution was the basis for both analyses. The ICP-MS solution had, however, been put through a dilution process. This, both reduced the sample volume and increased the uncertainty of the results. The uncertainty this caused was, however, very small and as shown previously in this chapter, the uncertainty was still minimal for both methods.

As illustrated in Table 4-6 and Table 4-7, the partitioning of the thin sections used for the µ-XRF analysis was not the same as those used in ICP-MS and titration, making a direct comparison of correlation difficult. They all have, however, a common point in the chloride profiles at a depth of 7.5mm. This point, for µ-XRF, represents a different sample selection of concrete than the two other methods. For the µ-XRF, these numbers represent the chloride concentration in a 5 mm thin section of an area, while it for titration and ICP-MS represent a 3 mm deep ground volume of the concrete. The difference in value at this point for all cores from all three methods of analysis are shown in Figure 5-37.

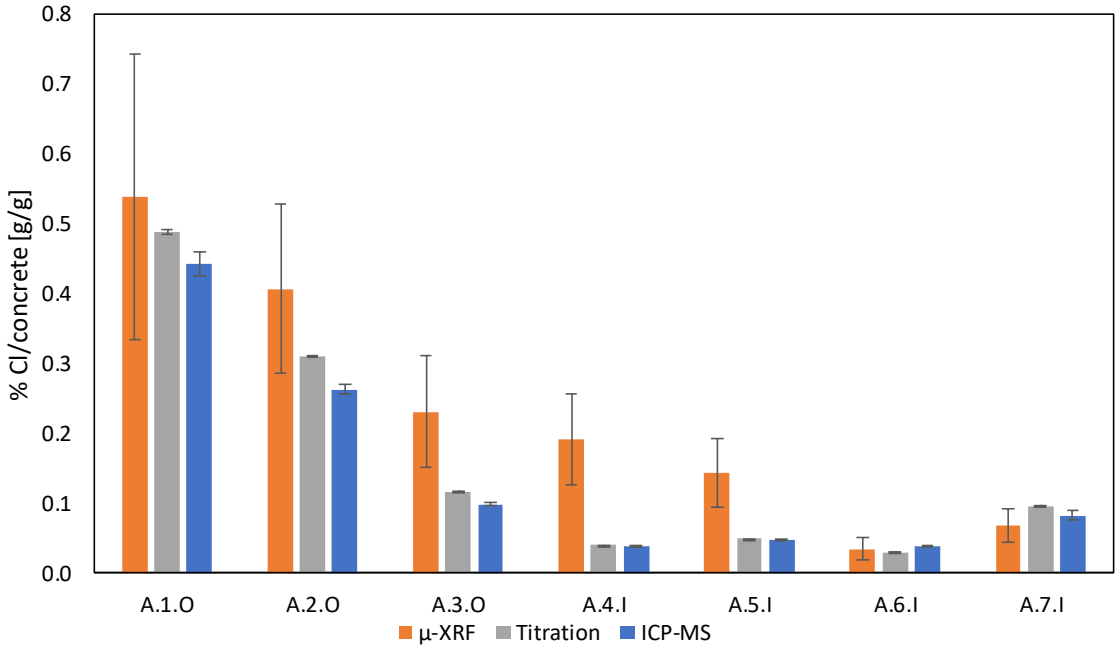

Figure 5-37: Chloride concentration at 7.5 mm depth, for all cores from Structure A.

The uncertainties of the µ-XRF results presented here are still based on the same uncertainty assumptions as given in Table 5-4.

As seen from both Figure 5-37 and the results presented in section 5.1, the µ-XRF seem to generally overestimate the chloride content compared to ICP-MS and titration. There are a few plausible reasons to why we see this pattern. Analysis run by µ-XRF is based solely on the conditions on the surface of the sawn concrete cores, which may or may not be representative for the rest of the volume. The surface may have been exposed to uncertain amounts of human contact during the procedure of analysis. This effect has been mitigated by using plastic gloves. This has, however, at times been forgot during re-levelling of the core inside the µ-XRF. Contaminations on the surface of the concrete core will make a bigger impact on an analysis solely performed on the surface area of the core, than analysis where the entire volume of the sample is included. This makes the µ-XRF analysis a lot more sensitive to contamination of the sample than ICP-MS and titration. On the other hand, the sawing of the cores demanded water as cooling fluid, which in worst case could have washed away some chlorides, resulting in fewer chlorides on the surface of the cores, again making a bigger impact on the µ-XRF results, than the other two methods.

Further, the results are based on a calibration curve which is made with the use of 1-year-old reference samples. The concentration of chlorides on the surface of these samples is assumed to be the same as at the time they were made. As shown in section 5.3 a polish of the reference samples made a significant change in the calibration graph, which indicates that the calibration is vulnerable to deterioration of the reference samples. They have spent a lot of time in a vacuum inside the µ-XRF, which may have contributed to the deterioration. In addition, our polishing procedure could have caused contamination of the samples. If we assume the concentration of chlorides in the samples to be the same amount as at the time they were made, while the real concentration is lower due to deterioration, each result obtained by using this curve is showing a higher Cl/paste value than it should.

In addition, the µ-XRF does, in general, overestimates the paste share in the concrete, as can be seen in section 5.2. As discussed in section 5.5.2, the µ-XRF tend to include parts of the aggregates in the cement paste phase during auto-phasing. In other words, the µ-XRF underestimates the volume share of aggregates. The lower volume of aggregates gives a lower concrete mass, as aggregates have a higher density than cement paste. Since the results are presented in a mass of chloride per mass of concrete, a lower mass of concrete will result in an overestimation of this ratio.

To be able to determine the state of chloride ingress in a structure, it is important to know how deep the chlorides have penetrated. Or, in other words, determine the depth where the chloride concentration has reached the critical value. As stated in section 3.2.2, the critical chloride concentration, Cl_{crit} = 0.07% Cl/concrete [g/g] is used.

As can be seen in Figure 5-28, the concentration and the uncertainty are proportional, leading to very low uncertainties around the critical chloride limit, Cl_{crit}. Hence, the estimation of the depth where the critical chloride content is reached could be of higher accuracy than the chloride concentrations in each section. This has been investigated further, by looking at the estimated depth of chloride ingress based on results and uncertainties from µ-XRF, titration and ICP-MS.

Table 5-8 and Figure 5-38 shows the depths of where the chloride concentration has reached Cl_{crit}, as determined by ICP-MS, titration, and µ-XRF. This procedure is presented in section 4.7.3.

Table 5-8: Depths where Cl_{crit} is reached in [mm].

	µ-XRF	Titration	ICP-MS
A.1.O	29±2	23.50±0.04	22.9±0.2
A.2.O	29±2	23.79±0.05	23.3±0.3
A.3.O	14±2	10.79±0.05	9.7±0.2
A.4.I	12±1	6.38±0.03	6.2±0.1
A.5.I	11±1	7.15±0.01	6.7±0.1
A.6.I	3±2	3.53±0.04	4.1±0.1
A.7.I	7±2	10.34±0.08	9.0±0.6

These results are graphically illustrated in Figure 5-38, below.

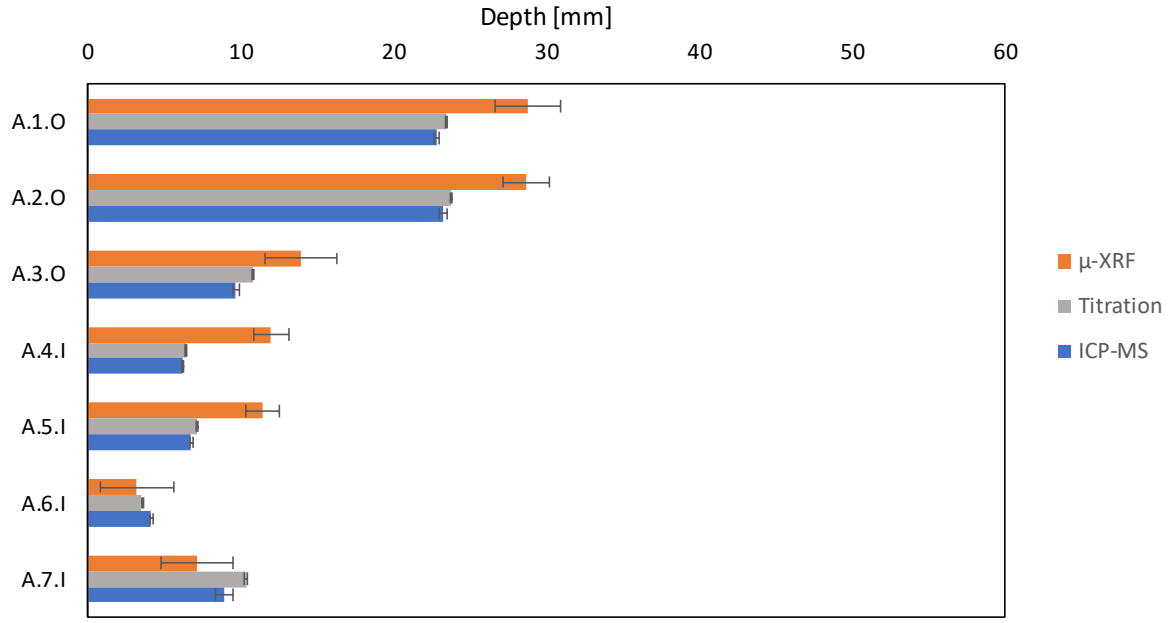

Figure 5-38: Depths where Cl_{crit} is reached, as determined by ICP-MS, titration and µ-XRF

Based on these results, µ-XRF seem to be able to determine the depth of chloride ingress within a 4mm margin, while ICP-MS and titration show an accuracy well within 1 mm for all cores. As the consecutive thin sections analysed by µ-XRF are all 5 mm thick, an uncertainty below 4mm must be considered adequate. The thin sections analysed by ICP-MS and titration are, in the outermost parts, as thin as 2 mm, making a better accuracy more important for these methods. With the uncertainty of paste and aggregate share in the concrete increased to respectively 0.2 and 0.3, we would get a considerable decrease in accuracy on ingress depth. This is illustrated in Table 5-9.

Table 5-9: Uncertainty regarding chloride ingress depth [mm] measurements using µ-XRF with different paste and aggregates fraction uncertainties. 0.3, 0.2 and 0.1, respectively.

	0.3	0.2	0.1
A.1.O	4	3	2
A.2.O	2	2	2
A.3.O	4	3	2
A.4.I	3	2	1
A.5.I	3	2	1
A.6.I	4	3	2
A.7.I	4	3	2

5.5.6 Complexity

The only method of analysis performed by us in this thesis is the µ-XRF, hence we are not able to make a full comparison of the complexity of the methods. However, both ICP-MS and titration require chemistry lab experience. A µ-XRF analysis, on the other hand, is done without any kind of potentially harmful chemicals involved. And with the X-ray tube being safely inside a chamber, µ-XRF is a very safe method to try and learn with little experience.

The µ-XRF is also, contrary to ICP-MS and titration, a non-destructive method. Meaning it is possible to perform an analysis on the same concrete core multiple times. This makes a trial and error process when learning this method, a lot easier. This also means few hours of guidance and supervision is necessary before one is ready to perform analyses alone. There are as mentioned in section 4.6 a lot of things to think about when performing this analysis, and a lot of factors are influencing the results. This, together with an extremely buggy software, increases the difficulty level of the µ-XRF analyses.

5.5.7 Efficiency

If one is to consider training in the use of the different analysis techniques as part of the cost and time measurements, that would favour the µ-XRF. As mentioned in the last section, the µ-XRF requires few training and supervision hours, compared to both titration and ICP-MS. This means both reduced time and cost. Also, a few hours of paid work are required when using a µ-XRF. The preparation of each scan is not time-consuming. A scan could be ready to run with less than one hour of preparation time. The µ-XRF machine, however, can use up to 24 hours to complete a full scan, with an overview, ten thin section scans, and reference sample scans. We had only one functioning detector for our scans, but if both were in use, the time consumption could be halved. As the software at this point, is still not very user-friendly, the post-processing of the raw data would still take some time.

An illustration of the time consumption for the three different methods is presented in Figure 5-39. The time presented is the time necessary from seven concrete cores are

received and to their chloride profiles are presentable. The time needed for potentiometric titration and ICP-MS is obtained from e-mail correspondence with Siri Trapnes (SINTEF) and Syverin Lierhagen (NTNU) respectively, while the time needed for µ-XRF is an estimate from the authors.

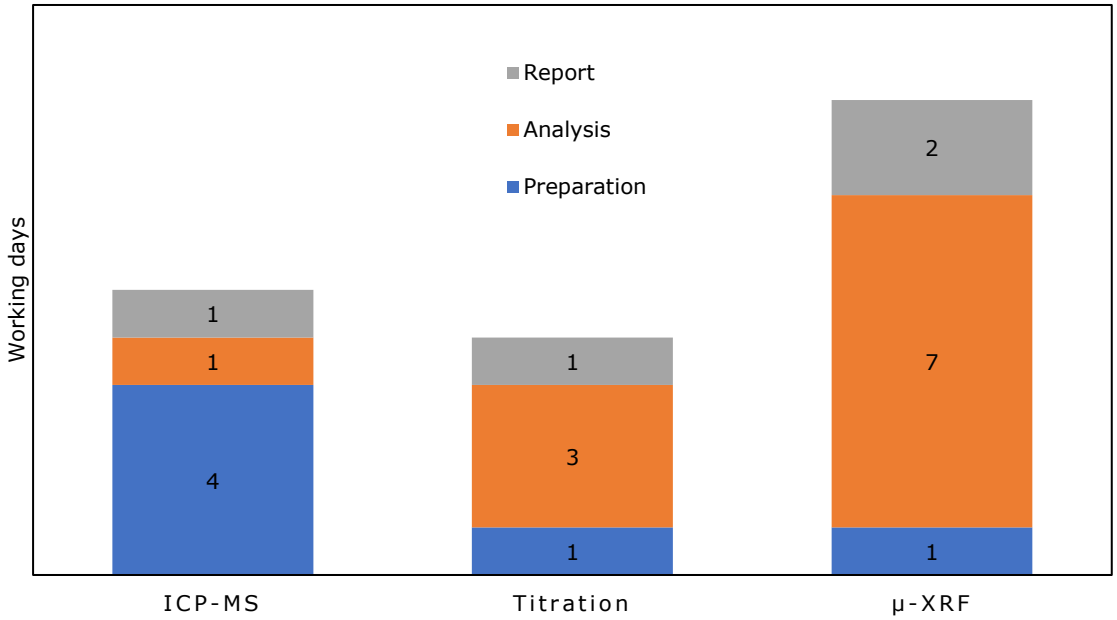

Figure 5-39: Illustration of the number of working days necessary to present chloride profiles from 7 concrete cores.

The working days are partitioned into three phases; preparation, analysis and report. It is important to mention that this is time consumption with ideal conditions. Due to logistics and other factors the delivery time of results may deviate from the estimate given in Figure 5-39.

5.5.8 Versatility

Potentiometric titration comes with solely one output, the concentration of chloride in mass percentage of concrete. Which is, for the case of chloride ingress, exactly what is needed.

The ICP-MS, however, can provide the concentration of several elements during the same analysis. This could provide additional useful information the titration analysis is not able to provide. For instance, by obtaining the concentration of calcium, one is able to evaluate paste variation within the concrete. Ingress of other potentially harmful elements, such as sulphur and magnesium, could also be detected using ICP-MS.

The µ-XRF is, as shown, dependent on a calibration method in order to give quantitative information of an element. The limitations of the software prevent the use of the direct method at the present time. Hence, reference samples with known chemical composition are needed to quantify different elements in the concrete. The µ-XRF does, however, contrary to the two other methods, give visual information regarding the distribution of different elements in concrete cores. In our case, the transport of chlorides in the concrete cores is of interest. Elemental heat maps can be produced for all elements

detected by the µ-XRF. This is a way of illustrating the concentration of the element of interest based on the warmth of the colour. The warmer the colour, the larger the concentration is. This can be used to study the transport of matter in the concrete in a more detailed way. Especially useful when analysing a core with crack formations. In Figure 5-40, the elemental map for chloride in A.1.O is presented.

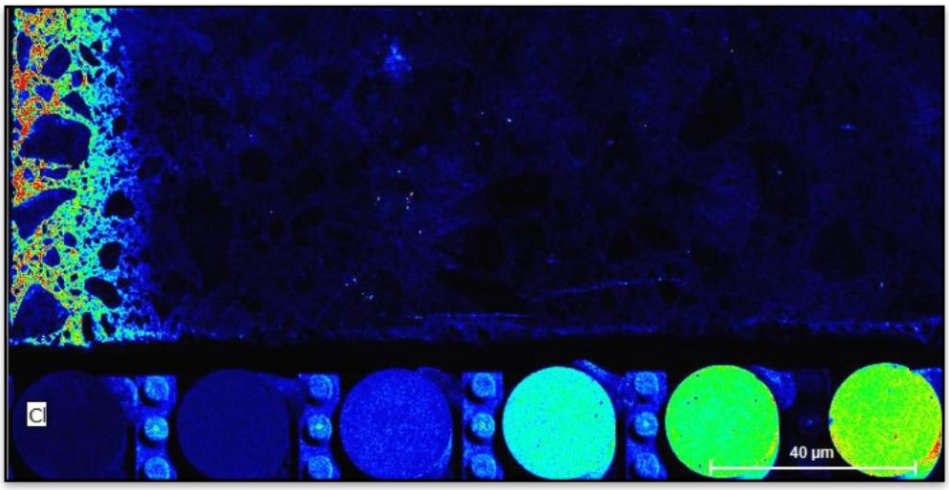

Figure 5-40: An elemental heat map for chloride created in the µ-XRF for A.1.O. The exposed surface is to the left in this image.

In this case, the elemental map shows a stable gradient of the chlorides, indicating a uniformly dense concrete in good condition. The same visual information is obtained from other elements as well. For a comparison of the elemental overviews obtained from µ-XRF to quantitative results from ICP-MS, see section 5.4

5.6 Conclusion

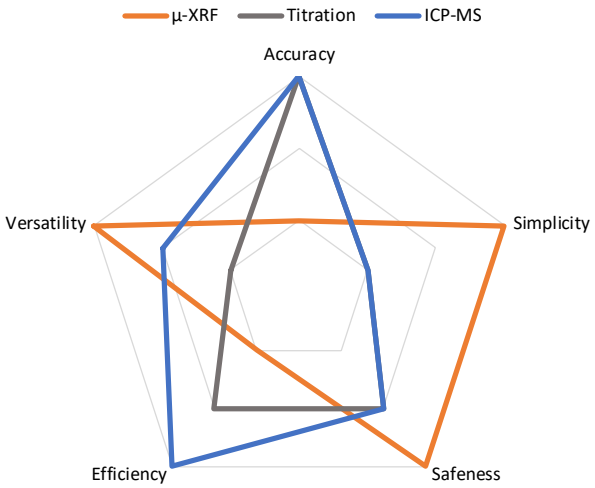

Figure 5-41: Illustration of the three methods of analysis' strengths and weaknesses

In Figure 5-41, a sum-up of all the previously discussed strengths and weaknesses of the different methods of analysis is presented as a radar chart. It is clear from the figure that the arguably most important factor, the accuracy, of both ICP-MS and titration is superior to the one we got from µ-XRF. However, the µ-XRF are well-off on almost all the other categories.

Compared to ICP-MS and titration, the µ-XRF seem to provide much lower accuracy regarding chloride concentration. The main contributor to the uncertainty of this method is the paste and aggregate fractions obtained from the auto-phasing tool in the µ-XRF software. In addition to a big uncertainty, the µ-XRF appears to consequently overestimate the chloride concentration in the cores. Since this very well could be due to deteriorated reference samples, one could not say that the µ-XRF always will give conservative results, thus we cannot say it is a conservative method of analysis. The results from the µ-XRF are not accurate enough to perform service life calculations, as these are dependent on both the chloride concentration on the surface (C_s) of the structure, in addition to a diffusion coefficient (D(x,t)) obtained from a curve fitting of the chloride profiles. See equation (2). However, the µ-XRF show sufficient accuracy for chloride ingress depth measurements. As each of the thin sections for the µ-XRF is 5mm thick, each of the data plots represents an area of 5 mm thickness. An ingress depth measurement with less than ±2 mm uncertainty, as we got from the µ-XRF will, therefore, have to be considered adequate. Of course, the assumed chloride concentration of the reference samples must be correct for this uncertainty to be representative.

Since our task is to evaluate the chloride ingress, and not to perform service life calculations for the structures, we can conclude that the results from µ-XRF are of sufficient accuracy to evaluate the chloride ingress in the two structures in question. The elemental heat maps obtained from the µ-XRF are also a very useful tool for a quick evaluation of the ingress of not only chlorides but also other aggressive ions, such as magnesium and sulphur. This is information that could be used to evaluate the transport within the concrete and could potentially be used to determine what transport mechanism is dominant in which area of the structures.

6 Chloride Ingress

In this chapter, the chloride ingress for two offshore concrete structures will be evaluated. The tool used for this analysis is μ-XRF with the calibration method. In section 6.1 the results and a discussion regarding chloride ingress in Structure A are presented. 6.2 presents the results and a discussion for Structure B. The chapter is finalised with a conclusion in section 6.3.

6.1 Structure A

6.1.1 Results

Results from Structure A obtained using CM in μ-XRF is here to be presented in two separate graphs. Chloride profiles from concrete cores collected from the outside of the seawater shaft and inside of the utility shaft are presented in Figure 6-1 and Figure 6-2 respectively. The exposed surface is to the left in all graphs.

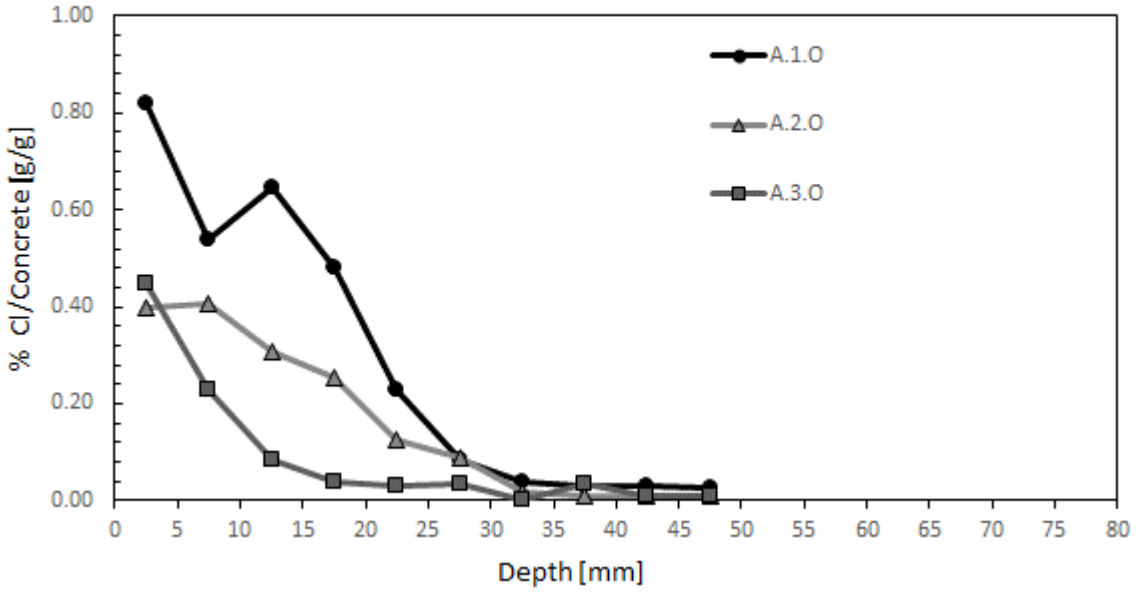

Figure 6-1: Mass concentration of chloride per dry concrete obtained by CM in A.1.O, A.2.O and A.3.O from the outside of Structure A. The exposed surface is to the left. Increasing numbers in core name indicate increasing height from sea level.

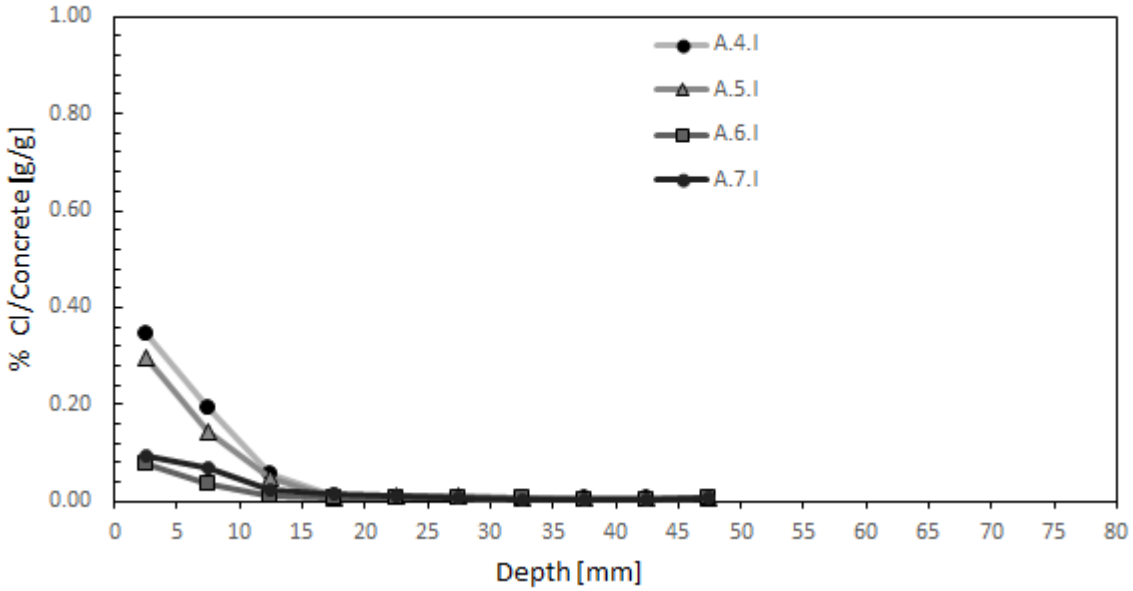

Figure 6-2: Mass concentration of chloride per dry concrete obtained by CM in A.4.I, A.5.I, A.6.I and A.7.I from the inside of Structure A. The core name numbers indicate increasing height from the seabed.

6.1.2 Discussion

Concrete cores collected from Structure A are obtained from both the inside and the outside. The inside samples are collected from the utility shaft, while the outside samples are collected from the seawater shaft. An overview of the locations is presented in Figure 6-3.

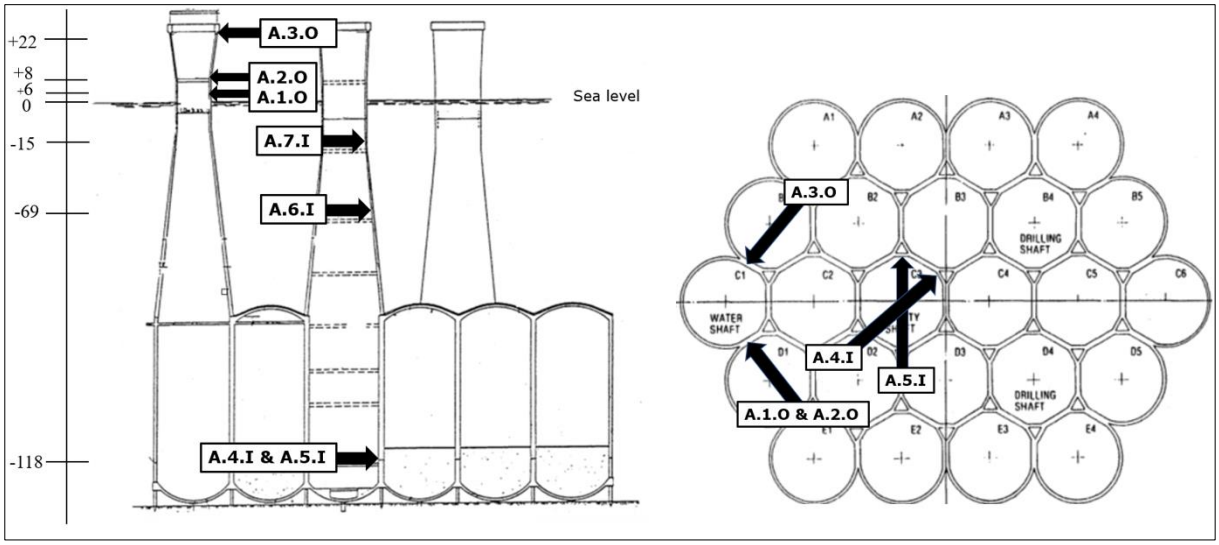

Figure 6-3: Overview of locations of concrete cores collected form structure A, 3 from the outside and 4 from the inside. The orientations of A.6.I and A.7.I are unknown. Picture reproduced from [7].

The three cores collected from the outside of the seawater shaft are taken from 6, 8 and 22 meters above sea level. As mentioned in 2.3, the structure can expect waves to reach heights of 20m annually. A wave height of up to 20 meters, combined with strong winds will generate a splash zone on the entire unsubmerged part of the shaft. Hence, all cores obtained from the outside, respectively A.1.O, A.2.O, and A.3.O, are obtained from an area classified as the splash zone, with corresponding exposure class XS3. As discussed in 3.1.4, the splash zone is known to be the area most vulnerable to chloride ingress.

The cores taken from the inside of the utility shaft are not experiencing regular, direct contact with seawater. One could, because of this, be tempted to classify the area these are obtained from as an atmospheric zone. There is, however, as mentioned in 2.3, installed a fire sprinkler system in the shaft, where seawater is used for extinguishing. This is run through a full-scale test every fourth year. Because of this, saying the exposure zone of the inside of the shafts is part of the atmospheric zone, would be an oversimplification. The reality is that these cores are subjected to an exposure equal to that of the atmospheric zone for the most part, in addition to becoming a splash zone once every fourth year. As seen in Figure 6-4, a sprinkler system is installed on the same floor as core A.4.I and A.5.I are obtained from. A sprinkler system is also installed a few floors up from where core A.6.I and A.7.I are collected from, which is assumed to make an impact on the chloride concentration in the floors below due to the drainage system in the shaft, described in 2.3. One would, because of this, expect some chloride ingress in core A.6.I and A.7.I, though not as deep as for A.4.1 and A.5.I.

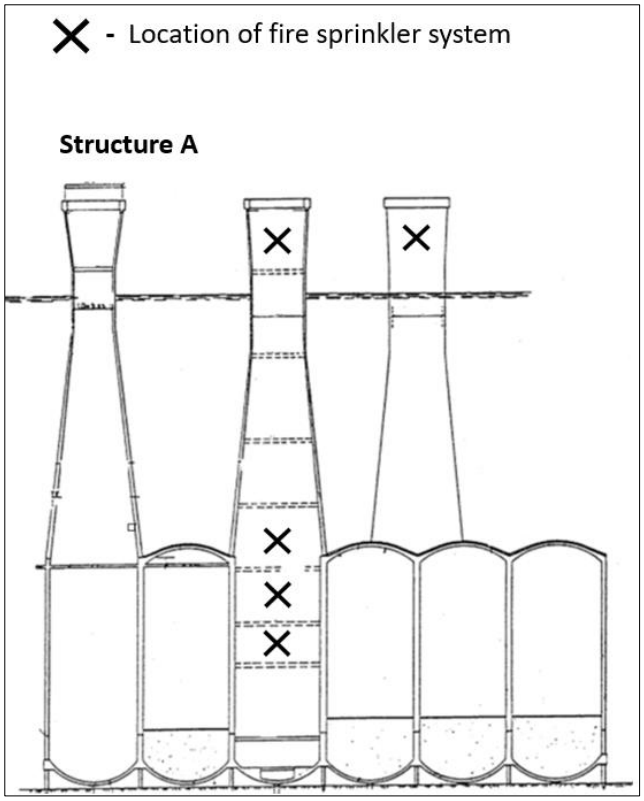

Figure 6-4: Location of all fire sprinkler systems in Structure A.

The chloride ingress depths of all cores from Structure A is presented in Figure 6-5.

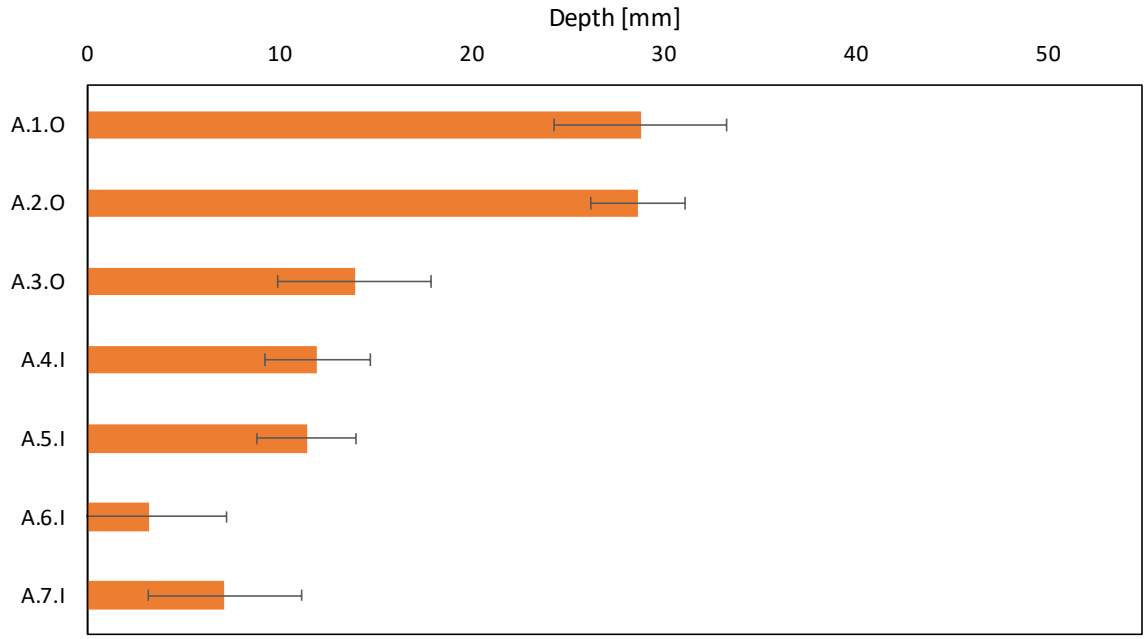

Figure 6-5: Depths where Cl_{crit} is reached for all cores in Structure A, from µ-XRF. These values and corresponding error bars are based on the calculations presented in section 4.7.3.

As seen from Figure 6-5 the cores with the deepest chloride ingress are A.1.O and A.2.O, followed by A.3.O. These are all obtained from the outside of the shaft, unlike the other four cores. It would therefore generally be expected a deeper ingress for these as they are exposed to a greater chloride load. The ingress depths are ranging from 14-29 mm dependent on the height above sea level. The deepest ingress is found in the cores obtained from 6 and 8 meters above sea level, A.1.O and A.2.O. Both have an ingress depth of 29 mm. This is almost twice as deep as the 14 mm ingress found in core A.3.O, collected from 22 m above sea level.

The cores obtained from the inside show an ingress depth ranging from 3-14 mm. Two of the inside cores are showing a noticeable degree of chloride ingress, A.3.O and A.4.O. These have a measured ingress depth of 14 and 12 mm, respectively. We have been assured that the inside of the utility shaft never was exposed to seawater during transport or construction [47]. And since the two cores collected from the level directly exposed to the deluge fire sprinkler system have a greater ingress depth than the two who are not, the system is believed to have a noticeable effect regarding chloride ingress. The small amounts of chlorides in the two remaining cores are believed to be due to a combination of airborne chlorides and extinguishing water from upper levels travelling downwards during drainage.

All of the ingress depths from the cores from Structure A are, however, still far from reaching the reinforcement. As stated in section 2.2, the cover depth for the structure is supposed to be 60 ± 10 mm. Thus, chloride-induced corrosion in these areas is not a concern at the present time.

6.2 Structure C

6.2.1 Results

Results from Structure C obtained using CM in μ-XRF is here to be presented in four separate graphs representing four different locations where the cores are collected from. All cores are obtained from the inside of the utility shaft. An increasing number in the core name indicate increasing height above the seabed. The exposed surface is to the left in all graphs.

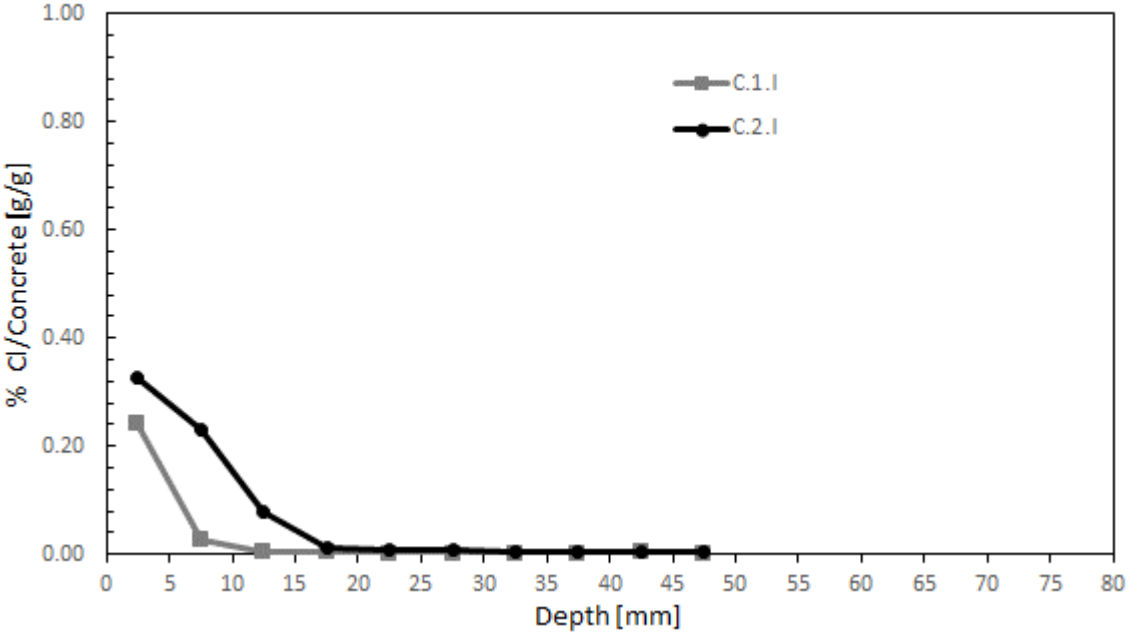

Figure 6-6: Mass concentration of chloride per dry concrete obtained by CM in C.1.I and C.2.I, from Structure C.

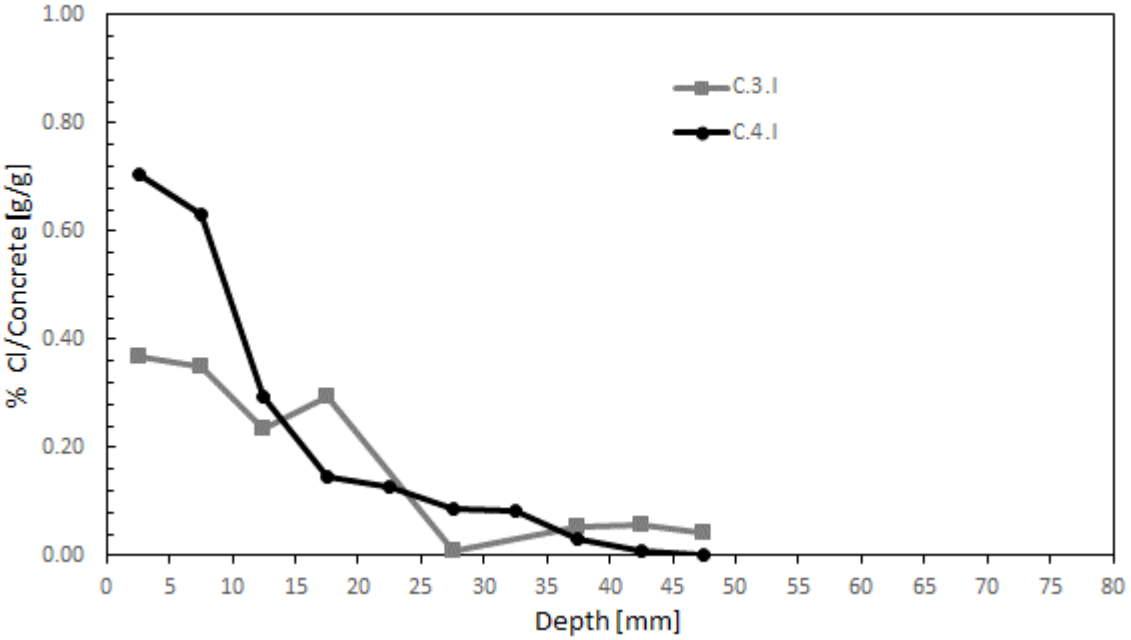

Figure 6-7: Mass concentration of chloride per dry concrete obtained by CM in C.3.I and C.4.I from Structure C.

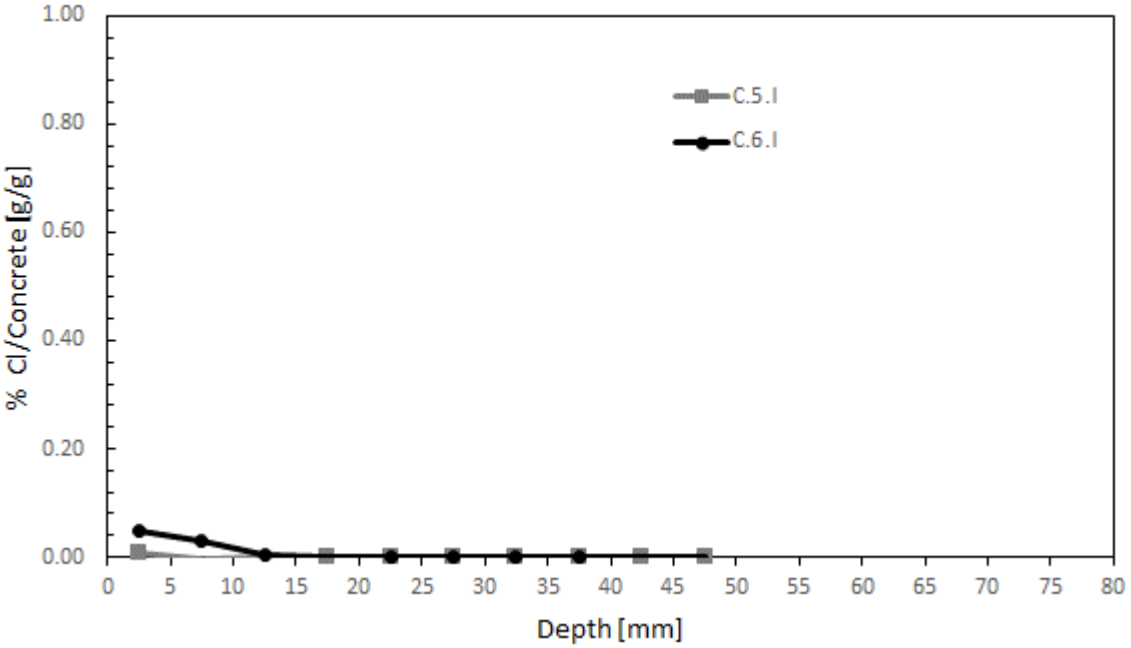

Figure 6-8: Mass concentration of chloride per dry concrete obtained by CM in C.5.I and C.6.I from Structure C.

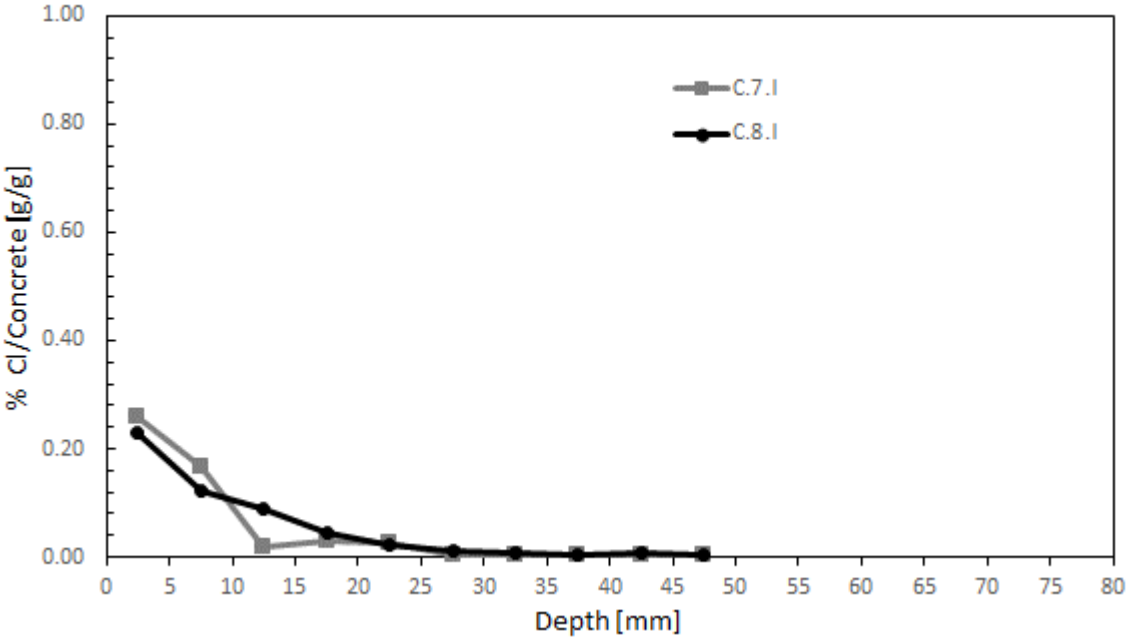

Figure 6-9: Mass concentration of chloride per dry concrete obtained by CM in C.7.I and C.8.I from Structure C.

6.2.2 Discussion

Concrete cores received from Structure C are solely collected from the inside of the utility shaft at different levels. See Figure 6-10 for a recap of the different locations.

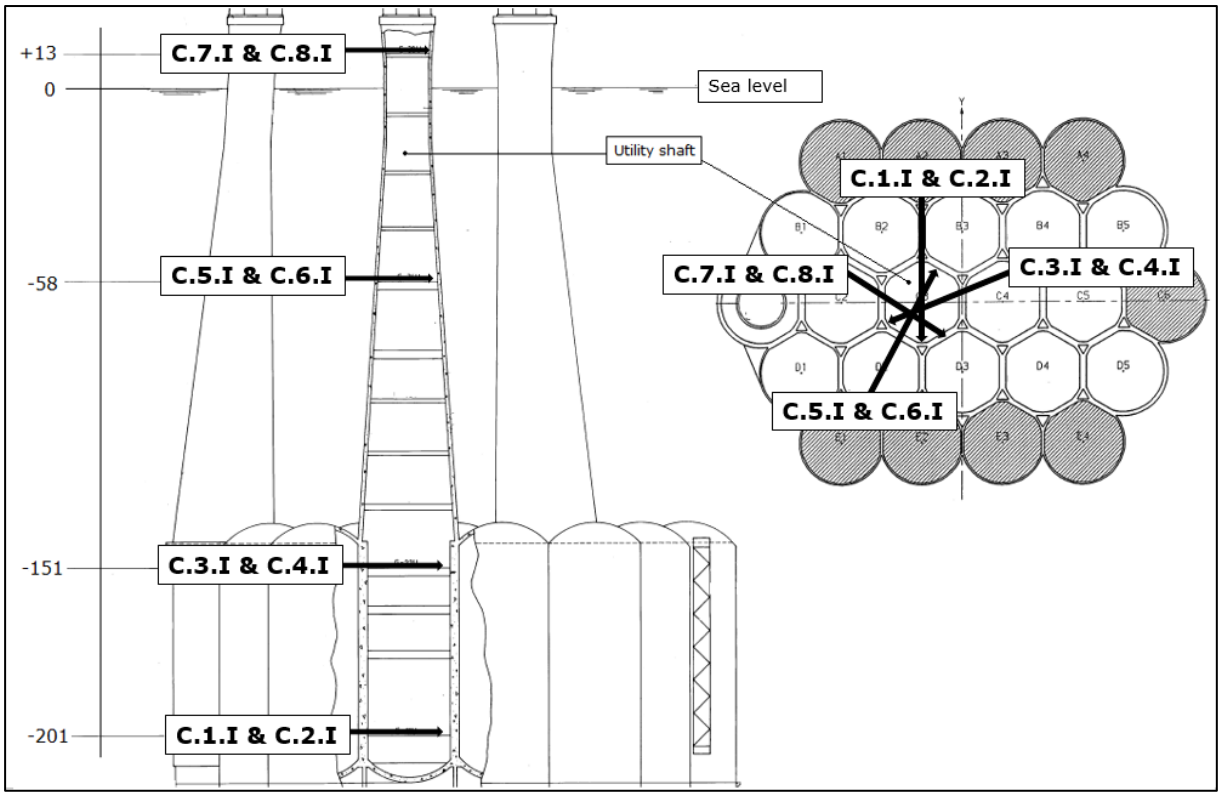

Figure 6-10: Overview of locations of concrete cores collected form structure C.

The inside of the utility shaft is not water filled, however, also in this structure, fire sprinkler systems using seawater for extinguishing is installed. See Figure 6-11 for an overview of the location of these fire sprinkler systems. A similar exposure for these cores, like those obtained from the inside of Structure A would, therefore, be assumed. Cores 1-8 are all obtained from areas where fire sprinklers are installed. In addition to this, a minor leakage in the area where C.3.I and C.4.I is collected from have been reported. This is a leakage causing an increased presence of chlorides for these specific cores. The extent of this leakage is unknown.

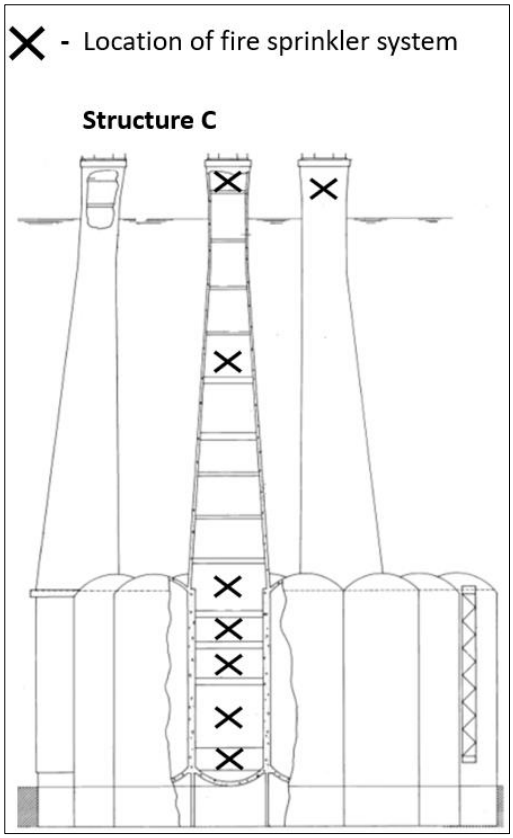

Figure 6-11: Location of all fire sprinkler systems in Structure C

Based on these different cases of exposure, we would expect C.3.I & C.4.I to have the deepest ingress, followed by the 6 other cores. The chloride ingress depths of all cores from Structure C are presented in Figure 6-12.

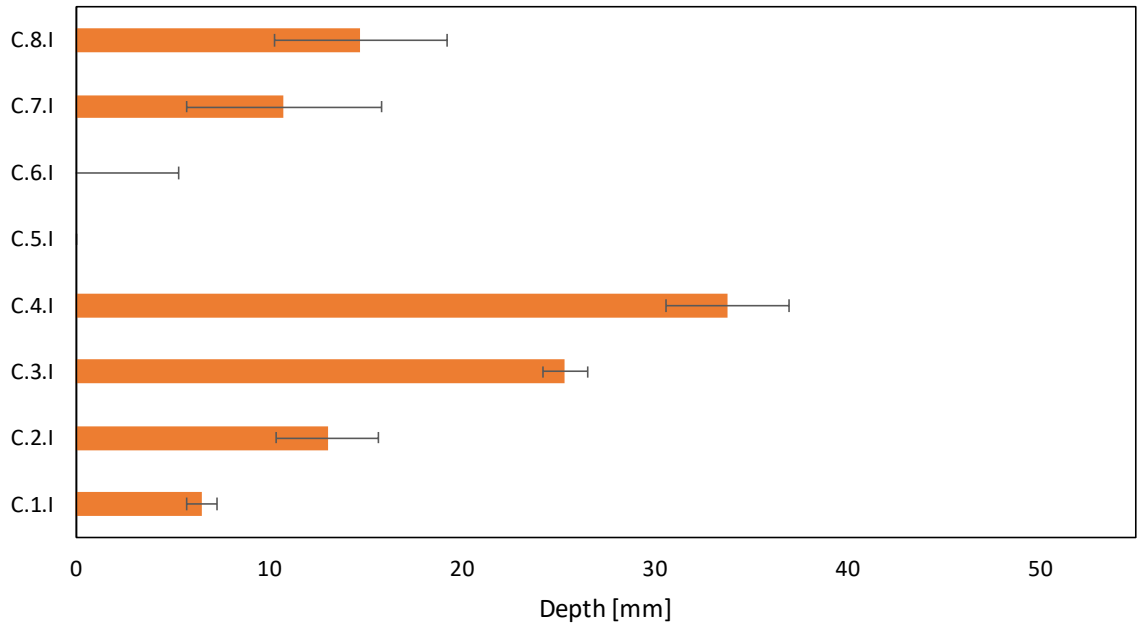

Figure 6-12: Depths where Cl_{crit} is reached for all cores in Structure A, from µ-XRF. These values and corresponding error bars are based on the calculations presented in section 4.7.3

Despite being in the presence of the fire sprinkler system, the chloride concentration of cores C.5.I and C.6.I do not exceed the critical chloride concentration at any point within the sample. The reason for this is unclear. One hypothesis would be that the cores have been collected from an area somehow sheltered from the extinguishing water. Another could be that the angle of the wall is preventing the seawater from penetrating the concrete in this area. Since there are two samples from the same area, and both show minimal ingress depth, we do not suspect this to be due to the method of analysis.

Cores C.1.I, C.2.I, C.7.I and C.8.I show an ingress depth ranging from 6-15 mm. The ingress depth is, as expected, most severe for C.3.I and C.4.I, with a penetration of 25 mm and 34 mm, respectively. Due to the minor leakage at the collection area, the chloride ingress is much deeper for these cores than the others. The ingress depths, however, are all too shallow to cause concern regarding chloride-induced corrosion, as the cover depth of the reinforcement is 60 ± 10 mm.

An additional feature to be discussed for Structure C is the possible effect of the hydraulic pressure. As can be seen from Figure 6-10, cores 1-4 are drilled from the inside and towards a tri-cell. A tri-cell is the volume between the bottom tanks, which is open and filled with water. As core C.1.I and C.2.I are obtained from 200 meters below sea level, we expect a severe hydraulic pressure acting on the outside of the concrete wall. The concrete walls have a thickness of 1.2 meters at this point, but we only have concrete cores with a length of 130-270 mm, obtained from the inside of the wall. We would still like to investigate the possibility of a contribution from the hydraulic pressure on the ingress observed. A combination of the hydraulic pressure and capillary suction could possibly, over time, lead to mass transportation through the wall from the outside. In a worst-case scenario, with a below 100% RH in the hollow shaft, evaporation of the moisture transported through the wall, will cause wick action to occur. This mechanism is discussed in 3.1.1.

To investigate this, we used the elemental maps of several elements, to see if we could see any indications of mass transport coming from the outside of the utility shaft wall. In Figure 6-13, elemental maps of all the most important elements in seawater of C.1.I are presented. Elemental maps of more elements can be found in Appendix A.12.

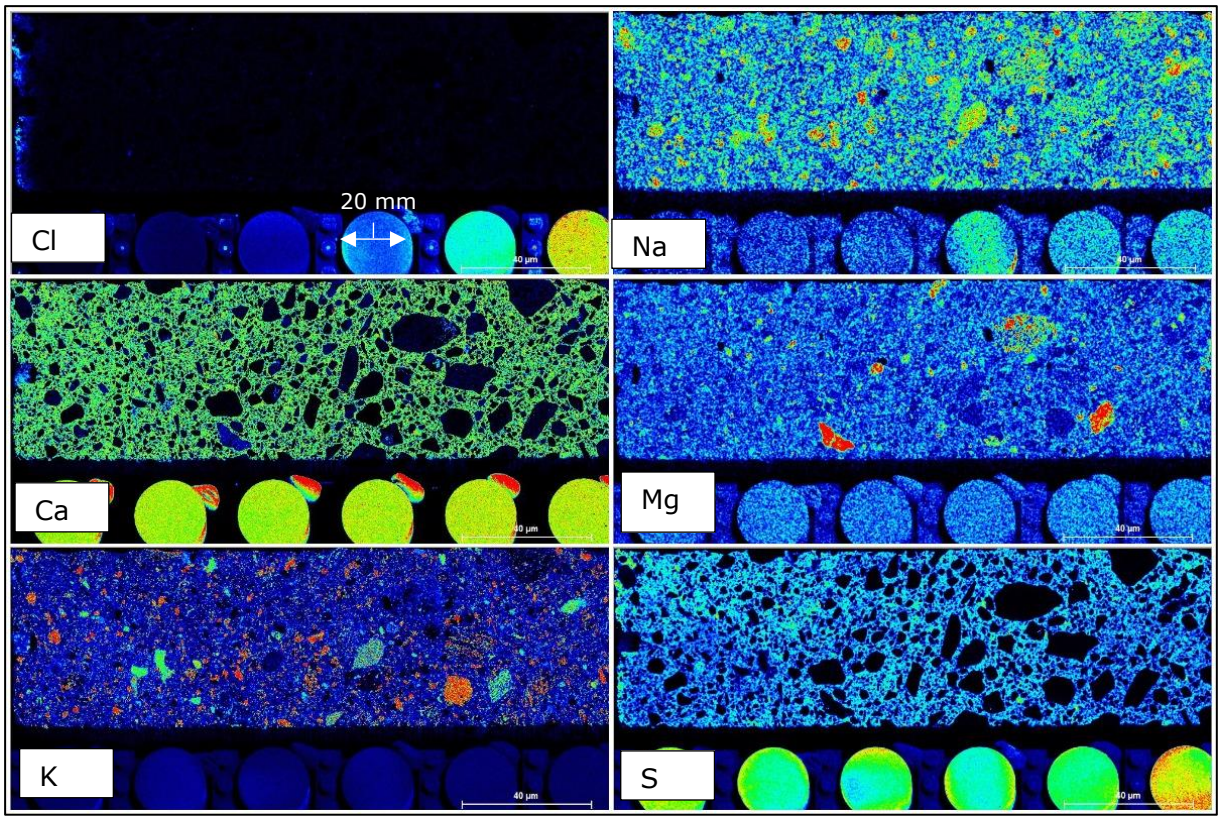

Figure 6-13: Elemental maps of Cl, Na, Ca, Mg, K and S in core C.1.I. The exposed surface is to the left in all the images. The tri-cell direction is to the right.

Chlorine and sulphur seem to be the only elements where a concentration gradient is visible in the elemental overviews. As discussed in section 5.4 we also expect a magnesium gradient, but this is not visible in the elemental overview. These three elements are all important parts of the chemical composition of seawater. Since no other elements show an indication of a concentration gradient, and the concentration of chlorides is decreasing towards the tri-cell direction, it is quite certain that these elements have come from seawater, penetrated from the inside of the shaft. The area we have analysed show no sign of mass transportation from the outside, indicating that mass has not been transported deep enough from the outside, to be detectable from our samples. To investigate the theoretical effect this hydraulic pressure should have on the structure, Darcy's law is used.

As seen from Darcy's law (1), the rate of transport from permeation is proportional to the pressure. In our case, this could both be from the hydraulic pressure of the seawater and the capillary action within the pores of the concrete. In the parts of the structure closest to the water surface, the hydraulic pressure would be close to negligible. Closer to the seabed, where C.1.I and C.2.I are collected, the hydraulic pressure would be expected to contribute considerably more to the transport of matter. To investigate this effect, the expected capillary underpressure in the concrete and the water pressure at this depth will be compared.

At a depth of 200 meters below sea level, the following hydraulic pressure is expected:

$$\Delta p_H = \rho_w * g * d = 2\ MPa \tag{25}$$

with

$$\rho_w - density\ of\ water = 1000\ \left[\frac{kg}{m^3}\right]$$

$$g - gravitational\ acceleration = 10\ \left[\frac{m}{s^2}\right]$$

$$d - depth\ below\ sea\ level = 200\ [m]$$

The capillary underpressure in the same area, where relative humidity (RH) of 90 % in the pores and a temperature of 5°C is assumed, is given from the Kelvin-Laplace equation:

$$\Delta p_C = -\frac{2\sigma_{ST}}{r_K} = -15\ MPa \tag{26}$$

with

$$\sigma_{ST} - surface\ tension = 0.0749\ \left[\frac{N}{m}\right]$$
$$r_K - kelvin\ radius = 10\ [nm]$$

Where the surface tension is obtained from [48] and the Kelvin radius from [49].

A degree of capillary saturation of right above 90% has been found from a concrete with similar w/b-ratio, submerged for 16 years. Because of this, 90% RH was assumed for this case.

As the relative humidity (RH) of the area of interest is uncertain, a table of plausible RH values and the corresponding Kelvin radius and underpressure, is presented in Table 6-1.

Table 6-1: Capillary suction at different RH in the concrete pores.

RH	**r_k** [nm]	**Δp_c** [MPa]
99.9	1000	-0.15
99	100	-1.50
95	21	-7.13
90	10	-14.98
80	5	-29.96

As seen from this table, if the RH is above 90%, the capillary suction is reduced to the same magnitude as the hydraulic pressure. However, if 90% is a reasonable assumption, these equations indicate that the hydraulic pressure is considerably lower than the capillary underpressure, also at these depths. This will again indicate that the hydraulic pressure should not be of much significance in this area, which corresponds well with the results obtained from the μ-XRF analysis.

6.3 Conclusion

For Structure A, the relative chloride ingress depths for the concrete cores corresponded well with the assumed chloride load. The deepest chloride ingress was found in the splash zone, which is expected. Core A.1.O and A.2.O both had a measured ingress depth of 29±2 mm and was located 6 and 8 meters above sea level, respectively. With a cover depth of 60±10 mm and a critical chloride content, Cl_{crit}=0.07 % Cl/concrete [g/g], the chloride ingress depths found in the seven cores from Structure A are all too shallow to cause concern regarding chloride-induced reinforcement corrosion at the present time.

For Structure C, the relative chloride ingress depths for the concrete cores did not fit as perfectly to the expected chloride load, as for Structure A. Two of the cores showed almost no chloride ingress at all, despite being in the presence of a fire sprinkler system. The deepest ingress depths were however as expected. These were found in the two cores obtained from an area subjected to seawater both from a leakage and from extinguishing water. These cores, C.3.I and C.4.I, had an ingress depth of 25±1 mm and 34±2 mm, respectively. Nonetheless, as the cover depth for the concrete in Structure C is 60±10 mm as well, all ingress depths were too shallow to cause concern regarding chloride-induced reinforcement corrosion for these areas at the present time.

There were no detectable signs of mass transport coming from the outside of the 1.2 m thick wall, in the 270 mm long concrete core, collected from the inside of Structure C. This indicates that the hydraulic pressure is not a dominating transport mechanism such a dense concrete, even at a depth of 201 m below sea level. This is supported by the Kelvin-Laplace equation, where the capillary underpressure were found to be significantly bigger than the hydraulic pressure, also at this depth.

7 Concluding Remarks

In this master thesis, an evaluation of the use of μ-XRF for determining chloride ingress in offshore concrete structures has been performed. Results indicate that μ-XRF is, compared to potentiometric titration and ICP-MS, less accurate in the determination of chloride profiles from a concrete core. The method does, however, surpass the other methods on several other evaluation criteria such as simplicity, versatility and safeness.

The μ-XRF does, despite the low accuracy of the chloride content measurements, show satisfactory accuracy regarding ingress depth determination. The depth at which the chloride concentration had reached below Cl_{crit}=0.07% Cl/concrete [g/g] was determined with an uncertainty of less than ±2 mm for all cores, and hence μ-XRF was assigned an adequate method of analysis for chloride ingress depth determination.

Based on the results from the μ-XRF analysis, the cores received indicate a high concrete quality. The deepest ingress in Structure A was at 29±2 mm, found in core A.1.O and A.2.O, both obtained from the splash zone. The range of ingress depths from the splash zone was from 14 mm to 29 mm, while the ingress depths of those obtained from the inside ranged between 3 mm and 14 mm. The cores from Structure C were all collected from the inside of the utility shaft, but at different elevations. The ingress depths of these cores ranged between 0 mm and 34 mm. The deepest ingress in this structure was the 34±2 mm ingress found in core C.4.I. This was suspected to be due to the combined exposure of seawater from both extinguishing water and a leakage at the collection area of this core. With a cover depth of 60 ± 10 mm, and an assumed critical chloride content of Cl_{crit}=0.07% Cl/concrete [g/g], the ingress depths of the concrete cores were all too shallow to cause concern regarding chloride-induced reinforcement corrosion, in the investigated areas at the present time.

There were no detectable signs of mass transport coming from the outside of the 1.2 m thick wall, in the 270 mm long concrete core, collected from the inside of Structure C, at a depth of 201 m below sea level. This indicates that the hydraulic pressure is not a dominating transport mechanism for a concrete of this quality, even at a depth of 201 m below sea level.

8 Future Research

The work done in this thesis regarding μ-XRF analysis has been a constant trial and error process. During the process, ideas for possible enhancement of the procedure have not been enabled due to limited time. Hence, a list of recommendations regarding μ-XRF analysis is given:

- The reference samples could be made containing small fractions of sand in addition to the cement. μ-XRF seems to be unable to separate these sand fractions from the paste during auto-phasing. By using reference samples as equal to the paste in the concrete of interest as possible, errors due to matrix effect may be minimized.
- During our work, we experienced a kind of deterioration or contamination of the reference samples. A study investigating whether it is the storage or the use of the reference samples that are causing most of the deterioration, would be of interest. What are the effects on the reference samples from being several hours in a vacuum inside the μ-XRF chamber?
- There should be a specific calibration curve for each scan session, i.e. for each concrete core analysed. This, instead of one calibration curve based on several scans. This will hopefully prevent errors caused by differences in the factors influencing the CPS/eV-values of each scan, like for instance the heat of the X-ray and the focus of the optics.
- Scan concrete cores, if possible, of bigger diameter. This to provide a bigger scan area. This will hopefully make the surface area more representative for the entire volume.
- Instead of calculating Cl/concrete from the Cl/paste, the results could rather be presented as Cl/Ca. A calibration is however still necessary. The same reference samples can be used as both Cl- and Ca content for these are known. Cl/Ca could also be calculated from the Cl/paste obtained from the original reference curve, if the w/b-ratio and CaO-content of the cement paste are known. Critical Cl/Ca values is then necessary in order to evaluate possible chloride-induced corrosion. This way, the error from auto-phasing is avoided, as the aggregate area percentage no longer are needed.
- Regarding post-processing of results – curve fitting could be used to obtain the entire area under the spectrum peak instead of only the value at the peak when using the calibration method with the μ-XRF. This will hopefully reduce the uncertainties of the calibration curve. In addition, the background noise from the spectra should be subtracted.

9 References

[1] Weerdt K de, Orsáková D, Müller ACA, Larsen CK, Pedersen B, Geiker MR. Towards the understanding of chloride profiles in marine exposed concrete, impact of leaching and moisture content 2016.

[2] Wikipedia. Condeep-Plattform. [May 30, 2019]; Available from: https://no.wikipedia.org/wiki/Condeep-plattform.

[3] Larsen S. Betongplattformene i Nordsjøen: Utviklingen av Condeep-plattformene og Statoils forhold til plattformkonseptet 1973-1995. [Master Thesis.]: Universitetet i Oslo; 2018.

[4] Store Norske Leksikon. Condeep. [May 23, 2019]; Available from: https://snl.no/Condeep.

[5] SINTEF. Undersøkelse av Gullfaks C betongskaft; 2017.

[6] Reistad M, Magnusson A.K, Haver S, Gudmestad O.T, Kvamme D. How severe wind conditions are possible on the Norwegian Continental Shelf? Marine Structures 2005;18:428–50.

[7] Det Norske Veritas. DFI-Resyme for Betongunderstell; 1986.

[8] Dr. techn. Olav Olsen. Engineering report, Design Resume, Gullfaks C.

[9] S.Jacobsen (ed.). Concrete Technology; 2016.

[10] Speweik J. Moisture - Part Two, Capillary Suction. [May 23, 2019]; Available from: https://johnspeweik.com/2011/10/14/moisture-part-two-capillary-suction/.

[11] Puyate YT, Lawrence CJ. Effect of solute parameters on wick action in concrete 1999.

[12] Nilsson L-O, Poulsen E, Sandberg P, Erndahl Sørensen H, Klinghoffer O. HETEK, Chloride penetration into concrete, State-of-the-Art. Transport processes, corrosion initiation, test methods and prediction models 1996.

[13] Bertolini L, Elsener B, Pedeferri P, Redaelli E, Polder R. Corrosion of steel in concrete: Prevention, diagnosis, repair. Weinheim: Wiley-VCH; 2004.

[14] Karen L. Scrivener, Alison K. Crumbie and Peter Laugesen. The Interfacial Transition Zone (ITZ) Between Cement Paste and Aggregates in Concrete. 2004.

[15] Europe. Eurokode 2: Prosjektering av betongkonstruksjoner: Del 1-1: Almenne regler og regler for bygninger;91.010.30;91.080.40: Standard Norge; 2008.

[16] Relling RH, Sellevold EJ. In Situ Moisture State of Coastal Concrete Bridges 2005.

[17] Wikipedia. North Sea: Hydrology. [June 05, 2019]; Available from: https://en.wikipedia.org/wiki/North_Sea#Hydrology.

[18] Wikipedia. Seawater. [November 18, 2018]; Available from: https://en.wikipedia.org/wiki/Seawater.

[19] Shigeyoshi Nagataki et al. Condensation of Chloride Ion in Hardened Cement Matrix Materials and on Embedded Steel Bars. MJ 1993;90(4).

[20] Hirao H, Yamada K, Takahashi H, Zibara H. Chloride Binding of Cement Estimated by Binding Isotherms of Hydrates. ACT 2005;3(1):77–84.

[21] Rivetti MLS, Neto JdSA, Júnior NSdA, Ribeiro DV. Corrosion Inhibitors for Reinforced Concrete (2018).

[22] Roar Myrdal. Corrosion of steel reinforcement in concrete; 2018.

[23] Cao Y, Gehlen C, Angst U, Wang L, Wang Z, Yao Y. Critical chloride content in reinforced concrete — An updated review considering Chinese experience. 2019.

[24] Tuutti K. Corrosion of steel in concrete. 1982.

[25] Angst U, Vennesland Ø. Critical chloride content. State of the art. 2007.

[26] Kjøs A-K. Critical chloride concentration for evaluation of chloride induced reinforcement corrosion; 2019.

[27] Alexander M, Bertron A, Belie N de. Performance of Cement-Based Materials in Aggressive Aqueous Environments. Springer; 2013.

[28] Weerdt K de, Justnes H, Geiker MR. Changes in the phase assemblage of concrete exposed to sea water. Cement and Concrete Composites 2014;47:53–63.

[29] Wikipedia. Micro-X-ray fluorescence. [May 20, 2019]; Available from: https://en.wikipedia.org/wiki/Micro-X-ray_fluorescence.

[30] Brouwer P. Theory of XRF. 3rd ed. PANalytical; 2010.

[31] Bruker. M4 Tornado. [May 23, 2019]; Available from: https://www.bruker.com/pt/products/x-ray-diffraction-and-elemental-analysis/micro-xrf-and-txrf/m4-tornado/technical-details/spot-size.html.

[32] Horiba Scientific. X-Ray Fluorescence - The Basic Process: Tutorial. [November 27, 2018]; Available from: http://www.horiba.com/scientific/products/x-ray-fluorescence-analysis/tutorial/x-ray-fluorescence-the-basic-process/.

[33] Wikipedia. Inductively coupled plasma mass spectrometry. [November 21, 2018]; Available from: https://en.wikipedia.org/wiki/Inductively_coupled_plasma_mass_spectrometry.

[34] Aceto M. The Use of ICP-MS in Food Traceability [Master Thesis]: Università degli Studi del Piemonte Orientale; 2016.

[35] Wikipedia. Mass spectrometry. [November 21, 2018]; Available from: https://en.wikipedia.org/wiki/Mass_spectrometry.

[36] Middle East Technical University. Potentiometric Titrations; Available from: http://users.metu.edu.tr/chem223/potentiometry.pdf.

[37] Aker Kværner Technology AS. Gullfaks 2030: Gullfaks A - GBS Design Basis; 2008.

[38] Aker Kværner Technology AS. Gullfaks 2030: Gullfaks C - GBS Design Basis; 2008.

[39] Kværner AS. Skader i ringbjelkeområdet av Utstyrskaftet; 2018.

[40] Fosså KT. Aggregates used in Structure A and Structure C; 2019.

[41] Rutland RWR, Sutherland DS. The chemical composition of granitic gneisses and spragmatic meta-sediments in the Glomfjord region, Northern Norway. 1967.

[42] Haug AK, Jakobsen B. In-Situ and Design Strength for Concrete in Offshore Platforms; 1990.

[43] Kaasa RI. Calibration Technique for Quantitative Chloride Measurements with micro-XRF in Cementious Materials. [Master thesis]: Norwegian University of Science and Technology; 2018.

[44] All Free Download. Free Vectors; 2019; Available from: https://all-free-download.com.

[45] Lane DM. Standard Error of the Estimate. [April 04, 2019]; Available from: http://onlinestatbook.com/2/regression/accuracy.html.

[46] Tolchard JR. Radiation Physics μ-XRF. NTNU; 2019.

[47] Fosså KT. Construction of Condeep Structures; 2019.

[48] Engineering ToolBox. Surface Tension of Water in contact with Air. [May 27, 2019]; Available from: https://www.engineeringtoolbox.com/water-surface-tension-d_597.html.

[49] Herholdt, Aage D. et al. Beton-Bogen. 2nd ed; 1985.

A Appendix

A.1 Raw data from Potentiometric Titration

Table A - 1: Raw data from potentiometric titration of concrete samples from the outside of Structure A including relative standard deviation.

Slice Range [mm]	A.1.O	RSD, %	A.2.O	RSD, %	A.3.O	RSD, %
			% Cl/dry concrete [g/g]			
0-2	0.856	0.5	0.443	0.5	0.49	0.5
2-4	0.878	0.5	0.404	0.5	0.361	0.5
4-6	0.587	0.5	0.362	0.5	0.2	0.5
6-9	0.489	0.5	0.31	0.5	0.117	1
9-13	0.476	0.5	0.286	0.5	0.067	1
13-17	0.319	0.5	0.218	0.5	0.008	1.1
17-23	0.14	1	0.123	1	<0.005	-
23-29	0.02	1	0.039	1	<0.005	-
29-35	<0.005	-	<0.005	-	<0.005	-
35-43	<0.005	-	<0.005	-	<0.005	-
43-51	<0.005	-	<0.005	-	<0.005	-
51-59	<0.005	-	<0.005	-	<0.005	-
59-67	<0.005	-	<0.005	-	<0.005	-
67-75	<0.005	-	<0.005	-	<0.005	-
75-85	<0.005	-	<0.005	-	<0.005	-

Table A - 2: Raw data from potentiometric titration of concrete samples from the inside of Structure A including relative standard deviation.

Slice Range [mm]	Concrete Core Number [% Cl/Concrete]							
	A.4.I	RSD, %	A.5.I	RSD, %	A.6.I	RSD, %	A.7.I	RSD, %
0-2	0.27	0.5	0.226	0.5	0.096	1	0.206	0.5
2-4	0.211	0.5	0.239	1	0.08	1	0.176	1
4-6	0.107	1	0.2	1	0.042	1	0.124	1
6-9	0.04	1	0.049	1	0.029	1	0.096	1
9-13	0.015	0.5	0.019	1	0.025	1	0.064	1
13-17	0.005	1.3	0.013	0.5	<0.005	-	0.03	1
17-23	<0.005	-	<0.005	-	<0.005	-	<0.005	-
23-29	<0.005	-	<0.005	-	<0.005	-	<0.005	-
29-35	<0.005	-	<0.005	-	<0.005	-	<0.005	-
35-43	<0.005	-	<0.005	-	<0.005	-	<0.005	-
43-51	<0.005	-	<0.005	-	<0.005	-	<0.005	-
51-59	<0.005	-	<0.005	-	<0.005	-	<0.005	-
59-67	<0.005	-	<0.005	-	<0.005	-	<0.005	-
67-75	<0.005	-	<0.005	-	<0.005	-	<0.005	-
75-85	<0.005	-	<0.005	-	<0.005	-	<0.005	-

A.2 Data from ICP-MS

Table A - 3: Raw data from ICP-MS of all concrete cores from Structure A corrected for blank samples, i.e. background level of elements.

Slice Range [mm]	Concrete Core Number						
	A.1.O	A.2.O	A.3.O	A.4.I	A.5.I	A.6.I	A.7.I
	Amount of Cl corrected for blanks [µg/L]						
0-2	8179.15	3721.85	3037.98	2264.66	2053.62	786.24	1778.00
2-4	7751.33	3411.74	3051.99	1909.31	2023.79	923.45	1351.09
4-6	5104.88	3099.72	2704.93	997.15	1226.29	510.95	-12.34
6-9	4379.36	2597.46	1443.56	376.45	460.48	376.82	813.84
9-13	4136.41	2396.93	973.21	158.41	181.10	996.79	518.43
13-17	2822.32	1901.95	518.96	78.47	-22.84	414.66	201.19
17-23	1183.14	1120.86	32.04	74.62	18.89	208.41	-16.88
23-29	148.52	333.84	-85.82	74.47	20.68	175.75	32.13
29-35	-4.42	93.97	-77.52	41.00	13.65	112.05	19.38
35-43	-12.98	63.48	-17.63	16.27	10.92	44.85	8.59
43-51	-44.08	23.25	-26.00	2.64	1.52	92.38	-15.53
51-59	-44.89	38.34	16.28	6.95	-53.19	68.40	-8.67
59-67	-46.08	44.28	23.66	-12.16	14.32	33.03	-62.36
67-75	-23.41	7.36	64.00	-12.92	-1.17	12.22	-48.26
75-85	10.65	16.22	66.75	34.74	-60.07	-18.42	-10.85

Table A - 4: Calculated data from ICP-MS of concrete cores from the inside of Structure A including relative standard deviation.

Slice Range [mm]	Concrete Core Number					
	A.1.O		A.2.O		A.3.O	
	% Cl/concrete [g/g]	RSD, %	% Cl/concrete [g/g]	RSD, %	% Cl/concrete [g/g]	RSD, %
0-2	0.79	1.8	0.38	1.3	0.42	2.6
2-4	0.78	2.0	0.35	2.6	0.30	3.3
4-6	0.52	3.2	0.31	2.3	0.18	2.2
6-9	0.44	1.6	0.26	2.8	0.10	6.0
9-13	0.42	4.2	0.24	3.3	0.05	3.2
13-17	0.29	5.0	0.19	7.2	0.00	-
17-23	0.12	6.4	0.11	4.5	0.00	-
23-29	0.02	31.8	0.03	7.2	0.00	-
29-35	0.00	-	0.01	-	0.00	-
35-43	0.00	-	0.01	-	0.00	-
43-51	0.00	-	0.00	-	0.00	-
51-59	0.00	-	0.00	-	0.00	-
59-67	0.00	-	0.00	-	0.00	-
67-75	0.00	-	0.00	-	0.00	-
75-85	0.00	-	0.00	-	0.00	-

Table A - 5: Calculated data from ICP-MS of concrete cores from the inside of Structure A including relative standard deviation.

Slice Range [mm]	Concrete Core Number							
	A.4.I		A.5.I		A.6.I		A.7.I	
	% Cl/concrete [g/g]	RSD, %	% Cl/concrete [g/g]	RSD, %	% Cl/concrete [g/g]	RSD, %	% Cl/concrete [g/g]	RSD, %
0-2	0.25	2.0	0.21	6.5	0.09	5.4	0.18	5.1
2-4	0.19	6.0	0.20	5.1	0.09	4.1	0.14	6.3
4-6	0.10	2.3	0.12	4.9	0.05	3.1	0.08	0.0
6-9	0.04	2.7	0.05	2.6	0.04	2.8	0.05	13.9
9-13	0.02	3.5	0.02	4.7	0.04	8.9	0.02	15.6
13-17	0.01	2.5	0.00	-	0.02	-	0.00	50.7
17-23	0.01	-	0.00	-	0.02	-	0.00	-
23-29	0.01	-	0.00	-	0.01	-	0.00	-
29-35	0.00	-	0.00	-	0.01	-	0.00	-
35-43	0.00	-	0.00	-	0.00	-	0.00	-
43-51	0.00	-	0.00	-	0.00	-	0.00	-
51-59	0.00	-	0.00	-	0.00	-	0.00	-
59-67	0.00	-	0.00	-	0.00	-	0.00	-
67-75	0.00	-	0.00	-	0.00	-	0.00	-
75-85	0.00	-	0.00	-	0.00	-	0.00	-

Table A - 6: Data from ICP-MS presenting magnesium concentration in all concrete cores from Structure A.

Slice Range [mm]	Concrete Core Number % Mg/Concrete [g/g]						
	A.1.O	A.2.O	A.3.O	A.4.I	A.5.I	A.6.I	A.7.I
0-2	0.49	0.48	0.47	0.40	0.38	0.35	0.38
2-4	0.30	0.33	0.47	0.29	0.30	0.29	0.28
4-6	0.27	0.30	0.31	0.31	0.29	0.26	-
6-9	0.26	0.26	0.26	0.32	0.30	0.24	0.26
9-13	0.27	0.26	0.25	0.28	0.28	0.28	0.27
13-17	0.28	0.26	0.27	0.27	-	0.27	0.26
17-23	0.27	0.28	0.24	0.25	0.29	0.27	-
23-29	0.26	0.27	0.26	0.27	0.27	0.26	0.25
29-35	0.26	0.28	0.27	0.23	0.29	-	0.25
35-43	0.27	0.32	0.27	0.29	0.27	-	0.25
43-51	0.31	0.28	0.25	0.26	0.28	0.28	0.27
51-59	0.32	0.26	0.25	0.28	-	0.24	0.25
59-67	0.31	0.25	0.31	0.24	0.27	0.25	-
67-75	0.24	0.22	0.48	0.26	0.25	0.23	-
75-85	0.24	0.26	0.34	0.25	-	-	0.24

Table A - 7: Data from ICP-MS presenting sulphur concentration in all concrete cores from Structure A.

Slice Range [mm]	Concrete Core Number % S/Concrete [g/g]						
	A.1.O	A.2.O	A.3.O	A.4.I	A.5.I	A.6.I	A.7.I
0-2	0.36	0.35	0.35	0.35	0.42	0.35	0.36
2-4	0.21	0.24	0.34	0.26	0.29	0.26	0.25
4-6	0.19	0.19	0.24	0.22	0.22	0.18	-
6-9	0.18	0.19	0.17	0.20	0.22	0.19	0.21
9-13	0.22	0.20	0.15	0.20	0.22	0.26	0.22
13-17	0.19	0.22	0.18	0.18	-	0.22	0.19
17-23	0.17	0.24	0.18	0.16	0.21	0.19	-
23-29	0.19	0.21	0.21	0.19	0.20	0.17	0.17
29-35	0.19	0.25	0.22	0.14	0.21	-	0.15
35-43	0.24	0.24	0.26	0.19	0.18	-	0.19
43-51	0.21	0.22	0.21	0.18	0.18	0.21	0.20
51-59	0.22	0.22	0.20	0.21	-	0.19	0.20
59-67	0.16	0.21	0.24	0.17	0.19	0.13	-
67-75	0.19	0.18	0.17	0.18	0.18	0.11	-
75-85	0.17	0.19	0.20	0.21	-	0.18	0.17

A.3 Raw data from µ-XRF from Structure A

Table A - 8: Raw data from µ-XRF for concrete core A.1.O.

A.1.O							
Area % of aggregate phase			**CPS/eV for Cl in paste phase**			**Weight %**	
Ca-map	**Ca-Si-map**	**Ca-Si-S-map**	**Ca-map**	**Ca-Si-map**	**Ca-Si-S-map**	**Cl**	**Ca**
64.7	73.00	64.1	21.19	22.53	20.94	0.62	14.08
71.00	72.00	71.7	16.48	16.72	16.65	0.42	12.85
56.7	55.5	55.8	12.52	12.37	12.4	0.39	16.95
54.6	51.00	52.1	8.8	8.5	8.59	0.28	17.94
53.9	55.3	55.5	4.51	4.58	4.6	0.14	17.04
56.00	56.1	57.5	1.99	1.99	2.02	0.06	16.45
64.00	61.9	62.8	1.29	1.27	1.28	0.03	14.49
68.9	66.9	65.00	1.2	1.18	1.16	0.02	12.61
57.00	54.1	57.2	1.06	1.04	1.06	0.02	16.96
65.9	65.00	63.5	1.06	1.06	1.05	0.02	14.77

Table A - 9: Raw data from µ-XRF for concrete core A.2.O.

A.2.O							
Area % of aggregate phase			**CPS/eV for Cl in paste phase**			**Weight %**	
Ca-map	**Ca-Si-map**	**Ca-Si-S-map**	**Ca-map**	**Ca-Si-map**	**Ca-Si-S-map**	**Cl**	**Ca**
58.2	59.50	57.6	8.29	8.44	8.22	0.22	15.35
61.60	61.20	61	9.17	9.18	9.15	0.24	15.64
60.9	58.2	58.7	6.77	6.59	6.62	0.18	15.93
54.3	53.80	53.2	4.92	4.9	4.86	0.14	17.47
49.3	51.7	48.3	3.43	0.61	3.37	0.1	19.08
49.30	-	-	1.82	-	-	0.04	18.72
54.30	57.7	-	0.8	0.8	-	0.01	18.84
71.8	56.5	56.10	0.69	0.67	0.67	0	16.87
62.10	62.2	62.4	0.65	0.65	0.65	0	15.62
60.3	59.20	58.5	0.67	0.67	0.66	0	16.29

Table A - 10: Raw data from µ-XRF for concrete core A.3.O.

A.3.O							
Area % of aggregate phase			**CPS/eV for Cl in paste phase**			**Weight %**	
Ca-map	**Ca-Si-map**	**Ca-Si-S-map**	**Ca-map**	**Ca-Si-map**	**Ca-Si-S-map**	**Cl**	**Ca**
62.1	61.50	61	10.20	10.1	10.10	0.28	15.63
67.90	68.00	68.5	6.55	6.56	6.6	0.14	14.1
72.7	65.9	65.6	2.59	2.69	2.68	0.05	14.29
52.9	53.50	53.3	1.11	1.12	1.11	0.01	18.39
60.7	60.7	61	1.07	1.07	1.07	0.01	15.69
51.40	51.4	51.7	1.03	1.03	1.03	0.02	18.78
-	-	-	-	-	-	0.01	22.23
60.1	59	59.40	1.2	1.19	1.19	0.02	17.59
84.40	84.5	84.6	1.03	1.03	1.03	0.03	8.89
73.9	73.60	-	0.76	0.76	-	0.01	11.61

Table A - 11: Raw data from µ-XRF for concrete core A.4.I.

A.4.I							
Area % of aggregate phase			**CPS/eV for Cl in paste phase**			**Weight %**	
Ca-map	**Ca-Si-map**	**Ca-Si-S-map**	**Ca-map**	**Ca-Si-map**	**Ca-Si-S-map**	**Cl**	**Ca**
77.6	65.50	64.7	9.91	10.03	10.14	0.24	12.28
67.70	68.30	65.5	5.38	5.41	5.33	0.12	13.1
60.8	62.3	62	1.72	1.69	1.63	0.02	14.73
80.2	65.40	65.6	0.76	0.71	0.72	0	12.78
72.8	72.7	74.1	0.68	0.68	0.66	0	11.24
73.00	73.1	73.5	0.7	0.7	0.7	0	10.96
84.10	82.9	83.9	0.68	0.69	0.67	0	7.73
69.6	68.9	70.80	0.71	0.71	0.69	0	12.4
75.40	72.4	71.2	0.67	0.67	0.66	0	10.44
72.8	73.10	73.3	0.68	0.67	0.68	0	11.66

Table A - 12: Raw data from µ-XRF for concrete core A.5.I.

A.5.I							
Area % of aggregate phase			**CPS/eV for Cl in paste phase**			**Weight %**	
Ca-map	**Ca-Si-map**	**Ca-Si-S-map**	**Ca-map**	**Ca-Si-map**	**Ca-Si-S-map**	**Cl**	**Ca**
62.3	62.00	62.7	7.17	6.81	6.91	0.17	14.41
66.80	66.10	67.4	4.32	4.03	3.99	0.08	13.38
55.6	55.9	54	1.4	1.35	1.35	0.02	17.01
69.5	61.50	62.9	0.6	0.57	0.58	0	15.38
59.3	56.6	60.3	0.64	0.64	0.65	0	16.35
62.10	59.8	59.7	0.68	0.7	0.67	0	16.01
65.50	62.6	61	0.62	0.63	0.62	0	14.36
63.9	66.5	63.50	0.66	0.67	0.64	0	14.46
56.80	56.8	60.2	0.58	0.57	0.6	0	16.38
64.8	64.80	66.6	0.6	0.6	0.61	0	13.71

Table A - 13: Raw data from µ-XRF for concrete core A.6.I.

A.6.I							
Area % of aggregate phase			**CPS/eV for Cl in paste phase**			**Weight %**	
Ca-map	**Ca-Si-map**	**Ca-Si-S-map**	**Ca-map**	**Ca-Si-map**	**Ca-Si-S-map**	**Cl**	**Ca**
48.8	52.10	49.4	1.68	1.67	1.66	0.03	14.81
60.30	60.30	59.4	1.17	1.17	1.17	0.01	13.39
59	58.5	58.2	0.7	0.7	0.69	0	13.71
63.3	63.40	64.2	0.66	0.66	0.65	0	13.61
52	54.2	54.5	0.56	0.57	0.57	0	15.29
59.40	57.9	58	0.57	0.57	0.57	0	14.41
62.50	62.5	60.6	0.61	0.61	0.61	0	14.17
65.5	64.5	65.20	0.56	0.56	0.56	0	12.82
62.50	61.2	60.3	0.55	0.56	0.56	0	13.52
52	51.20	49.3	0.56	0.55	0.55	0	16.28

Table A - 14: Raw data from µ-XRF for concrete core A.7.I.

A.7.I							
Area % of aggregate phase			**CPS/eV for Cl in paste phase**			**Weight %**	
Ca-map	**Ca-Si-map**	**Ca-Si-S-map**	**Ca-map**	**Ca-Si-map**	**Ca-Si-S-map**	**Cl**	**Ca**
66.7	66.30	65.8	2.82	2.8	2.78	0.05	13.54
61.50	60.40	60.6	1.87	1.94	1.88	0.03	16.05
66	65.5	65.5	1.23	1.26	0.58	0.01	13.84
44.5	45.90	46.2	0.66	-	0.66	0	20
43.7	46.2	45.6	0.6	0.6	-	0	20.03
42.00	42.4	43.4	0.55	0.54	-	0	20.39
56.10	56	58.6	0.54	0.54	0.53	0	16.47
63.9	63.6	63.90	0.56	0.55	0.56	0	14.68
90.90	91	91	0.54	0.54	0.54	0	5.66
61.3	63.40	62.8	0.63	0.59	0.61	0	14.34

A.4 Calculated data μ-XRF from Structure A

Table A - 15: Calculated data from μ-XRF for outside cores in Structure A, including relative standard deviation in percent.

Slice Range [mm]	A.1.O	RSD, %	A.2.O	RSD, %	A.3.O	RSD, %
			% Cl/dry concrete [g/g]			
2.5	0.82	100	0.40	83.5	0.45	88.4
7.5	0.54	113	0.41	87.9	0.23	103
12.5	0.65	80.2	0.31	84.8	0.08	103
17.5	0.48	76.3	0.25	77.8	0.04	88.1
22.5	0.23	79.1	0.13	74.9	0.03	98.5
27.5	0.08	83	0.09	76.0	0.03	89.9
32.5	0.04	97	0.02	115	-	-
37.5	0.03	107	0.01	156	0.04	93.2
42.5	0.03	93	0.01	172	0.01	203
47.5	0.03	106	0.01	160	0.01	153

Table A - 16: Calculated data from μ-XRF from inside cores in Structure A, including relative standard deviation in percent.

Slice Range [mm]	A.4.I	RSD, %	A.5.I	RSD, %	A.6.I	RSD, %	A.7.I	RSD, %
				% Cl/dry concrete [g/g]				
2.5	0.35	106	0.30	89.9	0.08	77.4	0.09	98.6
7.5	0.19	100	0.15	99.4	0.03	94.5	0.07	89.3
12.5	0.06	92	0.05	85.0	0.01	144	0.02	109
17.5	0.01	150	0.01	244	0.01	169	0.01	156
22.5	0.01	177	0.01	174	0.01	271	0.01	211
27.5	0.01	166	0.01	152	0.01	265	0.01	332
32.5	0.00	226	0.01	193	0.01	205	0.00	369
37.5	0.01	157	0.01	170	0.00	293	0.00	301
42.5	0.01	179	0.01	240	0.00	299	0.00	480
47.5	0.01	175	0.01	217	0.01	305	0.01	206

A.5 Raw data from µ-XRF from Structure C

Table A - 17: Raw data from µ-XRF for concrete core C.1.I.

C.1.I					
Area % of aggregate phase			**CPS/eV for Cl in paste phase**		
Ca-map	**Ca-Si-map**	**Ca-Si-S-map**	**Ca-map**	**Ca-Si-map**	**Ca-Si-S-map**
45.8	45.80	46.1	3.95	3.95	3.97
49.80	49.80	48.1	0.9	0.9	0.84
49	44.3	41.9	0.54	0.55	0.54
50	48.60	49.3	0.51	0.5	0.5
49.8	-	42.3	0.48	-	0.48
38.70	38.8	-	0.48	0.48	-
-	48.4	48.4	-	0.49	0.49
51.3	53.6	53.10	0.49	0.49	0.5
48.10	-	-	0.5	-	-
51.2	-	-	0.5	-	-

Table A - 18: Raw data from µ-XRF for concrete core C.2.I.

C.2.I					
Area % of aggregate phase			**CPS/eV for Cl in paste phase**		
Ca-map	**Ca-Si-map**	**Ca-Si-S-map**	**Ca-map**	**Ca-Si-map**	**Ca-Si-S-map**
74.1	70.10	72	10.82	10.03	10.42
65.70	65.50	65.3	6.05	6.06	6.04
58	57.6	57.6	1.94	1.94	1.96
50.5	50.40	50.2	0.63	0.63	0.63
49.2	49.2	51.3	0.59	0.6	0.61
53.50	53.5	54.4	0.57	0.58	0.59
63.30	64.7	64.8	0.57	0.58	0.58
60.3	60.3	60.00	0.57	0.57	0.57
58.80	57.7	58.8	0.55	0.54	0.55
49.7	52.10	51.4	0.55	0.56	0.55

Table A - 19: Raw data from µ-XRF for concrete core C.3.I.

C.3.I					
Area % of aggregate phase			**CPS/eV for Cl in paste phase**		
Ca-map	**Ca-Si-map**	**Ca-Si-S-map**	**Ca-map**	**Ca-Si-map**	**Ca-Si-S-map**
58.2	56.80	56.8	7.59	7.46	7.45
54.70	55.80	55.2	6.72	6.81	6.76
43.1	45.2	46.3	3.77	3.75	3.82
47	46.70	44.6	4.72	4.66	4.88
-	-	-	-	-	-
65.90	69.6	-	0.77	0.69	-
49.10	49.6	50	1.92	1.93	1.94
46.2	55.5	43.70	1.79	0.35	1.76
55.00	55.4	53.7	1.48	1.49	1.46
59	60.50	60.4	1.32	1.35	1.35

Table A - 20: Raw data from µ-XRF for concrete core C.4.I.

C.4.I					
Area % of aggregate phase			**CPS/eV for Cl in paste phase**		
Ca-map	**Ca-Si-map**	**Ca-Si-S-map**	**Ca-map**	**Ca-Si-map**	**Ca-Si-S-map**
68.9	68.90	68.8	19.53	19.54	19.53
54.00	54.00	53.5	11.54	11.45	11.38
58.5	59.2	59.2	6.29	6.34	6.34
70.9	70.40	69.8	4.61	4.58	4.55
62.8	65.4	62.6	3.3	3.39	3.29
55.00	49.2	50.8	2.58	2.56	0.58
47.60	47.6	45.2	1.71	1.71	1.68
54	52.8	53.60	1.03	1.01	1.02
54.00	53.6	53.6	0.6	0.6	0.6
60.7	63.10	64	0.5	0.51	0.51

Table A - 21: Raw data from µ-XRF for concrete core C.5.I.

C.5.I					
Area % of aggregate phase			CPS/eV for Cl in paste phase		
Ca-map	Ca-Si-map	Ca-Si-S-map	Ca-map	Ca-Si-map	Ca-Si-S-map
71.8	74.90	70.4	0.72	0.73	0.69
66.30	58.70	64.3	0.43	0.39	0.42
72.3	70.7	70.7	0.42	0.41	0.4
66.5	67.00	65.9	0.46	0.47	0.46
50.8	50.1	50.3	0.48	0.47	0.47
72.90	72	71.2	0.47	0.46	0.46
75.00	74.4	74.4	0.47	0.46	0.46
55.5	54.7	55.00	0.46	0.46	0.46
73.60	72.9	73	0.46	0.46	0.47
56.1	56.70	56	0.46	0.47	0.46

Table A - 22: Raw data from µ-XRF for concrete core C.6.I.

C.6.I					
Area % of aggregate phase			CPS/eV for Cl in paste phase		
Ca-map	Ca-Si-map	Ca-Si-S-map	Ca-map	Ca-Si-map	Ca-Si-S-map
53.3	51.20	51.5	1.26	1.22	1.23
54.80	54.80	53.5	0.99	0.99	0.97
52.3	53.5	53.9	0.51	0.51	0.51
59.6	59.60	57	0.45	0.45	0.44
63.8	63.8	62.7	0.5	0.5	0.5
52.00	50.5	50.6	0.48	0.47	0.47
47.20	48	47.9	0.48	0.48	0.47
55.6	55.6	56.00	0.47	0.47	0.48
66.50	67	66.6	0.45	0.46	0.46
58.4	58.00	58	0.46	0.45	0.45

Table A - 23: Raw data from µ-XRF for concrete core C.7.I.

C.7.I					
Area % of aggregate phase			CPS/eV for Cl in paste phase		
Ca-map	Ca-Si-map	Ca-Si-S-map	Ca-map	Ca-Si-map	Ca-Si-S-map
54.3	54.30	56.3	5.07	5.07	5.19
64.60	64.60	64.4	4.36	4.37	4.35
91.8	91.8	91.8	2.56	2.56	2.58
62.9	62.90	63.5	1.13	1.13	1.13
52.6	52.6	52.3	0.88	0.88	0.88
76.90	76.9	77	0.64	0.64	0.64
61.50	62.1	61.5	0.57	0.57	0.57
61.8	61.2	61.10	0.53	0.53	0.53
68.70	67.8	68.5	0.53	0.53	0.53
51.3	51.30	52	0.53	0.52	0.52

Table A - 24: Raw data from µ-XRF for concrete core C.8.I.

C.8.I					
Area % of aggregate phase			CPS/eV for Cl in paste phase		
Ca-map	Ca-Si-map	Ca-Si-S-map	Ca-map	Ca-Si-map	Ca-Si-S-map
65.9	63.70	66.1	6.01	5.81	6.02
63.60	64.70	64.5	3.3	3.36	3.35
51.8	51.4	50.7	1.95	1.94	1.93
43.6	43.60	42	1.08	1.09	1.08
62.4	61.8	62.4	0.95	0.95	0.95
66.60	67.8	68.2	0.71	0.72	0.72
58.40	58.1	58.4	0.63	0.63	0.64
73.8	73.7	73.90	0.61	0.61	0.61
66.00	66	66.3	0.64	0.64	0.65
66.4	62.20	62.2	0.53	0.61	0.61

A.6 Calculated data from μ-XRF from Structure C

Table A - 25: Calculated data from μ-XRF for concrete cores 1-4 in Structure C, including relative standard deviation in percent.

Slice Range [mm]	C.1.I	RSD, %	C.2.I	RSD, %	C.3.I	RSD, %	C.4.I	RSD, %
	% Cl/dry concrete [g/g]							
2.5	0.24	70.9	0.33	115	0.37	81.9	0.71	105
7.5	0.03	99.0	0.23	96.3	0.35	79.4	0.63	77.7
12.5	0.01	339	0.08	85	0.23	70	0.29	84
17.5	0.00	632	0.01	180	0.29	71	0.14	109
22.5	0.00	1310	0.01	212	-	-	0.13	93
27.5	0.00	1310	0.01	244	0.01	145	0.09	78
32.5	0.00	896	0.01	256	-	-	0.08	75
37.5	0.00	811	0.01	267	0.05	80	0.03	92
42.5	0.00	682	0.00	330	0.06	83	0.01	213
47.5	0.00	682	0.01	306	0.04	91	0.00	591

Table A - 26: Calculated data from μ-XRF for concrete cores 5-8 in Structure C, including relative standard deviation in percent.

Slice Range [mm]	C.5.I	RSD, %	C.6.I	RSD, %	C.7.I	RSD, %	C.8.I	RSD, %
	% Cl/dry concrete [g/g]							
2.5	0.01	160	0.05	83.9	0.26	79.1	0.23	95.7
7.5	0.00	629	0.03	94.8	0.17	94.3	0.12	94.0
12.5	0.00	591	0.00	552	0.02	368	0.09	77
17.5	0.00	5820	0.00	2378	0.03	100	0.05	82
22.5	0.00	1898	0.00	684	0.02	101	0.02	106
27.5	0.00	5821	0.00	1898	0.00	206	0.01	149
32.5	0.00	5821	0.00	1550	0.01	267	0.01	181
37.5	0.00	18752	0.00	1898	0.00	403	0.00	222
42.5	0.00	5821	0.00	15343	0.00	407	0.01	181
47.5	0.00	5820	0.00	5445	0.00	440	0.01	243

A.7 Script µ-XRF

```
//-------------------------------------------------------------
// Program to used to obtain elemental maps from concrete cores
// Output: Overview, 5mm slices of concrete core, 1cm3 scans of reference samples
// Joachim Slotten and Erik Vådahl 2018-2019
//-------------------------------------------------------------

Program TestHyperMap;

uses ControlFunctions;

var   running        : boolean;
      canceled       : boolean;
      line           : longint;
      state          : double;
      HyMapPositions : array of TRect;
      TimePerPixel   : array of double;
      Width          : array of integer;
      Stepwidth      : double;
      NumberOfMaps   : integer;
      i              : integer;
      aFileName      : string;

begin
   //Number of Hypermaps
   NumberOfMaps:=17;
   //Filename
   aFileName:='GFA 1 Scans'

   SetLength(HyMapPositions,NumberOfMaps);
   SetLength(TimePerPixel,NumberOfMaps);
   SetLength(Width,NumberOfMaps);
```

```
   //HyMapPositions[n]:=Rect(left,top,right,bottom) -> Motor positions
taken from the software GUI (in mm); StepWidth:=13 (in µm) ;
TimePerPixel:=1 (in ms)

   HyMapPositions[0] :=Rect(x.1, y.1, x.3, y.3);   StepWidth:=40;
TimePerPixel[0] :=2; (*calculation of the parameter actually understood by
the Software:*)    Width[0] :=ROUND(ABS(HyMapPositions[0].Left *1000-
HyMapPositions[0].Right *1000)/StepWidth);

   HyMapPositions[1] :=Rect(x.1, y.1, x.3, y.3);   StepWidth:=25;
TimePerPixel[1] :=3; (*calculation of the parameter actually understood by
the Software:*)    Width[1] :=ROUND(ABS(HyMapPositions[1].Left *1000-
HyMapPositions[1].Right *1000)/StepWidth);


   canceled:=false

   for i:=0 to NumberOfMaps-1 do

   begin

      try


HyMapStart(1,HyMapPositions[i].Left,HyMapPositions[i].Top,HyMapPositions[i]
.Right,HyMapPositions[i].Bottom,Width[i],TimePerPixel[i]/1000.0);

      except

         Writeln('Invalid number in edit control');

         Exit;

      end;

      StartProgress('Messung',0,100,0,'%');

      repeat

         HyMapGetStateEx(running,state,line);

         if not Progress(State) then

         begin

            Canceled:=true

            Break; // ---> raus

         end;

         sleep(200);

      until not running;

      if Canceled

         then Break; // ---> raus

      StopProgress;

      HyMapStop(true);

      HyMapSaveToFile('\\RTUser\'+aFileName+'_'+IntToStr(i+1)+'.bcf');

   end;

end.
```

A.8 Direct Method vs. Norcem

Weight percentages of all elements in cement paste were obtained directly from the µ-XRF software from three different scans of reference sample F. We assumed all elements were in oxide form and calculated the new mass percentages based on this assumption. These results were normalized and compared with the oxide overview of the cement used for the reference samples. Example: We got the weight percent of sodium, **Na**, to be 1.21%. This is not normalized. The sum of all these do not equal 100, because the µ-XRF software "knows" that it is certain elements it does not register. We know that a lot of the sodium in the concrete is part of the oxide Na2O. In this calculation, we have assumed that all elements are 100% bound as oxides. We then calculated the weight percent of this oxide, $\boldsymbol{Na_2O}$, based on the atomic masses of both sodium, M_{Na}, and oxygen, M_O.

$$\boldsymbol{Na_2O} = \boldsymbol{Na} * \frac{2 * M_{Na} + M_O}{2 * M_{Na}} = 1.21\% * \frac{2 * 22.99 + 16}{2 * 22.99} = 1.63\%$$

After we had done this to all elements, we normalized them, so that we could directly compare these values with those obtained from the Oxide overview of the cement. We got the following result:

Table A - 27: Oxide composition of reference sample F from direct method and from oxide overview % [g/g].

					Normalized		
Element	**µ-XRF data, ref F**	**Oxide**	**Norcem**	**µ-XRF**	**Norcem**	**µ-XRF**	**Difference**
Na	1.21	**Na**2O	0.35	1.63	0.35	1.97	-1.61
Mg	0.59	**Mg**O	1.71	0.98	1.73	1.18	0.54
Fe	3.65	**Fe**2O3	3.77	5.21	3.80	6.30	-2.50
Mn	0.06	**Mn**2O3	0.059	0.09	0.06	0.10	-0.05
K	0.68	**K**2O	0.4	1.65	0.40	1.99	-1.59
Al	1.42	**Al**2O3	4.6	2.69	4.64	3.25	1.39
Si	6.66	**Si**O2	21.12	14.25	21.31	17.22	4.09
S	1.15	**S**O3	3.39	2.87	3.42	3.47	-0.05
Ca	39.14	**Ca**O	63.21	52.89	63.78	63.90	-0.12
Ti	0.27	**Ti**O2	0.314	0.44	0.32	0.54	-0.22
P	0.03	**P**2O5	0.182	0.07	0.18	0.08	0.10
SUM	54.86		99.105	82.77	100.00	100.00	0.00

The same has been done for the weight percentages obtained from the cement paste phase of the concrete core A.1.O, using Ca and Si for auto-phasing. An average of the the oxide composition from all thin sections were calculated. This has been compared to the oxide overview of the cement used for this concrete, provided by Norcem. That gave the following result:

Table A - 28: Oxide composition of concrete core A.1.O from direct method and from oxide overview. Based on a Ca-Si auto-phase map and data from Norcem % [g/g].

					Normalized		
Element	**µ-XRF, phase separation data**	**Oxide**	**Norcem P30**	**µ-XRF**	**Norcem P30**	**µ-XRF**	**Difference**
Na	1.07	**Na**2O	0.345	1.07	0.35	2.13	-1.78
Mg	0.43	**Mg**O	2.305	0.43	2.32	0.86	1.46
Fe	3.32	**Fe**2O3	3.435	3.32	3.46	6.62	-3.16
Mn	0.07	**Mn**2O3	0	0.07	0.00	0.14	-0.14
K	0.83	**K**2O	1.06	1.66	1.07	3.32	-2.26
Al	0.03	**Al**2O3	4.73	0.03	4.76	0.06	4.70
Si	12.15	**Si**O2	20.41	12.15	20.56	24.27	-3.71
S	0.72	**S**O3	2.81	0.72	2.83	1.43	1.40
Ca	29.92	**Ca**O	64.195	29.92	64.65	59.76	4.89
Ti	0.37	**Ti**O2	0	0.37	0.00	0.75	-0.75
P	0.00	**P**2O5	0	0.00	0.00	0.01	-0.01
Cl	1.10	**Cl**	0	0.33	0.00	0.66	-0.66
SUM	50.00		99.11	51.42	100.00	100.00	0.00

A.9 Raw data from µ-XRF DM

Used to calculate the average values used in Table A - 28 are presented below. The numbers are obtained from the cement paste phase using Ca-Si phasing.

Table A - 29: Weight percentages of all elements in the paste phase of concrete core A.1.O.

A.1.I	**Ca-Si-phase**							
	Cl		**Ca**		**Fe**		**Si**	
	CPS	**wt-%**	**CPS**	**wt-%**	**CPS**	**wt-%**	**CPS**	**wt-%**
1	21.29	1.1	213.09	30.36	42.97	3.52	37.88	10.48
2	16.72	0.84	223.92	31.51	41.56	3.44	37.29	10.29
3	12.39	0.6	218.87	30.82	40.53	3.29	39.24	10.8
4	8.5	0.41	216.17	30.41	40.73	3.27	41.19	11.31
5	4.58	0.2	219.13	30.81	41.67	3.36	42	11.58
6	2.01	0.07	224.32	31.21	40.14	3.25	41.6	11.33
7	1.29	0.03	224.58	31.4	42.74	3.47	41.8	11.52
8	1.19	0.03	218.54	30.76	44.97	3.6	43.54	12.04
9	0.79	0.02	109.6	19.96	42.21	2.63	75.34	20.73
10	1.05	0.02	229.09	31.95	40.77	3.32	41.72	11.42
Avg			209.73	29.92	41.83	3.32	44.16	12.15
A.1.I	**Ca-Si-phase**							
	Al		**Na**		**Mg**		**K**	
	CPS	**wt-%**	**CPS**	**wt-%**	**CPS**	**wt-%**	**CPS**	**wt-%**
1	3.46	1.95	0.22	0.68	0.39	0.43	6.4	0.54
2	3.49	1.97	0.23	0.8	0.39	0.43	6.77	0.57
3	3.73	2.13	0.25	1.05	0.41	0.45	7.38	0.65
4	3.72	2.09	0.26	1.15	0.41	0.47	8.13	0.75
5	3.71	2.1	0.24	1.07	0.4	0.46	8.58	0.8
6	3.68	2.04	0.24	1.04	0.39	0.43	8.58	0.79
7	3.76	2.1	0.23	1.03	0.41	0.47	8.78	0.83
8	4.05	2.3	0.24	1.05	0.4	0.46	9.32	0.9
9	6.37	3.3	0.33	1.74	0.36	0.25	12.71	1.66
10	3.62	2.15	0.24	1.04	0.42	0.48	8.95	0.83
Avg	3.96	2.21	0.25	1.07	0.40	0.43	8.56	0.83
A.1.I	**Ca-Si-phase**							
	S		**Mn**		**Ti**		**P**	
	CPS	**wt-%**	**CPS**	**wt-%**	**CPS**	**wt-%**	**CPS**	**wt-%**
1	8.85	0.9	1.04	0.07	1.91	0.38	0.46	0
2	7.91	0.79	1.02	0.07	1.91	0.38	0.59	0.01
3	7.63	0.78	1	0.07	1.68	0.33	0.53	0
4	7.52	0.8	1.01	0.07	1.72	0.34	0.57	0.01
5	6.7	0.73	1.04	0.07	2.46	0.49	0.51	0
6	6.35	0.7	1.01	0.07	1.75	0.34	0.48	0
7	6.21	0.69	1.06	0.07	2.08	0.41	0.5	0
8	5.76	0.66	1.07	0.07	1.76	0.34	0.42	0
9	3	0.42	1.13	0.05	2.05	0.32	0.35	0
10	6.14	0.68	1.02	0.07	2.03	0.4	0.6	0.02
Avg	6.61	0.72	1.04	0.07	1.94	0.37	0.50	0.00

A.10 Cement used in the Concrete Structures

Norcem gave us the oxide overview of the P30 and HS65 they used in 1994. This was said to be almost identical to the one used for the last part of the 1980's. As P30-4A is three parts P30 and one part HS65, the oxide composition was calculated using this formula:

$$m_{oxide.P30-4A} = \frac{3}{4} m_{oxide.P30} + \frac{1}{4} m_{oxide.HS65}$$

Where

$$m_{oxide.P30-4A} = mass\ percentage\ of\ oxide\ in\ P30-4A\ [g/g]$$

$$m_{oxide.P30} = mass\ percentage\ of\ oxide\ in\ P30\ [g/g]$$

$$m_{oxide.HS65} = mass\ percentage\ of\ oxide\ in\ HS65\ [g/g]$$

The raw data provided by Norcem is presented below.

KJEMISKE NØKKELTALL

Måned : Mai / 94

TYPE:		P30		MP30		RP30		Type: SR		Type: HS65	
SEMENTMALING:		Per.	1993	Per.	1993	Per.	1993	Per.	1993	Per.	1993
Glødetap	x %	2,42	0,96	1,58	1,36	2,63	1,97	0,79	0,49	1,21	1,07
	max.	2,61	2,06	1,64	1,60	2,73	2,27	0,82	0,62	1,27	1,28
	min.	2,15	0,59	1,51	1,20	2,52	1,60	0,76	0,35	1,11	0,86
	Sx	0,21	0,33	-	0,11	-	0,19	-	0,06	-	0,11
SiO2	x %	20,16	20,66			19,64	20,03	21,79	21,66	21,69	21,87
	max.	20,63	21,14			19,68	20,53	21,81	22,00	21,82	22,29
	min.	19,70	19,99			19,59	19,52	21,77	21,19	21,56	21,38
	Sx	0,37	0,27			-	0,28	-	0,24	-	0,23
Al2O3	x %	4,68	4,78			4,94	4,81	3,61	3,57	4,10	4,10
	max.	4,76	5,03			4,94	5,03	3,62	3,72	4,12	4,31
	min.	4,57	4,62			4,93	4,65	3,59	3,45	4,09	4,00
	Sx	0,07	0,09			-	0,11	-	0,08	-	0,08
Fe2O3	x %	3,44	3,53			3,51	3,49	4,79	4,92	3,31	3,36
	max.	3,48	3,62			3,54	3,52	4,85	5,14	3,32	3,72
	min.	3,36	3,45			3,47	3,32	4,72	4,77	3,29	3,27
	Sx	0,05	0,05			-	0,08	-	0,13	-	0,08
CaO	x %	63,10	63,31			62,22	62,76	64,51	64,69	64,40	64,40
	max.	63,48	64,29			62,67	63,81	64,61	65,38	64,51	65,05
	min.	62,65	62,49			61,77	62,11	64,40	63,88	64,30	63,16
	Sx	0,33	0,43			-	0,39	-	0,39	-	0,45
MgO	x %	2,42	2,19			2,53	2,31	1,44	1,51	1,58	1,39
	max.	2,64	2,47			2,56	2,69	1,48	1,70	1,67	1,69
	min.	2,14	1,96			2,50	2,07	1,40	1,27	1,49	1,19
	Sx	0,20	0,12			-	0,15	-	0,17	-	0,18
SO3	x %	2,81	2,81	2,65	2,66	3,11	3,06	2,40	2,20	3,18	3,01
	max.	2,85	3,02	2,79	2,87	3,13	3,40	2,45	2,30	3,19	3,24
	min.	2,75	2,43	2,51	2,49	3,08	2,55	2,35	2,05	3,16	2,69
	Sx	0,04	0,14	-	0,10	-	0,18	-	0,09	-	0,15
Uopl.rest x%						0,45	0,39	0,18	0,20	-	-
	max.					-	0,56	0,24	0,36	-	-
	min.					-	0,15	0,12	0,12	-	-
	Sx					-	0,12	-	0,07	-	-

Figure A - 1: Chemical composition of cements P30 and HS65 from 1994, provided by Norcem.

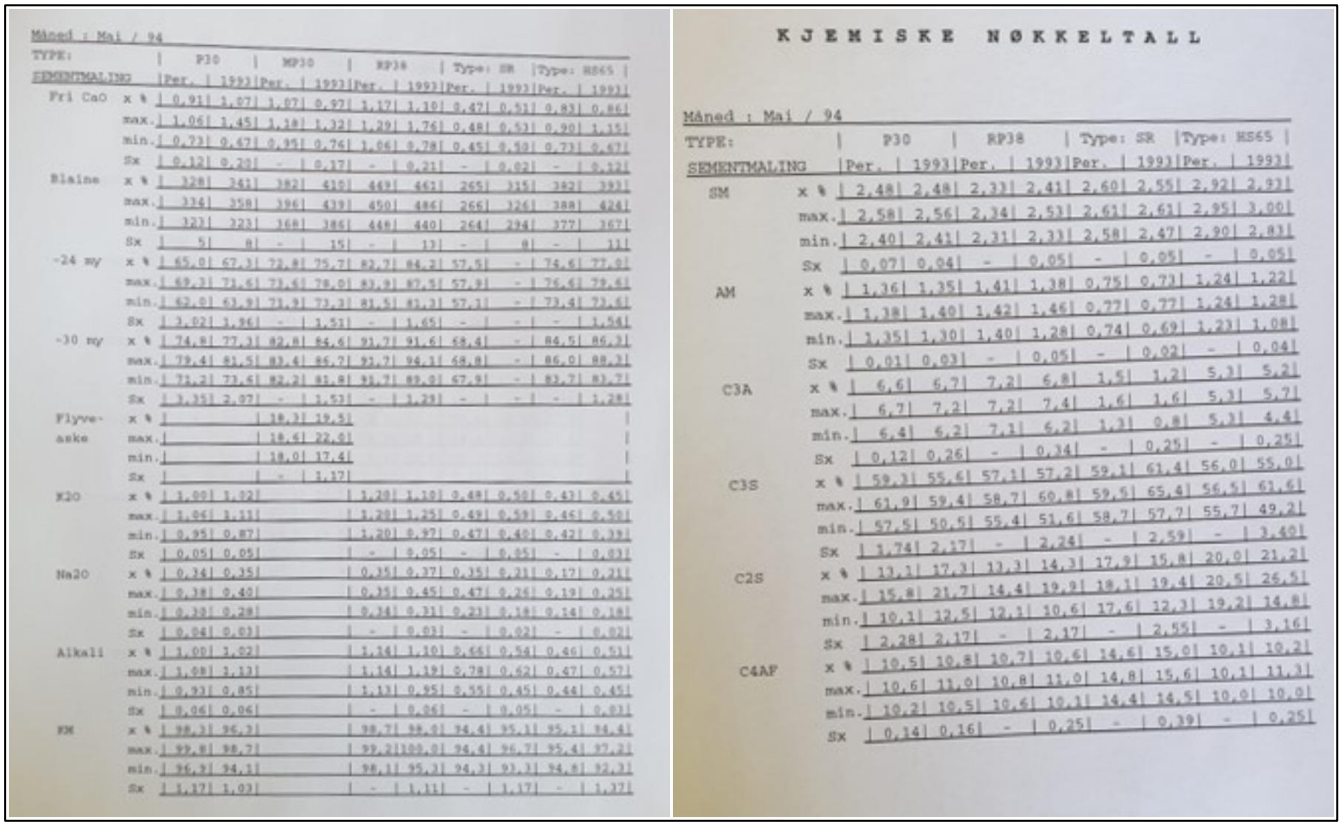

Måned : Mai / 94

TYPE:		P30		MP30		RP38		Type: SR		Type: HS65	
SEMENTMALING		Per.	1993	Per.	1993	Per.	1993	Per.	1993	Per.	1993
Fri CaO	x %	0,91	1,07	1,07	0,97	1,17	1,10	0,47	0,51	0,83	0,86
	max.	1,06	1,45	1,38	1,32	1,29	1,76	0,48	0,53	0,90	1,15
	min.	0,73	0,47	0,95	0,76	1,06	0,78	0,45	0,50	0,73	0,67
	Sx	0,12	0,20	-	0,17	-	0,21	-	0,02	-	0,12
Blaine	x %	328	341	382	410	449	461	265	315	392	393
	max.	334	358	396	439	450	486	266	326	388	424
	min.	323	323	368	386	448	440	264	294	377	367
	Sx	5	8	-	15	-	13	-	8	-	11
-24 my	x %	65,0	67,3	72,8	75,7	82,7	84,2	57,5	-	74,6	77,0
	max.	69,3	71,6	73,6	78,0	83,9	87,5	57,9	-	76,6	79,6
	min.	62,0	63,9	71,9	73,2	81,5	81,3	57,1	-	73,4	73,6
	Sx	3,02	1,96	-	1,53	-	1,65	-	-	-	1,56
-30 my	x %	74,8	77,3	82,8	84,6	91,7	91,6	68,4	-	86,5	86,3
	max.	79,4	81,5	83,4	86,7	93,7	94,3	68,8	-	86,0	88,2
	min.	71,2	73,6	82,2	81,8	91,7	89,0	67,9	-	83,7	83,7
	Sx	3,35	2,07	-	1,53	-	1,29	-	-	-	1,28
Flyve-aske	x %			18,3	19,5						
	max.			18,4	22,0						
	min.			18,0	17,4						
	Sx			-	1,17						
K2O	x %	1,00	1,02			1,20	1,10	0,48	0,50	0,43	0,45
	max.	1,06	1,11			1,28	1,25	0,48	0,59	0,46	0,50
	min.	0,95	0,87			1,20	0,97	0,47	0,40	0,42	0,39
	Sx	0,05	0,05			-	0,05	-	0,05	-	0,03
Na2O	x %	0,36	0,35			0,35	0,37	0,35	0,21	0,17	0,21
	max.	0,38	0,40			0,35	0,45	0,47	0,26	0,19	0,25
	min.	0,33	0,28			0,34	0,31	0,23	0,18	0,14	0,18
	Sx	0,04	0,03			-	0,03	-	0,02	-	0,02
Alkali	x %	1,00	1,02			1,14	1,10	0,66	0,54	0,46	0,51
	max.	1,08	1,13			1,14	1,19	0,78	0,62	0,47	0,57
	min.	0,93	0,85			1,13	0,95	0,55	0,45	0,44	0,45
	Sx	0,06	0,06			-	0,06	-	0,05	-	0,03
KK	x %	98,3	96,3			98,7	98,0	94,4	95,3	95,1	94,4
	max.	99,8	98,7			99,2	100,0	96,4	96,7	95,4	97,2
	min.	96,3	94,1			98,1	95,3	94,3	93,3	94,8	92,3
	Sx	1,17	1,03			-	1,11	-	1,17	-	1,17

KJEMISKE NØKKELTALL

Måned : Mai / 94

TYPE:		P30		RP38		Type: SR		Type: HS65	
SEMENTMALING		Per.	1993	Per.	1993	Per.	1993	Per.	1993
SM	x %	2,48	2,48	2,33	2,41	2,60	2,55	2,92	2,93
	max.	2,58	2,56	2,34	2,53	2,61	2,63	2,95	3,00
	min.	2,40	2,41	2,31	2,33	2,58	2,47	2,90	2,83
	Sx	0,07	0,04	-	0,05	-	0,05	-	0,05
AM	x %	1,36	1,35	1,41	1,38	0,75	0,77	1,24	1,22
	max.	1,38	1,40	1,42	1,46	0,77	0,77	1,24	1,28
	min.	1,35	1,30	1,40	1,28	0,74	0,69	1,23	1,08
	Sx	0,01	0,03	-	0,05	-	0,02	-	0,04
C3A	x %	6,6	6,7	7,2	6,8	1,5	1,2	5,3	5,2
	max.	6,7	7,2	7,2	7,4	1,6	1,6	5,3	5,7
	min.	6,4	6,2	7,1	6,2	1,3	0,8	5,3	4,4
	Sx	0,12	0,26	-	0,34	-	0,25	-	0,25
C3S	x %	59,3	55,6	57,1	57,2	59,1	61,4	56,0	55,0
	max.	61,9	59,4	58,7	60,8	59,5	65,4	56,5	61,6
	min.	57,5	50,5	55,4	51,6	58,7	57,7	55,7	49,2
	Sx	1,74	2,17	-	2,24	-	2,59	-	3,40
C2S	x %	13,1	17,3	13,3	14,3	17,9	15,8	20,0	21,2
	max.	15,8	21,7	14,4	19,9	18,1	19,4	20,5	26,5
	min.	10,1	12,5	12,1	10,6	17,6	12,3	19,2	14,8
	Sx	2,28	2,17	-	2,17	-	2,55	-	3,16
C4AF	x %	10,5	10,8	10,7	10,6	14,6	15,0	10,1	10,2
	max.	10,6	11,0	10,8	11,0	14,8	15,6	10,1	11,1
	min.	10,2	10,5	10,6	10,1	14,4	14,5	10,0	10,0
	Sx	0,14	0,16	-	0,25	-	0,39	-	0,25

Figure A - 2: More chemical information of cements P30 and HS65 from 1994, provided by Norcem.

A.11 Cement used in the Reference Samples

The overview of the chemical composition of the cement used in the reference samples, provided by Norcem, is presented below:

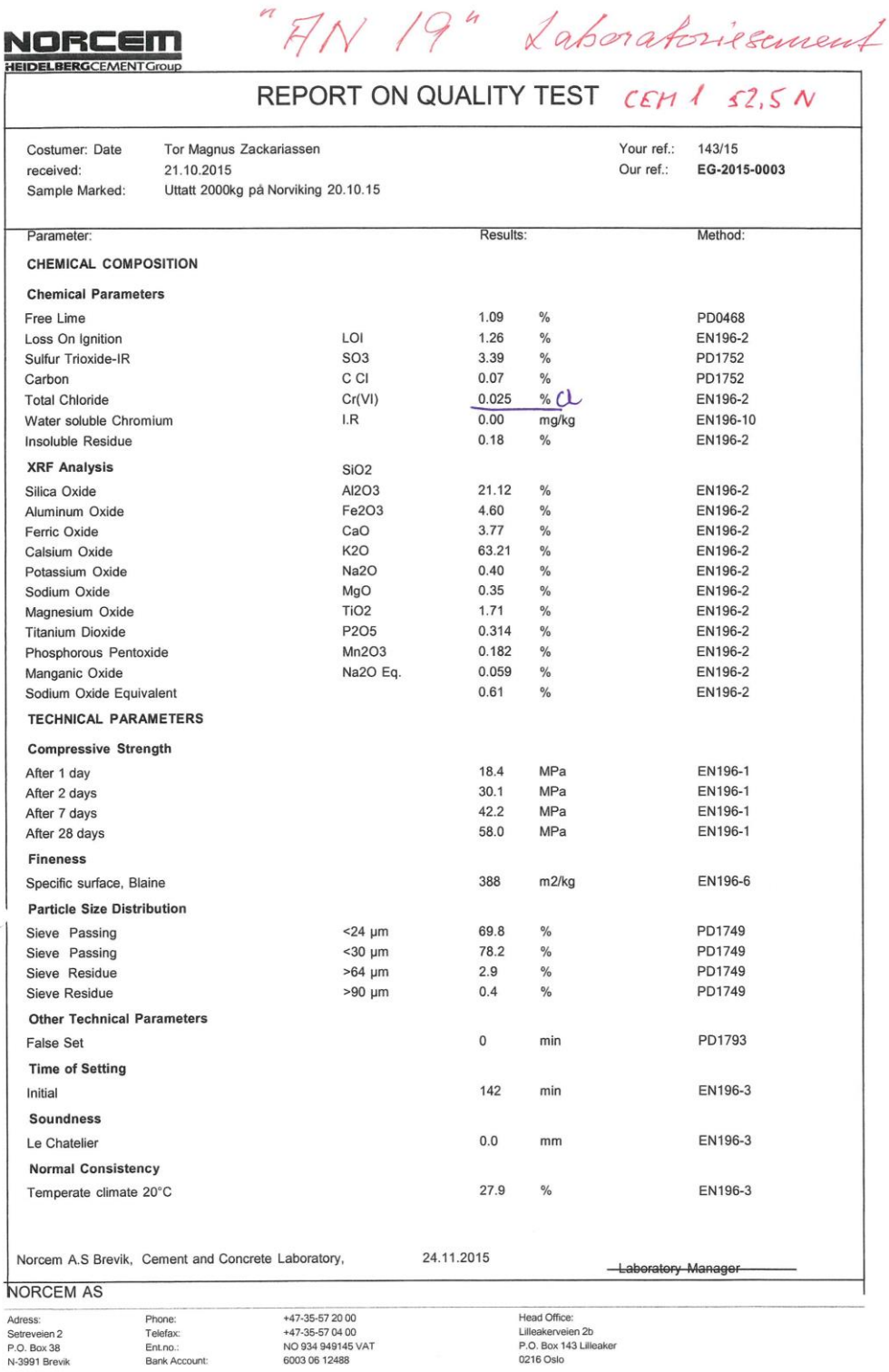

NORCEM
HEIDELBERGCEMENT Group

"FN 19" Laboratoriesement

REPORT ON QUALITY TEST CEM I 52,5 N

Costumer: Date received:	Tor Magnus Zackariassen 21.10.2015	Your ref.:	143/15
Sample Marked:	Uttatt 2000kg på Norviking 20.10.15	Our ref.:	**EG-2015-0003**

Parameter:		Results:		Method:
CHEMICAL COMPOSITION				
Chemical Parameters				
Free Lime		1.09	%	PD0468
Loss On Ignition	LOI	1.26	%	EN196-2
Sulfur Trioxide-IR	SO3	3.39	%	PD1752
Carbon	C CI	0.07	%	PD1752
Total Chloride	Cr(VI)	0.025	% Cl	EN196-2
Water soluble Chromium	I.R	0.00	mg/kg	EN196-10
Insoluble Residue		0.18	%	EN196-2
XRF Analysis	SiO2			
Silica Oxide	Al2O3	21.12	%	EN196-2
Aluminum Oxide	Fe2O3	4.60	%	EN196-2
Ferric Oxide	CaO	3.77	%	EN196-2
Calsium Oxide	K2O	63.21	%	EN196-2
Potassium Oxide	Na2O	0.40	%	EN196-2
Sodium Oxide	MgO	0.35	%	EN196-2
Magnesium Oxide	TiO2	1.71	%	EN196-2
Titanium Dioxide	P2O5	0.314	%	EN196-2
Phosphorous Pentoxide	Mn2O3	0.182	%	EN196-2
Manganic Oxide	Na2O Eq.	0.059	%	EN196-2
Sodium Oxide Equivalent		0.61	%	EN196-2
TECHNICAL PARAMETERS				
Compressive Strength				
After 1 day		18.4	MPa	EN196-1
After 2 days		30.1	MPa	EN196-1
After 7 days		42.2	MPa	EN196-1
After 28 days		58.0	MPa	EN196-1
Fineness				
Specific surface, Blaine		388	m2/kg	EN196-6
Particle Size Distribution				
Sieve Passing	<24 µm	69.8	%	PD1749
Sieve Passing	<30 µm	78.2	%	PD1749
Sieve Residue	>64 µm	2.9	%	PD1749
Sieve Residue	>90 µm	0.4	%	PD1749
Other Technical Parameters				
False Set		0	min	PD1793
Time of Setting				
Initial		142	min	EN196-3
Soundness				
Le Chatelier		0.0	mm	EN196-3
Normal Consistency				
Temperate climate 20°C		27.9	%	EN196-3

Norcem A.S Brevik, Cement and Concrete Laboratory, 24.11.2015 Laboratory Manager

NORCEM AS

Adress: Setreveien 2, P.O. Box 38, N-3991 Brevik
Phone: +47-35-57 20 00; Telefax: +47-35-57 04 00; Ent.no.: NO 934 949145 VAT; Bank Account: 6003 06 12488
Head Office: Lilleakerveien 2b, P.O. Box 143 Lilleaker, 0216 Oslo

Figure A - 3: Chemical composition of cement used for the reference samples.

A.12 Elemental µ-XRF Pictures

A.12.1 Core A.1.O

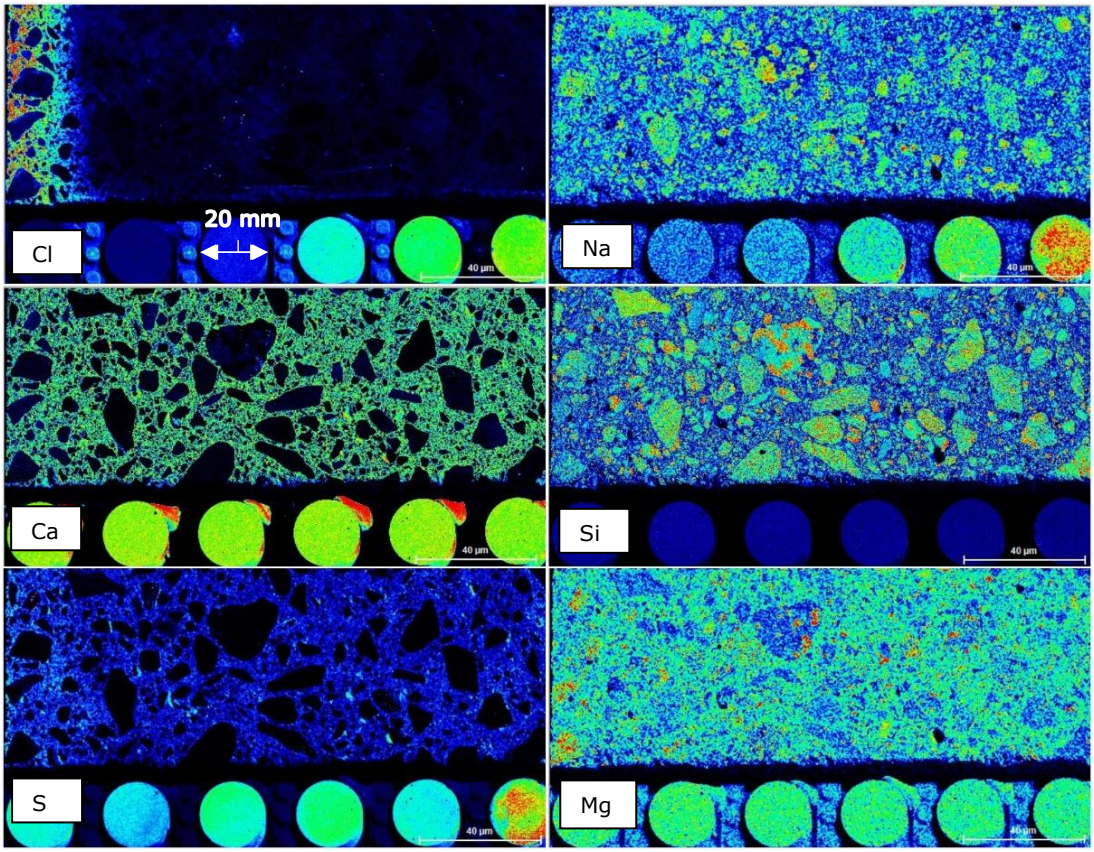

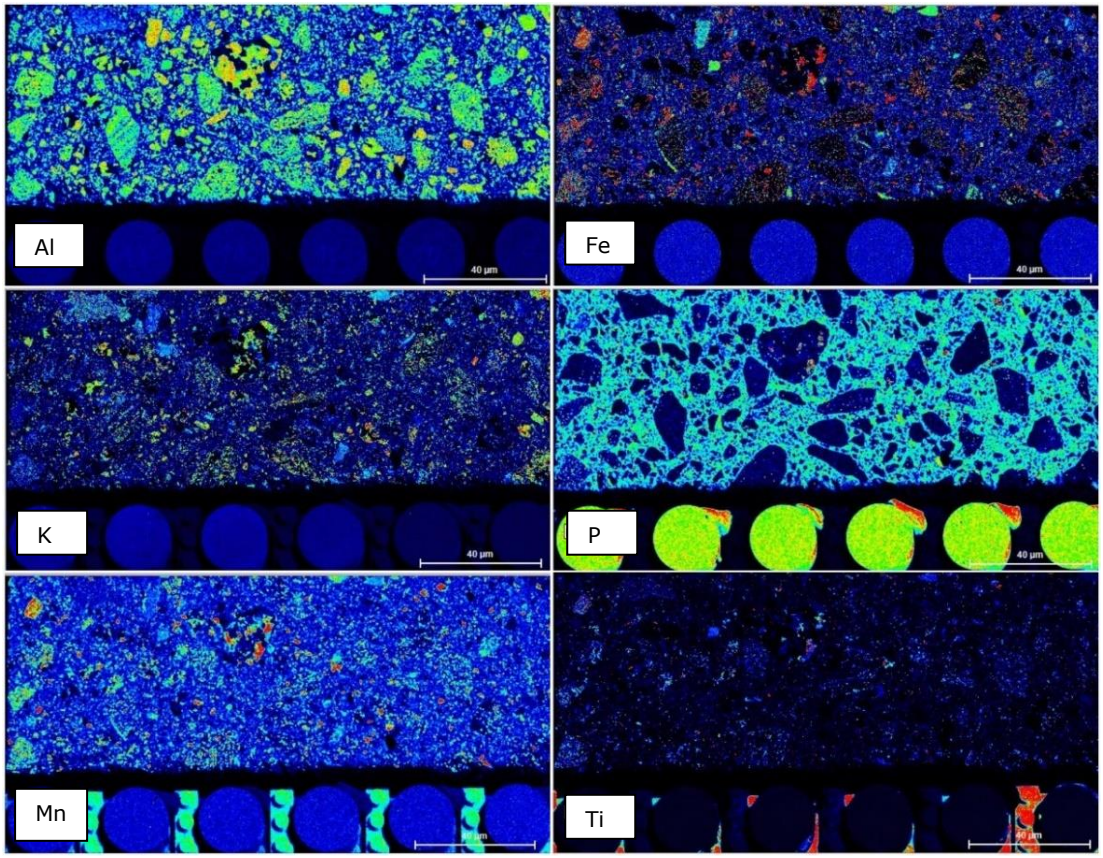

A.12.2 Core A.2.O

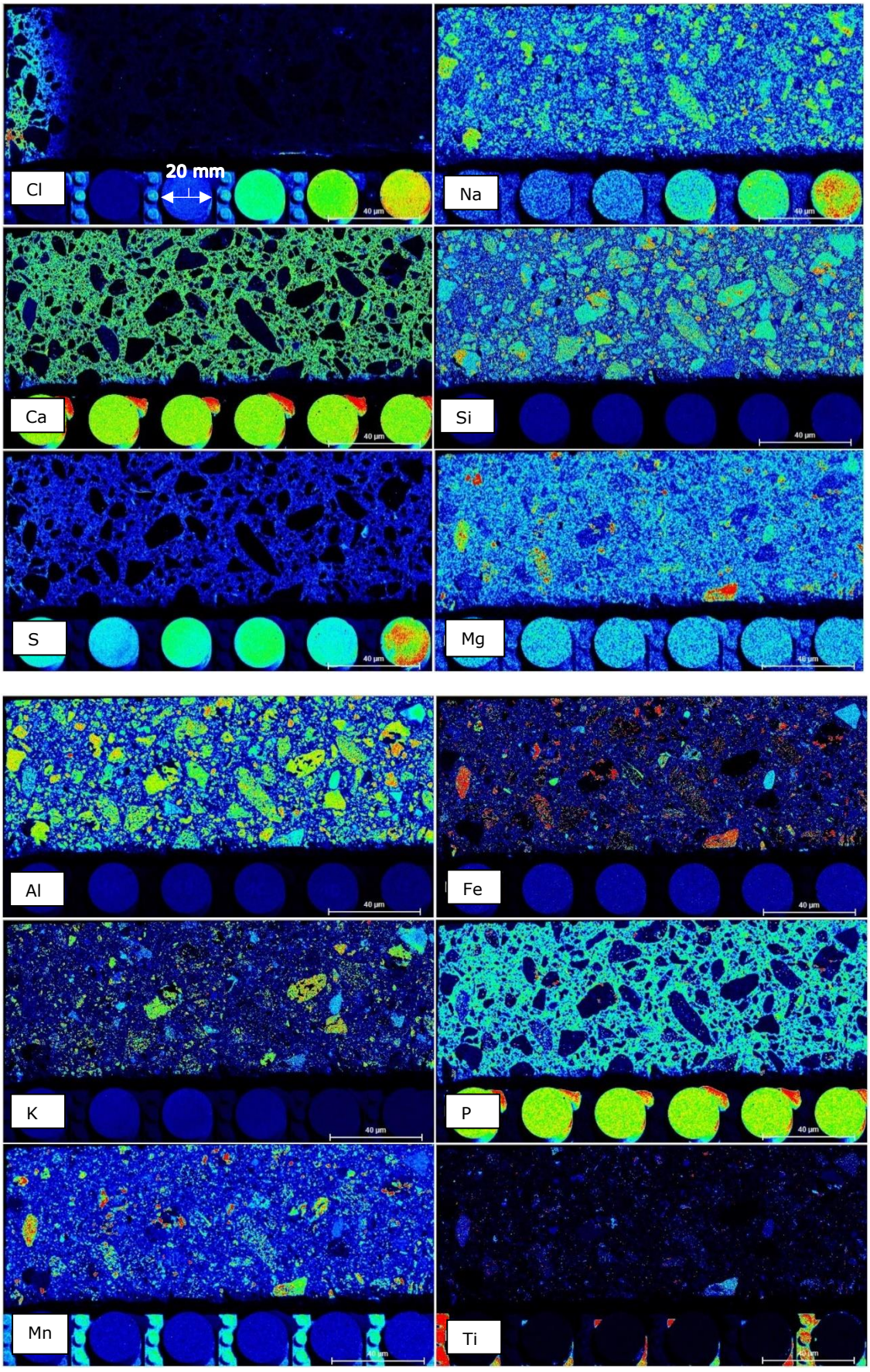

A.12.3 Core A.3.O

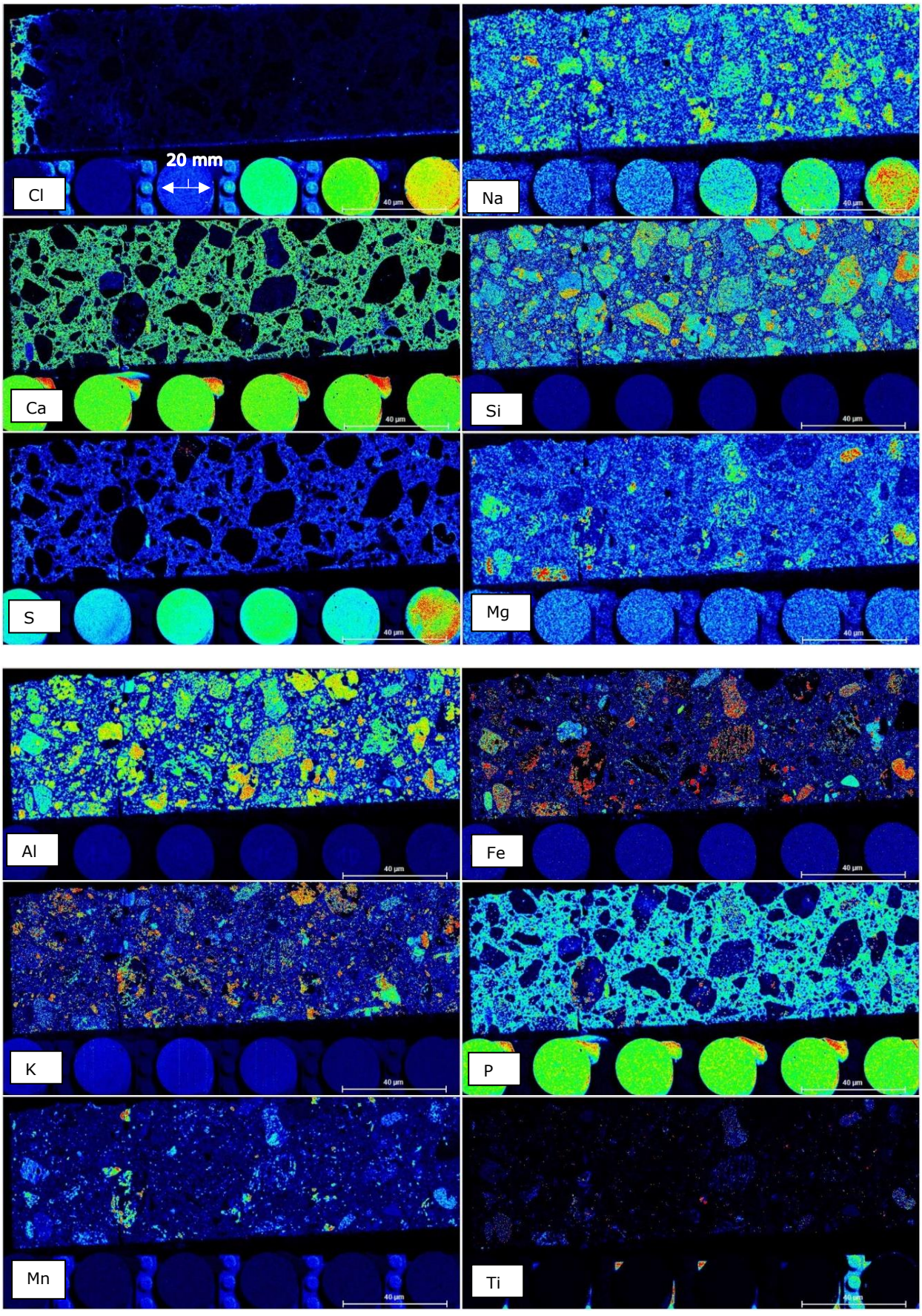

A.12.4 Core A.4.I

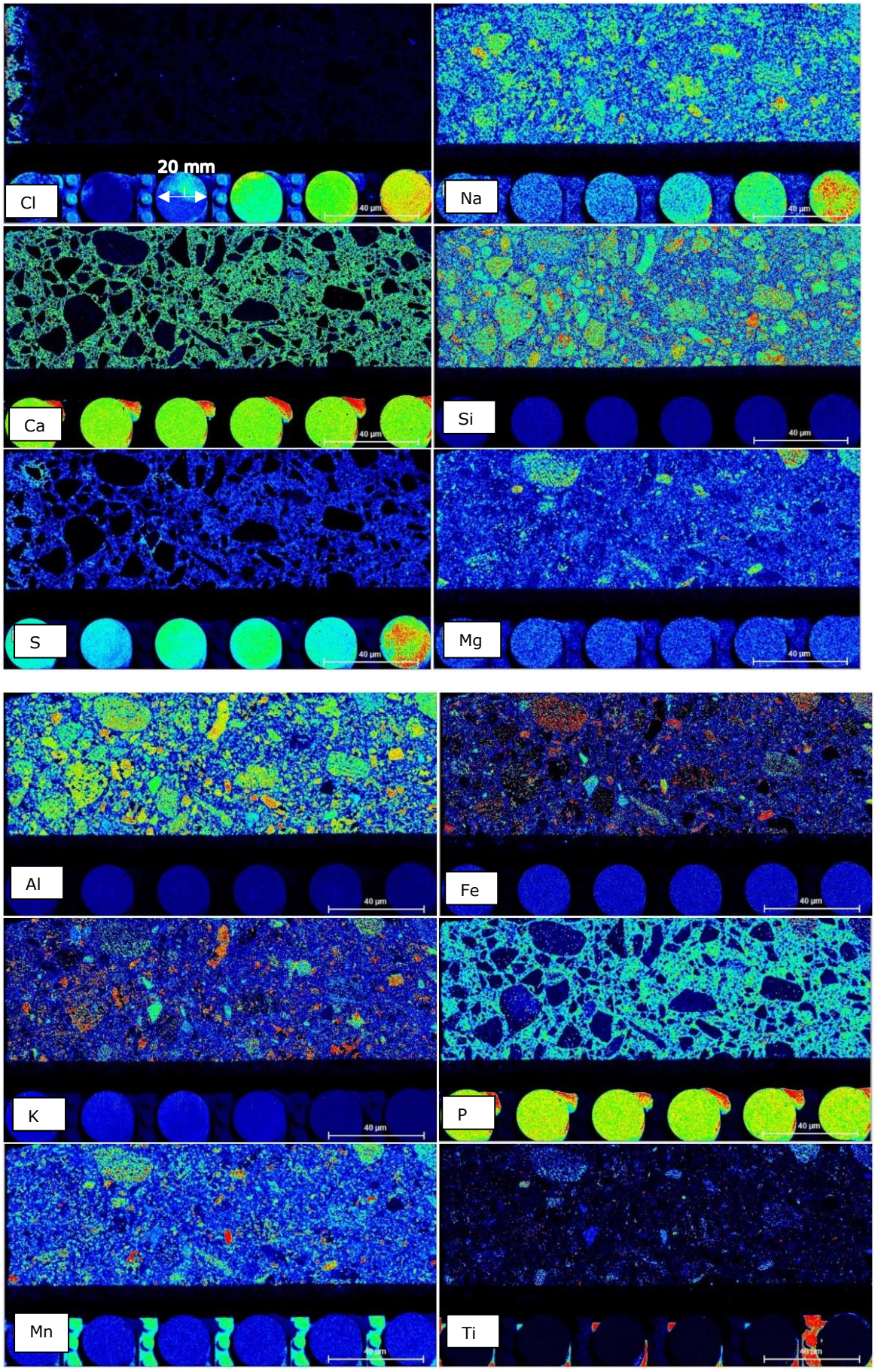

A.12.5 Core A.5.I

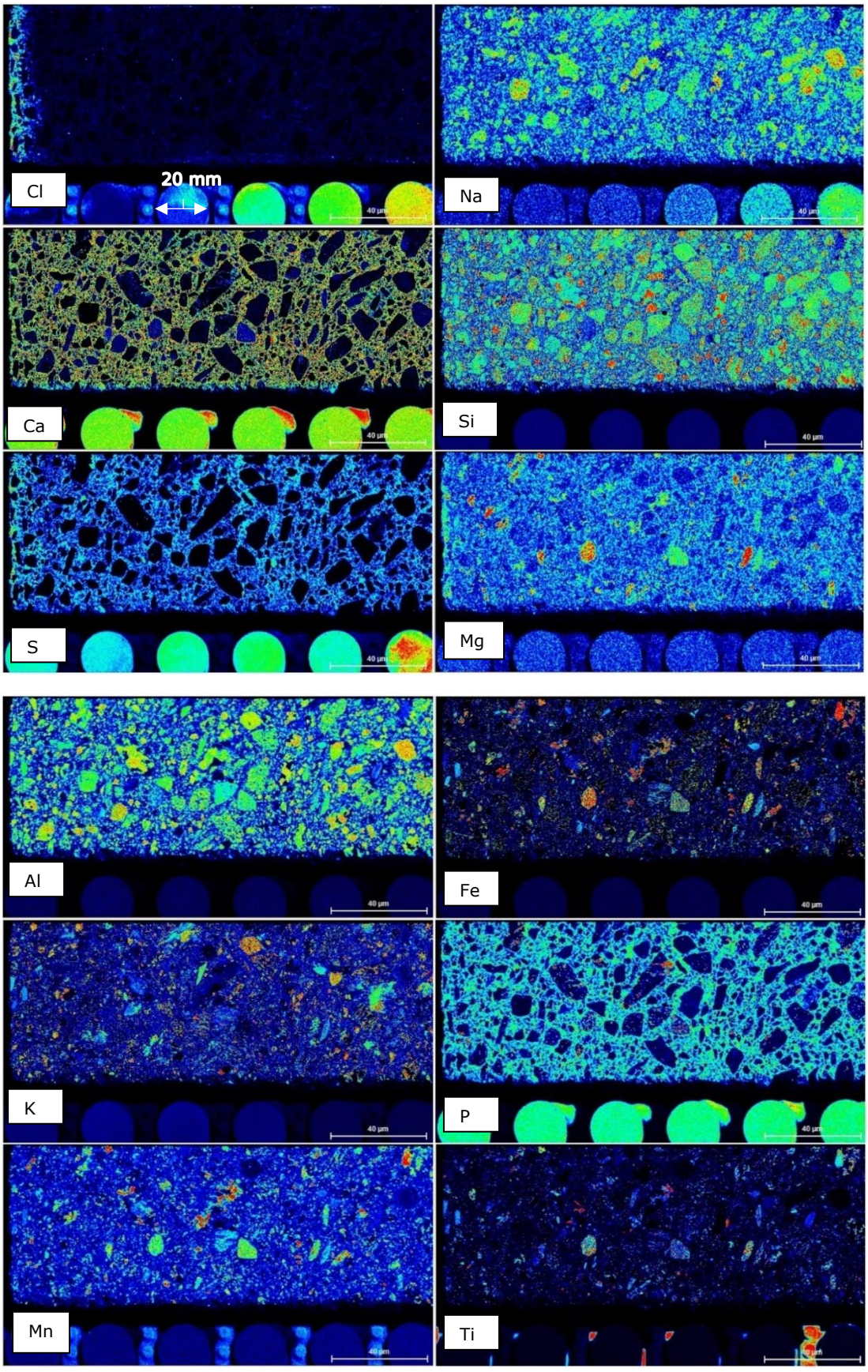

A.12.6 Core A.6.I

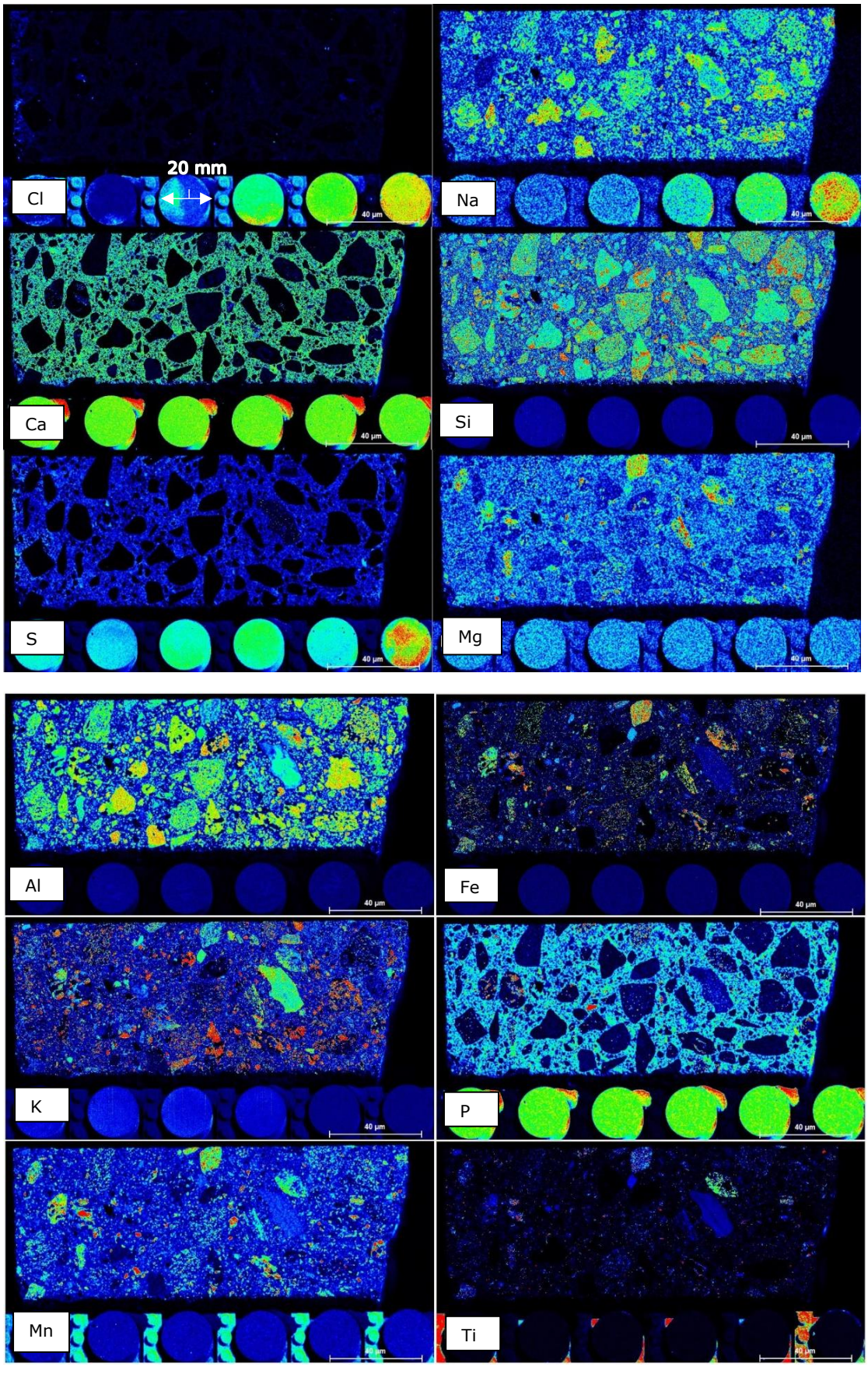

A.12.7 Core A.7.I

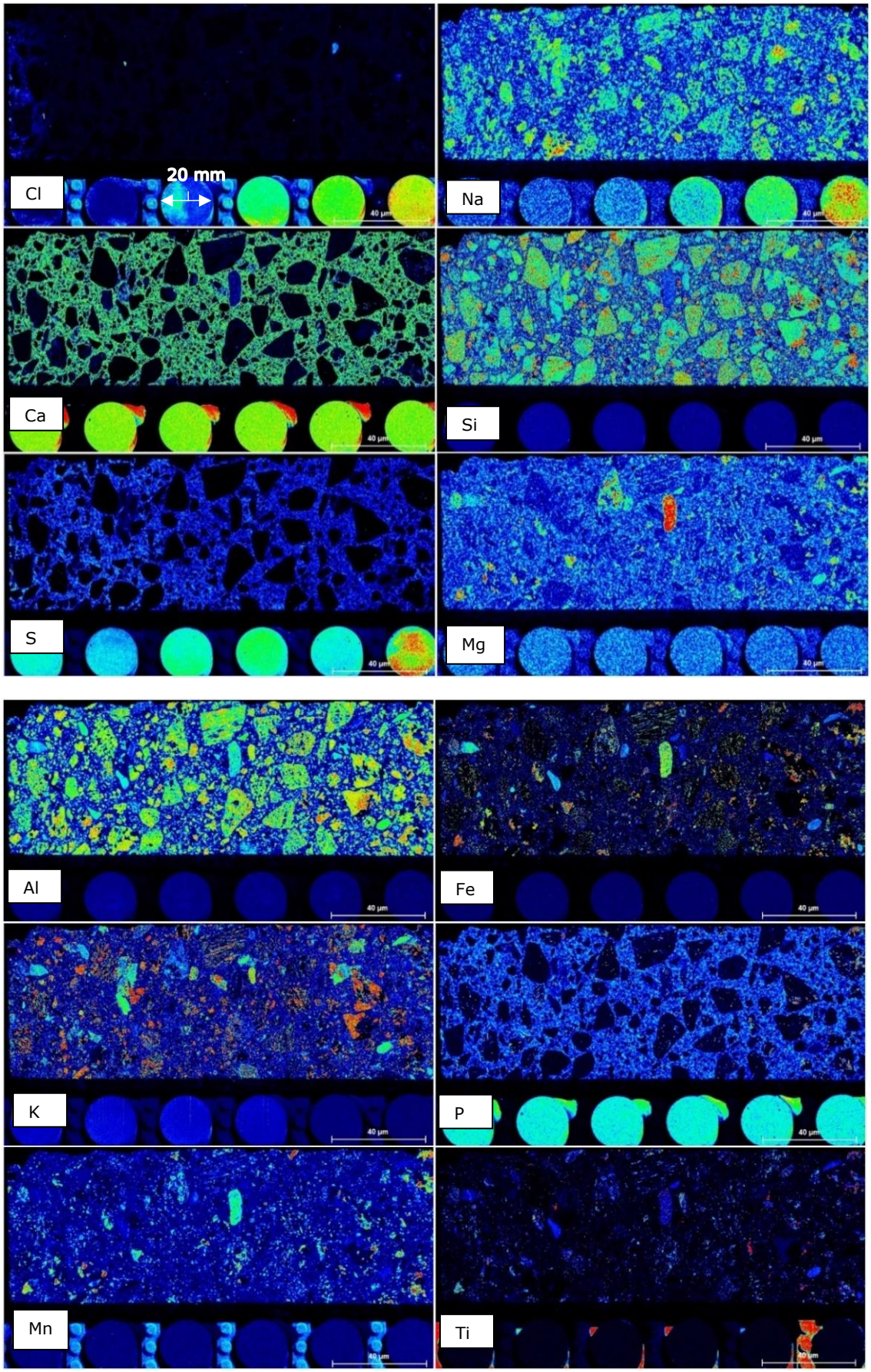

A.12.8 Core C.1.I

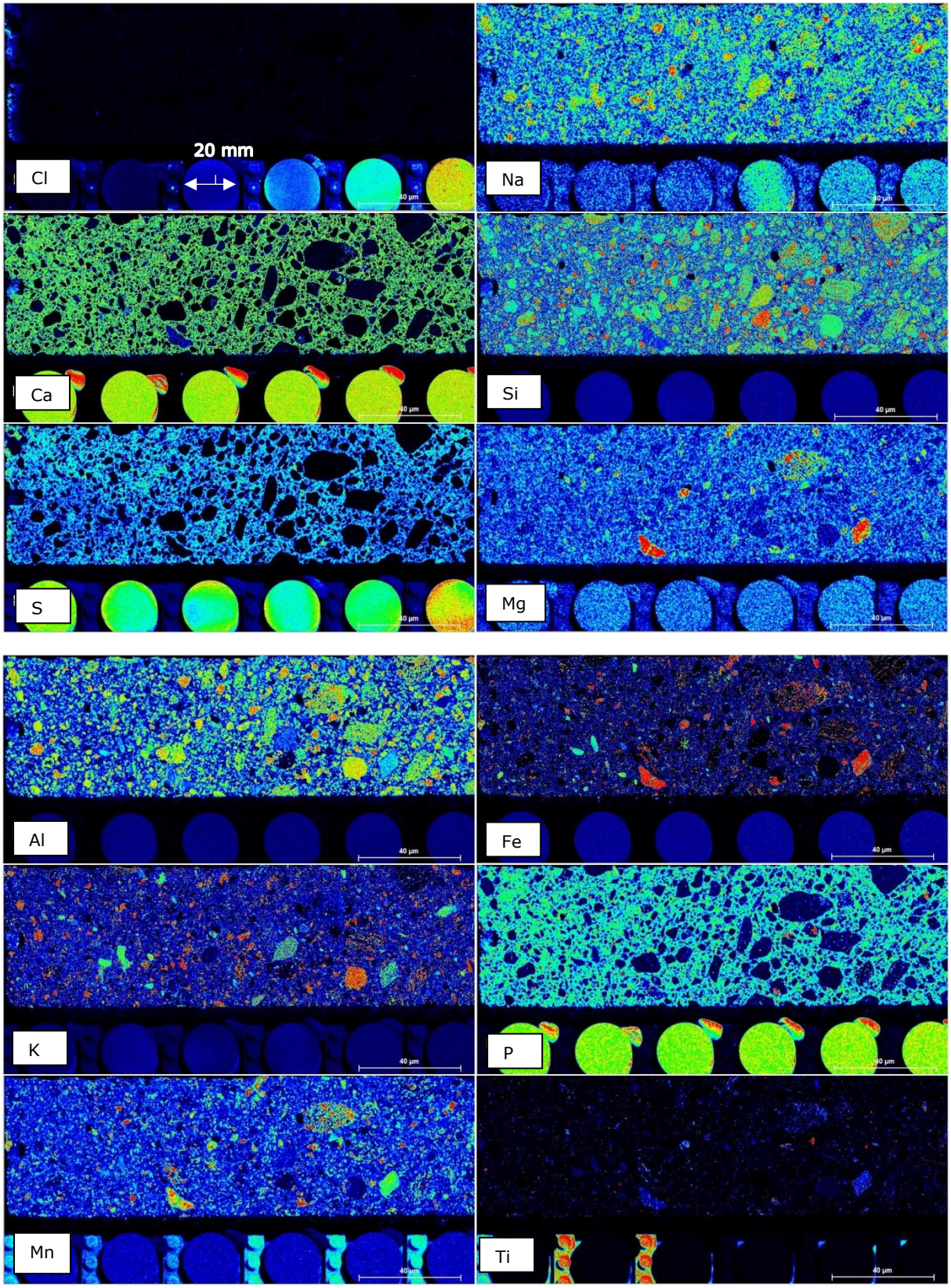

A.12.9 Core C.2.I

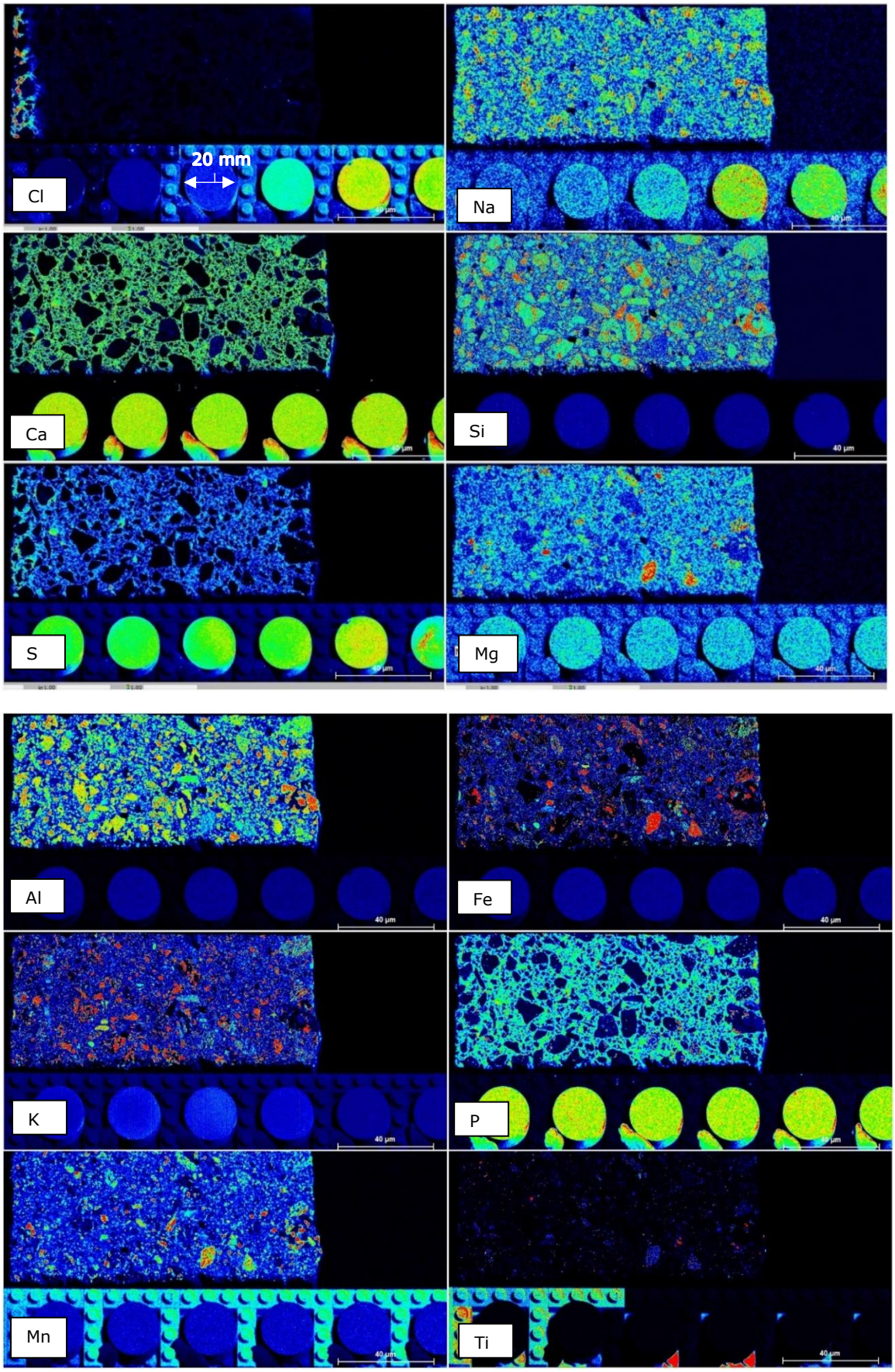

A.12.10 Core C.3.I

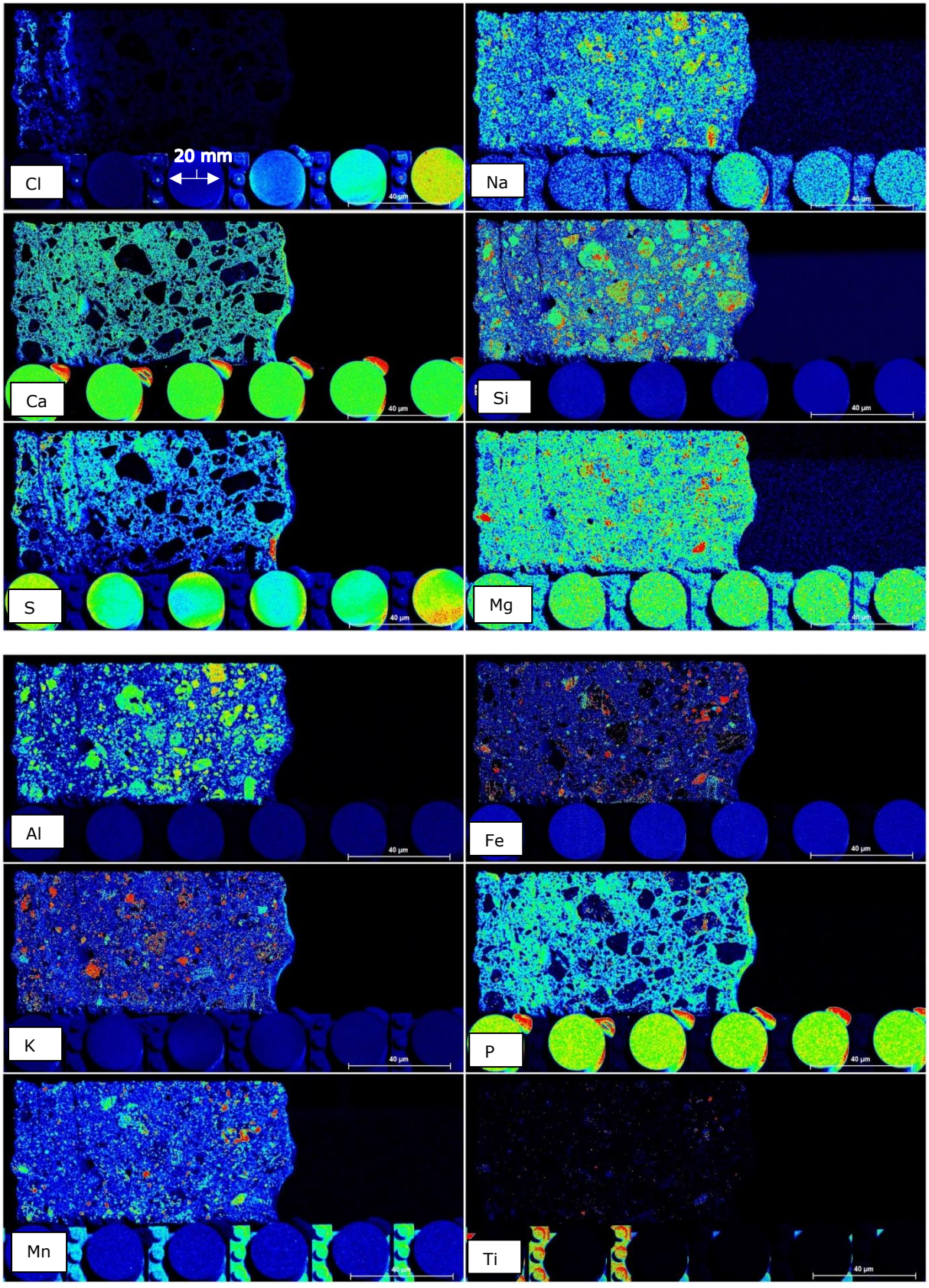

A.12.11 Core C.4.I

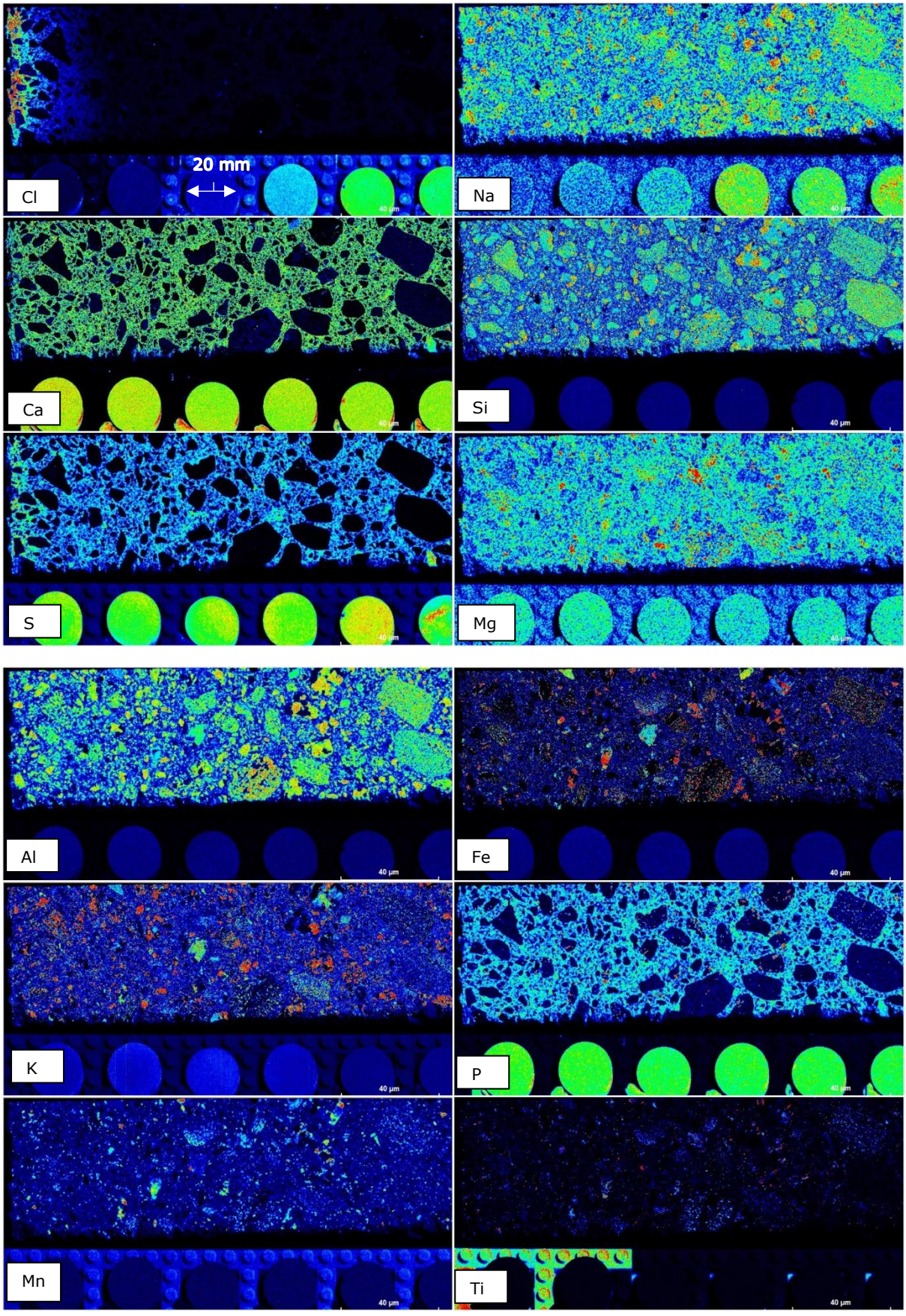

A.12.12 Core C.5.I

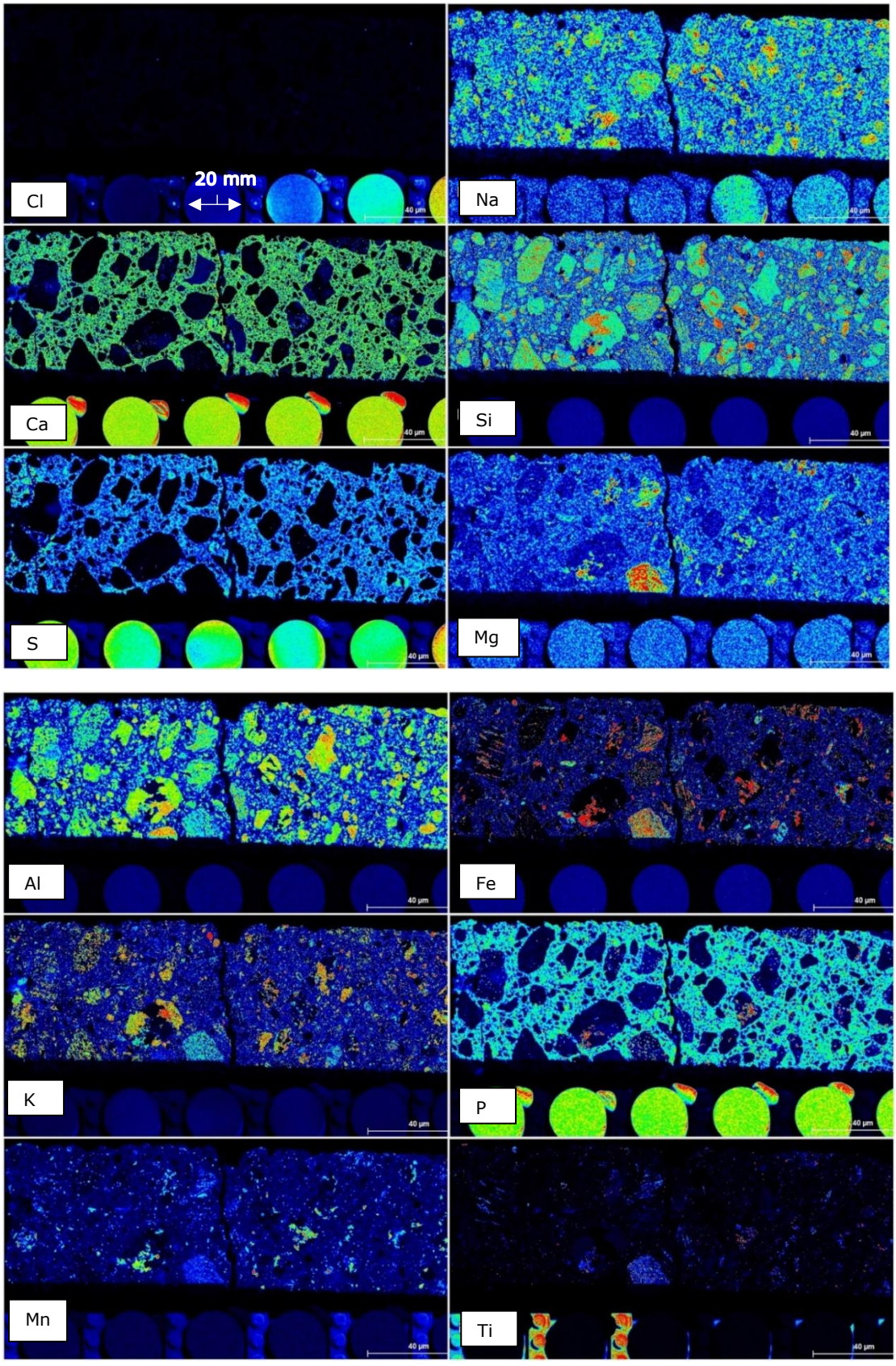

A.12.13 Core C.6.I

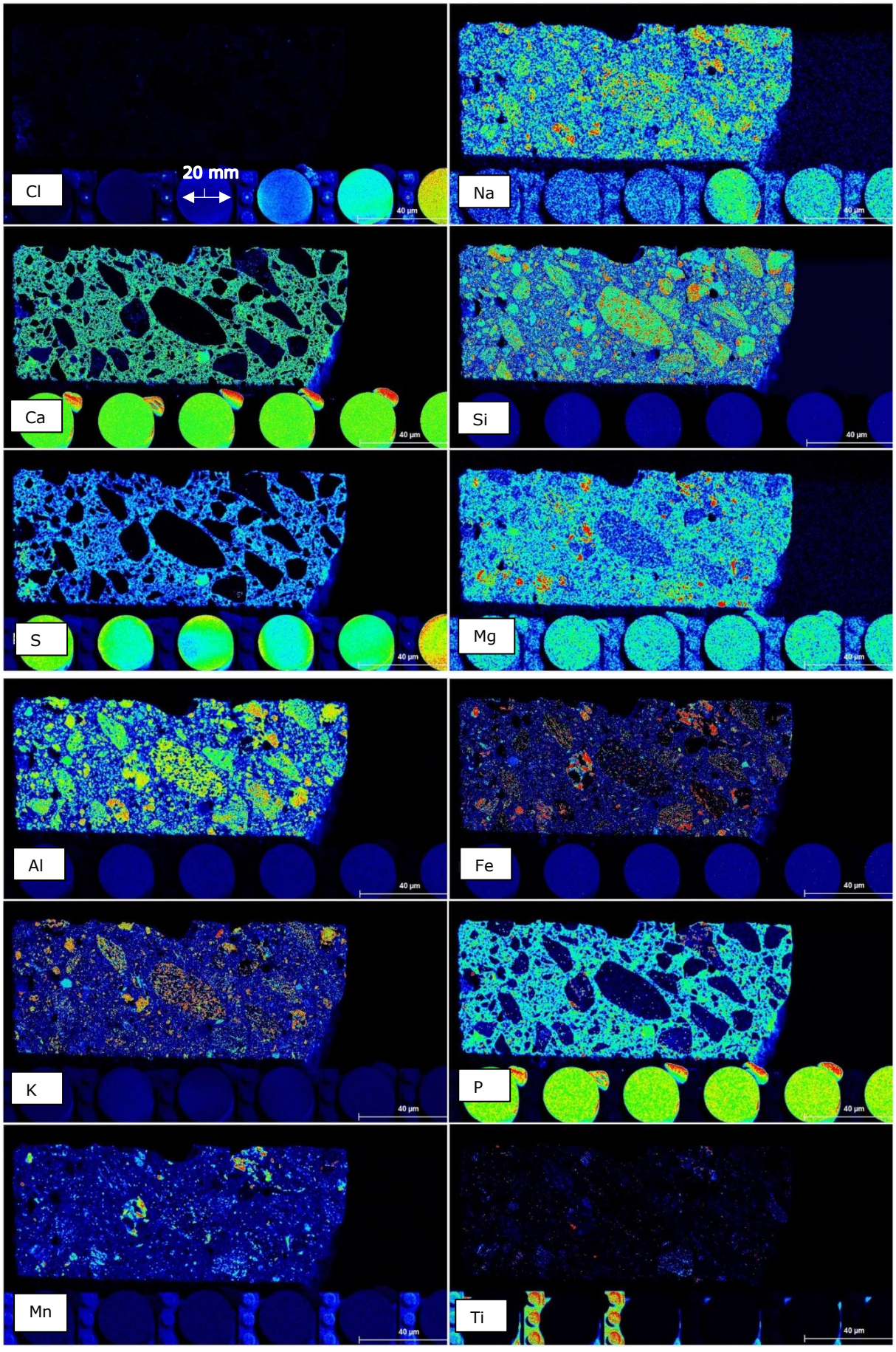

A.12.14 Core C.7.I

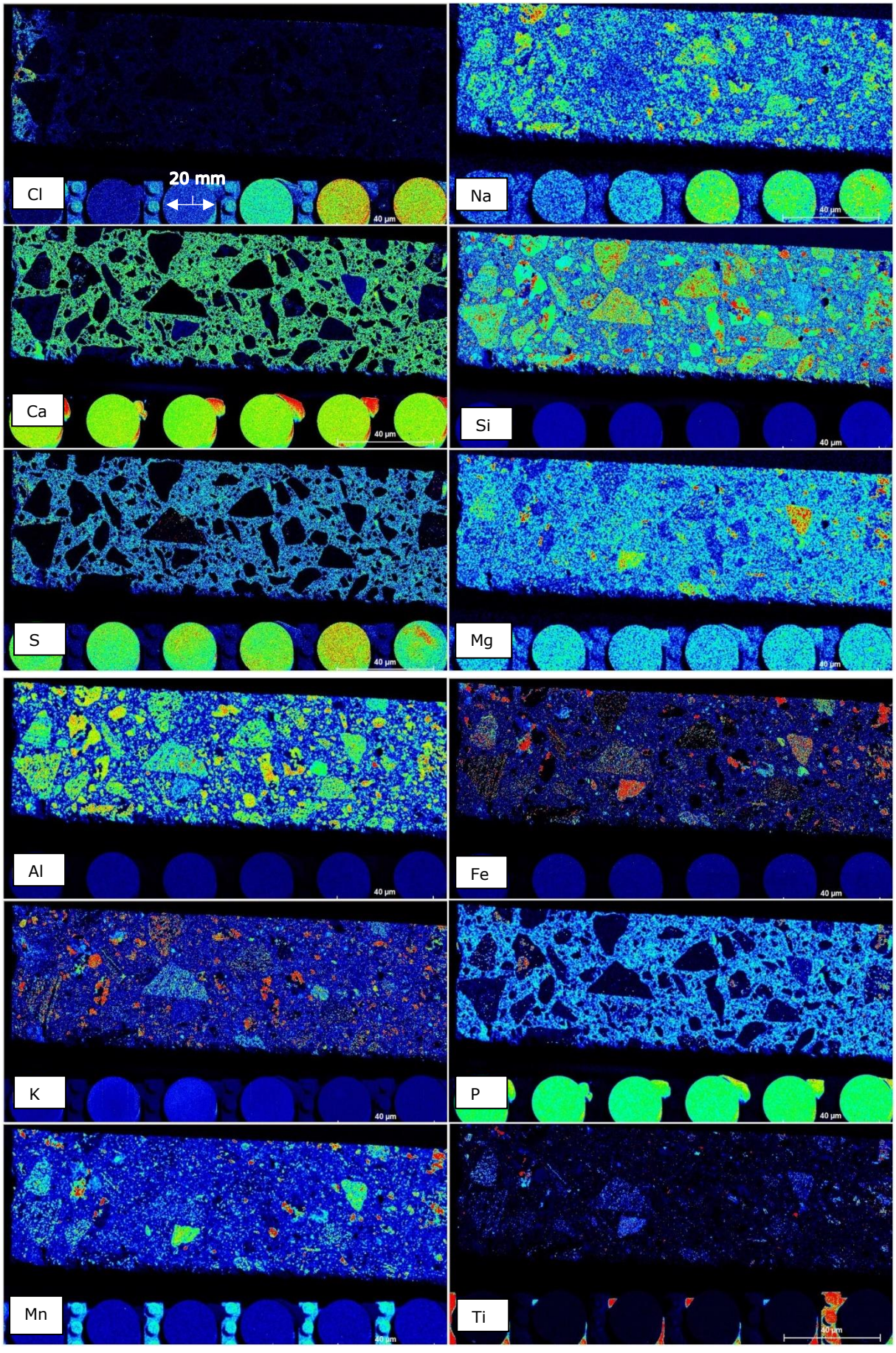

A.12.15 Core C.8.I

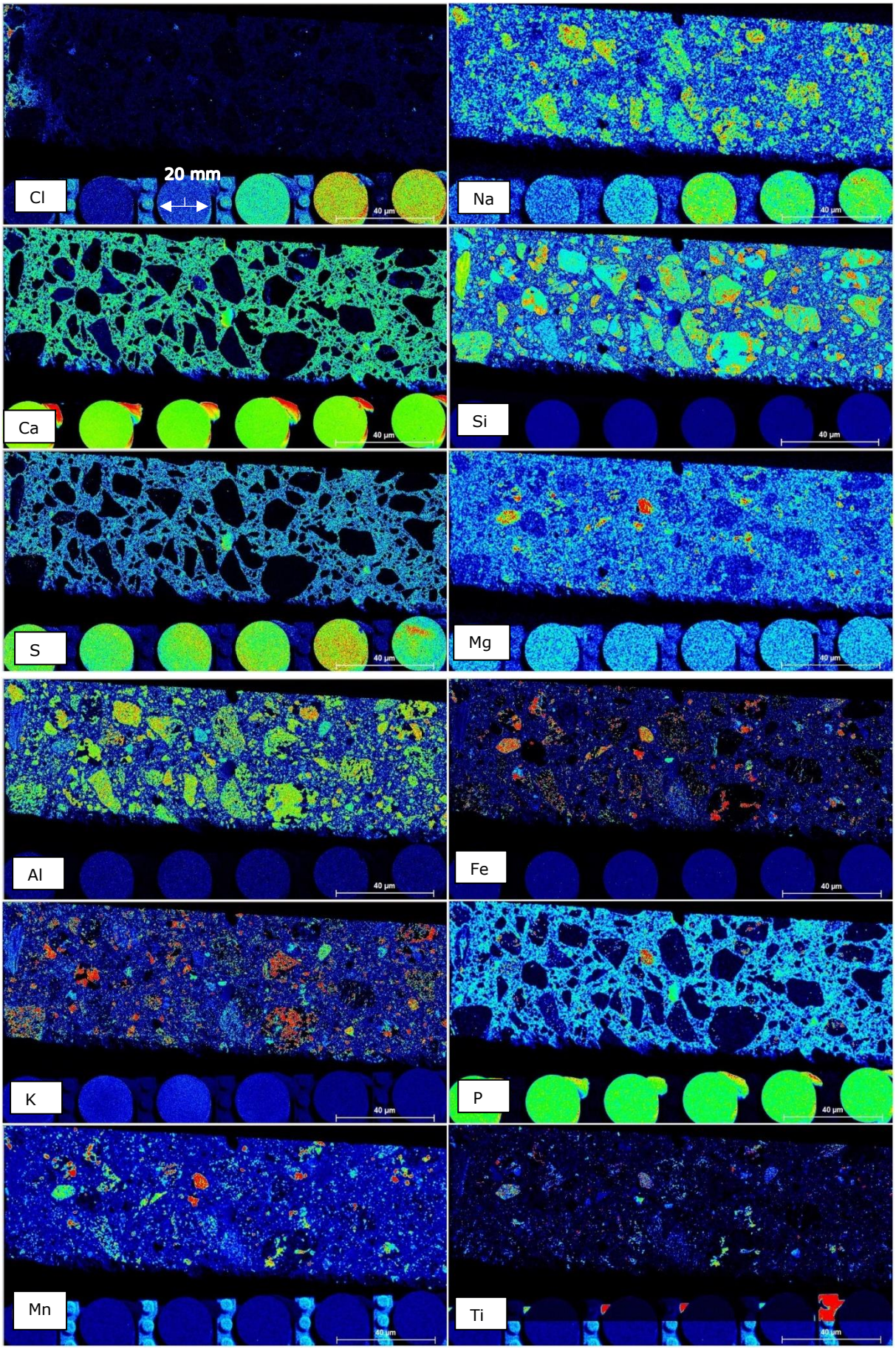

A.13 Propagation of uncertainty calculations

A.13.1 µ-XRF CM

The following equations were used to determine the uncertainty of the calibration curve:

$$\sigma_{Y.cali} = \sqrt{\frac{\sum(Y_i - Y'(x_i))^2}{N}} \quad \text{(A. 1)}$$

$$\sigma_{X.cali} = \frac{\sigma_{Y.cali} - b}{a} \quad \text{(A. 2)}$$

With

$$Y_i = y - value\ at\ point\ [CPS/eV]$$
$$N = Number\ of\ points$$
$$Y'(x_i) = Calibration\ curve = ax + b\ [CPS/eV]$$
$$x_i = The\ x - coordinate\ corrosponding\ to\ Y_i\ [g/g]$$

The following equations and tables were used to determine the uncertainty of the µ-XRF calculation.

$$\sigma_{\mu-XRF} = \frac{m_{Cl}}{m_{concrete}} * \sqrt{\left(\frac{\sigma_{m.p}}{m_{paste}}\right)^2 + \left(\frac{\sigma_{calibration}}{\frac{m_{Cl}}{m_{paste}}}\right)^2 + \left(\frac{{\sigma_{m.a}}^2 + {\sigma_{m.p}}^2}{(m_{aggregates} + m_{paste})^2}\right.} \quad \text{(A. 3)}$$

Table A - 30: Details relevant for (A. 3).

f	STD
$\frac{m_{Cl}}{m_{concrete}} = \frac{m_{Cl}}{m_{paste}} * \frac{m_{paste}}{m_{agg}+m_{paste}}$	$\sigma_{\mu.XRF}$
$m_{paste} = \rho_{paste} * V_{paste}$	$\sigma_{m.paste}$
$m_{agg} = \rho_{agg} * V_{agg}$	$\sigma_{m.a}$
$\frac{m_{Cl}}{m_{paste}}$ – from calibration curve	σ_{cali}

$$\sigma_{m.a} = m_{aggregates} * \sqrt{(\frac{\sigma_{\rho.a}}{\rho_{aggregates}})^2 + (\frac{\sigma_{V.a}}{V_{aggregates}})^2} \quad \text{(A. 4)}$$

Table A - 31: Details relevant for (A. 4).

f	STD
$\boldsymbol{m_{aggregates}=\rho_{aggregates} * V_{aggregates}}$	$\sigma_{m.a}$
$\boldsymbol{\rho_{aggregates}}$	$\sigma_{\rho.a}$
$\boldsymbol{V_{aggregates}}$	$\sigma_{V.a}$

$$\sigma_{m.p} = m_{paste} * \sqrt{(\frac{\sigma_{\rho.p}}{\rho_{paste}})^2 + (\frac{\sigma_{V.p}}{V_{paste}})^2} \quad \text{(A. 5)}$$

Table A - 32: Details relevant for (A. 5).

f	STD
$m_{paste}=\rho_{paste} * V_{paste}$	$\sigma_{m.p}$
$\rho_{paste} = \frac{\rho_{binder} * \rho_{water} * (\frac{w}{b} + 1)}{\rho_{binder} * \frac{w}{b} + \rho_{water}}$	$\sigma_{\rho.p}$
V_{paste}	$\sigma_{V.p}$

$$\sigma_{\rho.p} = f * \sqrt{\left(\frac{\sigma_x}{f_x}\right)^2 + \left(\frac{\sigma_y}{f_y}\right)^2} \quad \text{(A. 6)}$$

$$= \rho_{paste} * \sqrt{\left(\frac{\sigma_x}{(\rho_{binder} * \rho_{water}) + \left(\rho_{binder} * \rho_{water} * \frac{w}{b}\right)}\right)^2 + \left(\frac{\sigma_y}{\left(\rho_{binder} * \frac{w}{b}\right) + \rho_{water}}\right)^2}$$

Table A - 33: Details relevant for (A. 6).

f	STD
$f = \frac{f_x}{f_y} = \frac{f_C + f_B}{f_A + f_D} = \rho_{paste}$	$\sigma_{\rho.p}$
$f_x = f_C + f_B = (\rho_{binder} * \rho_{water}) + \left(\rho_{binder} * \rho_{water} * \frac{w}{b}\right)$	σ_x
$f_y = f_A + f_D = \left(\rho_{binder} * \frac{w}{b}\right) + \rho_{water}$	σ_y

$$\sigma_x = \sqrt{(\sigma_B)^2 + (\sigma_C)^2} \quad \text{(A. 7)}$$

Table A - 34: Details relevant for (A. 7).

f	STD
$f_x = f_B + f_C$	σ_x
$f_B = \rho_{binder} * \rho_{water}$	σ_B
$f_C = \rho_{binder} * \rho_{water} * \frac{w}{b}$	σ_C

$$\sigma_y = \sqrt{(\sigma_A)^2 + \left(\sigma_{\rho.w}\right)^2} \quad \text{(A. 8)}$$

Table A - 35: Details relevant for (A. 8).

f	STD
$f_y = f_A + f_D$	σ_y
$f_A = \rho_{binder} * \frac{w}{b}$	σ_A
$f_D = \rho_{water}$	$\sigma_D = \sigma_{\rho.w}$

$$\sigma_A = f_A * \sqrt{\left(\frac{\sigma_{w/b}}{f_{A1}}\right)^2 + \left(\frac{\sigma_{\rho.b}}{f_{A2}}\right)^2} = \rho_{binder} * \frac{w}{b} * \sqrt{\left(\frac{\sigma_{w/b}}{\frac{w}{b}}\right)^2 + \left(\frac{\sigma_{\rho.b}}{\rho_{binder}}\right)^2} \quad \text{(A. 9)}$$

Table A - 36: Details relevant for (A. 9).

f	STD
$f_A = f_{A1} * f_{A2}$	σ_A
$f_{A1} = \frac{w}{b}$	$\sigma_{w/b}$
$f_{A2} = \rho_{binder}$	$\sigma_{\rho.b}$

$$\sigma_B = f_B * \sqrt{\left(\frac{\sigma_{\rho.b}}{f_{B1}}\right)^2 + \left(\frac{\sigma_{\rho.w}}{f_{B2}}\right)^2} = \rho_{binder} * \frac{w}{b} * \sqrt{\left(\frac{\sigma_{\rho.b}}{\rho_{binder}}\right)^2 + \left(\frac{\sigma_{\rho.w}}{\rho_{water}}\right)^2} \quad \text{(A. 10)}$$

Table A - 37: Details relevant for (A. 10)

f	STD
$f_B = f_{B1} * f_{B2}$	σ_B
$f_{B1} = \rho_{binder}$	$\sigma_{\rho.b}$
$f_{B2} = \rho_{water}$	$\sigma_{\rho.w}$

$$\sigma_C = f_C * \sqrt{\left(\frac{\sigma_A}{f_{C1}}\right)^2 + \left(\frac{\sigma_{\rho.w}}{f_{C2}}\right)^2} \qquad \text{(A. 11)}$$

$$= \rho_{binder} * \frac{w}{b} * \rho_{water} * \sqrt{\left(\frac{\sigma_A}{\rho_{binder} * \frac{w}{b}}\right)^2 + \left(\frac{\sigma_{\rho.w}}{\rho_{water}}\right)^2}$$

Table A - 38: Details relevant for (A. 11)

f	**STD**
$f_C = f_{C1} * f_{C2}$	σ_C
$f_{C1} = f_A = \rho_{binder} * \frac{w}{b}$	σ_A
$f_{C2} = \rho_{water}$	$\sigma_{\rho.w}$

A.13.2 ICP-MS

The following equations and tables were used to determine the uncertainty of the ICP-MS calculation.

$$\sigma_{ICP-MS} = \frac{f_1}{m_{initial}} \sqrt{\frac{\sigma_{f_1}{}^2}{f_1} + \frac{\sigma_{m_{initial}}{}^2}{m_{initial}}} \qquad \text{(A. 12)}$$

Table A - 39: Details relevant for (A. 12).

f	σ
$\frac{\mu g}{g} = \frac{\mu g}{L} * 101.4 * \frac{V_{initial} * 0.001 \frac{L}{mL}}{m_{initial}}$	σ_{ICP-MS}
$V_{initial}$	$\sigma_{V_{initial}}$
$m_{initial}$	$\sigma_{m_{initial}}$
$f_z = \mu \frac{g}{L} * 101.4$	σ_{f_z}
$f_1 = f_z * V_{initial}$	σ_{f_1}
$\frac{\mu g}{g} = \frac{f_1 * 0.001 \frac{L}{mL}}{m_{initial}}$	σ_{ICP-MS}

$$\sigma_{101.4} = \frac{V_x * V_1}{V_0 * V_2} \sqrt{\frac{\sigma_{V_x}{}^2}{V_x} + \frac{\sigma_{V_1}{}^2}{V_1} + \frac{\sigma_{V_0}{}^2}{V_0} + \frac{\sigma_{V_2}{}^2}{V_2}} \qquad \text{(A. 13)}$$

Table A - 40: Details relevant for (A. 13).

f	σ
$101.4 = \frac{V_x * V_1}{V_0 * V_2}$	$\sigma_{101.4}$
V_x	σ_{V_x}
V_1	σ_{V_1}
V_0	σ_{V_0}
V_2	σ_{V_2}

A.13.3 Potentiometric Titration

The following equations and tables were used to determine the uncertainty of the potentiometric titration calculation.

$$\sigma_{titration} = \frac{f_a}{m_c * M_{Cl}} \sqrt{\left(\frac{\sigma_{C_{fa}}}{f_a}\right)^2 + \left(\frac{\sigma_{m_c}}{m_c}\right)^2} \quad \text{(A. 14)}$$

Table A - 41: Details relevant for (A. 14).

f	STD
$\frac{Cl}{Concrete}[\frac{g}{g}] = \frac{f_a}{m_c * M_{Cl}}$	$\sigma_{titration}$
m_c	σ_{m_c}

$$\sigma_{fa} = C_{Cl} * V_{HNO3} \sqrt{\left(\frac{\sigma_{C_{cl}}}{C_{Cl}}\right)^2 + \left(\frac{\sigma_{V_{HNO_3}}}{V_{HNO3}}\right)^2} \quad \text{(A. 15)}$$

Table A - 42: Details relevant for (A. 15).

f	STD
$f_a = C_{Cl} * V_{HNO3}$	σ_{f_a}
V_{HNO3}	$\sigma_{V_{HNO3}}$

$$\sigma_{Ccl} = \frac{n_{Cl}}{V_{sample}} * \sqrt{\left(\frac{\sigma_{n_{Cl}}}{n_{Cl}}\right)^2 + \left(\frac{\sigma_{Vsample}}{V_{sample}}\right)^2} \quad \text{(A. 16)}$$

Table A - 43: Details relevant for (A. 16).

f	STD
$C_{Cl} = \frac{n_{Cl}}{V_{sample}}$	$\sigma_{C_{cl}}$

$$\sigma_{n_{Cl}} = V_{AgNO_3} * C_{AgNO_3} * \sqrt{\left(\frac{\sigma_{VAgNO3}}{V_{AgNO_3}}\right)^2 + \left(\frac{\sigma_{CAgNO3}}{C_{AgNO_3}}\right)^2} \quad \text{(A. 17)}$$

Table A - 44: Details relevant for (A. 17).

f	STD
V_{AgNO_3}	σ_{VAgNO3}
C_{AgNO_3}	σ_{CAgNO3}

A.14 Transitioning between $m_{Cl}/m_{concrete}$ and m_{Cl}/m_{Ca}

We want to find the mass ratio of aggregates over paste. With the µ-XRF, we can uniquely determine the area percentage of aggregates, $A\%_{agg.\mu XRF}$, from each thin section, using the phase separation tool in the software. We are then assuming that the area percentage of the aggregates is equal to the volume percentage.

$$\frac{a}{p} = \frac{m_{agg}}{m_{paste}} = \frac{\rho_{agg} * V_{agg}}{\rho_{paste} * V_{paste}} = \frac{\rho_{agg} * A\%_{agg.\mu XRF}}{\rho_{paste} * (1 - A\%_{agg.\mu XRF})} \quad \text{(A. 18)}$$

This can be used to calculate the $\frac{m_{Cl}}{m_{paste}}$ from the $\frac{m_{Cl}}{m_{concrete}}$:

$$\frac{m_{Cl}}{m_{concrete}} = \frac{m_{Cl}}{m_{paste} + m_{agg}} = \frac{m_{Cl}}{m_{paste} * \left(\frac{m_{paste}}{m_{paste}} + \frac{m_{agg}}{m_{paste}}\right)} = \frac{m_{Cl}}{m_{paste} * \left(1 + \frac{m_{agg}}{m_{paste}}\right)}$$

$$= \frac{m_{Cl}}{m_{paste}\left(1 + \frac{a}{p}\right)} \quad \text{(A. 19)}$$

$$\rightarrow \frac{m_{Cl}}{m_{paste}} = \frac{m_{Cl}}{m_{concrete}} * (1 + \frac{a}{p})$$

Using the w/b-ratio, we are then able to go from cl/paste to Cl/binder:

$$\frac{w}{b} = \frac{m_{water}}{m_{binder}} = 0.38 \quad \text{(A. 20)}$$

$$\frac{m_{Cl}}{m_{paste}} = \frac{m_{Cl}}{m_{binder} + m_{water}} = \frac{m_{Cl}}{m_{binder} * \left(\frac{m_{binder}}{m_{binder}} + \frac{m_{water}}{m_{binder}}\right)} = \frac{m_{Cl}}{m_{binder} * \left(1 + \frac{m_{water}}{m_{binder}}\right)}$$

$$= \frac{m_{Cl}}{m_{binder}\left(1 + \frac{w}{b}\right)} \quad \text{(A. 21)}$$

$$\rightarrow \frac{m_{Cl}}{m_{binder}} = \frac{m_{Cl}}{m_{paste}} * (1 + \frac{w}{b})$$

To be able to take the next and final step from $\frac{m_{Cl}}{m_{binder}}$ to $\frac{m_{Cl}}{m_{Ca}}$, we need to know the weight percentage of CaO in the cement. This is obtained from the oxide overview provided by the cement manufacturer. By using the molar masses of both calcium and oxygen, we can calculate the weight% of calcium in the mix.

$$\frac{m_{CaO}}{m_{binder}} * \frac{M_{Ca}}{M_{Ca} + M_O} \frac{m_{Ca}}{m_{CaO}} = \frac{m_{Ca}}{m_{binder}} \quad \text{(A. 22)}$$

Then we get:

$$\frac{m_{Cl}}{m_{binder} * \frac{m_{Cl}}{m_{binder}}} = \frac{m_{Cl}}{m_{Ca}} \quad \text{(A. 23)}$$

With

$$M_{Ca} - Molar\ mass\ of\ calcium$$

$$M_{Cl} - Molar\ mass\ of\ chlorine$$

The same process can be followed backwards to go from $\frac{m_{Cl}}{m_{Ca}}$ to $\frac{m_{Cl}}{m_{concrete}}$ instead:

$$\frac{m_{Cl}}{m_{concrete}} = \frac{m_{Cl}}{m_{Ca}} * \frac{m_{Ca}}{m_{CaO}} * \frac{m_{CaO}}{m_{binder}} * \frac{1}{1 + \frac{w}{b}} * \frac{1}{1 + \frac{a}{p}} \quad \text{(A. 24)}$$

A.15 Cement paste density calculation

The cement paste is the sum of binder and water, hence $m_{paste} = m_{binder} + m_{water}$.
In the following equation it has been assumed that also $V_{paste} = V_{binder} + V_{water}$, which implies no autogenous shrinkage. This is not true but as we do not know the chemical shrinkage exact, this assumption is made to simplify the calculation.

$$\rho_{paste} = \frac{m_p}{V_p} = \frac{m_w + m_b}{V_w + V_b} = \frac{m_w + m_b}{\frac{m_w}{\rho_w} + \frac{m_b}{\rho_b}} = \frac{(m_w + m_b)}{\frac{\rho_b * m_w + m_b * \rho_w}{\rho_w * \rho_b}}$$

$$= \frac{(m_w + m_b) * \rho_w * \rho_b}{\rho_b * m_w + m_b * \rho_w} * \frac{1/m_b}{1/m_b} \qquad \text{(A. 25)}$$

$$= \frac{\left(\frac{m_w}{m_b} + \frac{m_b}{m_b}\right) * \rho_w * \rho_b}{\frac{\rho_{binder} * m_{water}}{m_{binder}} + \frac{m_b * \rho_w}{m_b}} = \frac{\rho_b * \rho_w * \left(\frac{m_w}{m_b} + 1\right)}{\rho_b * \frac{m_w}{m_b} + \rho_w} = \frac{\rho_b * \rho_w * (\frac{w}{b} + 1)}{\rho_b * \frac{w}{b} + \rho_w}$$

with

$$\frac{w}{b} = \frac{m_w}{m_b} - Mass\ ratio\ of\ water\ to\ binder\ in\ the\ paste$$

$$\rho_p - Density\ of\ paste$$

$$\rho_w - Density\ of\ water$$

$$\rho_b - Density\ of\ binder$$

$$m_p - Mass\ of\ paste$$

$$m_w - Mass\ of\ water$$

$$m_b - Mass\ of\ binder$$

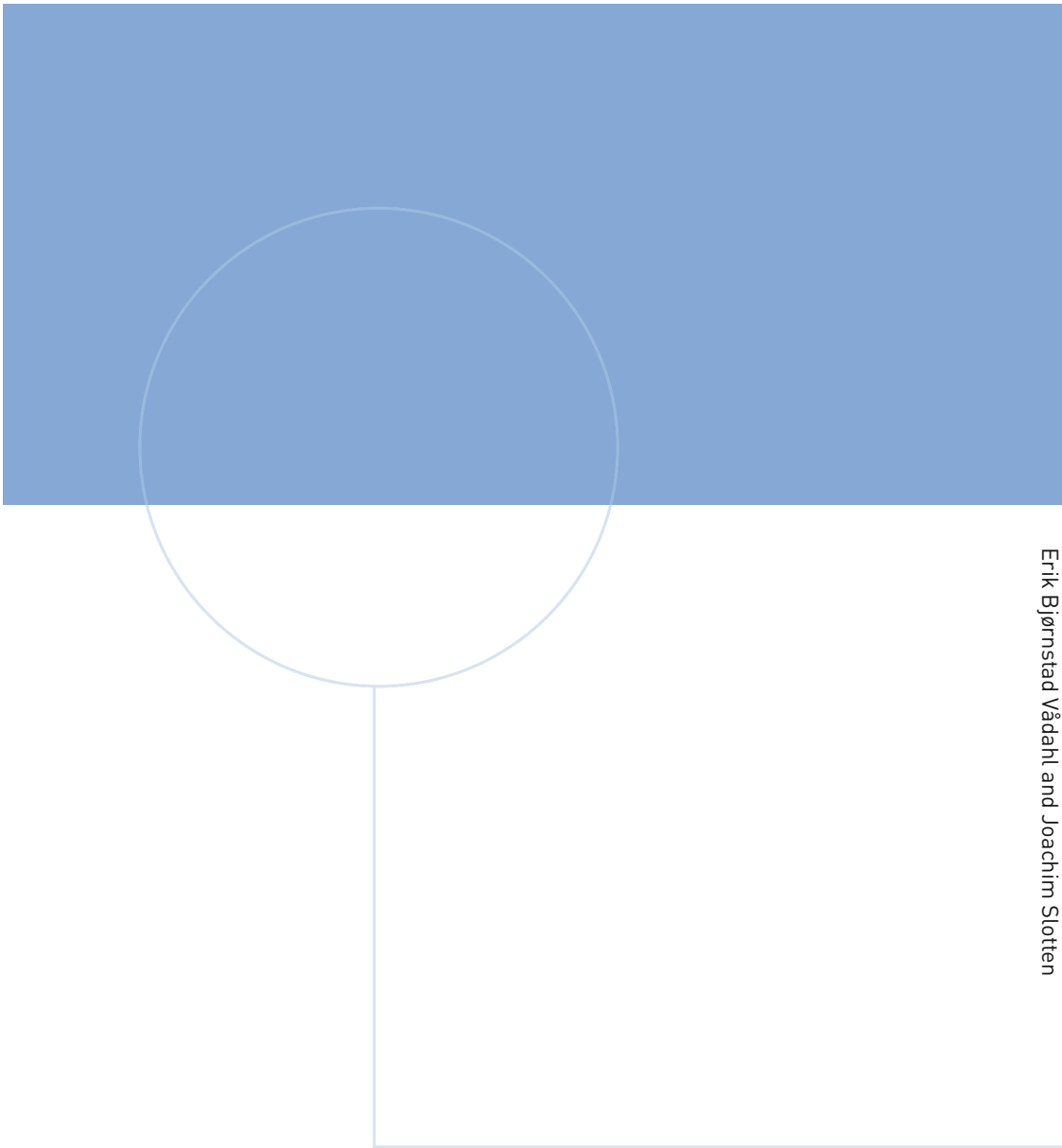

Erik Bjørnstad Vådahl and Joachim Slotten

NTNU
Kunnskap for en bedre verden